





# The Application of Non-invasive Inverse ECG Techniques in Cardiomyopathy

Machteld Johanna Boonstra

ISBN: 9789464198201

Cover en layout: MJ Boonstra

Printed by: Gildeprint

The research described in this thesis was supported by a grant of the Dutch Heart Foundation (PPS QRS-Vision, 2018B007).

Financial support by the Dutch Heart Foundation for the publication of this thesis is gratefully acknowledged.

Financial support by Chipsoft for the publication of this thesis is gratefully acknowledged.

© Machteld Johanna Boonstra, 2023

All rights reserved. No part of this thesis may be reproduced, stored or transmitted in any form or by any means without prior permission of the author, or the copyright owning journals for previously published papers.



# **The Application of Non-invasive Inverse ECG Techniques in Cardiomyopathy**

De toepassing van non-invasieve inverse ECG-technieken in hartspierziekten

*(met een samenvatting in het Nederlands)*

## **Proefschrift**

ter verkrijging van de graad van doctor aan de  
Universiteit Utrecht  
op gezag van de  
rector magnificus, prof.dr. H.R.B.M. Kummeling,  
ingevolge het besluit van het college voor promoties  
in het openbaar te verdedigen op

woensdag 21 juni 2023 des ochtends  
te 10.15 uur

door

**Machteld Johanna Boonstra**

geboren op 25 augustus 1993  
te Groningen

**Promotor**

Prof. dr. F.W. Asselbergs

**Copromotoren**

Dr. P.M. van Dam

Dr. P. Loh

**Beoordelingscommissie**

Prof. dr. O. Doessel

Prof. dr. P.A.F.M. Doevendans

Prof. dr. R.S. MacLeod

Prof. dr. J.P. van Tintelen (voorzitter)

Prof. dr. M.A. Vos

# Contents

<b>Chapter 1</b>	<b>General introduction and thesis outline</b>	7
<b>Part I - Incorporating physiological prior knowledge in inverse ECG methods</b>		
<b>Chapter 2</b>	Modeling the His-Purkinje Effect in Non-Invasive Estimation of Endocardial and Epicardial Ventricular Activation	23
<b>Chapter 3</b>	Comparing Non-invasive Inverse Electrocardiography With Invasive Endocardial and Epicardial Electroanatomical Mapping During Sinus Rhythm	47
<b>Chapter 4</b>	Non-invasive inverse ECG for the early detection and risk-stratification in arrhythmogenic cardiomyopathy, a proof-of-concept study	67
<b>Chapter 5</b>	Incorporating structural abnormalities in equivalent dipole layer based ECG simulation	91
<b>Part II - Linking the 12-lead ECGs to cardiac anatomy</b>		
<b>Chapter 6</b>	Novel CineECG enables anatomical 3D localization and classification of bundle branch blocks	117
<b>Chapter 7</b>	CineECG: A novel method to image the average activation sequence in the heart from the 12-lead ECG	133
<b>Part III - Enhancing the diagnostic value of the 12-lead ECG</b>		
<b>Chapter 8</b>	Feasibility study of a 3D camera to reduce electrode repositioning errors during longitudinal ECG acquisition	163
<b>Chapter 9</b>	Big Data and Artificial Intelligence: Opportunities and Threats in Electrophysiology	179
<b>Chapter 10</b>	<b>General discussion and future perspectives</b>	201
<b>Appendices</b>	English summary	212
	Nederlandse samenvatting	215
	List of publications	219
	Acknowledgements/Dankwoord	220
	Curriculum Vitae	225





## General introduction

The electrocardiogram (ECG) is a widely used clinical tool which provides insight in cardiac electrical activity to diagnose cardiac pathology. The technique itself has not undergone major changes since 1942, i.e. the assessment of the cardiac activation and recovery still relies on the interpretation from the standard 12-lead ECG. The ECG provides a rather distant view on the electrical activity of the heart as the electrodes placed on the skin only measure the potential resulting from the spatial summation of all simultaneous electrical activity. The view is further 'blurred' by the tissues between the electrodes and the cardiac electrical activity. Through invasive procedures, detailed insight in cardiac electrical activity can be obtained, but due to the high risk of such procedures, such procedures are not routinely performed. This thesis focusses on non-invasive ECG-based methods to obtain detailed insight on local cardiac activity, the so-called inverse ECG methods. The improvement and application of such techniques to detect disease onset and progression in cases of inherited arrhythmogenic cardiomyopathy is described. Additionally, new tools to enhance the diagnostic value of the 12-lead ECG are discussed.

### *Inherited cardiomyopathies*

In inherited cardiomyopathies, disease onset and progression are slow and the disease may develop over years from no phenotype to severe abnormalities.<sup>1,2</sup> Cardiomyopathies are characterized by a broad spectrum of disease phenotypes, potentially progressing into either heart failure or ventricular arrhythmia (VA).<sup>1,3</sup> Due to the identification of many pathogenic variants, predisposition for either hypertrophic-, dilated-, arrhythmogenic-, restrictive- or non-compaction cardiomyopathy is further unraveled. Throughout the last decade, our understanding of genotype-phenotype relation in inherited cardiomyopathies has improved substantially.<sup>4-7</sup>

However, disease penetrance is incomplete and phenotypic disease expression is heterogeneous, as indicated by the large variability in age of disease onset and the rate of progression. Overlap in phenotypic expression of underlying genotypic substrate is the rule rather than the exception.<sup>5-7</sup> Dilated cardiomyopathy (DCM) and arrhythmogenic cardiomyopathy (ACM) are two extremes of the cardiomyopathy spectrum. Whereas DCM usually manifests with symptoms of heart failure, in ACM electrical remodeling may precede structural changes and life-threatening VA can be the first disease manifestation. In family members of patients diagnosed with either ACM or DCM, deciding on the type and frequency of clinical evaluation is challenging due to the heterogeneous disease penetrance and progression. With increasing extent of structural abnormalities, prognosis worsens.<sup>8-11</sup>

Known genetic etiology of ACM comprises desmosomal, lamin A/C, filamin-C, and phospholamban gene variants impairing the electrical and structural stability of the myocardium. The known genetic etiology of DCM partially overlaps with these

genes.<sup>5,12-15</sup> Especially for asymptomatic variant carriers, it is important to determine whether carriers will develop either ACM or DCM as first phenotypical disease manifestation. However, besides genetic predisposition, environmental factors also play a pivotal role in disease manifestation as illustrated by the incomplete penetrance and heterogeneous disease expression of both ACM and DCM. For example, within one family carrying the same pathogenic variant; one member may suffer from lethal VA during the concealed phase of disease, whereas another remains unaffected.<sup>3,16</sup> On the other hand, in carriers already diagnosed with ACM, the identification of predictors of progression to a pure ACM-phenotype or a combination of A/DCM-phenotype is important to decide on appropriate clinical treatment regimen.

### *Current clinical diagnostic tools*

As in ACM first manifestation of disease may be life-threatening VA, the identification of yet asymptomatic individuals at-risk is crucial. Due to increased genetic cascade screening, more genotype-positive yet phenotype-negative at-risk family members are identified. These are often young, asymptomatic and healthy individuals who may or may not develop any sign of disease.<sup>3,8,13,17</sup> In these individuals, apart from the early identification of individuals at-risk for VA, selecting appropriate clinical follow-up intervals and deployed diagnostic tools to provide a personalized follow-up and treatment strategy is important.<sup>8</sup> However, due to the heterogeneous phenotypic disease expression and the either right-, left- or bi-ventricular involvement in disease, adequate risk-stratification remains challenging and very subtle signs of early manifestation of disease may easily go unnoticed.

Predictors to assess the first phenotypical expression and progression towards ACM and/or DCM-phenotype and left-/right-/bi-ventricular involvement are yet unidentified. Within the process of clinical follow-up, the decision on an individualized time interval for follow-up is difficult. Current guidelines recommend that individuals at-risk for ACM should undergo clinical evaluation every 1-3 years, starting at 10-12 years of age, as the disease is known to predominantly manifest in young adulthood.<sup>3,18-21</sup> With the identification of early signs of disease, treatment can be initiated and lifestyle changes may be proposed to reduce risk of VA. One example is the advice to reduce sport intensity, as individuals with a history of high-intensity exercise have a higher risk for VA.<sup>22,23</sup>

ACM diagnosis requires extensive clinical work-up aimed to identify any phenotypic expression of the disease. In ACM, the use of just one single test is not enough to identify disease. Therefore, a combination of diagnostic tools is usually used, as described in the task force criteria (TFC) for ARVC first published in 1994<sup>24</sup> and modified in 2010<sup>25</sup>. The TFC consists of six categories describing criteria with a high specificity for ACM as major and others as minor. The 12-lead electrocardiogram (ECG) plays a pivotal role in the TFC criteria as early electrical signs of disease may

precede first structural signs. With the ECG, electrical currents generated by the heart are measured as potentials at the body surface. The ECG provides direct insight in cardiac electrical activity and represents an indispensable, cheap, non-invasive and easy to use diagnostic tool in current clinical practice.

### *History of the ECG*

In 1895, a few years after the first measurement of human cardiac potentials on the body surface by Waller<sup>26</sup> (1887), Einthoven introduced a method to record the ECG in a way resembling the modern-day ECG recordings<sup>27</sup>. He introduced the 'Einthoven Triangle' to measure the three extremity leads I, II and III, wherewith general information about cardiac electrical activity is obtained. Additionally, he named the wave deflections that he observed during his recording as currently still used in clinical practice; the P-wave, QRS complex and T-wave. After the introduction of 'Wilson's Central Terminal' (WCT), an electrical reference computed from the extremity leads<sup>28</sup> (1931), precordial ECG leads (V1-V6) were introduced<sup>29</sup>. Using electrodes located at standardized positions close to the heart and referenced to the WCT, precordial leads are recorded. With these leads, more regional information about cardiac electrical activity is obtained, compared to the global information obtained with the extremity leads. Not long after<sup>30,31</sup> (1942), the augmented extremity leads were introduced, providing yet another global view on cardiac activity. The combination of the extremity leads (I, II, III), augmented extremity leads (aVR, aVL and aVF) and precordial leads (V1-V6) is what we know as the standard 12-lead ECG in current clinical practice.

### *Capturing cardiac electrical activity and function, the 12-lead ECG*

The ECG displays the spatial summation of the currents generated by depolarization and repolarization waves traveling through the myocardial tissue resulting in potentials at the body surface. By recording changes in these body surface potentials (BSP, also ECG), direct insight in cardiac electrical activity is obtained. The observed BSP are generated by changes in the transmembrane potential of myocardial cells due to a shift of intracellular and extracellular ion concentrations. The complex and correct interplay of different ion channels and electrolytes and cell-to-cell contact is essential for the initiation of cardiac contraction. As depolarization waves initiate cardiac contraction, a beat-to-beat pulsatile movement of blood is initiated. Disturbances in this process, due to electrolyte imbalance, channel dysfunction or conduction defects, may result in cardiac dysfunction or even arrhythmias.

Normal ventricular activation is initiated by the His-Purkinje system. The anatomy of the His-Purkinje was first described by Tawara et al.<sup>32</sup>, showing that the system consists of a branched network of isolated fast-conducting fibers. Further studies showed that there is a large anatomical variability<sup>33-36</sup> in the His-Purkinje system, and the study of Durrer et al.<sup>37</sup> showed that normal ventricular activation can be related to



the position of specific cardiac anatomical structures. Inter-individual differences in position of these structures (moderator band and papillary muscles) and the location of the septal initial sites of activation are directly related to QRS-morphology.<sup>38-40</sup>

In current clinical practice, the standard 12-lead ECG is used to assess rhythm (e.g. sinus rhythm, atrial fibrillation, ventricular arrhythmias), investigate waveform morphology to assess the presence of conduction disturbances (e.g. bundle branch block, scar, ischemia) and to perform measurements (e.g. QRS duration, QTc time). However, information about subtle progression of cardiac disease is more difficult to detect. Recently developed ECG-based deep learning algorithms do indicate that slight differences between ECGs can indicate for example reduced left ventricular ejection fraction<sup>41</sup> or hyperkalemia<sup>42</sup>. These observations indicate that the ECG does contain more information than currently accessible in clinical practice, it remains unknown where the algorithms based their decision on. To improve algorithm trustworthiness, current research is focused on the explainability of such algorithms.<sup>43</sup> Especially in progressive cardiomyopathies like ACM, subtle changes in ECG waveforms may indicate substrate development and such signs may be used for risk-stratification.<sup>44</sup> But accurate assessment is limited as (slight) inconsistencies in electrode positioning also cause ECG waveform changes. In such cases, it remains uncertain whether differences between subsequent ECGs is due to pathology or electrode positioning.

A second difficulty in ECG interpretation is linking cardiac electrical activity to cardiac anatomy. The vectorcardiogram was introduced to overcome this problem by representing cardiac electrical activity as a vector whereof the magnitude and direction changes over the cardiac cycle. It provides a three-dimensional representation of cardiac activity which is related to the thorax, but not to cardiac anatomy. Furthermore, the method requires the placement of additional leads in standardizes position and as is the case with the 12-lead ECG, the method remains sensitive to electrode placement.

#### *Solving the inverse problem of electrocardiography*

Solving an inverse problem is the process of estimating causal parameters underlying a set of observations, in particular, the factors resulting in observations are estimated from the observation itself. Specifically, solving the inverse problem of electrocardiography means that cardiac electrical activity resulting in observed body surface potentials (BSP) is non-invasively estimated. The application of iECG techniques in a slowly progressing disease like ACM may enable the early identification of disease even prior to structural or mechanical defects. Whereas in principle, the 12-lead ECG can be used to image the cardiac activation sequence, it only provides a succinct representation of cardiac electrical activity. By imaging the complex interplay of electrical waves underlying the ECG using iECG techniques, important additional knowledge about the underlying cardiac substrate can be obtained.<sup>45-54</sup>

In inherited cardiomyopathies, such an imaging technique may potentially be very valuable to study progression of the underlying cardiac substrate and to improve risk-stratification methods.<sup>45,55-57</sup>

In principle, the relation between ECG and cardiac electrical currents comes down to Ohms law ( $V=I \cdot R$ ), where the potentials observed at the body surface ( $V$ ) are the result of generated cardiac currents ( $I$ ) and the resistance between the heart and the body surface ( $R$ ). With iECG techniques, extensive BSP measurements are combined with subject specific anatomy to estimate cardiac electrical activity.<sup>51,53,58-61</sup> However, the problem is fundamentally hampered as completely different ventricular activation sequences can explain one BSP waveform, also referred to as ill-posedness.<sup>62-64</sup> The direct relation between cardiac electrical currents and recorded BSP is 'blurred', as recorded waveforms are the result of spatial summation of the current generated by simultaneous activation wavefronts, resulting in partial cancellation and amplification. With an increasing number of activation waves (sinus rhythm), solving the inverse problem of ECG inherently becomes more complicated.<sup>53</sup>

To allow for a robust approximation of the cardiac activation sequence, iECG procedures are regularized. Most used regularization methods in iECG are the zero order Tikhonov, regularizing local amplitude, and the second order Tikhonov, regularizing local acceleration and deceleration, also known as Laplacian regularization. These methods pose mathematical constraints to the estimated activation sequences to secure important physiological characteristics of the estimated activation sequence.<sup>65-68</sup> As most of the possible cardiac activation sequences explaining a BSP waveform are implausible from an electrophysiological point of view, regularization was the first basic attempt to constrain the inverse estimation towards the selection of a physiologically realistic solution. Such a regularization technique however only mathematically constrains one important characteristic, but others may still be electrophysiologically inaccurate.

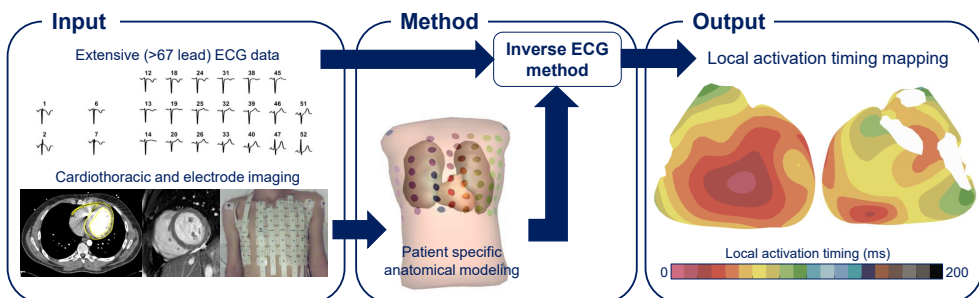


**Figure 1.** General overview of traditional inverse ECG techniques.

The potential-based formulation (Equivalent Potential Distribution, EPD<sup>69,70</sup>) and the wavefront-based formulation (Equivalent Dipole Layer, EDL<sup>71,72</sup>) are the two most well-known iECG techniques (Figure 1). Both methods require detailed patient specific anatomical data, extensive ECG measurements (>67 leads) and precise information regarding electrode positioning. The most commonly used method is the EPD-model, where the cardiac activation pattern is estimated by solving the mathematical linear relation between electrical potentials on the body surface and the epicardial surface. In recent studies<sup>73-76</sup>, a novel EPD based formulation was introduced to allow for the estimation of both endocardial and epicardial potentials, but assumptions made in this novel method remains under debate. EDL-based iECG relates endocardial and epicardial cardiac electrical currents at any time instant to body surface potentials. The foundation of the model lies in work by Wilson et al.<sup>77</sup> in 1933, who described activation wavefronts traveling through the myocardium using a dipole layer<sup>78,79</sup>. In 1978, Salu<sup>80</sup> showed the equivalence between this dipole layer at the wavefront and a dipole layer at the depolarized surface bounding the ventricular myocardium, based on the solid angle theory<sup>81</sup>. Along with the work of Geselowitz<sup>71,82</sup>, who observed that the local dipole layer strength is proportional to the local transmembrane potential and that the model also holds in homogeneous anisotropic tissue, the groundwork for the current EDL model was laid<sup>83,84</sup>. As the simulated currents in the heart follow the local transmembrane potential waveform, a direct link to cardiac electrophysiology was created. Both the EPD-based formulation and EDL-based formulation are ill-posed and therefore requires regularization. But as EDL-based iECG additionally requires an initial estimation due to the non-linearity of the formulation. This EDL-based initial estimate can be further optimized based on ventricular electrophysiological properties.

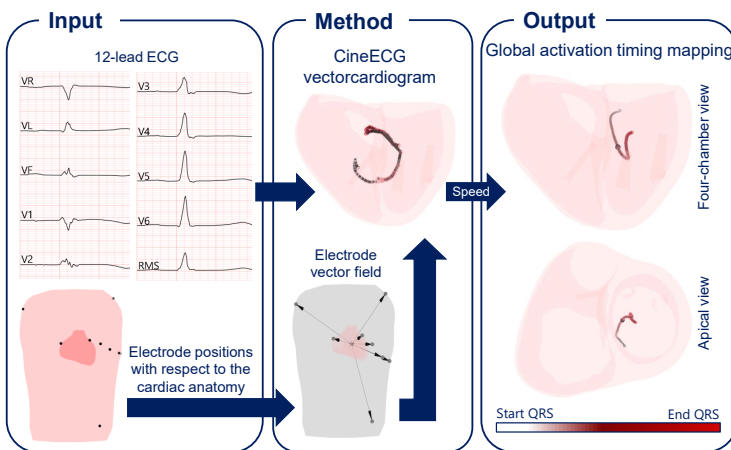


**Figure 2.** General overview of the CineECG technique.

As indicated previously, with decreasing QRS duration, the inverse problem becomes inherently more complex due to the interplay of several waveforms initiated through the His-Purkinje system at distinct sites at the ventricular endocardium.<sup>37</sup> This has been recently shown in a large cohort study using the EPD-based technique<sup>53</sup>, where with decreasing QRS duration, the inversely estimated activation sequence corresponded less well to invasive measurements. Therefore, in these cases, additional regularization is required to enable the application of iECG to identify early signs of disease.

Traditional iECG techniques (Figure 1, EPD- and EDL-based) are mathematically complex and computationally demanding. They require many more leads than the standard 12-lead ECG, which in application is expensive and time-consuming. CineECG was introduced in an attempt to image key temporo-spatial features of the activation sequence that are difficult to reliably obtain from the ECG using just the 12-lead ECG, thus the additional burden of electrode numbers is minimized. With CineECG, the average position of cardiac activity at each time instant is projected into the cardiac anatomy, thereby providing a direct link between cardiac anatomy and electrical activity. The computation is based on a simplified anatomical model combined with a vector direction-oriented approach and provides a mathematically and computationally lightweight and less complex alternative to traditional inverse ECG methods. CineECG has been shown to be a robust technique to detect substrate in Brugada Type-1 patients and differentiate between bundle branch blocks and may play an important additive role for the early detection of disease onset and progression.

## Thesis outline

With (the optimization of) iECG techniques, current clinical practice regarding ACM diagnosis and risk-stratification may be further enhanced. In this thesis, we describe several methods to enhance the diagnostic yield of the ECG in the identification and risk-stratification of ACM.

In **Part I**, we specifically focus on the optimization of EDL-based iECG for normal ventricular activation estimation. In **Chapter 2**, we describe the incorporation of subject-specific His-Purkinje model into the iECG method and we compare the non-invasively estimated activation maps to invasive maps in **Chapter 3**. In **Chapter 4**, we apply the improved method in pathogenic variant carriers and controls and compare findings to cardiac MRI examination and clinical characteristics. In **Chapter 5**, we describe a new method to model myocardial disease in EDL-based ECG simulations.

In **Part II**, we describe our novel 12-lead based inverse ECG method, CineECG, to estimate the average direction of cardiac electrical activity. We first conceptually validated the novel method in cases of bundle branch blocks, as described in **Chapter 6**. Thereafter, we further optimized the method and validated the method through a simulation study, as described in **Chapter 7**. In the same chapter, we test the method for its robustness in electrode positioning and use of a generic versus personalized anatomical model by using in-patient data and compare the obtained average activation sequence to invasively acquired local activation timing maps.

In **Part III**, we describe new tools to enhance the diagnostic yield of the 12-lead ECG. Therefore, in **Chapter 8**, a new 3D-camera based method is described to improve repositioning of ECG electrodes. Furthermore, in **Chapter 9**, the upcoming field of big data and artificial intelligence is described together with potentially promising new research directions to further unravel the complex nature of disease progression in ACM.

In **Chapter 10**, I discuss how the described techniques in this thesis can enhance diagnosis and risk-stratification in ACM. Therefore, the techniques are put into perspective within possible fields of application in current clinical practice and describe other techniques showing potential benefits in the early detection of disease onset and progression in inherited cardiomyopathies. Additionally, future studies are proposed to further improve the described methods.

## References

- Elliott P, Andersson B, Arbustini E, Bilinska Z, Cecchi F, Charron P, et al. Classification of the cardiomyopathies: a position statement from the European Society Of Cardiology Working Group on Myocardial and Pericardial Diseases. *Eur Heart J*. 2008;29(2):270-6.
- Rapezzi C, Arbustini E, Caforio AL, Charron P, Gimeno-Blanes J, Heliö T, et al. Diagnostic work-up in cardiomyopathies: bridging the gap between clinical phenotypes and final diagnosis. A position statement from the ESC Working Group on Myocardial and Pericardial Diseases. *Eur Heart J*. 2013;34(19):1448-58.
- Groeneweg JA, Bhonsale A, James CA, Te Riele AS, Dooijes D, Tichnell C, et al. Clinical presentation, long-term follow-up, and outcomes of 1001 arrhythmogenic right ventricular dysplasia/cardiomyopathy patients and family members. *Circulation*. 2015;8(3):437-46.
- Costa S, Cerrone M, Saguner AM, Brunchhorst C, Delmar M, Duru F. Arrhythmogenic cardiomyopathy: An in-depth look at molecular mechanisms and clinical correlates. *Trends in Cardiovascular Medicine*. 2021;31(7):395-402.
- Delmar M, McKenna WJ. The cardiac desmosome and arrhythmogenic cardiomyopathies: from gene to disease. *Circulation research*. 2010;107(6):700-14.
- James CA, Syrris P, Van Tintelen JP, Calkins H. The role of genetics in cardiovascular disease: arrhythmogenic cardiomyopathy. *Eur Heart J*. 2020;41(14):1393-400.
- Wilde Arthur A, Christopher S, Márquez Manlio F, Shamloo Alireza S, Ackerman Michael J, Ashley Euan A, et al. European Heart Rhythm Association (EHRA)/Heart Rhythm Society (HRS)/Asia Pacific Heart Rhythm Society (APHRS)/Latin American Heart Rhythm Society (LAHRS) Expert Consensus Statement on the state of genetic testing for cardiac diseases. *Journal of Arrhythmia*.
- Te Riele AS, James CA, Groeneweg JA, Sawant AC, Kammers K, Murray B, et al. Approach to family screening in arrhythmogenic right ventricular dysplasia/cardiomyopathy. *Eur Heart J*. 2016;37(9):755-63.
- Mast TP, Taha K, Cramer MJ, Lumens J, van der Heijden JF, Bouma BJ, et al. The prognostic value of right ventricular deformation imaging in early arrhythmogenic right ventricular cardiomyopathy. *JACC: Cardiovascular Imaging*. 2019;12(3):446-55.
- Taha K, Mast TP, Cramer MJ, van der Heijden JF, Asselbergs FW, Doevendans PA, et al. Evaluation of disease progression in arrhythmogenic cardiomyopathy: the change of echocardiographic deformation characteristics over time. *Cardiovascular Imaging*. 2020;13(2, Part 2):631-4.
- Chivulescu M, Lie ØH, Popescu BA, Skulstad H, Edvardsen T, Jurcut RO, et al. High penetrance and similar disease progression in probands and in family members with arrhythmogenic cardiomyopathy. *Eur Heart J*. 2020;41(14):1401-10.
- Corrado D, Basso C, Thiene G, McKenna WJ, Davies MJ, Fontaliran F, et al. Spectrum of clinicopathologic manifestations of arrhythmogenic right ventricular cardiomyopathy/dysplasia: a multicenter study. *Journal of the American College of Cardiology*. 1997;30(6):1512-20.
- Bhonsale A, Groeneweg JA, James CA, Dooijes D, Tichnell C, Jongbloed JD, et al. Impact of genotype on clinical course in arrhythmogenic right ventricular dysplasia/cardiomyopathy-associated mutation carriers. *Eur Heart J*. 2015;36(14):847-55.
- Tiso N, Stephan DA, Nava A, Bagattin A, Devaney JM, Stanchi F, et al. Identification of mutations in the cardiac ryanodine receptor gene in families affected with arrhythmogenic right ventricular cardiomyopathy type 2 (ARVD2). *Hum Mol Genet*. 2001;10(3):189-94.
- Van Der Zwaag PA, Van Rijsingen IA, Asimaki A, Jongbloed JD, Van Veldhuisen DJ, Wiesfeld AC, et al. Phospholamban R14del mutation in patients diagnosed with dilated cardiomyopathy or arrhythmogenic right ventricular cardiomyopathy: evidence supporting the concept of arrhythmogenic cardiomyopathy. *European journal of heart failure*. 2012;14(11):1199-207.
- Link MS, Laidlaw D, Polonsky B, Zareba W, McNitt S, Gear K, et al. Ventricular arrhythmias in the North American multidisciplinary study of ARVC: predictors, characteristics, and treatment. *Journal of the American College of Cardiology*. 2014;64(2):119-25.
- Towbin JA, McKenna WJ, Abrams DJ, Ackerman MJ, Calkins H, Darriueux FC, et al. 2019 HRS expert consensus statement on evaluation, risk stratification, and management of arrhythmogenic cardiomyopathy. *Heart rhythm*. 2019;16(11):e301-e72.
- Bauce B, Rampazzo A, Basso C, Mazzotti E, Rigato I, Steriotis A, et al. Clinical phenotype and diagnosis of arrhythmogenic right ventricular cardiomyopathy in pediatric patients carrying desmosomal gene mutations. *Heart Rhythm*. 2011;8(11):1686-95.
- Te Riele AS, James CA, Sawant AC, Bhonsale A, Groeneweg JA, Mast TP, et al. Arrhythmogenic right ventricular dysplasia/cardiomyopathy in the pediatric population: clinical characterization and comparison with adult-onset disease. *JACC: Clinical Electrophysiology*. 2015;1(6):551-60.
- Nava A, Bauce B, Basso C, Muriago M, Rampazzo A, Villanova C, et al. Clinical profile and long-term follow-up of 37 families with arrhythmogenic right ventricular cardiomyopathy. *Journal of the American College of Cardiology*. 2000;36(7):2226-33.
- Quarta G, Muir A, Pantazis A, Syrris P, Gehmlich K, Garcia-Pavia P, et al. Familial evaluation in arrhythmogenic right ventricular cardiomyopathy: impact of genetics and revised task force criteria. *Circulation*. 2011;123(23):2701-9.
- Lie ØH, Dejgaard LA, Saberniak J, Rootwelt C, Stokke MK, Edvardsen T, et al. Harmful effects of exercise intensity and exercise duration in patients with arrhythmogenic cardiomyopathy. *Clinical Electrophysiology*. 2018;4(6):744-53.
- Ruwald A-C, Marcus F, Estes III NM, Link M, McNitt S, Polonsky B, et al. Association of competitive and recreational sport participation with cardiac events in patients with arrhythmogenic right ventricular cardiomyopathy: results from the North American multidisciplinary study of arrhythmogenic right ventricular cardiomyopathy. *Eur Heart J*.

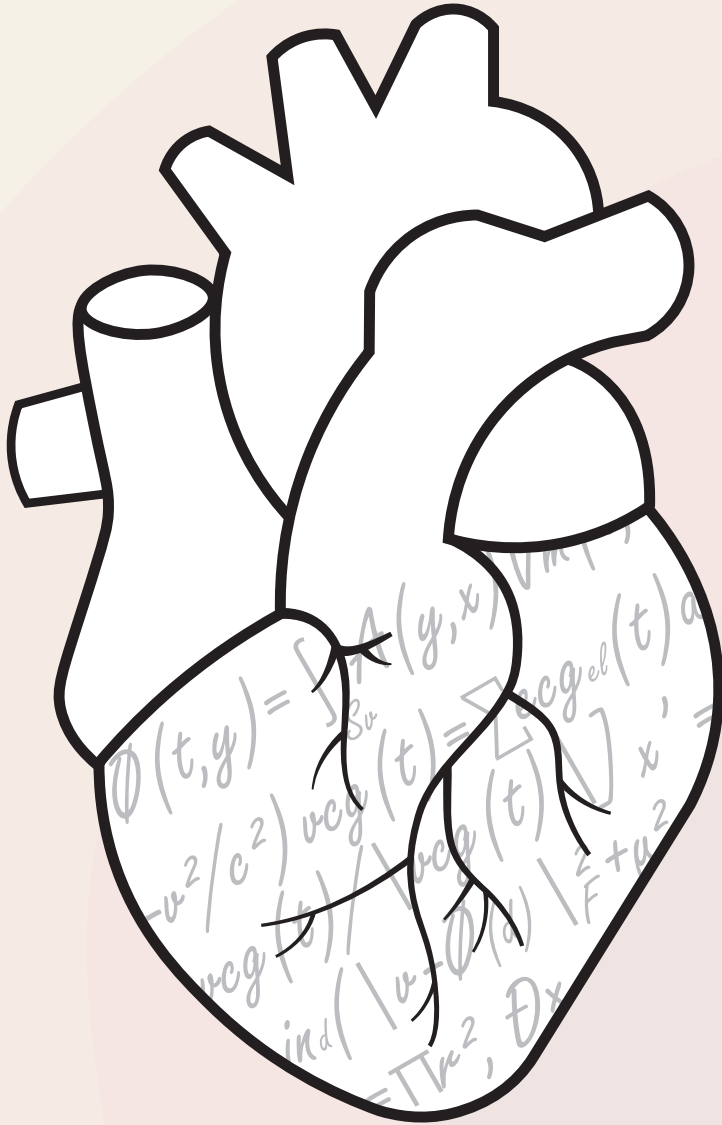
- 2015;36(27):1735-43.
24. McKenna WJ, Thiene G, Nava A, Fontaliran F, Blomstrom-Lundqvist C, Fontaine G, et al. Diagnosis of arrhythmogenic right ventricular dysplasia/cardiomyopathy. Task Force of the Working Group Myocardial and Pericardial Disease of the European Society of Cardiology and of the Scientific Council on Cardiomyopathies of the International Society and Federation of Cardiology. *British heart journal*. 1994;71(3):215.
  25. Marcus FI, McKenna WJ, Sherrill D, Basso C, Bauce B, Bluemke DA, et al. Diagnosis of arrhythmogenic right ventricular cardiomyopathy/dysplasia: proposed modification of the task force criteria. *Circulation*. 2010;121(13):1533-41.
  26. Waller A. A demonstration on man of the electromotive changes accompanying the heart's beat. *J Physiol*. 1887;8:229-34.
  27. Einthoven W. Ueber die Form des menschlichen Electrocardiogramms. *Pflügers Archiv European Journal of Physiology*. 1895;60(3):101-23.
  28. Wilson FN, Macleod AG, Barker PS. The potential variations produced by the heart beat at the apices of Einthoven's triangle. *American Heart Journal*. 1931;7(2):207-11.
  29. Barnes AR, Pardee HE, White PD, Wilson FN, Wolfarth CC. Standardization of precordial leads: supplementary report. *American Heart Journal*. 1938;15(2):235-9.
  30. Goldberger E. A simple, indifferent, electrocardiographic electrode of zero potential and a technique of obtaining augmented, unipolar, extremity leads. *American Heart Journal*. 1942;23(4):483-92.
  31. Goldberger E. The aVL, aVR, and aVF leads: a simplification of standard lead electrocardiography. *American Heart Journal*. 1942;24(3):378-96.
  32. Tawara S. Das Reizleitungssystem des Säugetierherzens. Eine Anatomisch-Histologische Studie über das Atrioventrikulärbündel und die Purkinjeschen Faden. Jena: Gustav Fischer; 1906.
  33. Keith A, Flack M. The auriculo-ventricular bundle of the human heart. *The Lancet*. 1906;168(4328):359-64.
  34. Ho SY, McCARTHY KP, Ansari A, Thomas PS, Sánchez-Quintana D. Anatomy of the atrioventricular node and atrioventricular conduction system. *International Journal of Bifurcation and Chaos*. 2003;13(12):3665-74.
  35. Massing GK, James TN. Anatomical configuration of the His bundle and bundle branches in the human heart. *Circulation*. 1976;53(4):609-21.
  36. Demoulin J, Kulbertus H. Histopathological examination of concept of left hemiblock. *British Heart Journal*. 1972;34(8):807.
  37. Durrer D, van Dam RT, Freud GE, Janse MJ, Meijler FL, Arzbaeher RC. Total excitation of the isolated human heart. *Circulation*. 1970;41:899-912.
  38. Loukas M, Klaassen Z, Tubbs RS, Derderian T, Paling D, Chow D, et al. Anatomical observations of the moderator band. *Clin Anat*. 2010;23(4):443-50.
  39. Hakacova N, Robinson AM, Olson CW, Selvester RH, Wagner GS. The relationship between mitral papillary muscles positions and characteristics of the QRS complex. *J Electrocardiol*. 2008;41(6):487-90.
  40. Saha A, Roy S. Papillary muscles of left ventricle—Morphological variations and it's clinical relevance. *Indian heart journal*. 2018;70(6):894-900.
  41. Yao X, Rushlow DR, Inselman JW, McCoy RG, Thacher TD, Behnken EM, et al. Artificial intelligence-enabled electrocardiograms for identification of patients with low ejection fraction: a pragmatic, randomized clinical trial. *Nat Med*. 2021;27(5):815-9.
  42. Galloway CD, Valys AV, Shreibati JB, Treiman DL, Petterson FL, Gundotra VP, et al. Development and validation of a deep-learning model to screen for hyperkalemia from the electrocardiogram. *JAMA cardiology*. 2019;4(5):428-36.
  43. van de Leur RR, Bos MN, Taha K, Sammani A, Yeung MW, van Duijvenboden S, et al. Improving explainability of deep neural network-based electrocardiogram interpretation using variational auto-encoders. *European Heart Journal-Digital Health*. 2022;3(3):390-404.
  44. van de Leur RR, Taha K, Bos MN, van der Heijden JF, Gupta D, Cramer MJ, et al. Discovering and visualizing disease-specific electrocardiogram features using deep learning: proof-of-concept in phospholamban gene mutation carriers. *Circ Arrhythm Electrophysiol*. 2021;14(2):e009056.
  45. Andrews CM, Srinivasan NT, Rosmini S, Bulluck H, Orini M, Jenkins S, et al. Electrical and structural substrate of arrhythmogenic right ventricular cardiomyopathy determined using noninvasive electrocardiographic imaging and late gadolinium magnetic resonance imaging. *Circ Arrhythm Electrophysiol*. 2017;10(7):e005105.
  46. Oosterhoff P, Meijborg VM, van Dam PM, van Dessel PF, Belterman CN, Streekstra GJ, et al. Experimental validation of noninvasive epicardial and endocardial activation imaging. *Circ Arrhythm Electrophysiol*. 2016.
  47. Gordon JP, Laks M, Boyle NG, van Dam PM. Advantages of the Cardiac Isochrone Positioning System for Localization of PVCs to the Endocardium, Epicardium, and Mid-myocardium from a 12 lead ECG. *Circulation*. 2014;130(Suppl 2):A19734.
  48. Potyagaylo D, Chmelevsky M, Van Dam P, Budanova M, Zubarev S, Treshkur T, et al. ECG Adapted Fastest Route Algorithm to Localize the Ectopic Excitation Origin in CRT Patients. *Frontiers in physiology*. 2019;10.
  49. Sapp JL, Dawoud F, Clements JC, Horáček BM. Inverse Solution Mapping of Epicardial Potentials: Quantitative Comparison With Epicardial Contact Mapping. *Circ Arrhythm Electrophysiol*. 2012;5(5):1001-9.
  50. Linnenbank AC, Van Oosterom A, Oostendorp TF, van Dessel P, Van Rossum AC, Coronel R, et al., editors. Non-invasive imaging of activation times during drug-induced conduction changes. *World Congress on Medical Physics and Biomedical Engineering, IFMBE*; 2006; Seoul.
  51. Rudy Y. Noninvasive Electrocardiographic Imaging of Arrhythmogenic Substrates in Humans. *Circulation Research*. 2013;112(5):863-74.
  52. Cluitmans MJ, Bear LR, et al. Noninvasive detection of spatiotemporal activation-repolarization interactions that prime idiopathic ventricular fibrillation. *Science Translational Medicine*. 2021;13(620):eab9137.



53. Duchateau J, Sacher F, Pambrun T, Derval N, Chamorro-Servent J, Denis A, et al. Performance and limitations of noninvasive cardiac activation mapping. *Heart Rhythm*. 2019;16(3):435-42.
54. Vijayakumar R, Silva JN, Desouza KA, Abraham RL, Strom M, et al. Electrophysiologic substrate in congenital long QT syndrome: noninvasive mapping with electrocardiographic imaging (ECGI). *Circulation*. 2014;130(22):1936-43.
55. Orini M, Graham AJ, Martínez-Naharro A, Andrews CM, de Marvao A, Statton B, et al. Noninvasive mapping of the electrophysiological substrate in cardiac amyloidosis and its relationship to structural abnormalities. *Journal of the American Heart Association*. 2019;8(18):e012097.
56. Graham AJ, Orini M, Zacur E, Dhillon G, Daw H, Srinivasan NT, et al. Simultaneous comparison of electrocardiographic imaging and epicardial contact mapping in structural heart disease. *Circ Arrhythm Electrophysiol*. 2019;12(4):e007120.
57. Graham AJ, Orini M, Zacur E, Dhillon G, Jones D, Prabhu S, et al. Assessing Noninvasive Delineation of Low-Voltage Zones Using ECG Imaging in Patients With Structural Heart Disease. *Clinical Electrophysiology*. 2022;8(4):426-36.
58. Huiskamp G, Van Oosterom A. The depolarization sequence of the human heart surface computed from measured body surface potentials. *IEEE Trans Biomed Eng*. 1988;35(12):1047-58.
59. Ramanathan C, Ghanem R, Jia P, Ryu K, Rudy Y. Noninvasive electrocardiographic imaging for cardiac electrophysiology and arrhythmia. *Nature medicine*. 2004;10(4):422-8.
60. Cluitmans MJ, Bonizzi P, Karel JM, Das M, Kietselaer BL, de Jong MM, et al. In vivo validation of electrocardiographic imaging. *JACC: Clinical Electrophysiology*. 2017;3(3):232-42.
61. van Oosterom A. Computing the depolarization sequence at the ventricular surface from body surface potentials. In: Rudy JLaRPaY, editor. *Pediatric and Fundamental Electrocardiography*. Dordrecht: Martinus Nijhoff Publ.; 1987. p. 75-89.
62. Cluitmans M, Brooks DH, MacLeod R, Dössel O, Guillem MS, van Dam PM, et al. Validation and opportunities of electrocardiographic imaging: from technical achievements to clinical applications. *Frontiers in physiology*. 2018;9:1305.
63. Cluitmans MJ, Clerx M, Vandersickel N, Peeters RL, Volders PG, Westra RL. Physiology-based regularization of the electrocardiographic inverse problem. *Med Biol Eng Comput*. 2017;55(8):1353-65.
64. Tikhonov AN, Arsenin VY. *Solutions of Ill-posed Problems*. New York: Wiley; 1977.
65. Brooks DH, Ahmad G, MacLeod RS, editors. *Multiply constraint inverse electrocardiography: Combined temporal, multiple spatial, and iterative regularization*. Engineering advances New opportunities for biomedical engineers Proceedings of the 16th Annual International Conference of the IEEE Engineering in Medicine and Biology Society; 1994; Piscataway: IEEE publishing services.
66. Clements JC, Carroll R, Horáček BM. On Regularization Parameters for Inverse Problems in Electrocardiography. In: Ghista DN, editor. *Biomedical and Life Physics*. Wiesbaden: Vieweg; 1996.
67. Colli-Franzone PC, Guerri L, Taccardi B, Viganotti C. The direct and inverse potential problems in electrocardiology. Numerical aspects of some regularization methods and application to data collected in dog heart experiments. Pavia: I.A.N.-C.N.R.; 1979.
68. Huiskamp G. Difference formulas for the surface Laplacian on a triangulated surface. *Journal of Computational Physics*. 1991;95(2):477-96.
69. Bear LR, LeGrice IJ, Sands GB, Lever NA, Loiselle DS, Paterson DJ, et al. How accurate is inverse electrocardiographic mapping? A systematic in vivo evaluation. *Circ Arrhythm Electrophysiol*. 2018;11(5):e006108.
70. Rudy Y, Messinger-Rapport BJ. The Inverse Problem in Electrocardiology: Solutions in Terms of Epicardial Potentials. *Crit Rev Biomed Eng*. 1988;16:215-68.
71. Geselowitz DB. Description of cardiac sources in anisotropic cardiac muscle. Application of bidomain model. *J Electrocardiol*. 1992;25 Supp.:65-7.
72. van Dam PM, Oostendorp TF, Linnenbank AC, van Oosterom A. Non-invasive imaging of cardiac activation and recovery. *Ann Biomed Eng*. 2009;37(9):1739-56.
73. Bokeriya L, Revishvili AS, Kalinin A, Kalinin V, Lyadzina O, Fetisova E. Hardware-software system for noninvasive electrocardiographic heart examination based on inverse problem of electrocardiography. *Biomed Eng*. 2008;42(6):273.
74. Kalinin A. Iterative algorithm for the inverse problem of electrocardiography in a medium with piecewise-constant electrical conductivity. *Computational Mathematics and Modeling*. 2011;22(1):30-4.
75. Revishvili AS, Wissner E, Lebedev DS, Lemes C, Deiss S, Metzner A, et al. Validation of the mapping accuracy of a novel non-invasive epicardial and endocardial electrophysiology system. *Ep Europace*. 2015;17(8):1282-8.
76. Rudic B, Chaykovskaya M, Tsyganov A, Kalinin V, Tülümen E, Papavassiliu T, et al. Simultaneous non-invasive epicardial and endocardial mapping in patients with Brugada syndrome: New insights into arrhythmia mechanisms. *Journal of the American Heart Association*. 2016;5(11):e004095.
77. Wilson FN, Macleod AG, Barker PS. The Distribution of Action Currents produced by the Heart Muscle and Other Excitable Tissues immersed in Conducting Media. *J Gen Physiol*. 1933;16:423-56.
78. Scher AM, Young AC, Malmgren AL, Paton RR. Spread of Electrical Activity Through the Wall of the Ventricle. *Cardiovasc Res*. 1953;1:539-47.
79. Durrer D, van der Tweel LH. Spread of activation in the left ventricular wall of the dog. *Am Heart J*. 1953;46:683-91.
80. Salu Y. Relating the Multipole Moments of the Heart to Activated Parts of the Epicardium and Endocardium. *Annals of Biomedical Eng*. 1978;6:492-505.
81. van Oosterom A. Solidifying the Solid Angle. *J Electrocardiol*. 2002;35S:181-92.
82. Geselowitz DB. On the Theory of the Electrocardiogram. *Proc IEEE*. 1989;77(6):857-76.
83. Huiskamp G. Simulation of depolarization in a membrane-equations-based model of the anisotropic ventricle. *IEEE Trans Biomed Eng*. 1998;45(7):847-55.
84. Simms HD, Geselowitz DB. Computation of Heart Surface Potentials Using the Surface Source Model. *J Cardiovasc Electrophysiol*. 1995;6:522-31.







# Part I

## Incorporating physiological prior knowledge in inverse ECG methods

### **Chapter 2**

Modeling the His-Purkinje Effect in Non-Invasive Estimation of Endocardial and Epicardial Ventricular Activation

### **Chapter 3**

Comparing Non-invasive Inverse Electrocardiography With Invasive Endocardial and Epicardial Electroanatomical Mapping During Sinus Rhythm

### **Chapter 4**

Non-invasive inverse ECG for the early detection and risk-stratification in arrhythmogenic cardiomyopathy, a proof-of-concept study

### **Chapter 5**

Incorporating structural abnormalities in equivalent dipole layer based ECG simulation



$\emptyset$

$(x, y) = \int_{S_u}$

$v_2 / c^2$

$v_{cg}$

$S_u$

ind

## Chapter 2

### Modeling the His-Purkinje Effect in Non-Invasive Estimation of Endocardial and Epicardial Ventricular Activation

MJ Boonstra\*, RW Roudijk\*, R Brummel, W Kassenberg, LJ Blom, TF Oostendorp,  
ASJM te Riele, JF van der Heijden, FW Asselbergs, P Loh, and PM van Dam.

\*The first two authors contributed equally to this manuscript

*Annals of Biomedical Engineering*. 2022 Mar; 50(3) :343-359

## **Abstract**

Inverse electrocardiography (iECG) estimates epi- and endocardial electrical activity from body surface potentials maps (BSPM). In individuals at risk for cardiomyopathy, non-invasive estimation of normal ventricular activation may provide valuable information to aid risk stratification to prevent sudden cardiac death. However, multiple simultaneous activation wavefronts initiated by the His-Purkinje system, severely complicate iECG. To improve the estimation of normal ventricular activation, the iECG method should accurately mimic the effect of the His-Purkinje system, which is not taken into account in the previously published multi-focal iECG. Therefore, we introduce the novel multi-wave iECG method and report on its performance.

Multi-wave iECG and multi-focal iECG were tested in four patients undergoing invasive electro-anatomical mapping during normal ventricular activation. In each subject, 67-electrode BSPM were recorded and used as input for both iECG methods. The iECG and invasive local activation timing (LAT) maps were compared.

Median epicardial inter-map correlation coefficient (CC) between invasive LAT maps and estimated multi-wave iECG versus multi-focal iECG was 0.61 versus 0.31. Endocardial inter-map CC was 0.54 respectively 0.22.

Modeling the His-Purkinje system resulted in a physiologically realistic and robust non-invasive estimation of normal ventricular activation, which might enable the early detection of cardiac disease during normal sinus rhythm.

## Introduction

Recorded body surface potential maps (BSPM) have a direct relation to the cardiac electrical activity. Methods to describe this relation are often referred to as 'solving the inverse problem of electrocardiography', 'epicardial electrocardiographic (ECG) imaging' or 'inverse electrocardiography (iECG)'. The most commonly used method is based on the Equivalent Potential Distribution (EPD) model.<sup>1,2</sup> In this method, the cardiac activation pattern is estimated by solving the mathematical linear relation between the electrical activity on the body surface and the epicardial surface. Recently this method has also been adjusted to estimate both endocardial and epicardial activation. Later, Equivalent Double Layer (EDL)-based iECG was introduced, relating body surface electrical activity to electrical activity both on the endocardium and the epicardium by simulating the generated cardiac currents.<sup>3,4</sup> The currents generated by the heart follow the local transmembrane potential waveform, thereby creating a direct link to cardiac electrophysiology. Furthermore, EDL-based iECG requires an initial estimate that can be based on ventricular electrophysiology, in contrast to EPD-based iECG.<sup>4,5</sup>

Inverse estimation of cardiac activity has been used to determine origins of arrhythmias<sup>6,7</sup> or to provide insight in electrophysiological substrates of structurally diseased hearts.<sup>8,9</sup> In individuals with genetic predisposition for cardiomyopathies, ventricular arrhythmias or sudden cardiac death can be the first manifestation of disease. In these individuals, adequate non-invasive identification of the arrhythmogenic substrate during normal His-Purkinje initiated ventricular activation, may prove to be of utmost importance to improve early detection of disease and aid early treatment. However, the non-invasive estimation of normal ventricular activation using BSPM is challenging, due to the nature of this complex activation pattern. Ventricular activation initiated by the His-Purkinje system is the result of multiple near simultaneous activation waves initiated at several endocardial locations (Figure 1).<sup>10-12</sup> Recorded BSPM waveforms are the result of spatial summation of the current generated by these simultaneous activation wavefronts, resulting in partial cancellation and amplification.<sup>10</sup> Therefore, the non-invasive estimation of normal ventricular activation is more complicated than of ventricular activation from a single focus such as premature ventricular contractions. Studies of the anatomy of the His-Purkinje system<sup>13-15</sup> and the Purkinje-myocardial junctions<sup>16,17</sup> showed inter-individual diversity and structural heart disease or conduction defects complicate the non-invasive estimation of normal ventricular activation even more.<sup>18,19</sup> Furthermore, the His-Purkinje system consists of numerous ramifications and terminates in Purkinje myocardial junctions distributed over a large part of the ventricular endocardium. However, the endocardium is not activated simultaneously as the dense distribution of Purkinje-myocardial junctions may suggest, but by multiple wavefronts initiated at distinct endocardial regions (Figure 1).<sup>13-15</sup> Characterization of the patient specific anatomy of the His-Purkinje system and the effect of the increased velocity of the

sub-endocardial layer has been studied previously in computer models, indicating the effect of these parameters on QRS derived parameters.<sup>20-23</sup> In our study, we incorporated a generic model of the His-Purkinje system in the iECG method, as, in line with the findings of the previous studies, this would provide a physiologically realistic estimation of the cardiac activation sequence.

In earlier EDL-based studies, the existence of multiple breakthroughs was mimicked through an iterative multi-foci search over the complete ventricular myocardium. However, this method was primarily designed to model focal ventricular activation.<sup>4-6</sup> In this study, we introduce a model for the His-Purkinje system, the multi-wave iECG method, to improve the non-invasive estimation of normal ventricular activation.

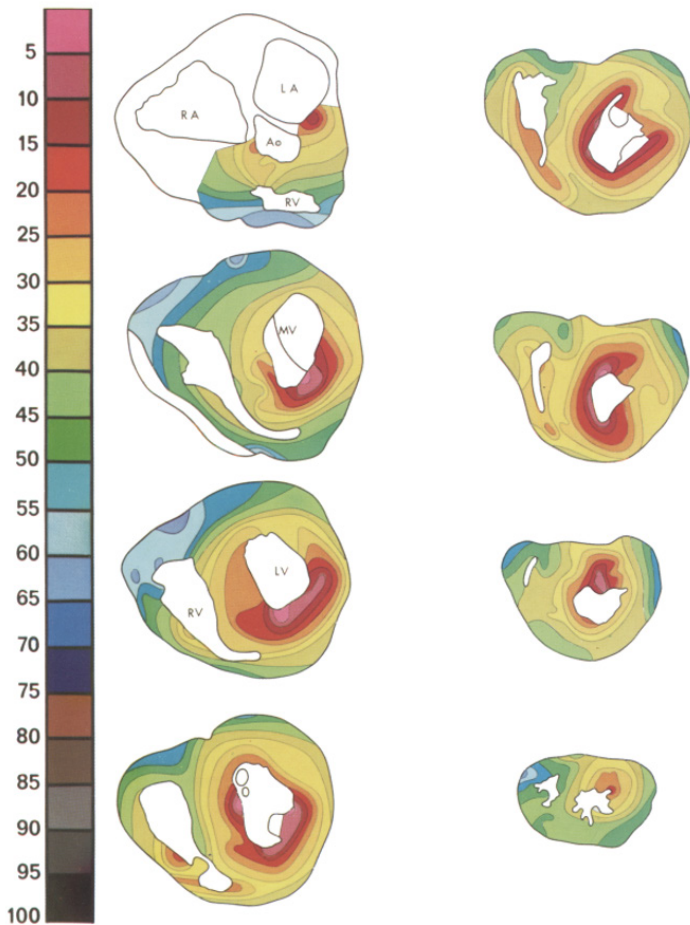


**Figure 1.** Normal ventricular activation. Normal ventricular activation in a healthy subject. In eight slices ventricular activation is displayed from early (pink) to late (blue). Around the endocardial structures in the LV (papillary muscles), around the RV moderator band, at the LV septal wall and near the MV, areas of early activation are observed. Reproduced with permission from.<sup>10,13</sup> LA=left atrium, RA=right atrium, Ao=aortic valve, RV=right ventricle, MV=mitral valve, LV=left ventricle.



To this end, we incorporated physiological and anatomical information about the His-Purkinje system in our model wherein the effect of the His-Purkinje system on ventricular activation is mimicked by incorporating anatomical structures associated with early activation (Figure 2). We then evaluate the performance of multi-wave iECG is and compare it to the previously described multi-focal iECG using patient specific invasive electro-anatomical mapping (EAM).

## Materials and Methods

### *Study population*

Four subjects referred for a clinical endocardial and epicardial electro-anatomical mapping (EAM) procedure were studied. Informed consent was obtained for each subject and all underwent iECG as described below.

### *Data acquisition*

Each subject underwent imaging, BSPM and invasive endocardial and epicardial EAM. Clinical cardiac imaging was performed whereof subject specific geometries of the complete ventricular myocardium, the left ventricular blood pool, the right ventricular blood pool, the thorax and the lungs were created (Figure 2A/B). The surface of the models of the segmented geometries was discretized by a closed triangulated surface meshes and created by dedicated software (GeomPEACS).<sup>24</sup> The effect of the volume conductor model was computed using the boundary element method, previously described.<sup>3,25</sup> Assigned conductivity values were 0.2 S/m for the thorax and ventricular muscles, 0.04 S/m for the lungs and 0.6 S/m for the blood cavities. Electrode positions on the thorax were reconstructed by aligning thorax geometries to 3D images of the thorax with electrodes.<sup>26</sup> Electro-anatomical structures associated with His-Purkinje mediated activation were incorporated in the imaging-based ventricular geometries (Figure 2B) as differences in location are known to affect QRS morphology.<sup>27-29</sup>

Prior to the invasive procedure, 67-electrode BSPM were recorded (sampling frequency 2048 Hz, Figure 2A). Recorded BSPM signals were resampled to 1000 Hz and baseline drift and 50Hz noise were removed. Per subject, five subsequent normal ventricular beats were selected and used as input for both iECG methods. Premature ventricular contractions were excluded from analysis.

Invasive EAM was performed under general anesthesia during sinus rhythm using commercial EAM systems (Carto or Ensite Precision) using multi-electrode catheters (PENTARAY® or HD Grid). Right ventricular endocardial access was obtained through the right femoral vein and left ventricular access was gained through transseptal puncture using a steerable sheath. Epicardial access was obtained by percutaneous subxiphoid puncture, thereby puncturing the pericardium. Local unipolar and bipolar contact electrograms at the endocardial and the epicardial ventricular surface

were sequentially recorded during normal ventricular activation with simultaneous measurement of the 12-lead ECG. The 12-lead ECG recorded during EAM was used as time-reference for both the BSPM signals and recorded electrograms. After the procedure, measured electrograms and LAT were manually checked for validity. The LAT was set at the maximal absolute amplitude of the bipolar signal, corresponding to the maximum downslope ( $dV/dt$ ) in unipolar signals, and taking into account neighboring measurements. Data were exported as raw electrograms with annotated LAT, local bipolar voltage and location.

#### Alignment of ventricular anatomical models from CT and EAM

Subject specific imaging-based ventricular iECG geometries were aligned to subject specific EAM point clouds in MATLAB using endocardial anatomical landmarks. The alignment was optimized using a rigid iterative least squares closest point matching algorithm.<sup>30</sup> LAT and local bipolar voltages were projected onto the nearest triangular surface of the imaging-based ventricular geometry. EAM points >10 mm from the imaging-based ventricular geometry were excluded from analysis. After projection, LAT and local bipolar voltage were averaged on each node of the imaging-based ventricular geometries.

#### *iECG method*

EDL-based iECG consists of two steps as the relation between activation time and simulated transmembrane potentials is non-linear. First, the required initial estimation of the ventricular activation sequence is computed and in the second step, local activation timings are mathematically optimized by minimizing the differences between recorded and computed BSPM by tuning LAT. In this study, two methods to determine the initial estimation were compared; multi-wave iECG and multi-focal iECG (Figure 2). In the initial estimation step, different activation sequences are simulated and corresponding BSPM are computed and directly compared to recorded BSPM. The ventricular anatomical model served as the source model (EDL) and at each node, the local transmembrane potentials were simulated which determined the local source strength. Resulting BSPM were computed per simulated activation sequence.<sup>31</sup>

In short, the multi-wave iECG procedure provided an estimation by mimicking the effect of the His-Purkinje system on ventricular activation, multi-focal iECG did not. In both methods, ventricular activation sequences with multiple distinct foci and initial activation timings were estimated using the fastest route algorithm (FRA).<sup>4,32</sup> For the simulation of activation sequences in both methods, an anisotropy ratio of two was used, meaning that the conduction velocity perpendicular to the myocardial fibers was two times lower than conduction velocity longitudinal to myocardial fibers.<sup>33-35</sup> BSPM were then computed using the boundary element method to determine to compare to the recorded BSPM.<sup>3,25</sup> The activation sequence yielding

highest correlation between recorded and computed BSPM was assumed to be the activation sequence best explaining the recorded BSPM and was selected as the initial estimation and used as input for the optimization procedure. Both methods to estimate the initial activation sequence are described in more detail below.

#### Multi-focal iECG: Adaptation of principal single focus activation

Multi-focal iECG has been described in several studies.<sup>4-6</sup> In short, this method serves an additive approach based on the FRA. First the 'fundamental activation sequence' originating from one focus that achieves the highest correlation between recorded BSPM and computed BSPM is determined. Therefore, myocardial conduction velocity was set by matching the total activation duration of the 'fundamental' activation sequence to the QRS duration up to a maximum of 2.5 mm/ms. After determining this fundamental activation sequence, up to six foci are iteratively added if adding improves the match between recorded and computed BSPM (Figure 2, multi-focal iECG).

#### Multi-wave iECG: Modeling the effect of the His-Purkinje system

In the novel multi-wave iECG method, the effect of His-Purkinje mediated ventricular activation is mimicked by combining activation sequences initiated at endocardial regions associated with the His-Purkinje system. Several endocardial regions are associated with early ventricular activation; the bases of the two left ventricular papillary muscles, the right ventricular moderator band and several septal regions (Figure 1/2).<sup>10,11,13-19</sup> Of note are the two breakthroughs at the LV septal wall, near the mitral valve and near the LV apex. All regions correspond to Purkinje anatomy and observed regions of early activation in more recent invasive mapping studies.<sup>10,11,13-19</sup>

These anatomical regions were localized in the subject specific imaging-based ventricular geometries based on anatomical landmarks (Figure 1/2). Foci were localized at the insertion of the two left ventricular papillary muscles and the moderator band on the ventricular free wall; all nodes connecting the structure to the free wall were treated as focus (e.g. assigned equal activation timings). On the septal wall, six regions with a radius of 10 mm were selected containing multiple potential foci and per septal region, one focus was selected. At the left ventricular septal wall, one region was localized at the inferior one-third from base to apex of the septal wall and one region was localized at superior one-third from base to apex of the antero-septal wall and two other regions were localized between those locations. At the right ventricular septal wall, the localized region was close to the RV apex and at the middle of the RV septal wall.

Activation sequences were calculated using a myocardial conduction velocity of 0.85 ms<sup>-1</sup>.<sup>10,16,35,36</sup> To account for increased subendocardial conduction velocities, myocardial conduction velocity in close vicinity (<15 mm) of foci was set at 1.7

m/s.<sup>16,17,36</sup> Per region, single focus activation sequences were computed with an initial timing ranging between 0-35 ms for the structure regions (e.g. papillary muscles and moderator band) and between 0-25 ms for the septal regions.<sup>10,11,13-15,19</sup> This procedure resulted in nine groups of single focus activation sequences initiated at one of the His-Purkinje associated regions with distinct initial activation timings and were selected based on the best matching computed and recorded BSPM.

Normal ventricular activation is affected by inter-individual diversity in His-Purkinje anatomy and by structural myocardial disease.<sup>18,19</sup> Structural myocardial disease may affect the number of active foci at the endocardium and consequently the ventricular activation sequence; in right and left bundle branch block less foci are active compared to normal ventricular activation. This diversity was incorporated in multi-wave iECG by automatically testing all  $511=(2^9)-1$  (all foci inactive) possible permutations of merged single foci activation sequences. Merged activation sequences with a total activation duration  $>115\%$  and  $<85\%$  of measured QRS duration were excluded. The activation sequence yielding highest correlation between recorded and computed BSPM was selected as the initial estimation.

#### *Optimization procedure*

The initial estimation is further optimized by matching computed BSPM to recorded BSPM. Therefore, a dedicated Levenberg-Marquardt optimization procedure was used.<sup>26</sup> The surface Laplacian of the activation times was used as regularization-operator and was performed through the iterative minimization of:

$$\arg \min_{\delta} (\|V - \phi(\delta)\|_F^2 + \mu^2 \|L\delta\|_F^2) \quad \text{Eq1}$$

With computed BSPM ( $\phi$ ), based on LAT ( $\delta$ ),  $\phi$  is minimized to the recorded BSPM ( $V$ ) by iteratively adjusting  $\delta$ . The operator  $L$  represents the numerical form of the surface Laplacian operator; by minimizing  $\|L\delta\|_F^2$  a spatially smooth solution is promoted. The regularization parameter  $\mu^2$  was set to a very small value  $5 \cdot 10^{-6} \text{mV}^2 \text{ms}^2 \text{m}^{-2}$  and chosen such that the optimized activation sequence was regularized to empirically correspond to realistic smoothness.<sup>4</sup> We refer to the discussion for the setting of the regularization parameter. A maximum of 25 iterations was needed to optimize  $\delta$ .

#### *Quantitative analysis*

Ventricular activation timing maps were displayed from early (red) to late (blue) activation. Recorded BSPM were compared to the computed BSPM by means of the Pearson's correlation coefficient (CC) and the relative difference. The relative difference is calculated by computing the Frobenius normal form of the difference between estimated and input BSPM divided by the Frobenius normal form of the recorded BSPM.

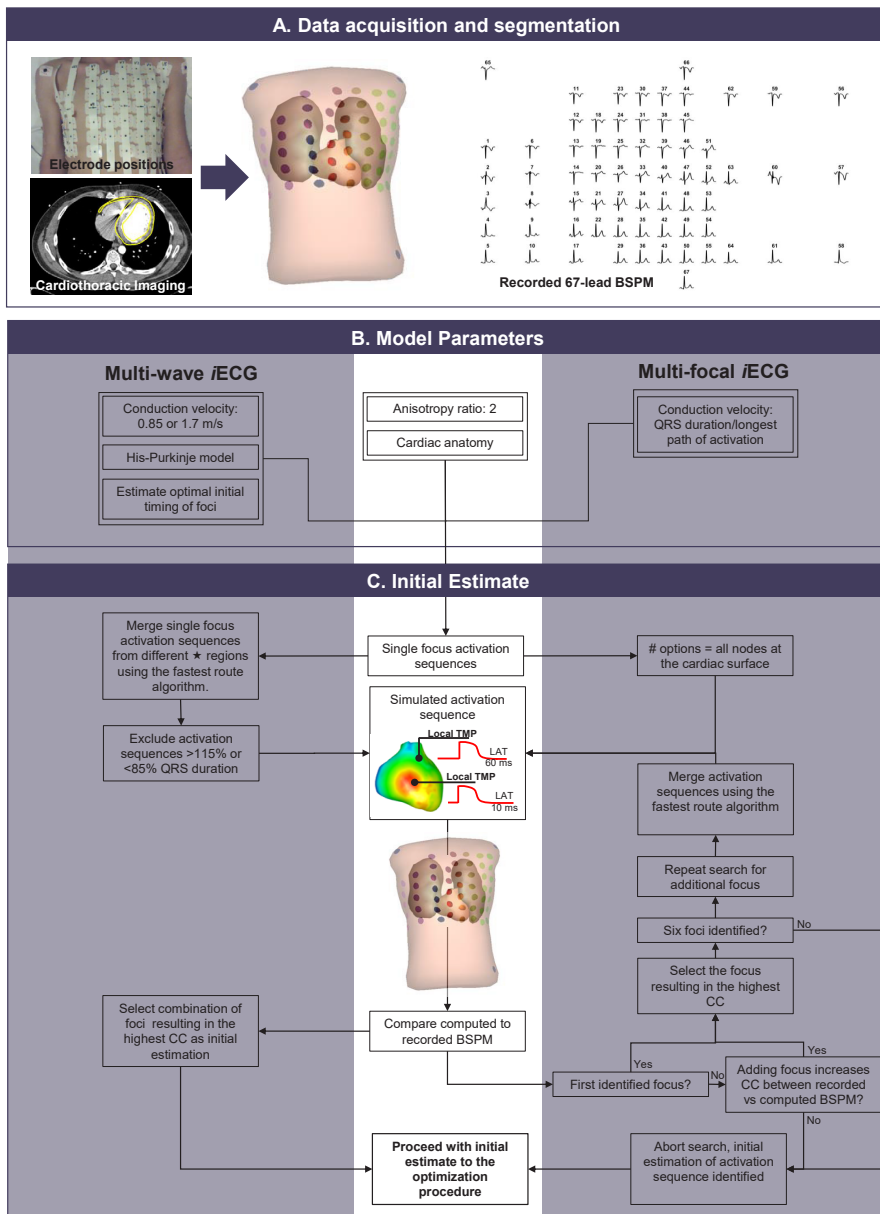


**Figure 2.** Study workflow and multi-wave and multi-focal iECG method. A: (cardiac) imaging and body surface potential maps (BSPM) data are obtained. B: The initial model parameters are defined for both the multi-wave and multi-focal iECG procedure. C: For both the multi-wave and multi-focal iECG procedure, the cardiac source model uses local transmembrane potentials (TMP) to determine activation timing, and using the volume conductor, BSPM are computed. Multi-wave iECG tests 511 combinations of the activation sequences and selects the activation sequence with the best matching BSPM based on correlation and QRS duration. Multi-focal iECG first defines one focus which best describes overall activation sequence and subsequently keeps adding foci which optimizes the match between recorded and computed BSP.

Per surface, estimated activation maps were compared to invasive activation maps by calculating inter-map CC (Pearson) and mean absolute difference in LAT. Therefore, estimated ventricular activation maps were timing-referenced to the same timing-reference used during the invasive procedure. Per triangle, the myocardial conduction velocity was calculated using the triangulation technique.<sup>37</sup> In short, the location and activation timing of the three nodes forming one triangle at the surface were used. The average conduction speed and direction can then be determined, assuming that the wavefront is locally planar, and moves with constant speed in the plane of the triangle. A detailed description of the method is explained in the Supplementary materials (Page 1). Velocities above 5 mm/ms were excluded from analysis. For both iECG methods, the computation time was determined. Values are displayed using mean  $\pm$  standard deviation or using median [range] where appropriate.

## Results

### *Invasive LAT mapping procedure*

EAM was performed in one subject who had symptomatic premature ventricular contractions originating in the right ventricular outflow tract without structural heart disease (male, 21 years, QRS duration 90 ms, Figure 3), the three other subjects had recurrent ventricular tachycardias with underlying arrhythmogenic cardiomyopathy (male, 59 years, QRS duration 104 ms, Figure 4) or dilated cardiomyopathy (female, 65 and 61 years QRS duration 142 and 162 ms, Figure 5 and 6). In three subjects (Figure 3-5) the epicardium and the right ventricular endocardium were mapped, in the last subject (Figure 6) the epicardium and the left ventricular endocardium were mapped.

**Table 1.** *Inter-map comparison*

	Multi-focal	Multi-wave	Invasive
Correlation coefficient			
Epicardial	0.31[-0.23,0.83]	0.61[0.41,0.91]	
Endocardial	0.22[-0.13,0.64]	0.54[0.19,0.81]	
Absolute difference (ms)			
Epicardial	21[17,27]	14[9,25]	
Endocardial	27[16,52]	20[10,30]	
Myocardial conduction velocity (mm/ms)			
Epicardial	1.4 $\pm$ 0.3	1.3 $\pm$ 0.2	1.2 $\pm$ 0.2
Endocardial	1.4 $\pm$ 0.3	1.1 $\pm$ 0.2	1.0 $\pm$ 0.1
Number of breakthroughs (n)			
Epicardial	2[2,4]	3[2,5]	3[2,3]
Endocardial	1[1,4]	2[1,3]	2[1,3]
Effect optimization procedure			
Correlation coefficient	-0.01[-0.17,0.20]	0.03[-0.11,0.24]	
Absolute difference	0.7[-3.7,6.8]	0.7[-4.8,3.0]	

*Quantitative inter-LAT map comparison between the invasive local activation (LAT) and the estimated LAT maps using both iECG methods. Values are displayed per surface as median[range] or mean  $\pm$  standard deviation where appropriate.*

Invasive maps consisted of a mean of  $5140 \pm 1865$  epicardial annotated electrocardiograms and  $1476 \pm 368$  endocardial annotated electrocardiograms. LATs were projected onto the subject specific imaging-based ventricular model. A mean of  $73 \pm 8\%$  of the epicardial surface and  $61 \pm 12\%$  of the endocardial surface was mapped with a mapping density (annotations/mm<sup>2</sup>) of  $19.5 \pm 7.1$  for the epicardial surface and  $11.8 \pm 3.3$  for the endocardial surface. In all subjects, the epicardial surface was mapped. In three subjects, the right ventricular endocardial surface was mapped and in the other subject, the left ventricular endocardial surface was mapped.

#### *Invasive vs. iECG local activation timing maps*

In all four subjects, ventricular activation was estimated with both iECG methods and compared to invasively measured LAT (Figure 3-6). Median epicardial inter-map CC of estimated multi-wave iECG versus multi-focal iECG was  $0.61[0.41,0.91]$  versus  $0.31[-0.23,0.83]$  and median endocardial inter-map CC was  $0.54[0.19,0.81]$  respectively  $0.22[-0.13,0.64]$ . With increasing QRS duration, inter-map CC stayed the same for multi-wave iECG, whereas it increased for multi-focal iECG (Figure 7, upper row, left panel). Inter-map CC, absolute difference, number of breakthroughs per surface and myocardial conduction velocity for all subjects are displayed in Table 1 (inter-map comparison). With shorter QRS durations, myocardial conduction velocity remains constant in multi-wave iECG, whereas it increases in multi-focal iECG (Figure 7, middle row, left panel). The optimization procedure did not always improve inter-map CC and absolute difference for both multi-wave and multi-focal iECG (Table 1).

Computed and recorded BSPM were similar between the two iECG methods (multi-wave vs multi-focal: CC  $0.98 \pm 0.01$  vs  $0.98 \pm 0.01$  and RD  $0.17 \pm 0.03$  vs  $0.17 \pm 0.04$ ). Per subject standard 12-lead ECGs of the recorded and computed BSPM are displayed in the Supplementary material (Page 2-5). The number of identified foci decreased with increasing QRS duration in multi-wave iECG, but did not in multi-focal iECG (Figure 7 middle row). Mean computation time was  $33 \pm 6$  seconds for multi-wave iECG and  $1014 \pm 726$  seconds for multi-focal iECG.

## **Discussion**

Modeling the effect of the His-Purkinje system by incorporating endocardial electro-anatomical structures in the iECG method improved the accuracy of non-invasive estimation of His-Purkinje mediated ventricular activation, especially in the estimation of normal ventricular activation (Figure 3-7). The overall performance of the multi-wave iECG was superior to multi-focal iECG, as is also shown in our previously published study in a larger patient cohort.<sup>38</sup>

#### *Comparison of EDL-based iECG*

A method to mimic the effect of the His-Purkinje system on ventricular activation should incorporate all possible variations of His-Purkinje mediated ventricular



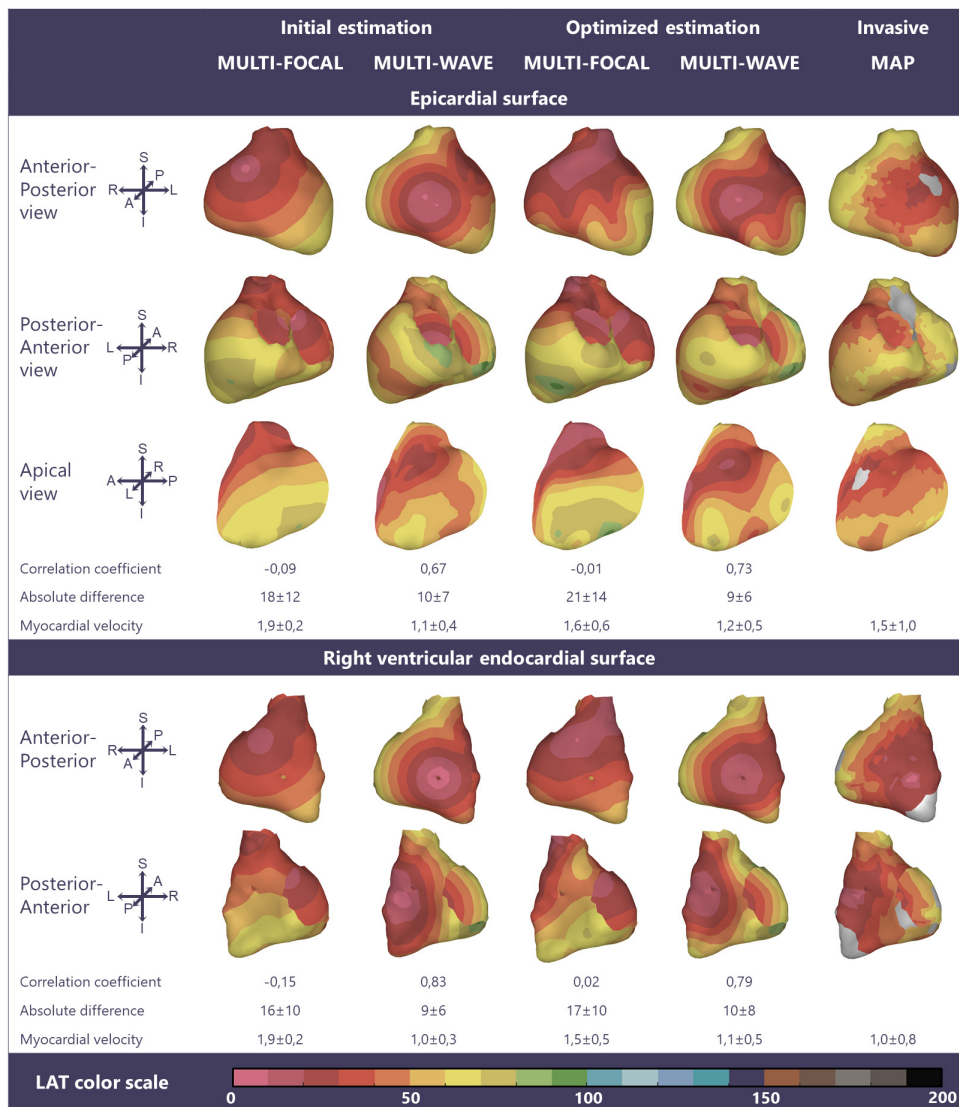


**Figure 3.** Invasive vs iECG maps in a QRS of 90 ms. Multi-focal iECG, multi-wave iECG and invasive activation maps of the epicardial and right ventricular endocardial surface (QRS 90 ms) from red (early) to purple (late). The multi-focal iECG map shows one prominent initial site of activation, multi-wave iECG map shows six and is comparable to the invasive map. Inter-map correlation coefficient (CC), absolute difference (ms), LAT time range (ms) and estimated myocardial conduction velocity (mm/ms) are displayed comparing iECG to invasive LAT maps. CC and relative difference between recorded and computed BSPM were  $0.99\pm 0.00$  respectively  $0.15\pm 0.00$  for multi-focal iECG and  $0.98\pm 0.00$  respectively  $0.15\pm 0.00$  for multi-wave iECG.



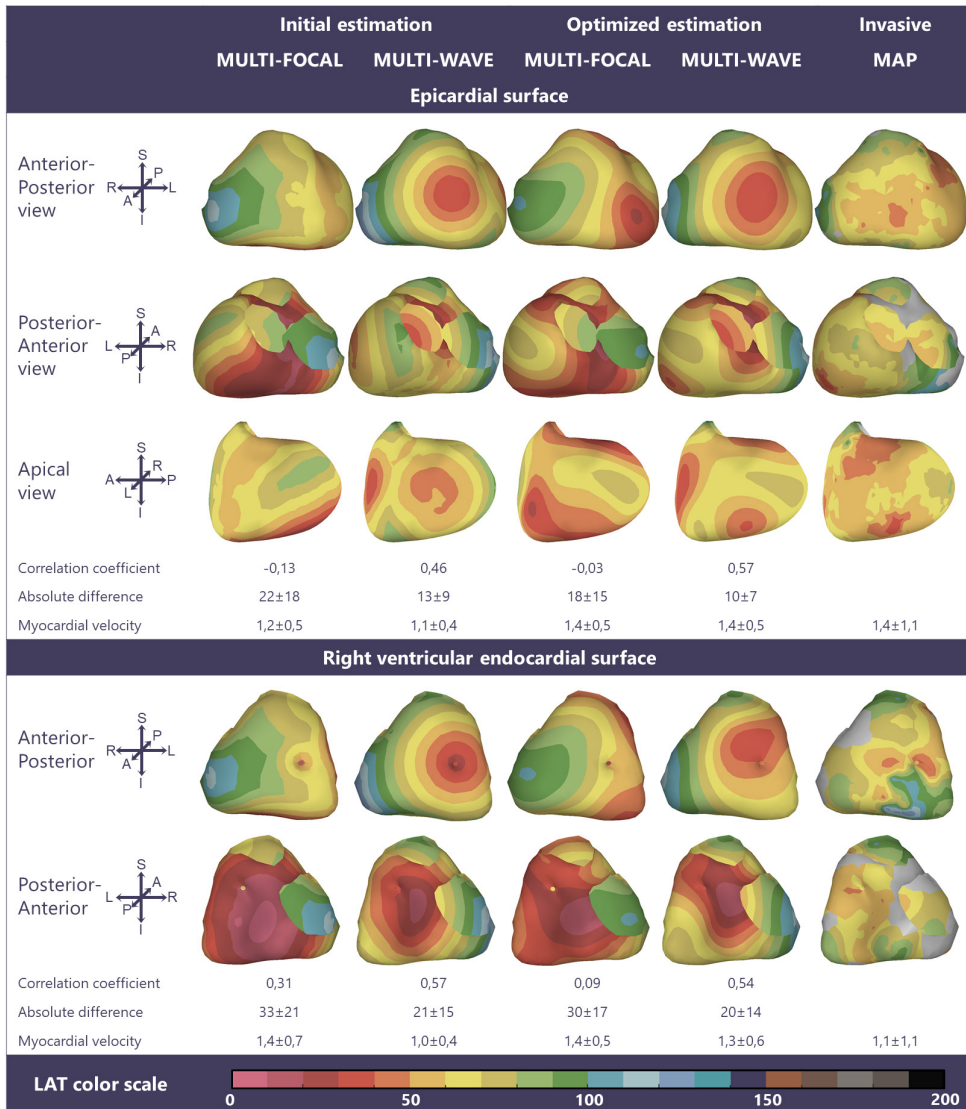


**Figure 4.** Invasive vs iECG maps in a QRS of 104 ms. Multi-focal iECG, multi-wave iECG and invasive activation maps of the epicardial and right ventricular endocardial surface (QRS 104 ms) from red (early) to purple (late). Inter-map correlation coefficient (CC), absolute difference (ms), LAT time range (ms) and estimated myocardial conduction velocity (mm/ms) are displayed comparing iECG to invasive LAT maps. CC and relative difference between recorded and computed BSPM were  $0.97 \pm 0.00$  respectively  $0.25 \pm 0.01$  for multi-focal iECG and  $0.97 \pm 0.00$  respectively  $0.25 \pm 0.01$  for multi-wave iECG.

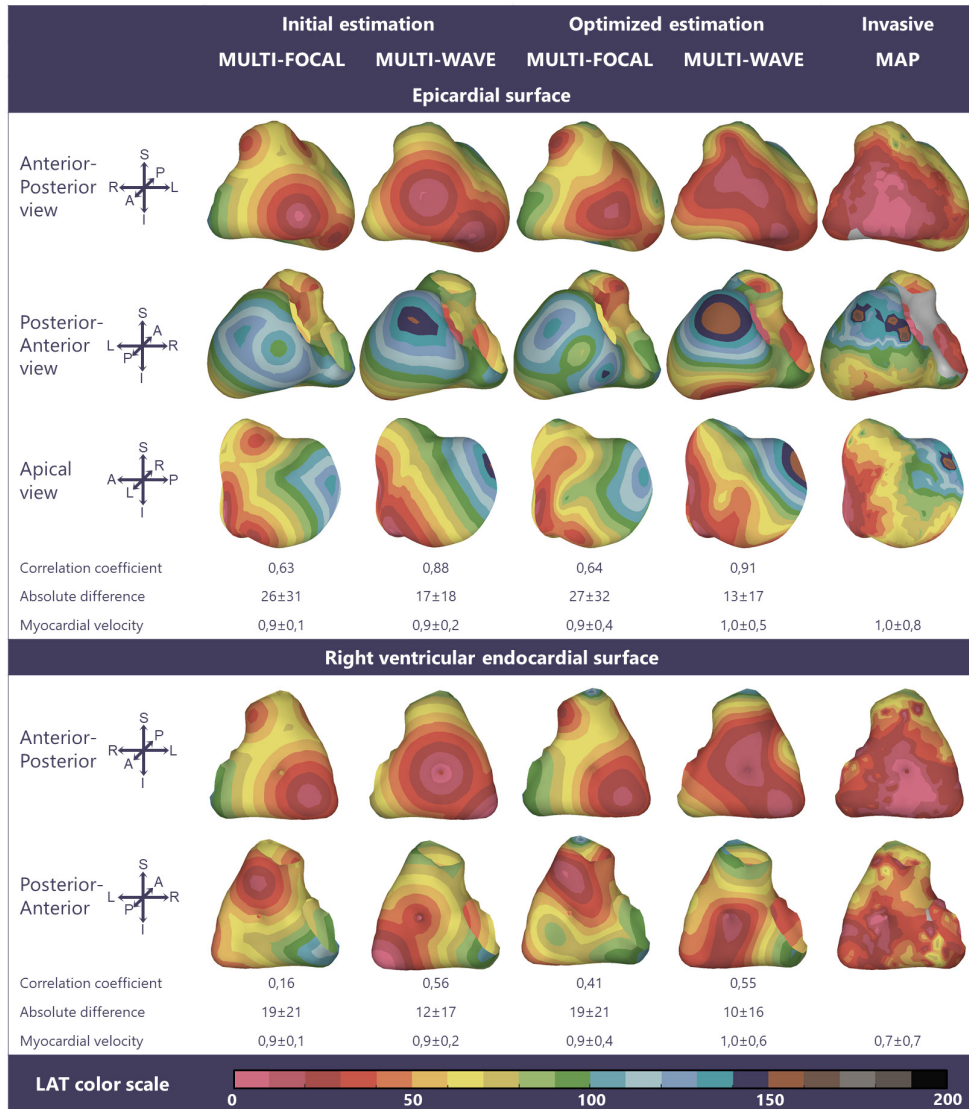


**Figure 5.** Invasive vs iECG maps in a QRS of 142 ms. Multi-focal iECG, multi-wave iECG and invasive activation maps of the epicardial and right ventricular endocardial surface (QRS 142 ms) from red (early) to purple (late). Inter-map correlation coefficient (CC), absolute difference (ms), LAT time range (ms) and estimated myocardial conduction velocity (mm/ms) are displayed comparing iECG to invasive LAT maps. CC and relative difference between recorded and computed BSPM were  $0.96 \pm 0.00$  respectively  $0.30 \pm 0.01$  for multi-focal iECG and  $0.95 \pm 0.00$  respectively  $0.32 \pm 0.01$  for multi-wave iECG.

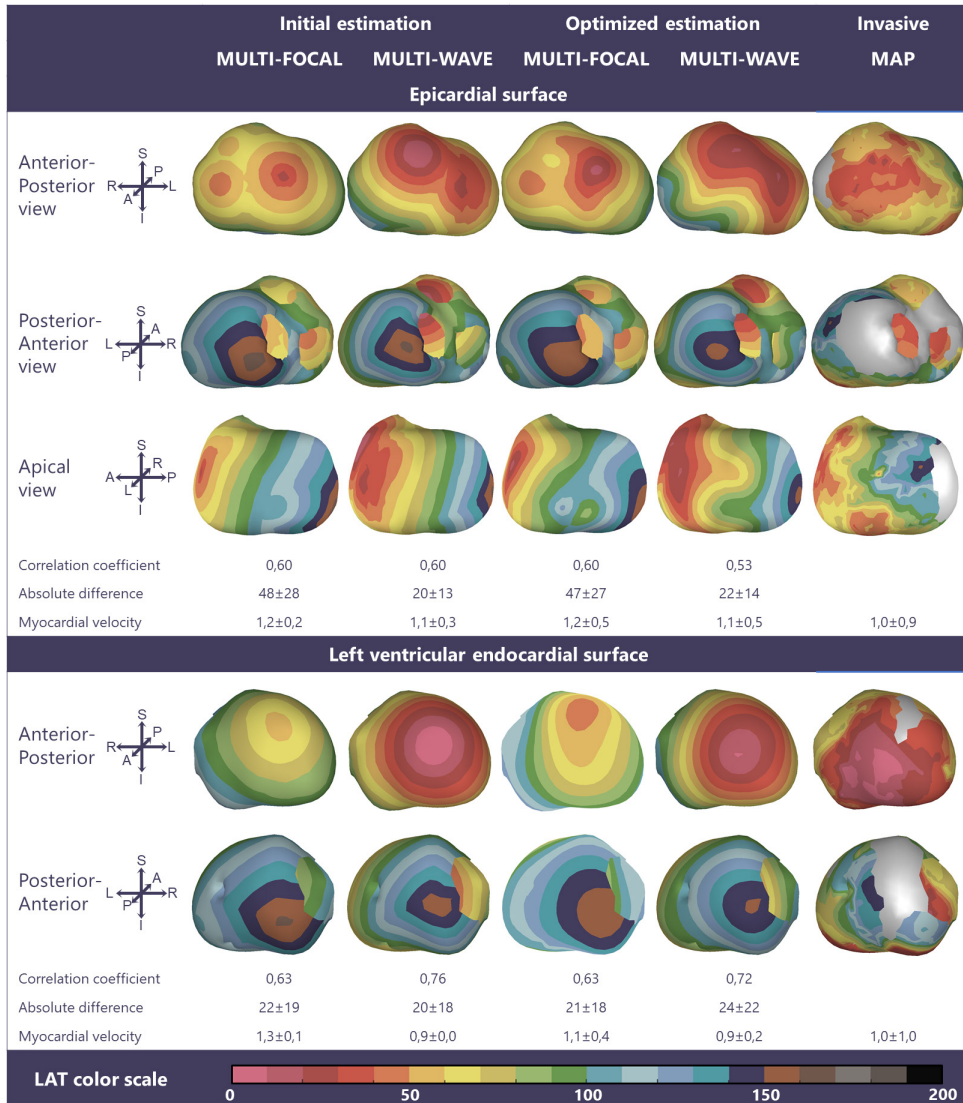


**Figure 6.** Invasive vs iECG maps in a QRS of 162 ms. Multi-focal iECG, multi-wave iECG and invasive activation maps of the epicardial and right ventricular endocardial surface (QRS 162 ms) from red (early) to purple (late). Inter-map correlation coefficient (CC), absolute difference (ms), LAT time range (ms) and estimated myocardial conduction velocity (mm/ms) are displayed comparing iECG to invasive LAT maps. CC and relative difference between recorded and computed BSPM were  $0.94 \pm 0.00$  respectively  $0.35 \pm 0.01$  for multi-focal iECG and  $0.93 \pm 0.00$  respectively  $0.38 \pm 0.01$  for multi-wave iECG.

activation; either healthy or diseased. Multi-focal iECG does not take the effect of the His-Purkinje system on ventricular activation into account. In this method, an additive iterative search over the complete myocardium is performed where the 'fundamental' activation sequence dominantly determines the final estimation thereby increasing the chance for an erroneous unphysiological activation sequence.<sup>4-6</sup> This algorithm was found to be the most effective in rather monophasic, simple activation patterns like premature ventricular contractions or ventricular tachycardia. In multi-wave iECG, diverse His-Purkinje anatomy was taken into account by the incorporation of subject specific locations of endocardial electro-anatomical structures associated with early ventricular activation. Flexibility was obtained by testing all permutations of the anatomically identified foci. Therefore, multi-wave iECG is more restrained in foci location, which resulted in more realistic estimations of the ventricular activation sequence in normal ventricular activation compared to multi-focal iECG (Figure 4-5). In broad QRS complexes, the performance of multi-focal iECG improved and became equal to the performance of multi-wave iECG, as reflected in inter-map CC and absolute difference (Figure 7). Thus, the fundamental difference between both methods lies within the first step of the initial estimation; whereas multi-focal iECG identifies an activation sequence with one focus best explaining the recorded BSPMs, multi-wave iECG provides an estimation with multiple foci (Figure 2).

### *Modeling the His-Purkinje system*

In our study, an anatomy-based model of the His-Purkinje system was used for the estimation of both the initial sites of activation and the myocardial conduction velocity. Incorporating a model of the His-Purkinje system has been shown to be essential to reliably simulate sinus rhythm.<sup>20-23</sup> In our study, a generic model of the His-Purkinje system was individualized by segmenting anatomical endocardial structures associated with the location of the Purkinje myocardial junctions using patient-specific cardiac imaging. Then, based on the recorded BSPM, location and timing of the initial sites of activation were estimated.

### Initial sites of activation

Physiologically, with shortening of QRS duration, an increased number of His-Purkinje foci will be active, as modeled in multi-wave iECG. With shortening of QRS duration, complexity of the estimation increases due to partial cancellation and amplification of wavefronts represented in the recorded BSPM. Multi-focal iECG is likely to identify an aggregation of near simultaneous wavefronts as the 'fundamental' activation sequence. Foci could be localized over the complete myocardium and their initial timings could range within QRS duration, resulting in inadequate estimated activation sequences.<sup>10,11,13-15,19</sup>

In His-Purkinje system disorders, the complexity of ventricular activation reduces and QRS duration increases. The performance of multi-focal iECG improved with increasing

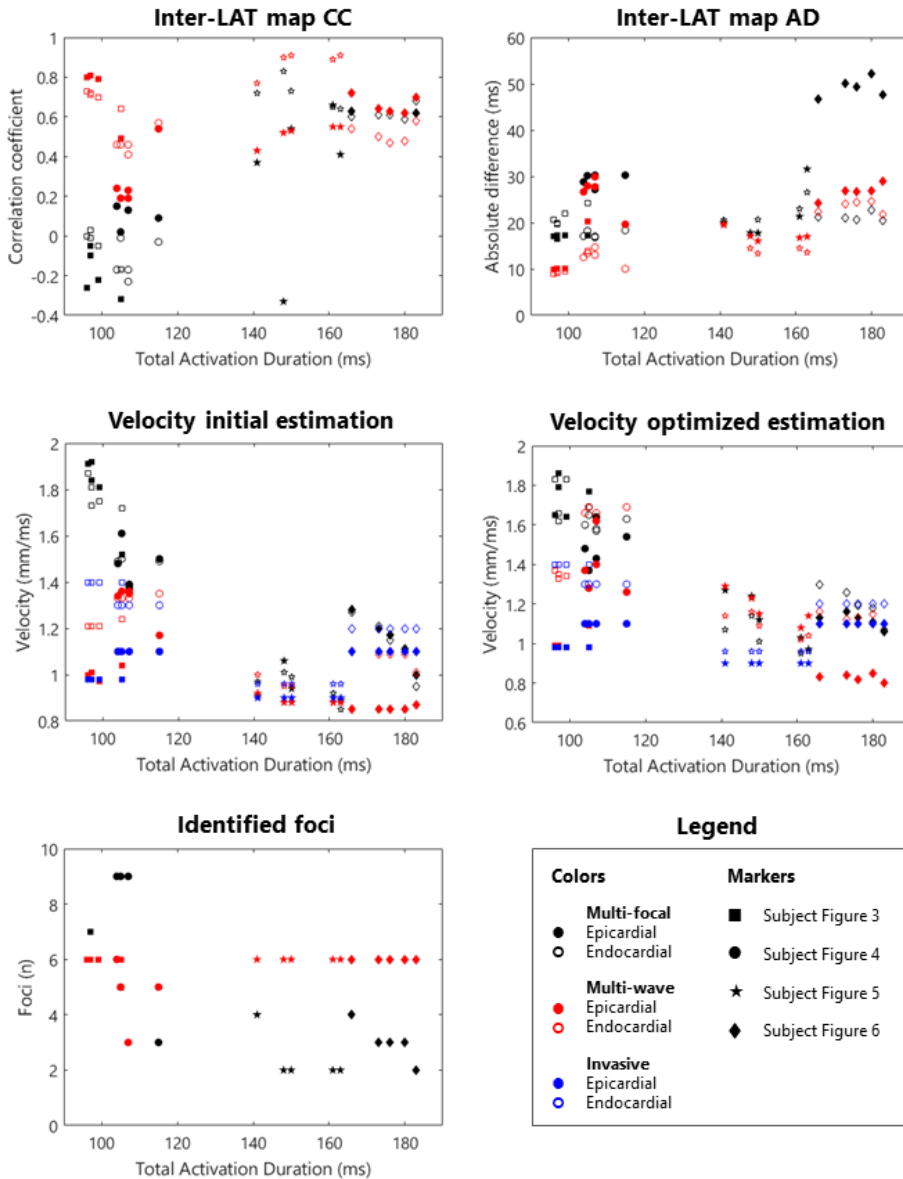


**Figure 7.** Quantitative comparison iECG and invasive methods. Quantitative comparison of multi-wave, multi-focal and invasive LAT maps. Diamonds represent the epicardial conduction velocity and dots the endocardial conduction velocity; the black color denotes the multi-focal iECG method, the red color the multi-wave iECG method and the blue color the invasive. Upper row: Inter-map correlation coefficient (CC, left) and inter-map absolute difference (right) per subject per plotted beat plotted against QRS duration. With increasing QRS duration, the multi-focal method improves in CC. Middle row: Myocardial conduction velocity estimated from the local activation timing (LAT) maps before (left) and after (right) the optimization procedure per iECG method and for the invasive study per myocardial surface. Bottom row: The number of identified foci in the initial estimation (left) and the legend of all displayed plots (right).

QRS duration as earlier observed in a EPD based iECG validation study.<sup>39</sup> However, multi-wave iECG showed that its performance was not affected by QRS duration. The effect of the His-Purkinje system was mimicked through the identification of nine distinct endocardial regions as potential foci. All possible activation patterns were tested by comparing computed to recorded BSPM. Additionally, multi-wave iECG excluded unrealistically long and short total activation durations referenced to QRS duration in the recorded BSPM. This combination resulted in a physiological robust non-invasive estimation of ventricular activation.

#### Myocardial conduction velocity

With decreasing QRS duration, the estimated myocardial conduction velocity increased in the initial estimation of multi-focal iECG whereas the number of foci increased in multi-wave iECG (Figure 7 middle/lower row). The estimation of multi-wave iECG is thus more realistic whilst taking normal physiology into account. In multi-focal iECG, myocardial conduction velocity was estimated between 0.8 and 2.0 mm/ms for the myocardium, increasing with decreasing QRS duration whereas in multi-wave iECG, myocardial conduction velocity was set. The optimization procedure affected the myocardial conduction velocity for both methods to some extent (Figure 7 middle row).

Values up to 2.0 mm/ms equal the conduction velocity of Purkinje fibers and may be observed in regions with a high density of Purkinje-myocardial junctions<sup>16,17</sup>, but are physiologically unrealistic for the normal myocardium. The estimated myocardial conduction velocities used for the multi-focal initial estimation may be physiologically realistic if ventricular activation is initiated by one focus, as the estimated myocardial conduction velocity was matched to measured QRS duration. If multiple foci contribute to the short QRS duration, myocardial conduction velocity increases in multi-focal iECG, which is physiologically unrealistic. Selecting nine foci as starting point of ventricular activation remains a simplification of the true dense distribution of Purkinje-Myocardial junctions. To account for the effect of this dense distribution, conduction velocity was doubled in the regions directly around foci in multi-wave iECG.

#### *Myocardial conduction velocity estimation*

In this study, the surface myocardial conduction velocity was computed (Figure 7 middle row). In the areas of breakthroughs at the epicardium, surface conduction velocity may seem to be increased as the wavefront moving from the endocardium to the epicardium almost simultaneously activates the epicardium. However, in endocardial breakthrough regions the dense distribution of Purkinje-Myocardial junctions is active which may realistically contribute to rapid activation of the myocardium. To correct for seemingly increased conduction velocities due to simultaneous breakthroughs at multiple nodes, estimated values above 3 mm/ms



were excluded from analysis.

#### *Comparison to EPD based iECG*

As described by Duchateau et al<sup>39</sup>, the performance of EPD based iECG during sinus rhythm is poor (inter-map CC:  $0.03 \pm 0.43$ , absolute difference:  $20.4 \pm 8.6$ ), especially in narrow QRS complexes. With increasing QRS duration, the performance of the method improved. The performance of multi-wave iECG showed a higher overall performance as reflected in inter-map CC and absolute difference and the performance of method seemed to be unaffected by QRS duration.

In contrast to EPD based method, the EDL based method defines the local source strength proportional to the transmembrane potential at both epicardium and endocardium instead of local electrograms at solely the epicardium. For both source models applies that the underlying inverse problem is ill-posed, i.e. completely different ventricular activation sequences can generate similar BSPM waveforms. Subsequently, the computed BSPM from the EDL based method also depend non-linearly on the activation and recovery timings. To obtain a realistic estimate for ventricular activation and recovery, EDL-based iECG requires an initial estimate which can be based on ventricular electrophysiology, in contrast to EPD-based iECG.<sup>4,5</sup> In multi-wave iECG a several foci are defined for this His-Purkinje mediated activation, thereby correctly reflecting cardiac electrophysiology.

#### *Optimization procedure*

Due to the non-linear relation between activation time and simulated potentials, the EDL based iECG requires an initial estimation which is then mathematically optimized by minimizing the differences between recorded and computed BSPM by tuning LAT regularized by the surface Laplacian. The optimization procedure both negatively and positively affected the inter-map correlation and absolute differences as compared to the invasive maps. Thus, the initial estimation will not extremely change, meaning that no foci will appear or disappear as an effect of the optimization procedure. However, by optimizing the LAT, modeled local conduction velocity is affected thereby possibly negatively affecting the agreement between the invasive and non-invasive maps. Furthermore, due to proximity effects, wavefronts traveling close to electrodes pose a larger effect in the optimization procedure compared to wavefronts traveling at the posterior side of the heart. The results in this paper thus emphasize both the need for a physiologically realistic initial estimation and necessity of an electrophysiological based regularization of the optimization procedure.<sup>40</sup>

In comparison to other EDL-based iECG methods, we used a lower value for our regularization parameter, meaning that the optimization procedure is less regularized by the surface Laplacian. We tested values between  $1.5 \cdot 10^{-4}$ , as used in previous studies<sup>4</sup>, and  $5 \cdot 10^{-8}$  and we observed that the optimized maps did not differ when

using a higher vs lower value. As with the decrease of the regularization parameter the optimized activation sequence remained equal, the initial estimation thus needs less physiological regularization.

### *Computation time*

A large difference in computation time was observed between the two iECG methods due to the difference in the selection of the initial estimation. This is mostly caused by limiting the search space to identify foci by matching computed to recorded BSPM. Thus, besides the fundamental difference in the methodology to select the initial sites of activation, also the reduction in the computation time favors multi-wave iECG for clinical implementation.

### *Limitations*

In both multi-focal iECG and multi-wave iECG conduction velocity is assumed to be only affected by anisotropy. The presence of structural heart disease, as present in the included subjects, on the estimation of both iECG methods was not assessed, but may be of great importance as conduction velocity is affected by the presence of abnormal myocardium and fibrous tissue. If local cardiac remodeling is present, a fixed conduction velocity in the iECG method is physiologically not realistic. Therefore, future research will focus on the incorporation of abnormal myocardium in the cardiac source model and the effect of local cardiac remodeling on cardiac conduction velocity and multi-wave iECG estimations. Structural information about the cardiac tissue will then be obtained from dedicated cardiac imaging, and per underlying substrate the appropriate modeling technique will be investigated.

In this study, extensive invasive mapping was used as the gold standard sequentially recorded beats and electrograms are used to estimate LAT. During both the invasive maps and the selection of the beats from the BSPM signals, no respiratory gating was used, possibly resulting in error caused by respiration. Visual comparison of the maps also shows a distinct difference between the invasive and non-invasive maps, where the non-invasive maps are more smoothed compared to the more speckled invasive maps. From the LAT maps Durrer presented, a smoother pattern is expected (like the iECG estimation), but other invasive LAT maps presented in quantitative iECG comparison studies and invasive studies show this more speckled pattern.<sup>7,11,39</sup> This difference is most likely caused by the density of obtained LAT measurements; the maps of Durrer et al are constructed using a large inherent smoothing pattern, due to the sparsity of the number of needles used to obtain the LAT. However, also both inaccuracy in the invasive mapping system or more physiologically based variation in the activation of (diseased) myocardial tissue, may contribute to this speckled pattern. The contribution of these factors is however yet unknown and should be verified as this fundamental difference in pattern will always severely affect presented inter-map correlations and absolute differences.



The His-Purkinje model used in this study can be optimized to the specific patient, however, it remains a crude representation of true cardiac anatomy and electrophysiology. In the model one node surrounded by a region of increased conduction velocity was used to simulate Purkinje-myocardial junction. However, in reality, these junctions are a much more complex system. Therefore, and due to the incompleteness of specifically the endocardial maps, we were not able to compare the EAM mapped focal sites to our iECG estimated focal sites.

## Conclusion

Modeling of the effect of the His-Purkinje system in our novel multi-wave iECG method provides a physiologically robust estimation of the ventricular activation sequence even in normal (narrow QRS) ventricular activation. The computation time required by multi-wave iECG was short, crucial for clinical use. Multi-wave iECG might thus enable the identification and progression of arrhythmogenic substrates in patients with structural heart disease. Future research will be directed towards the combination of the novel His-Purkinje model and the incorporation of myocardial tissue characteristics, e.g. scar, to improve our iECG method.

### *Acknowledgements*

This work was supported by the Netherlands Cardiovascular Research Initiative, an initiative with support of the Dutch Heart Foundation (grant numbers CVON2015-12 eDETECT and QRS-Vision 2018B007). Figure 1. is reproduced from the publication of D. Durrer, R.TH. van Dam, G.E. Freud, M.J. Janse, F.L. Meijer and R.C. Arzbacher, Total Excitation of the Isolated Human Heart, *Circulation* 1970;4:1899-912, <https://www.ahajournals.org/doi/10.1161/01.CIR.41.6.899>.

### *Supplementary material*

Available at: <https://link.springer.com/article/10.1007/s10439-022-02905-4#Sec25>  
Supplementary methods – Local myocardial conduction velocity estimation  
Supplementary Figures 1-4 – Inter BSPM comparison

## References

1. Bear LR, LeGrice IJ, Sands GB, Lever NA, Loiselle DS, et al. How accurate is inverse electrocardiographic mapping? A systematic in vivo evaluation. *Circ. Arrhythm. Electrophysiol.* 11:e006108, 2018.
2. Rudy Y, Messinger-Rapport BJ. The Inverse Problem in Electrocardiology: Solutions in Terms of Epicardial Potentials. *Crit. Rev. Biomed. Eng.* 16:215-68, 1988.
3. Geselowitz DB. Description of cardiac sources in anisotropic cardiac muscle. Application of bidomain model. *J. Electrocardiol.* 25 Sup.:65-7, 1992.
4. van Dam PM, Oostendorp TF, Linnenbank AC, van Oosterom A. Non-invasive imaging of cardiac activation and recovery. *Ann. Biomed. Eng.* 37:1739-56, 2009.
5. Janssen AM, Potyagaylo D, Dössel O, Oostendorp TF. Assessment of the equivalent dipole layer source model in the reconstruction of cardiac activation times on the basis of BSPMs produced by an anisotropic model of the heart. *Med. Biol. Eng. Comput.* 56:1013-25, 2018.
6. Oosterhoff P, Meijborg VM, van Dam PM, van Dessel PF, Belterman CN, et al. Experimental validation of noninvasive epicardial and endocardial activation imaging. *Circ. Arrhythm. Electrophysiol.* 2016.
7. Sapp JL, Dawoud F, Clements JC, Horáček BM. Inverse Solution Mapping of Epicardial Potentials: Quantitative Comparison With Epicardial Contact Mapping. *Circ. Arrhythm. Electrophysiol.* 5:1001-9, 2012.
8. Andrews CM, Srinivasan NT, Rosmini S, Bulluck H, Orini M, et al. Electrical and structural substrate of arrhythmogenic right ventricular cardiomyopathy determined using noninvasive electrocardiographic imaging and late gadolinium magnetic resonance imaging. *Circ. Arrhythm. Electrophysiol.* 10:e005105, 2017.
9. Rudy Y. Noninvasive Electrocardiographic Imaging of Arrhythmogenic Substrates in Humans. *Circulation Research* 112:863-74, 2013.
10. Durrer D, van Dam RT, Freud GE, Janse MJ, Meijler FL, Arzbaecher RC. Total excitation of the isolated human heart. *Circulation* 41:899-912, 1970.
11. Wyndham CRM, Smith T, Saxema A, Engleman S, Levitsky RM, Rosen KM. Epicardial activation of the intact human heart without conduction defect. *Circulation* 59/1:161-8, 1979.
12. Massing GK, James TN. Anatomical configuration of the His bundle and bundle branches in the human heart. *Circulation* 53:609-21, 1976.
13. Tawara S. Das Reizleitungssystem des Säugetierherzens. Eine Anatomisch-Histologische Studie über das Atrioventrikulärbündel und die Purkinjeschen Fäden. Jena: Gustav Fischer.1906.
14. Keith A, Flack M. The auriculo-ventricular bundle of the human heart. *The Lancet* 168:359-64, 1906.
15. Ho SY, McCARTHY KP, Ansari A, Thomas PS, Sánchez-Quintana D. Anatomy of the atrioventricular node and atrioventricular conduction system. *International Journal of Bifurcation and Chaos* 13:3665-74, 2003.
16. Taccardi B, Punske BB, Macchi E, MacLeod RS, Ershler PR. Epicardial and intramural excitation during ventricular pacing: effect of myocardial structure. *Am. J. Physiol. Heart Circ. Physiol.* 294:H1753-H66, 2008.
17. Porta-Sánchez A, Angaran P, Massé S, Nair K, Farid T, et al. The effect of left ventricular pacing on transmural activation delay in myopathic human hearts. *EP Europace* 20:719-28, 2018.
18. Cassidy DM, Vassallo JA, Miller JM, Poll DS, Buxton AE, et al. Endocardial catheter mapping in patients in sinus rhythm: relationship to underlying heart disease and ventricular arrhythmias. *Circulation* 73:645-52, 1986.
19. Hatala R, Savard P, Tremblay G, Page P, Cardinal R, et al. Three Distinct Patterns of Ventricular Activation in Infarcted Human Hearts : An Intraoperative Cardiac Mapping Study During Sinus Rhythm. *Circulation* 91:1480-94, 1995.
20. Vigmond EJ, Stuyvers BD. Modeling our understanding of the His-Purkinje system. *Progress in biophysics and molecular biology* 120:179-88, 2016.
21. Cardone-Noott L, Bueno-Orovio A, Minchola A, Zemezmi N, Rodriguez B. Human ventricular activation sequence and the simulation of the electrocardiographic QRS complex and its variability in healthy and intraventricular block conditions. *EP Europace* 18:iv4-iv15, 2016.
22. Pezzuto S, Prinzen FW, Potse M, Maffessanti F, Regoli F, et al. Reconstruction of three-dimensional biventricular activation based on the 12-lead electrocardiogram via patient-specific modelling. *EP Europace* 23:640-7, 2021.
23. Gillette K, Gsell MA, Prassl AJ, Karabelas E, Reiter U, et al. A Framework for the generation of digital twins of cardiac electrophysiology from clinical 12-leads ECGs. *Med. Image Anal.* 71:102080, 2021.
24. van Dam PM, van Der Graaf AWM, Gotte MJW. A new 3D patient specific morphing tool enabling clinical application of non-invasive cardiac activation imaging. *Proc. ESC, Muenchen, 2012*, 33:251:
25. Meijs, Weier OW, Peters MJ, van Oosterom A. On the Numerical Accuracy of the Boundary Element Method. *IEEE Trans. Biomed. Eng.* BME-36:1038-49, 1989.
26. Roudijk RW, Boonstra MJ, Ruisch J, Kastelein M, van Dam E, et al. Feasibility study of a 3D camera to reduce electrode repositioning errors during longitudinal ECG acquisition. *J. Electrocardiol.* 66:69-76, 2021.
27. Loukas M, Klaassen Z, Tubbs RS, Derderian T, Paling D, et al. Anatomical observations of the moderator band. *Clin. Anat.* 23:443-50, 2010.
28. Saha A, Roy S. Papillary muscles of left ventricle—Morphological variations and it's clinical relevance. *Indian heart journal* 70:894-900, 2018.
29. Hakacova N, Robinson AM, Olson CW, Selvester RH, Wagner GS. The relationship between mitral papillary muscles positions and characteristics of the QRS complex. *J. Electrocardiol.* 41:487-90, 2008.
30. Bergquist JA, Good WW, Zenger B, Tate JD, MacLeod RS. Grömer: A pipeline for geodesic refinement of mesh registration. *Proc. International Conference on Functional Imaging and Modeling of the Heart, 2019:37-45*: Springer
31. van Oosterom A. Solidifying the Solid Angle. *J. Electrocardiol.* 35S:181-92, 2002.

32. van Dam PM, Oostendorp TF, van Oosterom A. Application of the fastest route algorithm in the interactive simulation of the effect of local ischemia on the ECG. *Med. Biol. Eng. Comput.* 47:11-20, 2009.
33. Sano T, Takayama N, Shimamoto T. Directional Differences of Conduction Velocity in the Cardiac Ventricular Syncytium Studied by Microelectrodes. *Circulation Research* VII:262-7, 1959.
34. Clerc L. Directional differences of impulse spread in trabecular muscle from mammalian heart. *J Physiol* 255:335-46, 1976.
35. Greenbaum RA, Ho SY, Gibson DG, Becker AE, Anderson RH. Left ventricular fibre architecture in man. *Br Heart J* 45:248-63, 1981.
36. Myerburg RJ, Gelband H, Nilsson K, Castellanos A, Morales AR, Bassett AL. The role of canine superficial ventricular muscle fibers in endocardial impulse distribution. *Circulation research* 42:27-35, 1978.
37. Cantwell CD, Roney CH, Ng FS, Siggers JH, Sherwin SJ, Peters NS. Techniques for automated local activation time annotation and conduction velocity estimation in cardiac mapping. *Computers in biology and medicine* 65:229-42, 2015.
38. Roudijk RW, Boonstra MJ, Brummel R, Kassenberg W, Blom LJ, et al. Comparing non-invasive inverse electrocardiography with invasive endocardial and epicardial electroanatomical mapping during sinus rhythm. *Frontiers in physiology* 12:2021.
39. Duchateau J, Sacher F, Pambrun T, Derval N, Chamorro-Servent J, et al. Performance and limitations of noninvasive cardiac activation mapping. *Heart Rhythm* 16:435-42, 2019.
40. Cluitmans MJ, Clerx M, Vandersickel N, Peeters RL, Volders PG, Westra RL. Physiology-based regularization of the electrocardiographic inverse problem. *Med. Biol. Eng. Comput.* 55:1353-65, 2017.



$\emptyset$

$(x, y) = \int_{S_u}$

$v_2 / c^2$

$v_{cg}$

$v_{cg}$

ind

# Chapter 3

## Comparing Non-invasive Inverse Electrocardiography With Invasive Endocardial and Epicardial Electroanatomical Mapping During Sinus Rhythm

RW Roudijk\*, MJ Boonstra\*, R Brummel, W Kassenberg, LJ Blom, TF Oostendorp,  
ASJM te Riele, JF van der Heijden, FW Asselbergs, PM van Dam, and P Loh.

\*The first two authors contributed equally to this manuscript

*Frontiers in Physiology. 2021 Oct 4;12:730736*

## Abstract

This study presents a novel non-invasive equivalent dipole layer (EDL) based inverse electrocardiography (iECG) technique which estimates both endocardial and epicardial ventricular activation sequences. We aimed to quantitatively compare our iECG approach with invasive electro-anatomical mapping (EAM) during sinus rhythm with the objective of enabling functional substrate imaging and sudden cardiac death risk stratification in patients with cardiomyopathy.

Thirteen patients (77% males,  $48 \pm 20$  years old) referred for endocardial and epicardial EAM underwent 67-electrode body surface potential mapping and CT imaging. The EDL-based iECG approach was improved by mimicking the effects of the His-Purkinje system on ventricular activation. EAM local activation timing (LAT) maps were compared with iECG-LAT maps using absolute differences and Pearson's correlation coefficient, reported as mean  $\pm$  standard deviation [95% confidence interval].

The correlation coefficient between iECG-LAT maps and EAM was  $0.54 \pm 0.19$  [0.49–0.59] for epicardial activation,  $0.50 \pm 0.27$  [0.41–0.58] for right ventricular endocardial activation and  $0.44 \pm 0.29$  [0.32–0.56] for left ventricular endocardial activation. The absolute difference in timing between iECG maps and EAM was  $17.4 \pm 7.2$  ms for epicardial maps,  $19.5 \pm 7.7$  ms for right ventricular endocardial maps,  $27.9 \pm 8.7$  ms for left ventricular endocardial maps. The absolute distance between right ventricular endocardial breakthrough sites was  $30 \pm 16$  mm and  $31 \pm 17$  mm for the left ventricle. The absolute distance for latest epicardial activation was median 12.8 [IQR: 2.9–29.3] mm.

This first in-human quantitative comparison of iECG and invasive LAT-maps on both the endocardial and epicardial surface during sinus rhythm showed improved agreement, although with considerable absolute difference and moderate correlation coefficient. Non-invasive iECG requires further refinements to facilitate clinical implementation and risk stratification.

## Introduction

Non-invasive imaging of cardiac depolarization and repolarization sequences, known as electrocardiographic imaging, is based on body surface potentials maps and cardiovascular imaging.<sup>1-4</sup> Two major methods have been introduced: 1) the potential based Equivalent Potential Distribution (EPD) method<sup>1,3,5-9</sup>, which estimates electrograms on the epicardium in a linear relation whereof activation and recovery timings are determined on the epicardium, and 2) the wave-front formulation based on the Equivalent Dipole Layer (EDL).<sup>2,4,10,11</sup> The EDL-based method, used in this study and referred to as inverse electrocardiography (iECG), calculates transmembrane potentials at both the endocardium and epicardium as a local source, whereof activation and recovery times are derived.<sup>4,11</sup> More precisely, these transmembrane potentials represented in the EDL-based method create currents that are proportional to the second derivative of the local transmembrane potentials.<sup>12</sup> Since the relation between the transmembrane potentials and the body surface potential map is nonlinear, an initial estimation of the activation sequence is required.<sup>2,4,10</sup>

The implementation of electrocardiographic imaging in clinical practice is limited, which may partly be explained by poor results for estimations during sinus rhythm.<sup>13</sup> Whereas estimation of rhythms with a single ventricular focus, i.e. ventricular pacing or premature ventricular complexes, is promising.<sup>1,6,7,9,10,13</sup> Estimation of ventricular activation during sinus rhythm is complicated by the nearly simultaneous initiation of activation waves from multiple endocardial sites mediated by the His-Purkinje system.<sup>14</sup> Quantitative comparison studies during sinus rhythm are limited and have shown poor performance, represented by low correlation coefficients between non-invasive estimations and invasive mapping.<sup>7</sup>

The proposed iECG method mimics the effects of the His-Purkinje system on the initiation of ventricular activation waves to improve accuracy of estimation during sinus rhythm.<sup>1,4,5,7-9,11</sup> With improved accuracy of estimation during sinus rhythm, iECG techniques may enable functional imaging of electroanatomical substrates on both the epicardium and endocardium and aid early detection and noninvasive risk stratification of patients with cardiomyopathies.<sup>15</sup> Therefore, a quantitative comparison of this novel iECG method for estimation of ventricular activation during sinus rhythm was performed. In this study, invasive endocardial and epicardial high-resolution local activation timing (LAT) maps obtained during electro-anatomical mapping (EAM) were compared to non-invasively estimated activation patterns.

## Methods

### *Patient population*

Patients referred for endocardial and epicardial EAM and ablation were enrolled. Epicardial mapping was indicated because of either recurrent ventricular tachycardia with a suspected epicardial substrate or symptomatic premature ventricular complexes

with a prior failed endocardial ablation. Anti-arrhythmic drugs, except amiodarone, were discontinued for a minimum of three half-lives prior to the ablation procedure. Amiodarone was continued because of its long half-life. The study protocol was approved by the local institutional review board (University Medical Center Utrecht, Utrecht, The Netherlands; protocol nr.17/628). The study was conducted according to the declaration of Helsinki and all patients gave informed consent prior to non-invasive and invasive mapping.

### *Data acquisition*

The workflow of the study is depicted in Figure 1. Patients underwent 67-electrode body surface potential mapping (sampling frequency 2048 Hz, Biosemi, Amsterdam, The Netherlands) prior to the invasive mapping procedure and the electrode positions were captured using a 3-dimensional camera (Intel Realsense D435, Santa Clara, USA).<sup>16</sup> Per patient, cardiac computed tomography (CT, Philips Healthcare, Best, The Netherlands) was performed to manually create patient specific anatomical models of the ventricles with both epicardial and endocardial surfaces, ventricular blood pool, lungs and thorax. The ventricular anatomical models were supplemented with patient specific endocardial structures associated with early ventricular activation through the His-Purkinje system (e.g. the left ventricular papillary muscles and right ventricular moderator band).<sup>14</sup> Electrode positions were reconstructed by registering 3-dimensional images to the thorax model. The volume conductor model was computed using the boundary element method. Conductivity values of 0.2 S/m for the thorax and ventricular tissue, 0.04 S/m for the lungs and 0.6 S/m for the blood cavities were used. (Supplementary Methods).

### *Signal processing*

Baseline drift and 50 Hz noise were removed from the body surface potential map signals. Per patient, five subsequent sinus rhythm complexes were selected to be analyzed in the iECG procedure. Premature ventricular complexes and sinus rhythm complexes prior to premature ventricular complexes were excluded from analysis. The root mean square of all recorded signals was used to annotate QRS onset, J-point and T-wave end. One lead from the standard 12-lead ECG was used as timing reference to allow comparison of absolute timings between iECG estimations and invasive EAM timings.

### *Inverse ECG procedure*

The novel iECG method has been described in more detail in the Supplementary Methods.<sup>4,11,17,18</sup> In short: the iECG method simulates body surface potential maps using the patient specific EDL cardiac source model, the patient specific volume conductor model and the estimated ventricular activation sequence. Nine regions containing potential foci were localized: four at the left ventricular septum, two at the base of both the posterior and anterior papillary muscles of the left ventricle,



two at the right ventricular septum and one at the insertion of the moderator band at the right ventricular free wall free wall.<sup>14</sup> The fastest route algorithm was used to compute activation sequences emerging from these locations and combinations of foci.<sup>4</sup> All possible combinations of foci were tested as the initial estimation (Supplementary Methods). The activation sequence from the initial estimation with the highest correlation between the simulated body surface potential map and the recorded body surface potential map, was selected as input for the optimization step (Supplementary Methods).<sup>4</sup> The optimized activation sequence was used to assign LAT to each node in the patient specific ventricular anatomical model (Figure 1 and Supplementary Figure 1).

### *Invasive electro-anatomical mapping*

Invasive EAM was performed under general anesthesia during sinus rhythm or atrial pacing. Ventricular paced complexes and premature ventricular complexes were excluded from analysis. Epicardial access was obtained by percutaneous subxiphoid approach<sup>19</sup> and endocardial access was obtained through the right femoral vein. Access to the left ventricle was gained through a transeptal puncture, using a steerable sheath (Mobicath, Biosense-Webster Inc. Irvine, USA). Anatomical coordinates, LAT maps and voltage maps were automatically created with EAM systems (Carto-3,

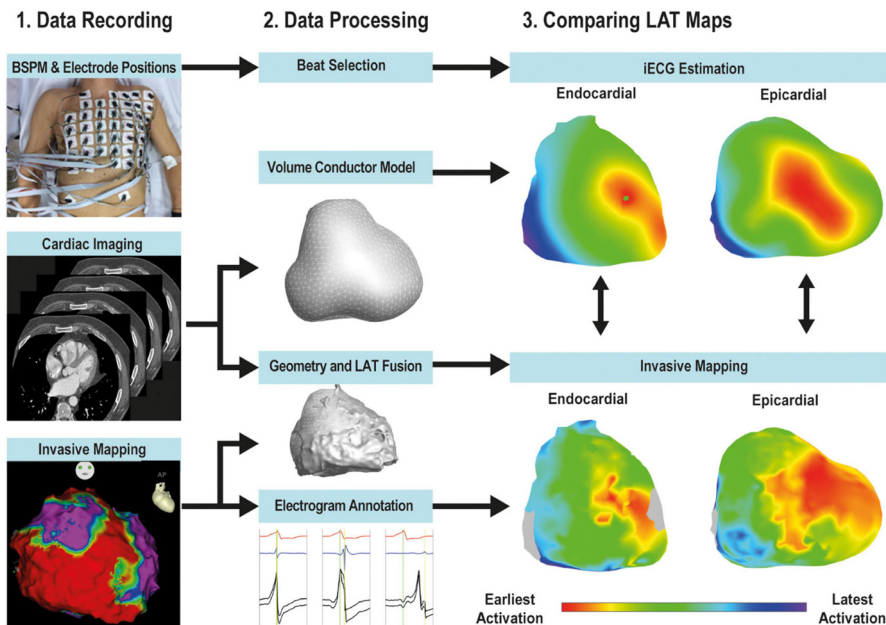


**Figure 1.** Workflow. The workflow of the study consisted of data recording (left panel), data processing (middle panel) and quantitative comparison (right panel). Body surface potential mapping (BSPM) using 67-electrodes was performed. CT imaging of the thorax and cardiac anatomy was performed and used to construct patient specific anatomical models and compute the volume conductor. The EAM anatomical point clouds were registered to the CT-based ventricular anatomy and LAT and bipolar values were projected on the CT-based anatomy. EAM-LAT maps were quantitatively compared to iECG-LAT maps.

Biosense-Webster Inc. Irvine, USA or EnSite Precision, Abbott, Chicago, USA) without prior integration of cardiac CT images. Endocardial and epicardial EAM was performed with multi-electrode catheters (PENTARAY® catheter, BiosenseWebster Inc. Irvine, USA or ADVISOR™ HD Grid mapping Catheter, Abbott, Chicago, USA). Unipolar and bipolar electrograms were simultaneously recorded with standard 12-lead ECG (band pass filters 30 Hz - 500 Hz, sampling frequency 1000 Hz), and one of these leads was used as timing reference for electrograms. Post-procedure, bipolar and corresponding unipolar electrograms were manually reviewed by investigators who were blinded to the information from the corresponding iECG map. LAT was set at the maximal amplitude of the bipolar signal, corresponding to maximum downslope (dV/dt) in unipolar electrograms (see Figure 2 for examples).<sup>20</sup> In case of doubt, recordings from neighboring electrograms were taken into consideration to determine LAT. Epicardial and endocardial myocardium with abnormal voltage electrograms was defined as bipolar voltage amplitude <1.5 mV.

#### *Comparison of non-invasive mapping and invasive mapping*

Anatomical coordinates with corresponding annotated LAT and bipolar voltage, obtained during EAM, were exported (MATLAB-2017a, The Mathworks Inc, Natick, USA). These anatomical coordinates were semi-automatically aligned to the CT-based ventricular anatomical model, according to anatomical landmarks (right ventricular outflow tract and the apex of the ventricles, Figure 1). Endocardial alignment was optimized using a closest point matching algorithm.<sup>21</sup> Surface Laplacian interpolation was used for areas with incomplete EAM, within a distance of 10 mm. To reduce misalignment errors, invasively collected datapoints for myocardial surfaces were projected onto the nearest node of the CTbased model and all projections per node were averaged. iECG-LAT maps were referenced to the same timing reference used during the EAM procedure. Pearson's inter-map correlation coefficient and intermap absolute difference in milliseconds (ms) were determined for the epicardium, right ventricular endocardium and left ventricular endocardium. Breakthrough of activation was defined as nodes with the lowest LAT value, and sites of latest activation were defined as the node with the highest LAT value. Euclidian distances between sites of earliest and latest activation were determined in millimeters (mm). Myocardial conduction velocity over surfaces was calculated as the minimum positive velocity between nodes, velocities more than 3 mm/ms were excluded. A relatively high cut-off of 3 mm/ms was used to account for velocities observed in regions with a high density of Purkinje-myocardial junctions as the conduction velocity of Purkinje fibers ranges between 2-3 mm/ms. This cut-off was used to take into account that the electrical pulse may spread via the Purkinje fibers to the neighboring myocardial tissue instead of via the myocardial tissue itself. Ventricular activation sequences were presented in right anterior oblique, left anterior oblique and inferior views.<sup>22</sup>

### *Statistical analysis*

Data were presented as mean±standard deviation or median [interquartile range], supplemented with 95% confidence interval (CI). Continuous data were compared using (un)paired Student's t-test or Mann–Whitney U test as appropriate. Differences between iECG-LAT maps and EAM-LAT maps were presented as absolute difference in ms for timings or absolute difference in mm for differences in sites of breakthrough, earliest activation or latest activation. iECG-LAT and EAM-LAT maps were compared with Pearson's linear correlation and presented as correlation coefficient. Agreement between iECG and EAM-LAT timings was quantitatively compared by Bland-Altman plots. A 2-sided P-value of <0.05 was considered significant. Statistical analysis was performed in MATLAB (MATLAB 2017a, The Mathworks Inc, Natick, USA).

## **Results**

### *Study population*

Thirteen patients (77% males, age 48±20 years) referred for epicardial and endocardial mapping and ablation of ventricular tachycardia (n=10) or symptomatic premature ventricular complexes (n=3) were included. Patients were diagnosed with arrhythmogenic cardiomyopathy (n=5), dilated cardiomyopathy (n=2), symptomatic premature ventricular complexes (n=3) or ventricular arrhythmias after healed myocarditis (n=3). Patients had either sinus rhythm (n=10) or atrial pacing by an implanted permanent pacemaker (n=3) during body surface potential recording and the EAM procedure, see Supplementary Table 1 for a summary of the included population and Supplementary Table 2 for a detailed description per included patient.

### *iECG procedure quality*

The patient cardiac anatomical models had an inter-node spatial resolution of 8±1 mm. The QRS complex morphology of the recorded body surface potential maps correlated with the QRS complex morphology of the simulated body surface potential maps in the iECG procedure (correlation coefficient=0.97±0.02). The QRS morphology of the timing reference lead during EAM correlated with the timing reference lead of the recorded body surface potential map (correlation coefficient=0.94±0.02).

### *EAM quality*

Epicardial EAM was performed in all patients, right ventricular endocardial EAM in 10 patients and left ventricular endocardial EAM in four patients. EAM consisted of median 4611[3369-5633] epicardial electrograms, 910[280-1638] right ventricular endocardial electrograms and 605[247-1412] left ventricular endocardial electrograms. The number of annotations per square mm was 20±11 for the epicardium, 10±5 for the right ventricular endocardium and 8±4 for the left ventricular endocardium. The percentage of EAM per surface was on average 67[range:48-82]% of anatomical nodes for the epicardium, 45[range:15-79]% for the right ventricular endocardium

and 48[range:22-71]% for the left ventricular endocardium. The anatomical EAM model was limited to the locations where the catheter had been positioned during the EAM procedure.

### *Local Activation Timing*

Figure 2A shows an example of the comparison of iECG and EAM for LAT maps, and the comparison between earliest and latest activated nodes for both the epicardium and endocardium. The ranges between earliest and latest ventricular activation were not significantly different between iECG-LAT maps and EAM-LAT maps ( $111 \pm 23$  vs.  $124 \pm 39$  ms,  $p=0.311$ ). The ranges of earliest and latest activation per patient are included in Supplementary Table 3. Figure 2B shows an example of the iECG and the EAM approach in a patient with a healed myocarditis with right bundle branch block. The fast and His-Purkinje mediated activation of the left ventricular myocardium is shown in contrast to the relatively slower activation of the right ventricle due to the right bundle branch block. Figure 2C shows an example of the activation pattern and epicardial electrogram annotation in a patient with arrhythmogenic cardiomyopathy. Furthermore, all LAT and voltage maps of each included patient are available as Supplementary Figure 1. The mean correlation coefficient between iECG-LAT maps and EAM-LAT maps was  $0.54 \pm 0.19$ ; [95% CI:0.49-0.59] for epicardial maps,  $0.50 \pm 0.27$ ; [95% CI:0.41-0.58] for endocardial right ventricular maps and  $0.44 \pm 0.29$ ; [95% CI:0.32-0.56] for endocardial left ventricular maps (Table 1). The moderate agreement of LAT between iECG and EAM maps is shown in Figure 3A for all included electrograms on the epicardium ( $R=0.632$ ,  $p<0.001$ ), right ventricular endocardium ( $R=0.597$ ,  $p<0.001$ ) and left ventricular endocardium ( $R=0.546$ ,  $p<0.001$ ). Figure 3B shows that a prolonged QRS duration of the included complexes did not affect correlation coefficient or absolute difference.

Figure 3C suggest that a higher density of mapped electrograms per mm<sup>2</sup> reduces the scatter of correlation coefficients. The absolute difference for epicardial LAT maps was  $17.4 \pm 7.2$  ms; [95% CI:15.6-19.2], for endocardial right ventricular maps  $19.5 \pm 7.7$  ms; [95% CI:17.2-21.7], and for endocardial left ventricular maps  $27.9 \pm 8.7$  ms; [95% CI:24.2-31.5]. The relation between the percentage of mapped anatomical points during EAM and the agreement for LAT values is shown in Figure 3D. The correlation coefficient between iECG-LAT maps and EAM-LAT maps was not significantly affected by the absolute number of EAM electrograms ( $p=0.324$ ), the number of electrograms with abnormal voltage ( $p=0.306$ ) or the QRS duration ( $p=0.485$ ) (see Supplementary Figure 2). However, the annotation density and the percentage of mapped anatomical points per map affected the agreement between iECG and EAM. In maps with a low annotation density or lower percentage of mapped anatomical points the correlation coefficients were low (Figure 3 C/D). This may have negatively affected the observed correlation coefficients in this study because endocardial EAM was often limited to either the right ventricular or left ventricular surface. The

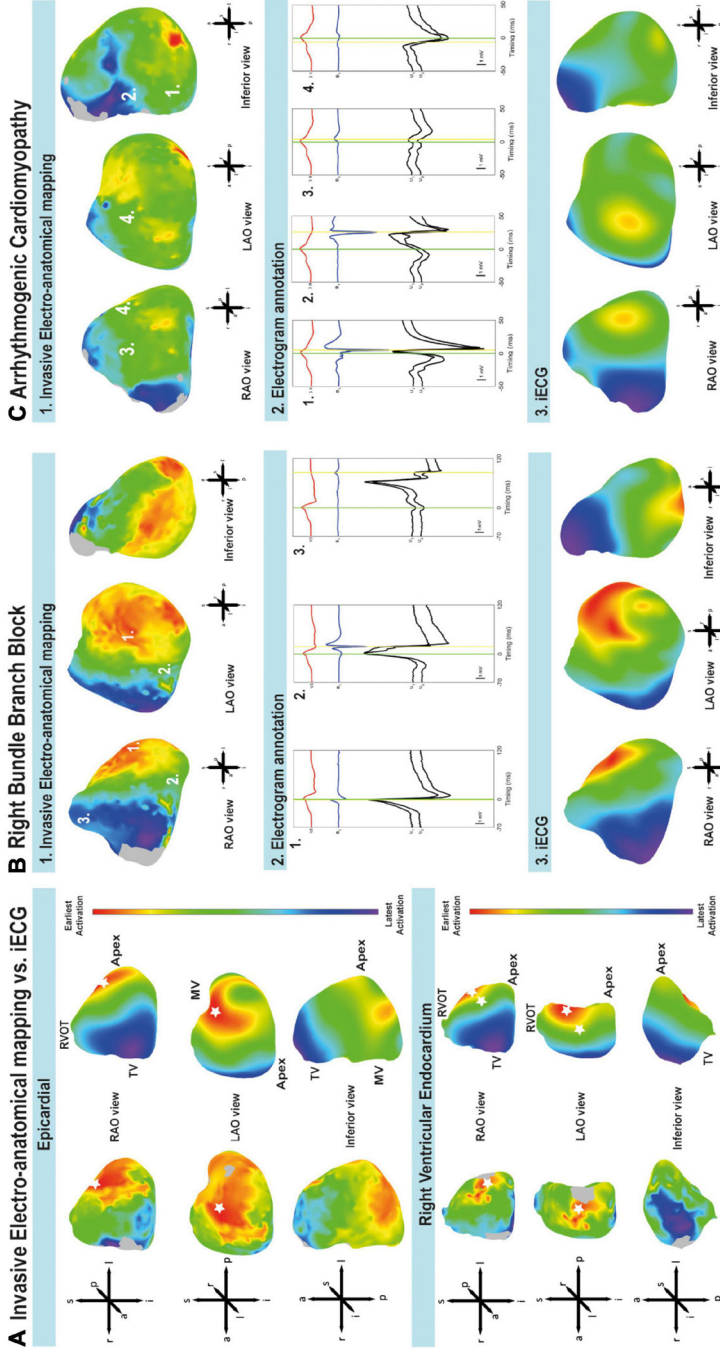


**Figure 2.** Comparison of early and latest activated myocardium and annotation of local activation timing. A: LAT maps derived from iECG and EAM from early (red) to late (blue) activation. Breakthroughs of ventricular activation are indicated with a white asterisk. Epicardium: both EAM and iECG estimation showed breakthrough of activation at the right ventricular free wall and the left ventricular free wall. Endocardial activation of the right ventricular free wall: iECG estimation corresponds to EAM. Intra-ventricular septum activation was located more toward the apex in the EAM. Imaging views are based on the anatomical approach for EAM<sup>22</sup>. MV, mitral valve; RVOT, right ventricular outflow tract; TV, tricuspid valve. B: Patient with healed myocarditis and right bundle branch block. C: Epicardial activation and electrogram annotation in a patient with arrhythmic cardiomyopathy. B/C: Imaging views are based on the anatomical approach for EAM<sup>23</sup>. 1: Epicardial EAM-LAT map from early (red) to late (blue) activation. The early regions in the left ventricle and late regions in the right ventricle suggest a right bundle branch block. 2: EGM annotation of bipolar electrograms. The green line corresponds to the timing reference. The yellow line shows annotation to the maximal amplitude of the bipolar signal. 3: iECG-LAT map of epicardial activation from early (red) to late (blue).

iECG estimations were based on five QRS complexes selected from the body surface potential maps, but a Bland-Altman analysis did not result in divergent results per included QRS complex. These scatter plots and Bland-Altman plots for each included patient are available in Supplementary Figure 2.

#### *Localization of earliest breakthrough and areas of latest activation*

The number of endocardial breakthrough points was similar when comparing iECG-LAT maps and EAMLAT maps:  $3.3 \pm 0.8$  vs  $3.2 \pm 0.9$  for epicardial maps,  $1.8 \pm 0.6$  vs  $2.1 \pm 0.6$  for right ventricular endocardial maps and  $1.8 \pm 0.5$  vs  $1.8 \pm 1.0$  for left ventricular endocardial maps (Table 1). These findings were in line with the observations of Durrer et al. and the assumptions of the iECG initial estimation. (14) Epicardial breakthrough of activation had an absolute difference between iECG-LAT maps and EAM-LAT maps of  $42.1 \pm 18.6$  mm; [95% CI:36.7-47.5]. For endocardial breakthrough of activation, the absolute difference was  $29.9 \pm 16.0$  mm; [95% CI:25.1-34.8] for the right ventricular endocardium and  $31.0 \pm 16.8$  mm; [95% CI:23.8-38.1] for the left ventricular endocardium. The latest activated nodes had an absolute difference between iECG and EAM of  $54.1 \pm 26.9$  mm; [95% CI:47.5-60.7] for epicardial maps,  $46.7 \pm 28.8$  mm; [95% CI:38.8-54.7] for right ventricular endocardial maps and  $32.7 \pm 17.2$  mm; [95% CI:25.1-40.4] for left ventricular endocardial maps (Table 1). The timing of the latest activated nodes differed  $12.8$ [2.9-29.3] ms; [95% CI:6.4-31.7] for epicardial maps,  $15.2$ [10.1-28.7] ms; [95% CI:8.5-32.5] for right ventricular endocardial maps and  $20.8$ [10.4-57.3] ms; [95% CI:-12.5-71.4] for left ventricular endocardial maps. The myocardial conduction velocity was not significantly different between iECG and EAM maps for respectively the epicardium ( $1.26 \pm 0.16$  vs  $1.26 \pm 0.20$  m/s,  $p > 0.999$ ), right ventricular endocardium ( $1.13 \pm 0.09$  vs  $0.94 \pm 0.17$  m/s,  $p = 0.069$ ) or left ventricular endocardium ( $1.03 \pm 0.11$  vs  $0.92 \pm 0.07$  m/s,  $p = 0.968$ ).

## **Discussion**

This is the first study to quantitatively compare non-invasive, EDL-based iECG estimation of ventricular activation sequences during sinus rhythm with invasive high density endocardial and epicardial EAM in humans. Comparison of agreement between iECG-LAT maps with EAM-LAT maps showed moderate agreement. However, this observed agreement (correlation coefficient =  $0.54 \pm 0.19$ ) was remarkably higher compared to a recent validation study (correlation coefficient =  $-0.04 \pm 0.3$ ) performed during sinus rhythm.<sup>7</sup> Mimicking the effects of the His-Purkinje system on ventricular activation in the iECG method resulted in activation patterns corresponding to observations of Durrer et al. in experiments with explanted human hearts.<sup>14</sup> In contrast to prior EPD-based studies which were limited to estimations on the epicardium, estimation of both the endocardial and epicardial activation sequences was achieved. Although accuracy and spatial resolution require further improvement before implementation of this diagnostic tool in clinical practice, these findings may be of clinical importance for functional non-invasive substrate imaging during



**Table 1.** Comparison between iECG and EAM

Parameters	Mean $\pm$ SD	Median [IQR]
<b>Epicardium</b>		
Correlation coefficient	54.1 $\pm$ 19.0	51.0 [44.0 – 71.5]
Absolute difference (ms)	17.4 $\pm$ 7.2	15.1 [12.8 – 19.6]
Absolute difference earliest breakthrough (mm)	42.1 $\pm$ 18.6	37.9 [28.4 – 58.5]
Absolute difference terminal site of activation (mm)	54.1 $\pm$ 26.9	51.0 [33.4 – 69.6]
<b>Absolute difference timing of latest activation (ms)</b>	19.1 $\pm$ 20.9	12.8 [2.9 – 29.3]
EAM breakthroughs (n)	3.15 $\pm$ 0.9	3.0 [2.5 – 4.0]
iECG breakthroughs (n)	3.3 $\pm$ 0.8	3.4 [2.9 – 4.0]
Right ventricular endocardium		
<b>Correlation coefficient</b>	49.6 $\pm$ 27.3	55.5 [46.0 – 62.0]
Absolute difference (ms)	19.5 $\pm$ 7.7	17.4 [13.2 – 24.4]
Absolute difference earliest breakthrough (mm)	29.9 $\pm$ 16.0	28.3 [22.3 – 47.4]
Absolute difference terminal site of activation (mm)	46.7 $\pm$ 28.8	37.0 [24.5 – 69.4]
Absolute difference timing of latest activation (ms)	20.4 $\pm$ 16.7	15.2 [10.1 – 28.7]
EAM breakthroughs (n)	2.1 $\pm$ 0.6	2.0 [2.0 – 2.25]
<b>iECG breakthroughs (n)</b>	1.8 $\pm$ 0.6	2.0 [1.2 – 2.3]
Left ventricular endocardium		
Correlation coefficient	44.0 $\pm$ 28.8	53.5 [13.5 – 65.0]
Absolute difference (ms)	27.9 $\pm$ 8.7	27.3 [20.1 – 36.2]
Absolute difference earliest breakthrough (mm)	31.0 $\pm$ 16.8	31.1 [14.7 – 47.1]
<b>Absolute difference terminal site of activation (mm)</b>	32.7 $\pm$ 17.2	39.2 [14.8 – 44.1]
Absolute difference timing of latest activation (ms)	29.5 $\pm$ 26.3	20.8 [10.4 – 57.3]
EAM breakthroughs (n)	1.8 $\pm$ 1.0	1.5 [1.0 – 2.8]
iECG breakthroughs (n)	1.8 $\pm$ 0.5	2.0 [1.3 – 2.0]

Abbreviations as in manuscript.

sinus rhythm to improve the value of ECG screening and risk stratification of sudden cardiac death.<sup>15</sup>

### Quantitative comparison

Previous quantitative EPD-based validation studies showed higher agreement between ventricular paced complexes and EAM, compared to sinus rhythm complexes.<sup>7,9</sup> Duchateau et al. showed poor epicardial inter-map correlation coefficient ( $-0.04 \pm 0.3$ ) during sinus rhythm, although correlation coefficients increased with increasing QRS duration. This relation is most likely explained by the complexity of multiple simultaneous ventricular activation waveforms occurring during sinus rhythm, which decreases in rhythms with a single focus.<sup>7</sup> In the present study, a considerably higher agreement (correlation coefficient  $0.54 \pm 0.19$ ) between EAM and the novel iECG-LAT maps was observed during sinus rhythm. This improved performance is attributed to the incorporation of the effects of the HisPurkinje system on the initiation of ventricular activation.<sup>10</sup> Previously reported absolute difference for breakthrough of epicardial pacing was smaller compared to the present study (13.2-20.7 mm vs.  $42.1 \pm 18.6$  mm).<sup>6,9,10</sup> However, previously reported absolute difference for epicardial

breakthrough during sinus rhythm was higher compared to our results ( $75.6 \pm 38.1$  mm vs.  $42.1 \pm 18.6$  mm).<sup>7</sup> Again, these differences may be explained by estimations of rhythms originating from a single ventricular focus and sinus rhythm. Thus, spatial resolution observed in this study was comparable to the earlier studies in paced complexes.<sup>5,6</sup> Due to the complex nature of the His-Purkinje system and the Purkinjomyocardial coupling, the implemented methods remain an approximation of the true myocardial activation and His-Purkinje physiology.<sup>14,23,24</sup>

We observed a high agreement between estimated and measured body surface potential maps, whereas the inter-map agreement was less. As the inverse problem is ill-posed, completely different ventricular activation sequences can result in similar body surface potential map waveforms, consequently we found a high agreement between body surface potential maps but a lower agreement in myocardial activation patterns.

The conduction velocities calculated on the epicardial and endocardial surfaces in this study for both the EAM-LAT maps and iECG-LAT maps were quite high ( $> 1$  m/s). However, we note that these conduction velocities are mostly determined by the velocity estimated at the surface of the myocardium. Consequently, in a Purkinje dense region, surface velocity may appear high because it also reflects the effect of the activation spread by the Purkinje fibers and not only by the myocardial tissue at the endocardial surface. Furthermore, at the epicardial surface, velocities may appear high due to the occurrence of transmural waves.

#### *Modelling the effects of the His-Purkinje system during sinus rhythm*

In this study, initial sites of activation were determined in the iECG method based on the observations of Durrer et al and nine possible sites of early activation were localized.<sup>14</sup> Sets of these initial sites of activation were tested based on the correlation coefficient between the computed and recorded body surface potential maps, as described in more detail in the Supplementary Methods. This hypothesis was partially tested by comparing the EAM-LAT maps to the iECG-LAT maps. However, as endocardial EAM-LAT maps were often either of the right or the left endocardial surface and also did not cover the complete endocardial surface for each patient, the comparison between the number of identified EAM foci and iECG foci was hampered. This was also reflected in the absolute difference in location of identified foci of approximately 30 mm comparing iECG foci to EAM foci.

Previous versions of EDL-based methods estimating His-Purkinje mediated activation (e.g. sinus rhythm) were based on a multi-focal search algorithm over the complete endocardium and epicardium, where the first identified focus was chosen based on the highest correlation between recorded and simulated body surface potentials.<sup>4,10</sup> Consequently, this algorithm directly assumed that by using one focus, most of



**A LAT of iECG and EAM for each annotated node**

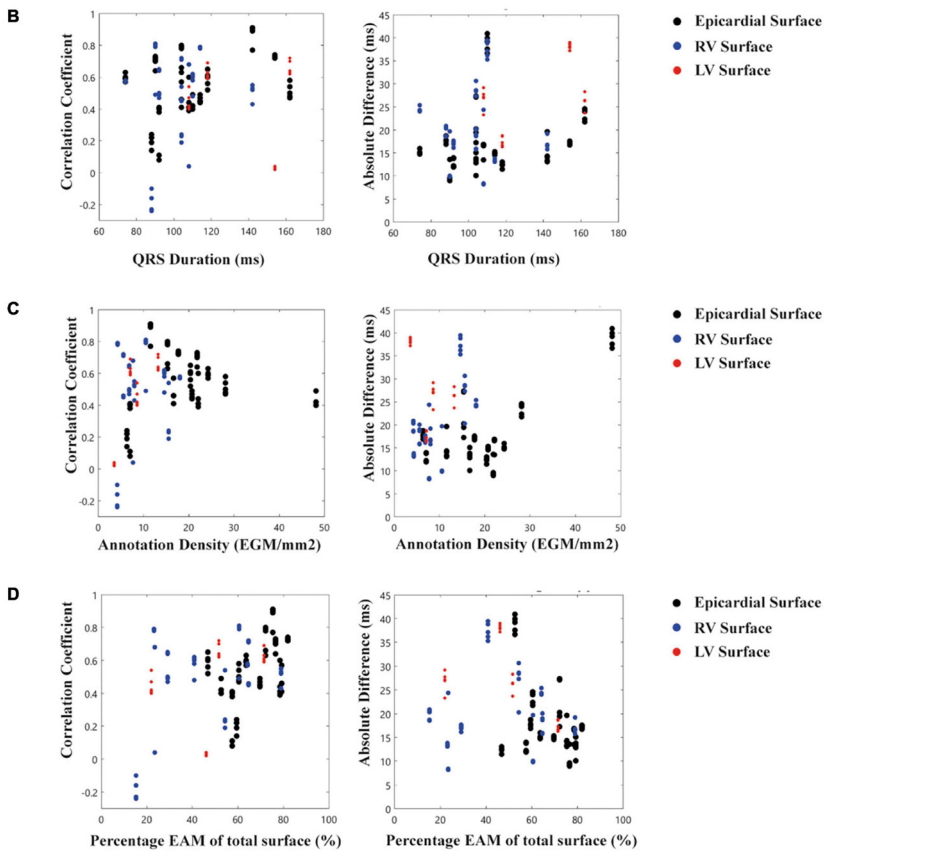
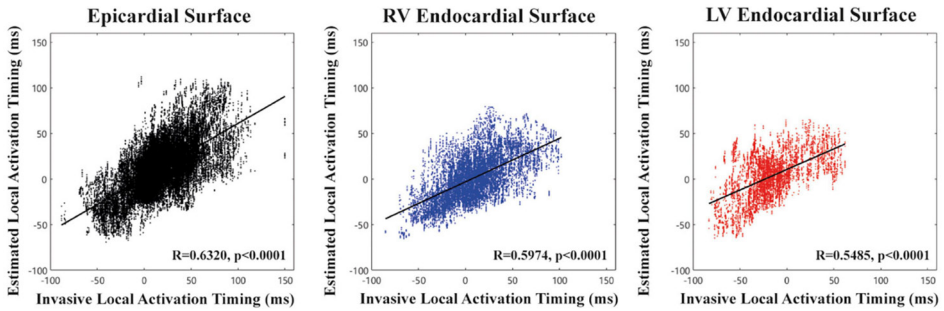


**Figure 3.** Scatter plots of local activation timing stratified for epicardial and endocardial surfaces. A: For each node in the ventricular anatomy the EAM-LAT values (X-axis) are scattered against iECG-LAT values (Y-axis). The black line in each plot represents the linear regression line and R-value and p-value are shown in each plot. B: Relation between QRS duration (X-axis) for the 5 selected complexes in the iECG procedure and correlation coefficient/absolute difference for the LAT values (Y-axis). C: Relation between annotation density (X-axis) per mm<sup>2</sup> and correlation coefficient/absolute difference for LAT values for the 5 selected complexes in the iECG procedure (Y-axis). (D) Relation between percentage of EAM of the total surface (X-axis) and correlation coefficient/absolute difference for LAT values (Y-axis).

the underlying activation sequence could be 'explained'. However, sinus rhythm, and especially narrow QRS complex sinus rhythm is an interplay between multiple activation wavefronts. Implementation of the His-Purkinje system excludes these unrealistic estimates and provides the possibility to test multiple near simultaneous foci. At the same time the initial estimation is restricted to the physiologically realistic anatomical areas and the computational burden of the iECG algorithm is minimized.

#### *Post-processing and reference standard*

Post-processing of ECG signals, electrogram signals, and cardiac imaging influences iECG accuracy.<sup>9,13</sup> To achieve high quality EAM-LAT maps, which were used as gold standard for comparison, electrograms derived from multi-electrode catheters required re-annotation using bipolar and unipolar signals and timing to a timing reference.<sup>9,20</sup> However, inhomogeneity in LAT distributions of EAM-LAT maps were observed even after re-annotation, which may have influenced the observed agreement between iECG and EAM-LAT maps. Both the epicardial and endocardial surfaces had an adequate spatial distribution of electrograms as reflected in the number of LAT per mm<sup>2</sup> (see Figure 3C). Furthermore, the percentage of mapped surfaces was variable and some EAM procedures resulted in incomplete endocardial EAM anatomical point clouds, which affects calculated inter-map correlation coefficient (see Figure 3C/D).

#### *Clinical implications and future directions*

Despite a considerable improvement of the iECG approach for sinus rhythm, the technique requires further adaptations and refinements that will facilitate implementation in clinical practice. Further integration of cardiovascular imaging techniques may improve performance and spatial resolution.<sup>15</sup> Currently, the patient specific anatomical models were limited in spatial resolution by the computational models of the iECG procedure, allowing at maximum 3000 cardiac nodes, which directly affects the resolution of the cardiac anatomical model resulting in an inter-node spatial resolution of  $8 \pm 1$ mm. Diffuse or local myocardial fibrosis affects ventricular activation patterns in structurally diseased hearts. Integration of these structural abnormalities in the iECG method and refinement of the cardiac anatomical models is likely to improve imaging of electro-anatomical substrates.<sup>4,10,15</sup> Since electro-anatomical substrates are not limited to solely the epicardium or endocardium, iECG may allow functional imaging of such 3-dimensional substrates in patients with arrhythmias or cardiomyopathy.<sup>15</sup> Besides diagnostic implications, non-invasive sinus rhythm iECG may play a role in the monitoring of disease progression and in sudden cardiac death risk stratification in patients with complex electroanatomical substrates, such as inherited cardiomyopathies. Eventually, reducing the number of electrodes of the body surface potential map that currently ranges from 67-256 electrodes, may improve clinical applicability.<sup>16</sup> For EDL-based studies, also this study, the 64-electrode setup is often used.<sup>4,10</sup> Mathematically this setup suffices,

as the number of independent signals is adequately captured using this number of electrodes and additionally, the electrodes are distributed with a high resolution in the high-gradient potential regions on the surface of the thorax.<sup>16</sup>

### *Limitations*

This single center study with a small sample size included patients with structural heart disease, which may influence the generalizability of the results. Additionally, we used a set conduction velocity over the model to determine the initial estimation. This assumption may not hold in the presence of pathologies or myocardial scarring after prior ablation, but the EDL holds for homogeneous anisotropic tissue.<sup>25</sup>

EAM procedures and body surface potential maps were not simultaneously recorded, but in similar conditions especially concerning anti-arrhythmic drugs. During EAM, complexes were selected using dedicated Carto/Ensite EAM systems. Furthermore, sinus rhythm complexes directly following a premature ventricular complex were excluded for analysis in both the EAM and iECG-LAT map. However, a possible influence of variations in heart rate, autonomic tonus or general anesthesia cannot be excluded. The quality of gold standard EAM may have been influenced by vendor specific algorithms within the EAM systems and regional mapping by the operator during the procedure. Inherent to invasive electrophysiological studies, EAM maps consisted of electrograms recorded from consecutive sinus rhythm complexes, whereas iECG maps were derived from five sinus rhythm complexes selected from the body surface potential map.

### **Conclusions**

Quantitative comparison of EDL-based iECG during sinus rhythm in patients undergoing invasive endocardial and epicardial electro-anatomical mapping showed improved agreement when compared to prior validation studies, although with considerable absolute difference in both timing and breakthrough of ventricular activation. Non-invasive iECG of both the epicardium and endocardium may prove valuable as a diagnostic tool for functional imaging of electro-anatomical substrates in sinus rhythm where activation always starts at the endocardial surface, to improve the value of the ECG in screening for cardiomyopathy and sudden cardiac death risk stratification. Future research should focus on improving accuracy and spatial resolution before implementation into clinical practice to enable imaging of functional electro-anatomical substrates.

### *Acknowledgements*

This work was supported by the Dutch Heart Foundation (grant numbers CVON2015-12 eDETECT and QRS-Vision 2018B007).

## References

1. Rudy Y. Noninvasive electrocardiographic imaging of arrhythmogenic substrates in humans. *Circ Res.* 2013;112(5):863-74.
2. Huiskamp G, Van Oosterom A. The depolarization sequence of the human heart surface computed from measured body surface potentials. *IEEE Trans Biomed Eng.* 1988;35(12):1047-58.
3. Ramanathan C, Ghanem RN, Jia P, Ryu K, Rudy Y. Noninvasive electrocardiographic imaging for cardiac electrophysiology and arrhythmia. *Nat Med.* 2004;10(4):422-8.
4. van Dam PM, Oostendorp TF, Linnenbank AC, van Oosterom A. Non-invasive imaging of cardiac activation and recovery. *Ann Biomed Eng.* 2009;37(9):1739-56.
5. Cluitmans MJM, Bonizzi P, Karel JMH, Das M, Kietselaer B, de Jong MMJ, et al. In Vivo Validation of Electrocardiographic Imaging. *JACC Clin Electrophysiol.* 2017;3(3):232-42.
6. Hohmann S, Rettmann ME, Konishi H, Borenstein A, Wang S, Suzuki A, et al. Spatial Accuracy of a Clinically Established Noninvasive Electrocardiographic Imaging System for the Detection of Focal Activation in an Intact Porcine Model. *Circ Arrhythm Electrophysiol.* 2019;12(11):e007570.
7. Duchateau J, Sacher F, Pambrun T, Derval N, Chamorro-Servent J, Denis A, et al. Performance and limitations of noninvasive cardiac activation mapping. *Heart Rhythm.* 2019;16(3):435-42.
8. Sapp JL, Dawoud F, Clements JC, Horacek BM. Inverse solution mapping of epicardial potentials: quantitative comparison with epicardial contact mapping. *Circ Arrhythm Electrophysiol.* 2012;5(5):1001-9.
9. Graham AJ, Orini M, Zacur E, Dhillon G, Daw H, Srinivasan NT, et al. Simultaneous Comparison of Electrocardiographic Imaging and Epicardial Contact Mapping in Structural Heart Disease. *Circ Arrhythm Electrophysiol.* 2019;12(4):e007120.
10. Oosterhoff P, Meijborg VM, van Dam PM, van Dessel PF, Belterman CN, Streekstra GJ, et al. Experimental Validation of Noninvasive Epicardial and Endocardial Activation Imaging. *Circ Arrhythm Electrophysiol.* 2016;9(8):e004104.
11. van Oosterom A. A comparison of electrocardiographic imaging based on two source types. *Europace.* 2014;16 Suppl 4:iv120-iv8.
12. Leon LJ, Witkowski FX. Calculation of transmembrane current from extracellular potential recordings: a model study. *J Cardiovasc Electrophysiol.* 1995;6(5):379-90.
13. Cluitmans M, Brooks DH, MacLeod R, Dossel O, Guillem MS, van Dam PM, et al. Validation and Opportunities of Electrocardiographic Imaging: From Technical Achievements to Clinical Applications. *Front Physiol.* 2018;9:1305.
14. Durrer D, van Dam RT, Freud GE, Janse MJ, Meijler FL, Arzbacher RC. Total excitation of the isolated human heart. *Circulation.* 1970;41(6):899-912.
15. Tung R, Raiman M, Liao H, Zhan X, Chung FP, Nagel R, et al. Simultaneous Endocardial and Epicardial Delineation of 3D Reentrant Ventricular Tachycardia. *J Am Coll Cardiol.* 2020;75(8):884-97.
16. Hoekema R, Uijen GJ, van Oosterom A. On selecting a body surface mapping procedure. *J Electrocardiol.* 1999;32(2):93-101.
17. Greensite F, Huiskamp G, van Oosterom A. New quantitative and qualitative approaches to the inverse problem of electrocardiology: their theoretical relationship and experimental consistency. *Med Phys.* 1990;17(3):369-79.
18. Huiskamp G, Greensite F. A new method for myocardial activation imaging. *IEEE Trans Biomed Eng.* 1997;44(6):433-46.
19. Sosa E, Scanavacca M, d'Avila A, Pilleggi F. A new technique to perform epicardial mapping in the electrophysiology laboratory. *J Cardiovasc Electrophysiol.* 1996;7(6):531-6.
20. Cantwell CD, Roney CH, Ng FS, Siggers JH, Sherwin SJ, Peters NS. Techniques for automated local activation time annotation and conduction velocity estimation in cardiac mapping. *Comput Biol Med.* 2015;65:229-42.
21. Bergquist JA, Good WW, Zenger B, Tate JD, MacLeod RS. GRÖMeR: A Pipeline for Geodesic Refinement of Mesh Registration. *Funct Imaging Model Heart.* 2019;11504:37-45.
22. Cosio FG, Anderson RH, Kuck KH, Becker A, Borggrefe M, Campbell RW, et al. Living anatomy of the atrioventricular junctions. A guide to electrophysiologic mapping. A Consensus Statement from the Cardiac Nomenclature Study Group, Working Group of Arrhythmias, European Society of Cardiology, and the Task Force on Cardiac Nomenclature from NASPE. *Circulation.* 1999;100(5):e31-7.
23. Myerburg RJ. The gating mechanism in the distal atrioventricular conducting system. *Circulation.* 1971;43(6):955-60.
24. Veenstra RD, Joyner RW, Rawling DA. Purkinje and ventricular activation sequences of canine papillary muscle. Effects of quinidine and calcium on the Purkinje-ventricular conduction delay. *Circ Res.* 1984;54(5):500-15.
25. Geselowitz DB. Description of cardiac sources in anisotropic cardiac muscle. Application of bidomain model. *J Electrocardiol.* 1992;25 Suppl:65-7.

*Supplementary material*

Available at: <https://www.frontiersin.org/articles/10.3389/fphys.2021.730736/full#S10>

Supplementary Figure 1 – All iECG, EAM maps, and voltage maps.

Supplementary Figure 2 – Factors associated with correlation coefficients and absolute differences.

Supplementary Figure 3 – Scatterplot and Bland-Altman plot per included patient.

Supplementary Table 1 – Summary data of the study population.

Supplementary Table 2 – Detailed study population per included patient.

Supplementary Table 3 – Ranges of earliest and latest activation per subject.

Supplementary Methods – Detailed methods section on iECG multi-wave initial estimation.

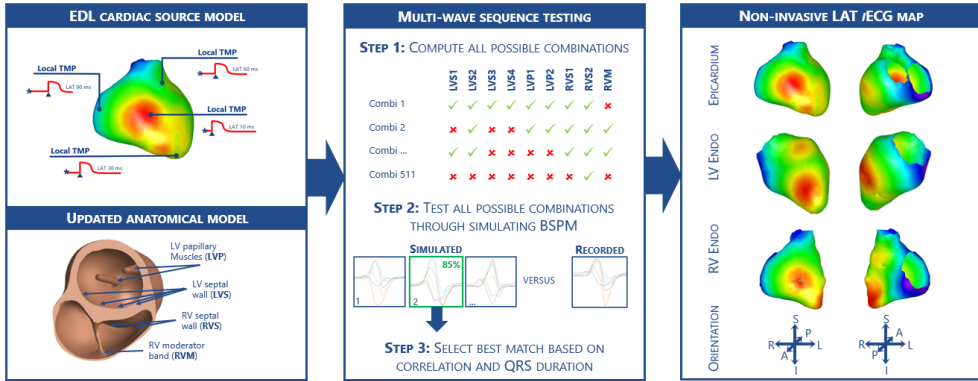
**Supplementary Table 1.** *Study population summary*

<b>Study Population</b>	<b>Mean ± SD, median [IQR] or n (%)</b>
<b>Demographics</b>	
Age (years)	48 ± 20
Male sex	10 (77)
Sustained ventricular tachycardia	10 (77)
Symptomatic premature ventricular complexes	3 (23)
<b>12-lead ECG</b>	
Sinus rhythm	10 (77)
Atrial pacing	3 (23)
QRS duration (ms)	112 ± 26
<b>Electroanatomical Mapping</b>	
Epicardial mapping (number of electrograms)	4611 [3369 - 5633]
RV endocardial mapping (number of electrograms)	910 [280 - 1638]
LV endocardial mapping (number of electrograms)	605 [247 - 1412]
Carto mapping system	10 (77)
EnSite Precision mapping system	3 (23)
<b>Substrate</b>	
Arrhythmogenic cardiomyopathy	5 (39)
Dilated cardiomyopathy	2 (15)
Healed myocarditis	3 (23)
Pathogenic genetic variant*	8 (62)
<b>Treatment prior to ablation procedure</b>	
Sotalol	7 (77)
Beta blocker	2 (15)
Beta blocker combined with anti-arrhythmic drugs	3 (23)
Implantable cardioverter defibrillator	10 (77)
Prior failed endocardial ablation	6 (46)

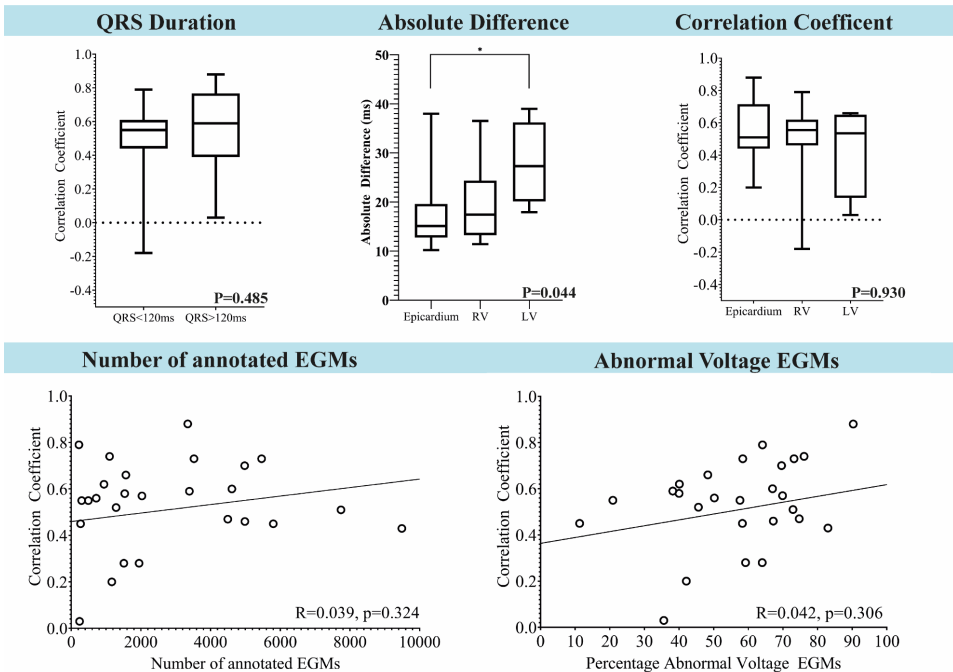
**Supplementary Table 3.** Ranges of earliest and latest activation per subject

ID	iECG			EAM		
	Total Activation Timing Mapped (ms)	Earliest Activation Mapped Surfaces (ms)	Latest Activation Mapped Surfaces (ms)	Total Activation Timing Mapped (ms)	Earliest activation Mapped Surfaces (ms)	Latest activation Mapped Surfaces (ms)
<b>1</b>	91.6 ± 3.0	-32.0 ± 1.6	58.5 ± 3.5	74	-17	57
<b>2</b>	93.3 ± 8.4	-33.5 ± 0.4	50.5 ± 0.6	90	-22	68
<b>3</b>	111.0 ± 4.7	-30.9 ± 1.9	73.0 ± 4.3	172	-22	150
<b>4</b>	90.9 ± 5.4	-35.6 ± 1.7	50.8 ± 5.2	83	-45	38
<b>5</b>	103.0 ± 1.3	-64.6 ± 0.8	38.1 ± 1.2	124	-85	39
<b>6</b>	101.0 ± 4.1	-37.1 ± 1.3	57.9 ± 2.9	94	-20	74
<b>7</b>	147.0 ± 11.6	-50.4 ± 2.8	92.2 ± 8.7	201	-88	113
<b>8</b>	108.0 ± 2.2	-31.6 ± 8.1	72.7 ± 4.3	104	-36	68
<b>9</b>	82.0 ± 4.5	-32.2 ± 1.2	42.5 ± 1.5	147	-45	102
<b>10</b>	156.0 ± 5.7	-25.3 ± 2.1	118.0 ± 6.0	159	-67	92
<b>11</b>	103.0 ± 5.5	-47.1 ± 3.1	50.5 ± 1.5	110	-47	63
<b>12</b>	107.0 ± 2.8	-34.8 ± 1.3	70.4 ± 2.4	104	0	104
<b>13</b>	145.0 ± 0.9	-71.6 ± 0.9	73.0 ± 1.0	152	-83	69
<b>Total</b>	111.0 ± 23.4	-40.5 ± 13.8	65.1 ± 21.5	124 ± 39	-44 ± 29	80 ± 32

Ranges in total activation duration of both the iECG LAT maps and the invasive LAT maps over all invasively mapped surfaces per subject. The timing of the earliest activated node and the latest activated node were stated. Abbreviations: iECG = inverse electrocardiography; EAM = electro-anatomical mapping.



**Supplementary Figure 1.** Multi-wave iECG. First, (cardiac) imaging and body surface potential maps (BSPM) data are acquired (Panel A). Using the volume conductor, BSPM are simulated. Multi-wave iECG selects the best matching activation sequence by testing 511 combinations of initial activation sequences. The output of the procedure is local activation timing maps (D). In Panel D, three examples of the 511 possible activation maps are shown with respectively six, four or two initial sites of activation. Local activation timing is depicted from red (early activation) to (blue latest activation).



**Supplementary Figure 2.** Factors associated with correlation coefficients and absolute differences. Both QRS duration or the surface did not significantly affect the correlation coefficient or absolute differences (upper row). There was a trend between the number of annotations and abnormal voltage EGMs of the invasive map and the correlation coefficient, low density and percentages were associated with lower CC. Legend figure: EGM = electrogram; LV = left ventricle; RV = right ventricle.



$\emptyset$

$(x, y) = \int_{S_u}$

$v_2 / c^2$

$v_{cg}$

$v_{cg}$

ind



# Chapter 4

Non-invasive inverse ECG for the early detection  
in arrhythmogenic cardiomyopathy,  
a proof-of-concept study

MJ Boonstra, RW Roudijk, M Bourfiss, M Kloosterman, LJ Blom, J Ruisch,  
I van der Schaaf, BK Velthuis, FW Asselbergs, ASJM te Riele, PM van Dam,  
and P Loh.

*Submitted*

## Abstract

In arrhythmogenic cardiomyopathy (ACM), life-threatening ventricular arrhythmias can be the first manifestation of disease. Task Force Criteria (TFC) were established to standardize clinical ACM diagnosis, but early diagnosis remains difficult. Non-invasive local activation imaging with inverse electrocardiographic (iECG) techniques may improve our understanding of the underlying ACM substrate. In this proof-of-concept study, we investigated the potential value of iECG to detect early signs of ACM.

Sixty-nine ACM-associated pathogenic variant carriers and twelve controls underwent late gadolinium enhancement cardiac magnetic resonance imaging (LGE-cMR) and 67-leads body surface potential mapping. The iECG local activation timing (LAT) maps were estimated during sinus rhythm and minimal local propagation velocity, transmural (T-)LAT and total LAT ranges were determined for the right- and left ventricular (RV/LV) free wall. The iECG derived characteristics were compared to TFC-score and LGE-presence.

The study population consisted of 81 subjects (40% male, mean age  $38\pm 16$  years, median [range] TFC-score 2 [0;9]). With increasing disease manifestation, RV total LAT range significantly increased ( $102\pm 20$  (overt ACM) versus  $82\pm 10$  ms,  $p<0.01$ ). Presence of RV-LGE was associated with increased RV total LAT range ( $96\pm 19$  versus  $84\pm 14$  ms,  $p<0.01$ ), and increased number of RV T-LAT maxima ( $10\pm 4$  versus  $7\pm 2$ ,  $p<0.01$ ) suggesting activation delay as observed by isochronal crowding in iECG maps. In the presence of RV-LGE and LV-LGE, the number of local LAT maxima was significantly lower ( $2\pm 1$  versus  $3\pm 1$ ,  $p<0.05$ ), suggesting a decreased number of separate activation waves. In all pathogenic variant carriers, a significant correlation existed between the number of local RV T-LAT maxima and RV total LAT range ( $R^2=0.25$ ,  $p<0.05$ ). Increased ( $>95$  ms) RV total LAT range was observed in 3/19 ACM-associated pathogenic variant carriers without signs of ACM.

This proof-of-concept study indicates that iECG enables early identification and quantification of local electrophysiological characteristics of the ACM substrate, even prior to structural abnormalities.

## Introduction

Arrhythmogenic cardiomyopathy (ACM) is associated with potentially fatal phenotypes.<sup>1,2</sup> Historically, ACM was described as a primarily right sided disease and called arrhythmogenic right ventricular cardiomyopathy (ARVC); the best characterized form of ACM. ARVC is defined by predominant (but not exclusive) right ventricular (RV) involvement. To standardize clinical ARVC diagnosis, Task Force Criteria (TFC) were established<sup>3</sup> and improved<sup>4</sup>.

ACM is characterized by defects in the intercalated disc<sup>5-7</sup>, resulting in altered intercellular impulse propagation and progressive fibro-fatty replacement of healthy myocardium. The combination of structural and electrical myocardial remodeling can result in increased susceptibility for life-threatening ventricular arrhythmias (VA), even in the absence of clinical signs of disease.<sup>6,7</sup> Due to the structural remodeling, local wall thinning and mechanical dysfunction occurs, which may lead to heart failure in a more severe stage. Our understanding of the genotype-phenotype relation of ACM has improved substantially.<sup>5,8</sup> However, phenotypic expression of ACM is heterogeneous as illustrated by the incomplete penetrance and high variability in disease onset, progression and severity.<sup>2</sup> Predictors such as age, sex and the presence of T-wave inversion in the inferior leads are associated with adverse events<sup>9-11</sup>, but subtle signs may go unnoticed, as indicated by the occurrence of sudden cardiac death in individuals already under clinical follow-up.<sup>2,12</sup> This indicates that accurate early detection of disease to identify individuals at-risk for life-threatening VA, is still beyond the capability of diagnostic tests.

Criteria based on the 12-lead electrocardiogram (ECG) have a central role in the TFC for ACM, as the ECG provides succinct insight in cardiac electrical activity. But subtle changes due to slow progressive substrate development may be missed when solely using the 12-lead ECG.<sup>13</sup> With inverse ECG (iECG) techniques, combining patient-specific  $\geq 67$ -lead body surface potential (BSP) data with patient-specific anatomical heart/torso models, detailed insight in local activation sequences can be obtained by non-invasively imaging cardiac electrical activity.<sup>14-16</sup> With iECG techniques, local activation patterns in the substrate consisting of intertwined strands of healthy myocardium and fibro-fatty tissue can be imaged. In-depth substrate characterization is likely to provide additional information to improve the early detection and monitoring of disease progression. Additionally, with detailed insight in substrate development, treatment may be initiated or adjusted prior to worsening of symptoms and to provide measures to prevent lethal VA. Especially in pathogenic variant carriers without any signs of disease, non-invasive iECG may provide important insight into ACM substrate development, on top of the information obtained using the 12-lead ECG.

To date, iECG techniques are studied for their application in the identification

of suspected origins of VA<sup>17,18</sup> or to obtain electrophysiological insight in substrates<sup>14,16,19,20</sup>. However, iECG estimation of local activation timing (LAT) maps during normal ventricular activation (e.g., sinus rhythm) is complicated by the complex interplay of multiple near simultaneous activation wavefronts initiated at the endocardium through the His-Purkinje system.<sup>16,21-23]</sup> The direct relation between recorded BSP and cardiac electrical activity is 'blurred' by multiple activation waves amplifying or canceling each other, volume conductor effects and wave-proximity effects. Recently, equivalent dipole layer (EDL)-based iECG was optimized to image normal ventricular activation by incorporating patient-specific His-Purkinje models.<sup>24-26</sup> With this improved iECG technique, additional insight in local electrical and structural substrates may be obtained during normal ventricular activation, thereby possibly providing valuable insight into the ACM substrate.

In the current proof-of-concept study, we aimed to evaluate whether non-invasive EDL-based iECG can uncover the electrical ACM substrate by imaging local activation patterns. Characterizing the electrical substrate, may enable early detection and monitoring of disease progression to improve risk-stratification in individuals with and without detectable structural and/or functional ACM manifestation. To this end, iECG estimated LAT-maps during normal ventricular activation in ACM-associated pathogenic variant carriers with variable ACM expression were evaluated. iECG LAT map derived characteristics were compared to clinical disease manifestation and the presence of structural disease as identified using late gadolinium enhancement cardiac magnetic resonance (LGE-cMR) imaging to determine the association between abnormal electrical activation and the development of a structural ACM substrate.

## Methods

### *Study design*

We performed a proof-of-concept prospective study at a single tertiary academic expert center for ACM. Pathogenic variants in the plakophilin-2 (PKP2) and phospholamban (PLN) gene are amongst others associated with the development of ACM. Therefore, pathogenic PKP2 and PLN variant carriers, as determined by clinical genetic testing, who underwent clinical LGE-cMR imaging were included in this study. As a control group, patients with symptomatic premature ventricular complexes or atrial tachycardia without structural heart disease, as identified by LGE-cMR imaging, were included. After giving informed consent, subjects underwent 67-lead BSP mapping and cMR imaging within a two-month period, but preferably on the same day. The study protocol was approved by the local institutional review board (UMC Utrecht, The Netherlands, protocol nr. 17/628) and conducted according to the declaration of Helsinki. The study-workflow is displayed in Figure 1.

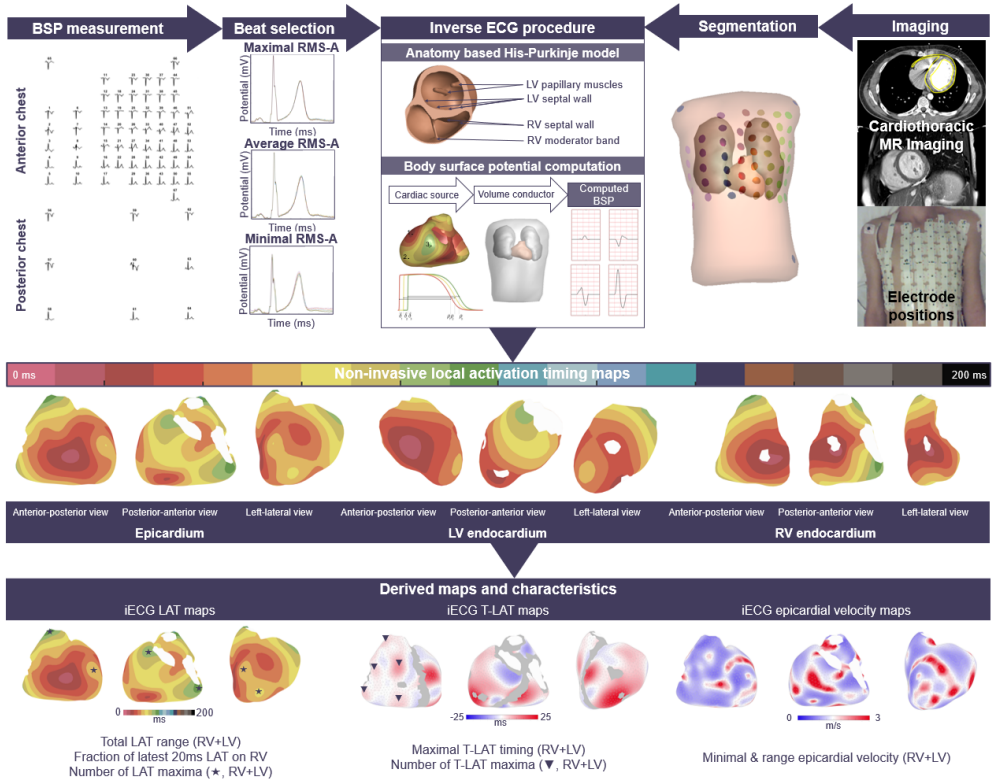


**Figure 1.** Study procedure and inverse ECG pipeline. From obtained body surface potential (BSP) maps, beats were selected using QRS/QRST-segment template matching. Beats with maximal, average and minimal root mean square QRS amplitude (RMS-A) were obtained and averaged. From the patient specific cardiothoracic magnetic resonance (cMR) imaging, anatomical models of the ventricles, lungs and torso were created. The three averaged beats were selected as input for the inverse ECG procedure to compute the non-invasive local activation timing (LAT) maps for the epicardial, left ventricular (LV)- and right ventricular (RV) endocardium.

### Phenotypic evaluation of included subjects

In this study, we use ACM throughout the manuscript to indicate presence of disease as we also include pathogenic PLN variant carriers, who are known for their left ventricular (LV) involvement. ACM diagnosis was defined according to the 2010 revised ARVC TFC<sup>4</sup> in which  $\geq 4$  TFC points are required for a definite diagnosis, specifically describing ARVC phenotype in all subjects. Major, minor or no TFC fulfillment was scored per category: i.e., imaging, tissue, depolarization, repolarization, arrhythmia and genetics/family. Besides the official TFC score, we also determined total TFC score not taking into account criteria of the family/genetic\* category to only consider phenotypic ACM manifestations per subject. We indicated this TFC score as non-genetic TFC (ngTFC).

\* Of note, PKP2 variant carriers were always assigned a major TFC in the family/genetic category as PKP2 is one of the desmosomal mutations whereas PLN-variant carriers only receive major points based on family history.

*BSP signal acquisition and processing*

A 67-lead BSP measurement (sampling frequency = 2048 Hz, Biosemi, Amsterdam, The Netherlands) was obtained for at least 240 seconds in resting supine position. BSP signals were loaded into MATLAB (2017a, The Mathworks, Natick, MA, USA) and baseline drift (<0.25 Hz) and high frequency noise (>200 Hz) were removed. Presence of powerline artifacts was assessed based on visual inspection and if present, BSP signals were additionally filtered using a 50 Hz notch filter. The root mean square (RMS) signal was computed wherein one QRST complex was manually segmented by annotating P-onset, QRS-onset, QRS-end and T-end. Template matching of the complete QRST-segment and QRS-complex was performed by computing the relative difference  $RD_i$  for each sample  $i$  in the RMS-signal:

$$RD_{i\{1:m-n\}} = \frac{\sum |RMS_{BSP}[i:i+n] - RMS_{QRS(T)}|}{n}$$

with  $RMS_{BSP}$  indicating the RMS signal of the complete BSP signal,  $RMS_{QRS(T)}$  the selected RMS-QRS or -QRST segment,  $m$  the number of samples of the complete RMS signal and  $n$  the number of samples of the template beat. All samples  $i$  with a local minimum in  $RD_i < 0.035$  for the QRS-segment was selected. Subsequently, QRS-RMS amplitude was determined and five beats were selected and averaged for minimum, maximum and average QRS-RMS amplitude (Figure 1), resulting in three average beats used as input for the iECG procedure.

*Image acquisition and processing*

Electrode positions were captured using a 3D camera system during BSP mapping. The cMR images were obtained using a 1.5 or 3 Tesla scanner (Philips Medical Systems, the Netherlands) according to the standardized clinical ACM protocol. Scout images of the torso were obtained in the axial, sagittal and coronal plane to localize the heart and position the scan region. Cine-images were obtained in the cardiac short- and longitudinal-axes. A single bolus of contrast (0.1 cc gadovist/kg) was injected for 3 Tesla and a double bolus (0.2 cc gadovist/kg) for 1.5 Tesla and after 10 minutes, LGE images were obtained in the short-axis, four-chamber, RV two-chamber and RV outflow tract (RVOT) views to assess the accumulation of gadolinium in the ventricular myocardium. For the purpose of this study, LGE-presence was determined from the clinical report in which it was scored by an experienced cardiovascular radiologist. LGE-presence was scored using the 17-segment American Heart Association (AHA) model for the left ventricle (LV) and four additional segments (RVOT, basal, mid and apical segments) for the RV. LGE-maps were displayed using the 17+4 segment model with red denoting segments with LGE-presence.

Patient specific anatomical models were created with GeomPEACS.<sup>27</sup> The anatomical models of the ventricles and blood pools were created using cine-images obtained

at end-diastole. The LV papillary muscles and RV moderator band were segmented as a part of the ventricular model. Anatomical models of the torso and lungs were created using the scout images and electrode positions were registered onto the torso. All anatomical models were discretized as closed triangulated surface meshes.

#### *Inverse ECG procedure*

In this study, an Equivalent Dipole Layer (EDL)-based iECG technique with incorporated His-Purkinje model was used to non-invasively estimate endocardial and epicardial local activation timing (LAT) maps during sinus rhythm.<sup>24,25</sup> In short, LAT maps were estimated by optimizing the match between recorded and computed BSP. To compute BSP, (1) a cardiac source model representing local cardiac electrical currents and (2) a volume conductor model describing the effect of these currents on potentials on the torso were required. Simulated local transmembrane potentials generated the local electrical currents, and the effect of these currents on BSP was described using the boundary element method. Assigned conductivity values to compute the volume conductor model were 0.2 S/m for the thorax and ventricular muscles, 0.04 S/m for the lungs and 0.6 S/m for the blood cavities.<sup>28,29</sup>

Due to the non-linear relation between the transmembrane potentials and BSP, the EDL-based iECG procedure consists of two steps. In the first step, an initial estimation of the activation sequence is required and in the second step, the selected activation sequence is further optimized to match recorded to computed BSP. The initial estimate is based on the patient-specific His-Purkinje anatomy in combination with the fastest route algorithm. Activation sequences starting at sites associated with the His-Purkinje system were only considered and combined to obtain a smooth, physiologically realistic activation sequence.<sup>21-23</sup> The computed initial activation sequence corresponding to the best match (e.g., highest correlation) between recorded and computed BSP was selected and used as an input for the optimization step. In the optimization step, the estimated activation sequence was further optimized by iteratively tuning LAT to minimize the error between recorded and computed BSP. Therefore, a dedicated Levenberg-Marquardt optimization procedure was used with a maximum of 25 iterations.<sup>30</sup> The optimization procedure was regularized using the surface Laplacian and the regularization parameter  $\mu^2$  was set to a relatively small value of  $5 \cdot 10^{-6} \text{mV}^2 \text{ms}^2 \text{m}^{-2}$  as used previously to correspond to realistic spatial smoothness, while focusing on optimization of the match between recorded and computed BSP.<sup>24</sup>

#### *iECG LAT derived characteristics*

Per subject, three iECG LAT maps were estimated using the three averaged beats as input. The LAT map with total activation duration closest to segmented QRS duration was selected for further analysis. LAT maps of the epicardial and endocardial surfaces were presented in anterior-posterior, posterior-anterior and/or left-lateral views<sup>31</sup>

using the Durrer color map with isochronal lines at 10 ms intervals<sup>21</sup>. As ACM is characterized by diffuse fibro-fatty replacement of healthy myocardium, thereby disrupting local activation wavefront propagation, several pathophysiological-based characteristics were derived from the iECG LAT maps to quantitatively describe this disruption (Figure 1). First, to quantify local activation wave slowing (observed as isochronal crowding), epicardial local surface propagation velocity was computed using the triangulation method.<sup>24,32</sup> From the velocity maps, minimal propagation velocity and range were determined. Furthermore, RV and LV total LAT range of the ventricular free walls was determined and the fraction of latest 20ms of activation on the RV was assessed to quantify whether the terminal activation occurred in the LV and/or RV. Additionally, transmural (T-) LAT activation was determined as the activation wave traveling from the endocardium towards the epicardium, which is likely to be disrupted in the presence of (intramural) diffuse fibro-fatty tissue. From these maps, the maximal RV and LV T-LAT value was determined. Furthermore, to quantify heterogeneity in LAT and T-LAT maps, the number of local maxima in the maps were automatically identified (Figure 1, ★/▼) by taking into account all directly surrounding nodes.

#### *Statistical analysis*

Data were assessed for normality using Shapiro-Wilk's test. Normally distributed variables were reported as mean  $\pm$  standard deviation and non-normally distributed data were reported as median with range. Differences between normally distributed data were tested for significance using ANOVA and unpaired students t test. Non-normal data were compared using Mann-Whitney U test. For categorical data, Fishers exact test was used to test for significant differences between groups. A p-value  $<0.05$  was considered statistically significant. Subjects were stratified regarding TFC-fulfillment in two ways. First, we stratified according to total TFC score, not taking into account TFC from the family/genetic category, indicated as ngTFC. All subjects were stratified in five ngTFC groups; ngTFC=0, ngTFC=1, ngTFC=2, ngTFC=3 and ngTFC $\geq$ 4. Second, we stratified subjects according TFC category (e.g., depolarization, repolarization, imaging and arrhythmia) to either having no versus minor/major TFC category criterium fulfillment. Additionally, we stratified according to LGE-presence, whether it was either present in the RV, LV or both according to the clinical report as described above.

## **Results**

The study population consisted of 81 subjects (40% male, mean age 38 $\pm$ 16 years) including 39 pathogenic PKP2 variant carriers, 30 pathogenic PLN variant carriers and 12 controls. Their clinical characteristics are shown in Table 1 per subgroup. The median time interval between BSPM and cMR was 0 days (IQR [0;0]) with an overall range of 0 to 56 days. No subject included in this study was diagnosed with a dilated cardiomyopathy. In the control group, 7/12 subjects had 1 TFC in the arrhythmic



category, as they had >500 PVC/24 hours. Created ventricular anatomical models had an average inter-node spatial resolution of  $5 \pm 1$  mm. Both in control subjects (Figure 2) and pathogenic mutation carriers (Figure 3&4), non-invasively estimated activation sequences originated from His-Purkinje associated regions and ended in the basal areas.

*Correlation with Task Force Criteria*

Median [IQR] total TFC-score was 2 [0;3] with a total range of 0 to 9 and median [IQR] ngTFC was 0 [0;2] with a total range of 0 to 7 for the complete population (Table 1). With increasing ngTFC, the RV total LAT range significantly increased from

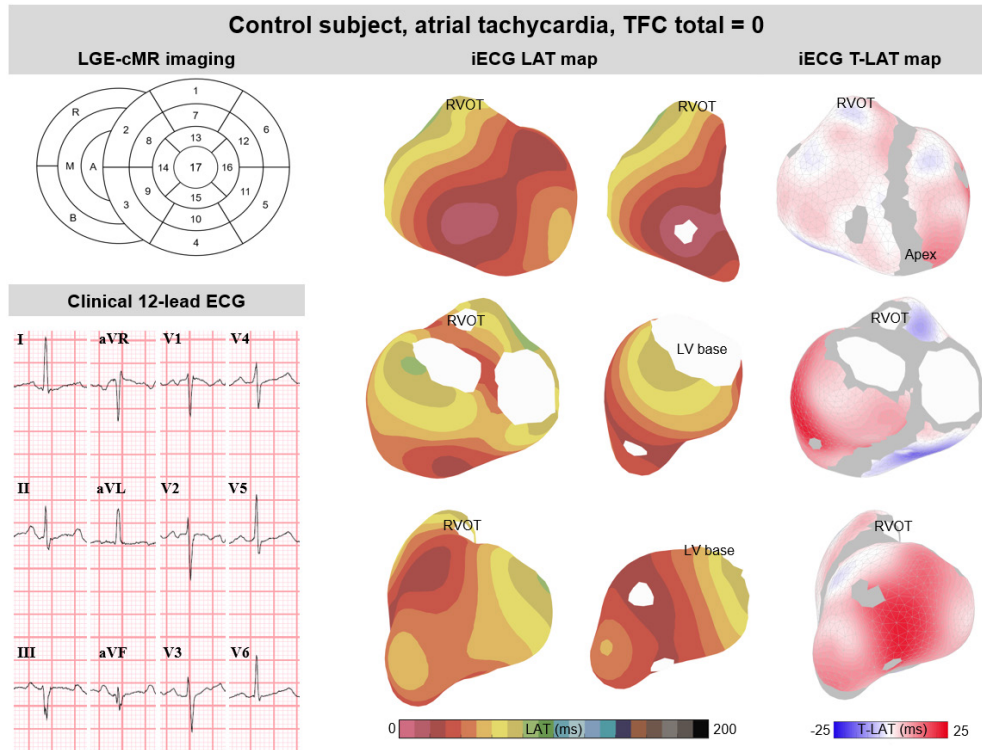


**Figure 2.** Endocardial and epicardial iECG LAT and T-LAT maps in a control subject. Findings from late gadolinium enhancement (LGE) cardiac MR imaging are displayed using the 17-segment AHA model for the left ventricle (LV) and extended for the right ventricle (RV), with R=right ventricular outflow tract (RVOT), B = RV basal area, M = the RV mid segment and A = the RV apical segment. LGE presence is indicated in red (no LGE present). A representative beat from the clinical 12-lead ECG is presented with a small box indicating 40ms and 0.1 mV. Inverse ECG local activation maps (LAT) maps are displayed using the Durrer colormap and isochronal lines with 10 ms spacing. Epicardial LAT maps are displayed in the left column and endocardial in the middle column with the upper row showing the RV endocardium and the middle and bottom row the LV endocardium. Epicardial transmural LAT (T-LAT) maps are displayed in the right column from blue (indicating earlier epicardial than endocardial activation) to red (indicating later epicardial than endocardial activation). All maps are displayed in the anterior posterior view (upper row), posterior-anterior view (middle row) and left lateral view (bottom row) and the RVOT location is annotated as anatomical landmark.

82±10 ms (ngTFC=0) to 102±20 ms (ngTFC>3) ( $p<0.01$ , Figure 5-A1). Furthermore, a significant correlation was observed between terminal activation duration in V1 and the RV total LAT range ( $R^2=0.53$ ,  $p<0.01$ , Figure 5-A4). In subjects fulfilling TFC in the depolarization and/or imaging category, RV total LAT range and the fraction of latest activation on the RV were significantly higher (Table 2). Furthermore, a trend towards significance in number of RV T-LAT maxima and fraction of latest 20ms of total activation time on the RV free wall was observed in subjects with TFC in the arrhythmia category (Table 2).

#### *LGE-presence and TFC imaging criteria*

With RV-LGE presence, the number of local RV T-LAT maxima was significantly higher compared to cases without (10±4 versus 7±2,  $p<0.01$ , Figure 5-A3, Table 2). In the presence of LV-LGE, the number of local LV LAT maxima was significantly lower (2±1 vs 3±1,  $p<0.05$ , Table 2). As can be appreciated in Figure 3 and 4, isochronal crowding, increased T-LAT values and increased total LAT range were observed in regions with LGE-presence. When comparing LGE-presence specifically to TFC imaging criteria fulfillment (Table 2), a RV total LAT range was significantly higher in subjects with RV-LGE presence (96±19 versus 84±14 ms,  $p<0.01$ ) and in subjects fulfilling TFC imaging criteria (100±19 versus 82±11,  $p<0.01$ ). Additionally, when fulfilling TFC imaging criteria (9±4 versus 7±3,  $p=0.06$ ) a trend towards significance was observed.

#### *Gene specific characteristics to identify (subclinical) ACM progression*

In all included pathogenic variant carriers, a significant correlation existed between the number of RV T-LAT maxima and RV total LAT range ( $R^2=0.25$ ,  $p<0.05$ ) and between the number of LV T-LAT maxima and LV total LAT range ( $R^2=0.36$ ,  $p<0.01$ ), which was not observed in the control population. The correlation improved when excluding the cases with LGE (Figure 5B). A total of 3/19 subclinical (ngTFC=0) PKP2 variant carriers without LGE presence had a RV total LAT range >95 ms, whereas in the control group none were identified meeting this criterium. In PKP2 variant carriers, the number of RV T-LAT maxima was significantly higher (9±4 vs 6±3,  $p<0.05$ ) in subjects fulfilling at least one ngTFC (Figure 5C1) when compared to subjects without ngTFC fulfillment. In PLN variant carriers, the number of LV LAT maxima was significantly lower (2±1 vs 3±1,  $p<0.01$ ) and RV total LAT range was significantly higher (94±22 vs 77±8,  $p<0.01$ ) in subjects fulfilling at least one ngTFC (Figure 5C2&C3) when compared to subjects without ngTFC fulfillment, suggesting a role in early detection of subtle activation delay.

## **Discussion**

This paper describes new iECG LAT map derived characteristics during normal ventricular activation to non-invasively image the electrophysiological ACM substrate in subjects with and without detectable structural manifestation of disease. ACM is a heterogeneous disease and currently, a diagnostic tool to identify the earliest signs

**Table 1.** Baseline characteristics.

	Controls (n=12)	PKP2 variant carriers (n=39)	PLN variant carriers (n=30)
<b>Patient characteristics</b>			
Male	1 (8)	19 (49)	12 (40)
Age	36±16	37±16	39±16
Body mass index	25±5	25±5	24±5
ACM diagnosis	0 (0)	11 (28)*	6 (20)
ICD	0 (0)	0 (0)	1 (3)
Proband status	0 (0)	1 (3)	2 (7)
Days between cMR and BSPM	0 [0;0]	0 [0;31]	0 [0;56]
<b>Cardiac medication</b>			
ACEi/ARB	0 (0)	4 (10)	3 (10)
Antiarrhythmic	1 (8)	2 (5)	1 (3)
Beta blocker	4 (33)	2 (5)*	2 (7)*
Diuretic	0 (0)	2 (5)	1 (3)
<b>Total TFC score (major+minor)</b>	1 [0;1]	2 [2;9]	0 [0;7]
TFC imaging	0	7 (18)	10 (33)*
TFC tissue	0	0	0
TFC repolarization	0	5 (13)	5 (17)
TFC depolarization	0	7 (18)	3 (10)
TFC arrhythmia	7 (58)	14 (36)	10 (33)
TFC family/genetics	0	39 (100)	3 (10)
ngTFC = 0	5 (42)	20 (51)	17 (57)
<b>ECG characteristics</b>			
Heart rate	79±24	66±9*	69±13
QRS duration	89±12	95±15	89±13
QTc time	432±51	414±24	408±23*
QRS axis	54±24	54±53	57±73
Atrial fibrillation	0 (0)	1 (3)	0 (0)
T-wave inversion > 2 leads (V1-6)	0 (0)	5 (13)*±	4 (13)
PVC count/24h	14211±16425	581±1102*	653±1932*
<b>cMR characteristics</b>			
LVEDV/BSA (ml/m <sup>2</sup> )	98±23	90±15	96±15
LVEF	55±7	56±5	53±7
RVEDV/BSA (ml/m <sup>2</sup> )	99±21	101±30	99±16
RVEF	52±7	51±10	51±8
LGE LV (n)	0	4 (10)	11 (37)
LGE RV (n)	0	8 (21)	5 (17)

Values are presented as either mean ± standard, median [total range] or n (%). \* Significant difference ( $p < 0.05$ ) with the control group and ± significant difference ( $p < 0.05$ ) with the PLN group. LGE = late gadolinium enhancement, ICD = implantable cardioverter defibrillator, ACEi = angiotensin converting enzyme inhibitors, ARB = angiotensin receptor blockers, TFC = task force criteria, ngTFC = non-genetic TFC, n = number, LV = left ventricle, RV = right ventricle, EDV = End Diastolic Volume, BSA = Body Surface Area (Dubois&Dubois), EF = ejection fraction, cMR = cardiac Magnetic Resonance, BSM = body surface potential mapping.

of disease is lacking. The results presented in this study indicate that with iECG, early signs may be detected, even prior to the identification of abnormalities on echocardiography, ECG or MRI imaging. Local irregularities in the activation sequence were imaged with the technique, suggesting the potential of iECG to detect subtle signs of disease progression. In pathogenic variant carriers, several iECG derived characteristics were associated to the typically observed findings in right-sided ACM (ARVC); as indicated by TFC fulfillment in the depolarization-, arrhythmia- and imaging category and RV-LGE presence. These findings indicate that findings in iECG LAT maps adhere to disease manifestation in the sub-tricuspid region (Figure 3). By monitoring both LAT and T-LAT maps, the presence of mid-mural fibrous tissue may be revealed using the non-invasive iECG technique.

#### *Transmural activation assessment*

The number of local T-LAT maxima was significantly higher in subjects that were assigned TFC in the depolarization category and in the presence of RV-LGE\* (Table 2). Additionally, for both the LV and RV, a significant weak-to-moderate correlation between the number of T-LAT maxima and the total LAT range was observed in all pathogenic variant carriers (Figure 5B). These findings indicate that in the presence of structural remodeling of the RV, local activation waves slowing is indicated by increased total LAT range, and heterogeneous (transmural) propagation of activation becomes apparent through an increased number of T-LAT maxima.<sup>33</sup>

In invasive LAT mapping studies, mid-myocardial scar is difficult to identify during sinus rhythm.<sup>34</sup> Anisotropic transmural activation is present in the healthy heart, but in the presence of diffuse (mid-)myocardial fibro-fatty tissue, transmural activation patterns progressively become more heterogeneous as observed in pacing studies.<sup>35,36</sup> In the current study we found that evidence suggesting the presence of mid-myocardial fibrosis may also be detected during sinus rhythm by assessing total LAT range and the number of local T-LAT maxima. This theory is further substantiated in cases with RV LGE-presence, where we observed a significant higher number of T-LAT maxima (Figure 3, T-LAT maps, Figure 5A1). Presence of fibrofatty tissue likely manifests in this manner due to the thin-walled structure of the RV, resulting in T-LAT map heterogeneity, increased total RV LAT range and decreasing maximal RV T-LAT timing as an effect to RV-wall thinning, which is typically observed in severe ACM.<sup>6</sup> In the LV, we observed other changes in LAT maps in the presence of structural remodeling. In these cases, less LV LAT maxima (Table 2) and steep LV T-LAT gradients (Figure 4) were observed in the presence of LV-LGE. This finding indicates a rather homogeneous epicardial activation wavefront which may be dissociated from endocardial activation, as also observed during invasive electro-anatomical mapping procedures in the presence of advanced structural remodeling. Furthermore, T- LAT heterogeneity may be associated with increased risk of VA, as it may set the stage for

\* Of note, the presence of LGE is not part of the 2010 TFC.



reentrant circuits. We observed a trend towards significance in subjects fulfilling TFC in the arrhythmia category having an increased T-LAT heterogeneity, indicating the potential incremental value of iECG regarding risk-stratification to prevent sudden cardiac death.

#### *Relationship between iECG derived characteristics and cardiac repolarization*

The presence of structural heart disease may cause disturbances in the interplay between depolarization and repolarization which may increase vulnerability for life-threatening VA.<sup>20,37</sup> A significantly higher minimal LV propagation velocity and a trend towards significance for RV propagation velocity were observed in individuals fulfilling TFC repolarization criteria. Therewith, a possible relation between local activation wavefront propagation and repolarization abnormalities may have been identified, which may be related to increased VA vulnerability. This should however be further investigated by characterizing both depolarization and repolarization iECG maps.

#### *Previous and current iECG studies in structural heart disease*

Previous iECG studies in ACM patients were conducted in subjects fulfilling at least two minor TFC for ACM and/or in the presence of structural heart disease.<sup>16,19,38-40</sup> In these studies, equivalent potential distribution (EPD)-based iECG was used to reconstruct cardiac potentials at the epicardial surface, thereby not providing insight in transmural activation sequences. Although the performance of EPD-based iECG decreases in narrow QRS complexes<sup>16</sup>, the studies observed regions of low-voltages, fragmented cardiac potentials and non-uniform conduction in the iECG maps of pathogenic variant carriers. In subjects in the early stage of disease, non-uniform conduction and fractionated cardiac potentials were observed and with increasing disease severity, ventricular activation sequences prolonged. These findings all adhere to findings also observed during invasive electroanatomical mapping in ACM patients. In the current study, we specifically observed an increase in total RV LAT range in subjects with more severe disease manifestation (Figure 5A1), thereby adding information to the iECG techniques previously studied. The findings indicate that iECG derived characteristics correspond to the expected findings in more severe cases of ACM (i.e., increased TFC score, Figure 5A1&A4). Whereas LAT and velocity iECG maps provide important insight in local wave propagation on the surface, mid-myocardial fibrofatty replacement may however still be missed. The assessment of T-LAT maps, as done in the current study, provides a first step towards the three-dimensional characterization of the ACM substrate, enabling the detection of mid-myocardial structural disease, and provides much needed additional insight in all stages of ACM substrate development.

#### *Initial estimation and optimization procedure*

In EDL-based iECG, an initial estimation is required due to the non-linear relation



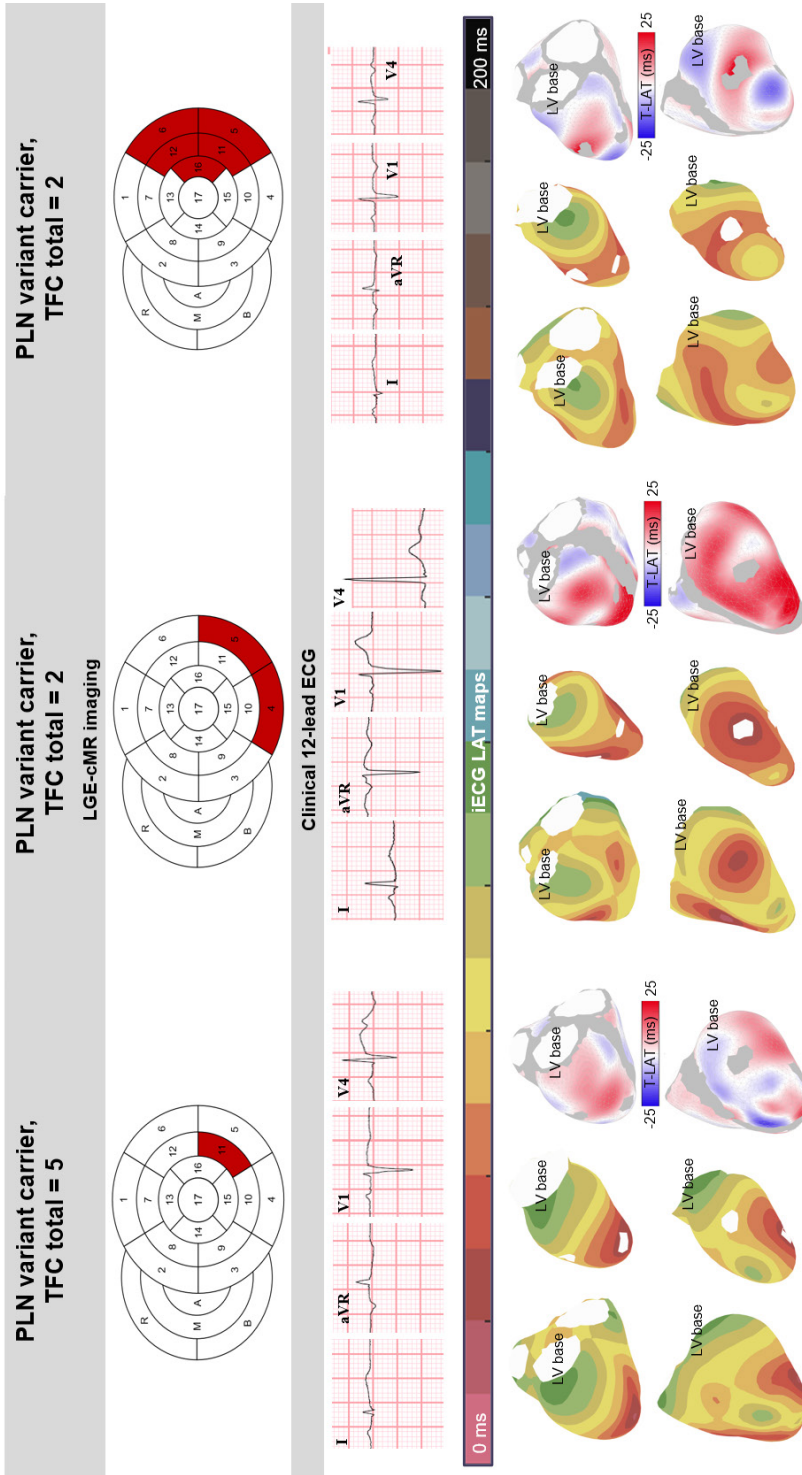


**Figure 4.** iECG LAT and T-LAT maps in PLN variant carriers. Findings from late gadolinium enhancement (LGE) cardiac MR imaging are displayed using the 17-segment AHA model for the left ventricle (LV) and extended for the right ventricle (RV), with R=right ventricular outflow tract (RVOT), B = RV basal area, M = the RV mid segment and A = the RV apical segment. LGE presence is indicated in red. A representative beat from the clinical 12-lead ECG is presented with a small box indicating 40ms and 0.1 mV. Total task score criteria (TFC) score is indicated in the upper row, taking into account the TFC family/genetics category. Inverse ECG local activation maps (LAT) maps are displayed using the Durrer colormap and isochronal lines with 10 ms spacing. Inverse ECG local activation maps (LAT) are displayed of the epicardial (left column) and LV endocardial (middle column) surface displayed in the anterior posterior view (upper row) and posterior-anterior view (bottom row). Transmural activation maps are shown in the right column. The LV base is annotated as an anatomical landmark.

between activation time and simulated potentials. In order to obtain a physiologically realistic initial estimate during sinus rhythm, we used patient specific anatomy-based His-Purkinje models. For the optimization procedure, we used a small regularization parameter value, meaning that the optimization procedure is almost unregularized by the surface Laplacian. The optimized LAT maps still showed activation originating from the regions associated with His-Purkinje anatomy<sup>21</sup> and stayed smooth over the surface. However local T-LAT differences and isochronal crowding became apparent after optimization, indicating local myocardial disease. These observations indicate that by combining a His-Purkinje regularized initial estimation with the relatively unregularized optimization procedure, a physiologically realistic estimation of local activation is obtained also uncovering local activation pattern abnormalities in the ACM substrate.

#### *The potential role of iECG techniques in current clinical practice*

In ACM, early detection and risk-stratification remains challenging. With the development of imaging techniques based on both echocardiography and cMR early signs of structural and/or mechanical dysfunction in ACM were uncovered, even prior to identifiable pathological changes in the 12-lead ECG.<sup>41-44</sup> These findings indicated that the standard 12-lead ECG may not be sensitive enough to detect subtle signs of disease progression. With iECG techniques, detailed electrophysiological and imaging data can be combined to provide additional insight in ACM development and uncover subtle signs of ACM development. In combination with more advanced cMR imaging techniques like T1-mapping to image diffuse structural myocardial remodeling, further in-depth characterization of both the electrical and structural substrate is enabled.<sup>41,42</sup> Ultimately, by combining findings from echocardiography, cMR imaging and iECG, complementary insight into the onset and progression of ACM is obtained to assess electrical, structural and functional disease manifestation in both ventricles. To date, the optimal set of diagnostic tools to identify subtle disease progression in ACM remains unknown and the potential role of iECG substrate characterization to improve diagnosis and risk-prediction in individuals with and without detectable structural and/or functional manifestation of ACM should be further investigated in prognostic studies.

With non-invasive iECG, additional insight into ACM progression and specifically the underlying electrophysiological substrate can be obtained. Imaging the ACM substrate and combining this with information about ACM progression, treatment choices and clinical outcomes, may provide additional information regarding treatment effect. After careful evaluation, this information may be used to evaluate and guide treatment. For example, the choice for a certain treatment regimen (e.g., medication, ablation or ICD implantation) can be substantiated and evaluated and where needed the regimen can be adjusted. Additionally, invasive and non-invasive ablation procedures may be guided using the information obtained from iECG maps.

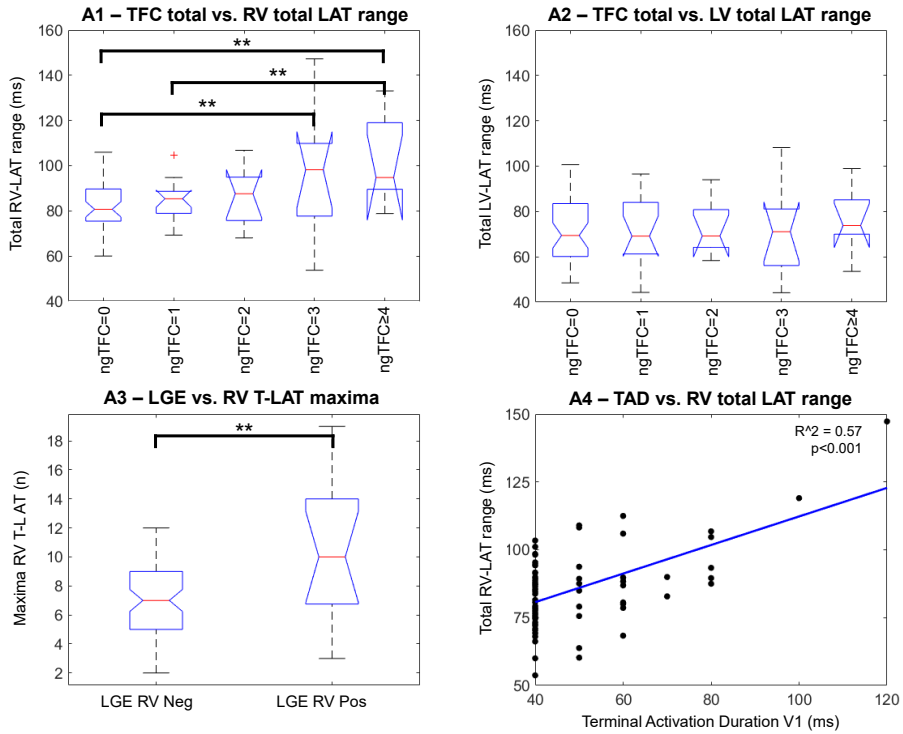


**Table 2.** iECG derived characteristics stratified to TFC criteria assigned and LGE presence.

	TFC imaging			TFC depolarization			TFC repolarization			TFC arrhythmia			LGE RV			LGE LV			
	0	1 or 2	p	0	1 or 2	p	0	1 or 2	p	0	1 or 2	p	Neg.	Pos.	p	Neg.	Pos.	p	
	n=64	n=4/13		n=71	n=10/0		n=71	n=2/8		n=50	n=26/5		n=68	n=13		n=63	n=18		
<b>Total free wall local activation timing range (ms)</b>																			
<b>RV</b>	82±11	100±19	<0.01	84±15	97±14	<0.01	86±14	89±23	0.51	84±12	89±19	0.13	84±14	96±19	<0.01	85±14	90±19	0.17	
<b>LV</b>	71±14	76±15	0.17	71±15	77±14	0.30	73±15	68±16	0.41	73±15	71±15	0.64	72±14	74±16	0.64	71±14	74±17	0.45	
<b>Local activation timing maxima free wall (n)</b>																			
<b>RV</b>	2±1	2±1	0.85	2±1	2±1	0.58	2±1	2±1	0.25	2±1	2±1	0.19	2±1	2±1	0.22	2±1	2±1	0.78	
<b>LV</b>	3±1	2±1	<0.01	3±1	2±1	0.16	3±1	2±1	<0.01	3±1	2±1	0.13	3±1	2±1	<0.05	3±1	2±1	<0.05	
<b>Fraction latest 20 ms of total activation time</b>																			
<b>RV</b>	0.63±0.31	0.79±0.27	<0.05	0.65±0.30	0.76±0.38	0.27	0.64±0.32	0.78±0.22	0.21	0.61±0.31	0.74±0.29	0.08	0.64±0.32	0.76±0.25	0.17	0.66±0.31	0.67±0.3	0.89	
<b>Minimal propagation velocity free wall</b>																			
<b>RV</b>	0.55±0.13	0.54±0.12	0.68	0.56±0.13	0.56±0.12	0.19	0.54±0.12	0.62±0.17	0.07	0.53±0.12	0.58±0.13	0.11	0.55±0.13	0.56±0.13	0.73	0.54±0.13	0.58±0.11	0.29	
<b>LV</b>	0.6±0.15	0.62±0.18	0.64	0.59±0.15	0.68±0.2	0.12	0.58±0.14	0.74±0.22	<0.01	0.6±0.15	0.62±0.18	0.57	0.59±0.15	0.68±0.16	0.07	0.6±0.15	0.63±0.17	0.45	
<b>Range propagation velocity free wall</b>																			
<b>RV</b>	3.56±0.79	3.39±1.04	0.45	3.56±0.77	3.32±1.25	0.41	3.48±0.87	3.84±0.53	0.21	3.61±0.72	3.39±1.01	0.25	3.62±0.64	3.06±1.46	<0.05	3.65±0.48	3.08±1.49	<0.01	
<b>LV</b>	3.86±0.45	3.69±0.27	0.15	3.84±0.39	3.7±0.58	0.30	3.84±0.44	3.72±0.29	0.40	3.84±0.45	3.8±0.37	0.73	3.83±0.44	3.8±0.31	0.81	3.85±0.44	3.74±0.33	0.32	
<b>Maximal local transmural activation time (ms)</b>																			
<b>RV</b>	18±8	17±10	0.74	18±9	16±6	0.46	19±9	14±3	0.10	19±8	17±9	0.25	19±9	15±9	0.14	18±8	19±10	0.14	
<b>LV</b>	26±8	23±12	0.24	26±9	23±7	0.26	25±8	27±14	0.52	25±8	26±11	0.65	26±9	21±7	0.06	26±8	24±12	0.63	
<b>Local transmural activation timing maxima (n)</b>																			
<b>RV</b>	7±3	9±4	0.06	7±3	10±4	<0.05	8±3	7±5	0.87	7±3	8±4	0.07	7±2	10±4	<0.01	7±3	8±3	0.59	
<b>LV</b>	4±2	3±2	0.43	4±2	3±1	<0.05	4±2	3±2	<0.05	4±2	4±2	0.48	4±2	3±1	0.07	4±2	4±2	0.86	

Presented iECG derived characteristics are indicated as subheadings in the table (*italic+bold*) and values are presented as mean ± standard deviation. Per derived characteristic, LV (left ventricle) and RV (right ventricle) in the left column indicates whether the characteristic was assessed in the LV or RV free wall, respectively. Groups were stratified according to fulfilling TFC category, where '0' indicates no TFC fulfillment and '1' or '2' indicates the fulfillment of either a minor (1) or major (2) criterion in the designated category. In the row below, the number of subjects fulfilling no or one/two TFC. For the latter, the number of subjects is indicated with n-minor/n-major. Per variable, statistical significance is indicated with the p-value and a p-value <0.05 is considered significant and all significant differences are indicated in bold. TFC = task force criterion, ms = millisecond, n = number, LGE = late gadolinium enhancement, p = p-value, Pos = positive, Neg = negative.

**A. Complete population**



**B. Pathogenic variant carriers**

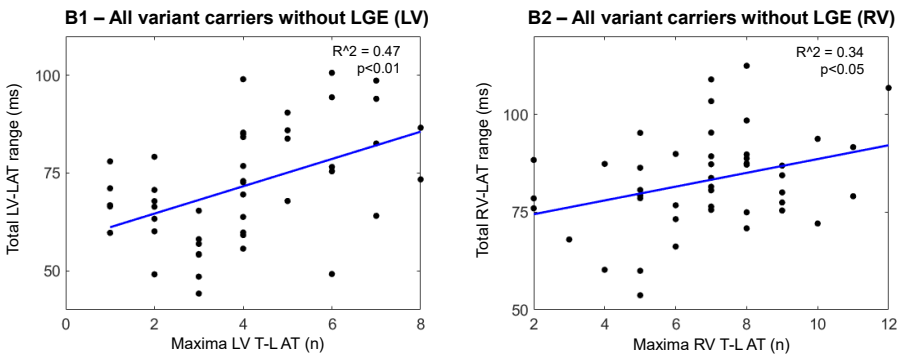


**Figure 5A/B.** Relation between iECG derived characteristics and task force criteria (TFC) fulfillment and LGE-presence. Statistical significance is denoted with \*  $p$ -value  $< 0.05$  and \*\*  $p$ -value  $< 0.01$ , in the box-plots, median (red line), 25th and 75th percentiles (blue box), extreme outliers not considered outliers (dashed lines) and outliers (red plus) are indicated. Of note: in the figures non-genetic TFC (ngTFC) is indicated, thus not taking into account a TFC point for the TFC category family/genetics. A: differences and correlations in the complete population (variant carriers and controls) with increasing TFC and LGE presence related to the increase in LV and RV local activation timing (LAT) range and number of maxima in transmural-LAT (T-LAT). Linear regression was computed between the total RV-LAT range and terminal activation duration (measured in the clinical 12-lead ECG). B: Stratification according to TFC fulfillment and the assignment of either a major (2), minor (1) or no (0) assigned TFC.

On top of that, as implied by the difference in underlying genetical substrate, different iECG derived characteristics may be associated with disease progression in either pathogenic PKP2 or PLN variant carriers (Figure 5C).<sup>43,44</sup> Whereas our sample size is small, the observed findings warrant a gene-specific approach in the identification of new iECG derived parameters, but findings should be confirmed in a larger cohort.

*Future studies*

In the current study, a relatively large group of subclinical subjects was included, partially also displaying iECG characteristics as observed in cases fulfilling TFC. Specifically, we observed >95 ms total RV-LAT range in 3/19 pathogenic PKP2 variant carriers without any detectable structural and/or functional manifestation of ACM

**C. Subgroup stratification**

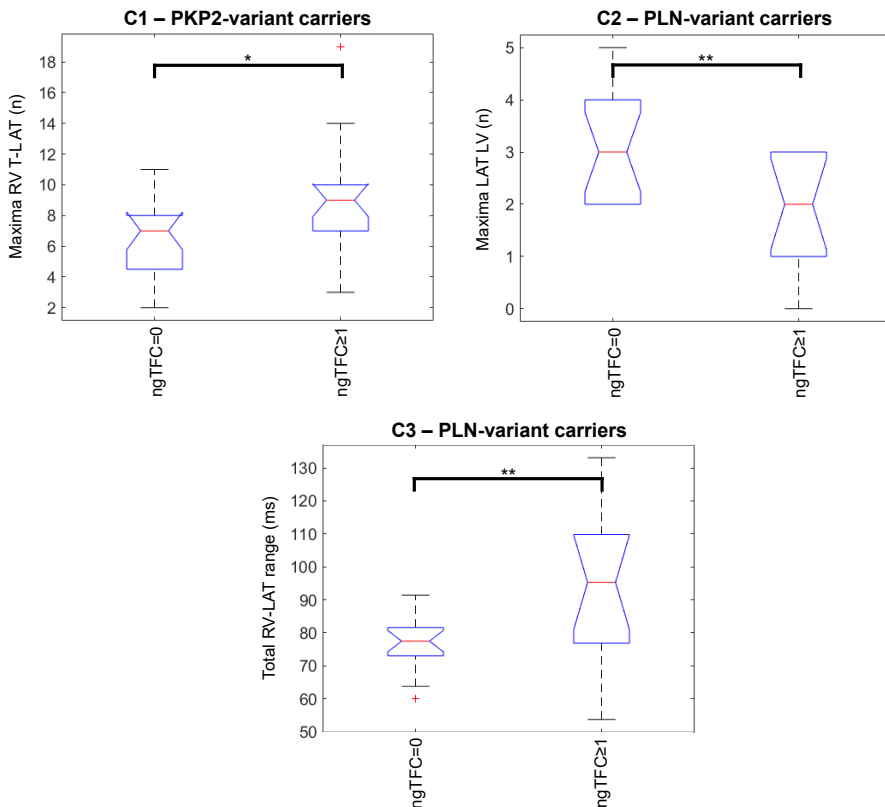


**Figure 5C.** Relation between iECG derived characteristics and task force criteria (TFC) fulfillment and LGE-presence. Statistical significance is denoted with \* p-value <0.05 and \*\* p-value < 0.01, in the boxplots, median (red line), 25th and 75th percentiles (blue box), extreme outliers not considered outliers (dashed lines) and outliers (red plus) are indicated. Of note: in the figures non-genetic TFC (ngTFC) is indicated, thus not taking into account a TFC point for the TFC category family/genetics. C: Stratification according to type of variant carrier either having ( $\geq 1$ ) or no (0) assigned TFC. Linear regression was computed between the total RV-LAT range and the number of local T-LAT maxima in all pathogenic variant carriers without LGE presence.

(ngTFC = 0 and no LGE-presence), possibly indicating a first sign of disease (Figure 5A, Table 2). Future follow-up studies, preferably including iECG re-mapping and in collaboration with the Netherlands Arrhythmogenic Cardiomyopathy Registry<sup>45</sup>, should be performed to estimate the prognostic relationship between iECG derived characteristics and the occurrence of life-threatening VA. Furthermore, the proposed theories explaining the observations in iECG maps should be further investigated and most importantly, where possible, also compared to other modalities, for example cMR T1-mapping observations.<sup>41</sup>

When combining findings of both EDL- and EPD-based iECG techniques, in-depth electrophysiological substrate characterization in complex substrates is likely to be improved even further. The application of such a patch-work technique creates the opportunity to combine the strengths of different iECG methods, thereby likely improving the accuracy of the non-invasive estimation of LAT maps.<sup>46</sup> Additionally, both EDL- and EPD-based iECG methods are physics-based models regularized with electrophysiological information. By combining insights from such physic-based models with insights from data-driven models, accurate iECG characterization of substrates may be improved even further.<sup>47,48</sup>

### *Limitations*

The presence of diseased myocardium breaks the equivalence of the dipole layer used in EDL-based iECG. Therefore, the non-invasive estimation in severely diseased myocardium may be less reliable. The incorporation of a method to represent myocardial disease in the iECG method may therefore further improve the accuracy of non-invasive LAT estimation, specifically in cases of severe ACM. Whereas EDL-based iECG is mainly known for the estimation of local activation timings, local voltages can also be estimated. Such non-invasively estimated local voltage maps potentially may also be of added value in the characterization of the ACM substrates but the accuracy of these voltage maps should be first evaluated in comparison to invasive measurements.<sup>49,50</sup> In this single center study, the total number of included patients is relatively small and part of the control subjects fulfilled one minor TFC in the arrhythmia category and were prescribed beta blockers (Table 1). These controls mimicking ACM phenotype could be differentiated from pathogenic mutation carriers, but results should be affirmed in a larger study.

### **Conclusion**

This proof-of-concept study shows that with EDL-based iECG, local electrophysiological characteristics of the ACM substrate can be imaged. With the technique, additional electrophysiological information of the substrate is obtained in subjects with and without a ACM phenotype. With the iECG LAT derived characteristics, potential metrics to improve diagnosis and risk-stratification in individuals at-risk for ACM were identified. The results suggest the incremental value of iECG for the early

detection and monitoring of the electrical ACM substrate, which should be confirmed in future studies. Specifically, future studies should focus on the repolarization phase and investigate the prognostic role of the iECG techniques in both ACM and ARVC diagnosis and accurate risk-stratification for life-threatening VA.

*Acknowledgements*

This work was supported by the Dutch Heart Foundation (grant numbers CVON2015-12 eDETECT and QRS-Vision 2018B007).

## References

1. Elliott P, Andersson B, Arbustini E, Bilinska Z, Cecchi F, Charron P, et al. Classification of the cardiomyopathies: a position statement from the European Society Of Cardiology Working Group on Myocardial and Pericardial Diseases. *Eur Heart J*. 2008;29(2):270-6.
2. Groeneweg JA, Bhonsale A, James CA, Te Riele AS, Dooijes D, Tichnell C, et al. Clinical presentation, long-term follow-up, and outcomes of 1001 arrhythmogenic right ventricular dysplasia/cardiomyopathy patients and family members. *Circulation: Cardiovascular Genetics*. 2015;8(3):437-46.
3. McKenna WJ, Thiene G, Nava A, Fontaliran F, Blomstrom-Lundqvist C, Fontaine G, et al. Diagnosis of arrhythmogenic right ventricular dysplasia/cardiomyopathy. Task Force of the Working Group Myocardial and Pericardial Disease of the European Society of Cardiology and of the Scientific Council on Cardiomyopathies of the International Society and Federation of Cardiology. *British heart journal*. 1994;71(3):215.
4. Marcus FI, McKenna WJ, Sherrill D, Basso C, Bauce B, Bluemke DA, et al. Diagnosis of arrhythmogenic right ventricular cardiomyopathy/dysplasia: proposed modification of the task force criteria. *Circulation*. 2010;121(13):1533-41.
5. van der Voorn SM, Te Riele AS, Basso C, Calkins H, Remme CA, van Veen TA. Arrhythmogenic cardiomyopathy: pathogenesis, pro-arrhythmic remodelling, and novel approaches for risk stratification and therapy. *Cardiovascular research*. 2020;116(9):1571-84.
6. Costa S, Cerrone M, Saguner AM, Brunckhorst C, Delmar M, Duru F. Arrhythmogenic cardiomyopathy: An in-depth look at molecular mechanisms and clinical correlates. *Trends in Cardiovascular Medicine*. 2021;31(7):395-402.
7. Delmar M, McKenna WJ. The cardiac desmosome and arrhythmogenic cardiomyopathies: from gene to disease. *Circulation research*. 2010;107(6):700-14.
8. James CA, Syrris P, Van Tintelen JP, Calkins H. The role of genetics in cardiovascular disease: arrhythmogenic cardiomyopathy. *Eur Heart J*. 2020;41(14):1393-400.
9. Link MS, Laidlaw D, Polonsky B, Zareba W, McNitt S, Gear K, et al. Ventricular arrhythmias in the North American multidisciplinary study of ARVC: predictors, characteristics, and treatment. *Journal of the American College of Cardiology*. 2014;64(2):119-25.
10. Mazzanti A, Ng K, Faragli A, Maragna R, Chiodaroli E, Orphanou N, et al. Arrhythmogenic right ventricular cardiomyopathy: clinical course and predictors of arrhythmic risk. *Journal of the American College of Cardiology*. 2016;68(23):2540-50.
11. Bosman LP, Sammani A, James CA, Cadrin-Tourigny J, Calkins H, van Tintelen JP, et al. Predicting arrhythmic risk in arrhythmogenic right ventricular cardiomyopathy: a systematic review and meta-analysis. *Heart rhythm*. 2018;15(7):1097-107.
12. Bosman LP, Cadrin-Tourigny J, Bourfiss M, Aliyari Ghasabeh M, Sharma A, Tichnell C, et al. Diagnosing arrhythmogenic right ventricular cardiomyopathy by 2010 Task Force Criteria: clinical performance and simplified practical implementation. *EP Europace*. 2020;22(5):787-96.
13. Kommata V, Elshafie M, Sciaraffia E, Perez M, Augustine R, Blomström-Lundqvist C. QRS dispersion detected in ARVC patients and healthy gene carriers using 252-leads body surface mapping: an explorative study of a potential diagnostic tool for arrhythmogenic right ventricular cardiomyopathy. *Pacing and Clinical Electrophysiology*. 2021;44(8):1355-64.
14. Rudy Y. Noninvasive Electrocardiographic Imaging of Arrhythmogenic Substrates in Humans. *Circulation Research*. 2013;112(5):863-74.
15. Huiskamp G, Van Oosterom A. The depolarization sequence of the human heart surface computed from measured body surface potentials. *IEEE Trans Biomed Eng*. 1988;35(12):1047-58.
16. Duchateau J, Sacher F, Pambrun T, Derval N, Chamorro-Servent J, Denis A, et al. Performance and limitations of noninvasive cardiac activation mapping. *Heart Rhythm*. 2019;16(3):435-42.
17. Oosterhoff P, Meijborg VM, van Dam PM, van Dessel PF, Belterman CN, Streekstra GJ, et al. Experimental validation of noninvasive epicardial and endocardial activation imaging. *Circ Arrhythm Electrophysiol*. 2016.
18. Sapp JL, Dawoud F, Clements JC, Horáček BM. Inverse Solution Mapping of Epicardial Potentials: Quantitative Comparison With Epicardial Contact Mapping. *Circ Arrhythm Electrophysiol*. 2012;5(5):1001-9.
19. Andrews CM, Srinivasan NT, Rosmini S, Bulluck H, Orini M, Jenkins S, et al. Electrical and structural substrate of arrhythmogenic right ventricular cardiomyopathy determined using noninvasive electrocardiographic imaging and late gadolinium magnetic resonance imaging. *Circ Arrhythm Electrophysiol*. 2017;10(7):e005105.
20. Cluitmans MJ, Bear LR, Nguyễn UC, van Rees B, Stoks J, Ter Bekke RM, et al. Noninvasive detection of spatiotemporal activation-repolarization interactions that prime idiopathic ventricular fibrillation. *Science Translational Medicine*. 2021;13(620):eabi9317.
21. Durrer D, van Dam RT, Freud GE, Janse MJ, Meijler FL, Arzbaecher RC. Total excitation of the isolated human heart. *Circulation*. 1970;41:899-912.
22. Hakacova N, Robinson AM, Olson CW, Selvester RH, Wagner GS. The relationship between mitral papillary muscles positions and characteristics of the QRS complex. *J Electrocardiol*. 2008;41(6):487-90.
23. Loukas M, Klaassen Z, Tubbs RS, Derderian T, Paling D, Chow D, et al. Anatomical observations of the moderator band. *Clin Anat*. 2010;23(4):443-50.
24. Boonstra MJ, Roudijk RW, Brummel R, Kassenberg W, Blom LJ, Oostendorp TF, et al. Modeling the His-Purkinje Effect in Non-invasive Estimation of Endocardial and Epicardial Ventricular Activation. *Ann Biomed Eng*. 2022:1-17.
25. Roudijk RW, Boonstra MJ, Brummel R, Kassenberg W, Blom LJ, Oostendorp TF, et al. Comparing non-invasive inverse electrocardiography with invasive endocardial and epicardial electroanatomical mapping during sinus rhythm. Fron-

- tiers in physiology. 2021;12.
26. van Dam PM, Oostendorp TF, Linnenbank AC, van Oosterom A. Non-invasive imaging of cardiac activation and recovery. *Ann Biomed Eng.* 2009;37(9):1739-56.
  27. van Dam PM, Gordon JP, Laks MM, Boyle NG. Development of new anatomy reconstruction software to localize cardiac isochrones to the cardiac surface from the 12 lead ECG. *J Electrocardiol.* 2015;48(6):959-65.
  28. Geselowitz DB. Description of cardiac sources in anisotropic cardiac muscle. Application of bidomain model. *J Electrocardiol.* 1992;25 Sup.:65-7.
  29. Meijs, Weier OW, Peters MJ, van Oosterom A. On the Numerical Accuracy of the Boundary Element Method. *IEEE Trans Biomed Eng.* 1989;BME-36:1038-49.
  30. Marquardt D. An Algorithm for Least-Squares Estimation of Nonlinear Parameters. *Journal of the Society for Industrial and Applied Mathematics.* 1963;11(2):431-41.
  31. Cosío FG, Anderson RH, Kuck K-H, Becker A, Borggreffe M, Campbell RW, et al. Living anatomy of the atrioventricular junctions. A guide to electrophysiologic mapping: a consensus statement from the Cardiac Nomenclature Study Group, working group of arrhythmias, European Society of Cardiology, and the task force on cardiac nomenclature from NASPE. *Circulation.* 1999;100(5):e31-e7.
  32. Cantwell CD, Roney CH, Ng FS, Siggers JH, Sherwin SJ, Peters NS. Techniques for automated local activation time annotation and conduction velocity estimation in cardiac mapping. *Computers in biology and medicine.* 2015;65:229-42.
  33. De Bakker J, Van Capelle F, Janse MJ, Tasseron S, Vermeulen JT, de Jonge N, et al. Slow conduction in the infarcted human heart. 'Zigzag' course of activation. *Circulation.* 1993;88(3):915-26.
  34. Anter E. Limitations and pitfalls of substrate mapping for ventricular tachycardia. *JACC: Clinical Electrophysiology.* 2021;7(4):542-60.
  35. Anderson RD, Rodriguez Padilla J, Joens C, Masse S, Bhaskaran A, Magtibay K, et al. On the electrophysiology and mapping of intramural arrhythmic focus. *Circ Arrhythm Electrophysiol.* 2022;15(5):e010384.
  36. Richardson TD, Kanagasundram AN, Stevenson WG. Plumbing the Depths of Intramural Ventricular Arrhythmias: The Surface May Not Always Reveal What Lies Below. *Am Heart Assoc;* 2022. p. e011032.
  37. Coronel R, Wilms-Schopman FJ, Opthof T, Janse MJ. Dispersion of repolarization and arrhythmogenesis. *Heart Rhythm.* 2009;6(4):537-43.
  38. Graham AJ, Orini M, Zacur E, Dhillon G, Jones D, Prabhu S, et al. Assessing Noninvasive Delineation of Low-Voltage Zones Using ECG Imaging in Patients With Structural Heart Disease. *Clinical Electrophysiology.* 2022;8(4):426-36.
  39. Orini M, Graham AJ, Martínez-Naharro A, Andrews CM, de Marvao A, Statton B, et al. Noninvasive mapping of the electrophysiological substrate in cardiac amyloidosis and its relationship to structural abnormalities. *Journal of the American Heart Association.* 2019;8(18):e012097.
  40. Graham AJ, Orini M, Zacur E, Dhillon G, Daw H, Srinivasan NT, et al. Evaluation of ECG imaging to map hemodynamically stable and unstable ventricular arrhythmias. *Circ Arrhythm Electrophysiol.* 2020;13(2):e007377.
  41. Bourfiss M, Prakken NH, van der Heijden JF, Kamel I, Zimmerman SL, Asselbergs FW, et al. Diagnostic value of native T1 mapping in arrhythmogenic right ventricular cardiomyopathy. *JACC: Cardiovascular Imaging.* 2019;12(8 Part 1):1580-2.
  42. Haugaa KH, Basso C, Badano LP, Bucciarelli-Ducci C, Cardim N, Gaemperli O, et al. Comprehensive multi-modality imaging approach in arrhythmogenic cardiomyopathy—an expert consensus document of the European Association of Cardiovascular Imaging. *European Heart Journal-Cardiovascular Imaging.* 2017;18(3):237-53.
  43. Kirkels FP, Bosman LP, Taha K, Cramer MJ, van der Heijden JF, Hauer RN, et al. Improving Diagnostic Value of Echocardiography in Arrhythmogenic Right Ventricular Cardiomyopathy Using Deformation Imaging. *Cardiovascular Imaging.* 2021;14(12):2481-3.
  44. Taha K, Te Rijdt WP, Verstraelen TE, Cramer MJ, de Boer RA, de Bruin-Bon RH, et al. Early mechanical alterations in phospholamban mutation carriers: identifying subclinical disease before onset of symptoms. *Cardiovascular Imaging.* 2021;14(5):885-96.
  45. Bosman LP, Verstraelen T, van Lint F, Cox MG, Groeneweg JA, Mast TP, et al. The Netherlands arrhythmogenic cardiomyopathy registry: design and status update. *Netherlands Heart Journal.* 2019;27(10):480-6.
  46. Bouhamama O, Potse M, Bear L, Weynans L, editors. A patchwork method to improve the performance of the current ECGI methods for sinus rhythm. *VPH 2020-International Conference on the Virtual Physiological Human;* 2020.
  47. Dogrusoz YS, Dubois R, Abell E, Cluitmans M, Bear LR, editors. Electrocardiographic Imaging of Sinus Rhythm in Pig Hearts Using Bayesian Maximum A Posteriori Estimation. *2021 Computing in Cardiology (CinC);* 2021: IEEE.
  48. Popescu DM, Shade JK, Lai C, Aronis KN, Ouyang D, Moorthy MV, et al. Arrhythmic sudden death survival prediction using deep learning analysis of scarring in the heart. *Nature Cardiovascular Research.* 2022;1(4):334-43.
  49. Perez-Alday EA, Haq KT, German DM, Hamilton C, Johnson K, Phan F, et al. Mechanisms of arrhythmogenicity in hypertrophic cardiomyopathy: insight from non-invasive electrocardiographic imaging. *Frontiers in physiology.* 2020;11:344.
  50. Hutchinson MD, Gerstenfeld EP, Desjardins B, Bala R, Riley MP, Garcia FC, et al. Endocardial unipolar voltage mapping to detect epicardial ventricular tachycardia substrate in patients with nonischemic left ventricular cardiomyopathy. *Circ Arrhythm Electrophysiol.* 2011;4(1):49-55.



$\emptyset$

$(x, y) = \int_{x_0}^{x_1} \int_{y_0}^{y_1} \dots$

$v_2 / c^2$

$v_{cg}$

$S_u$

ind



# Chapter 5

## Incorporating Structural Abnormalities in Equivalent Dipole Layer Based ECG Simulations

MJ Boonstra, TF Oostendorp, RW Roudijk, M Kloosterman, FW Asselbergs, P Loh, and PM van Dam.

*Frontiers in Physiology. 2022 Dec 22;13:2690*

## **Abstract**

Electrical activity of the myocardium is recorded with the 12-lead ECG. ECG simulations can improve our understanding of the relation between abnormal ventricular activation in diseased myocardium and body surface potentials (BSP). However, in equivalent dipole layer (EDL)-based ECG simulations, the presence of diseased myocardium breaks the equivalence of the dipole layer. To simulate diseased myocardium, patches with altered electrophysiological characteristics were incorporated within the model. The relation between diseased myocardium and corresponding BSP was investigated in a simulation study.

Activation sequences in normal and diseased myocardium were simulated and corresponding 64-lead BSP were computed in four models with distinct patch locations. QRS-complexes were compared using correlation coefficient (CC). The effect of different types of patch activation was assessed. Of one patient, simulated electrograms were compared to electrograms recorded during invasive electro-anatomical mapping.

Hundred-fifty-three abnormal activation sequences were simulated. Median QRS-CC of delayed versus dyssynchronous were significantly different (1.00 vs. 0.97,  $p < 0.001$ ). Depending on the location of the patch, BSP leads were affected differently. Within diseased regions, fragmentation, low bipolar voltages and late potentials were observed in both recorded and simulated electrograms.

A novel method to simulate cardiomyopathy in EDL-based ECG simulations was established and evaluated. The new patch-based approach created a realistic relation between ECG waveforms and underlying activation sequences. Findings in the simulated cases were in agreement with clinical observations. With this method, our understanding of disease progression in cardiomyopathies may be further improved and used in advanced inverse ECG procedures.

## Introduction

The ECG provides valuable insight into the electrical activity of the heart.<sup>1</sup> In clinical practice, interpretation of changes in the ECG due to pathology are mainly based on ECG-based pattern recognition.<sup>2-4</sup> General understanding of the effect of abnormal electrical activity in diseased myocardium on intracardiac and body surface potentials (BSP) is obtained with invasive electro-anatomical mapping (EAM) studies and ECG simulation studies. Through ECG simulation, better understanding of the electrophysiological behavior of myocardial substrate can be achieved.<sup>5</sup> For example, the effect of different types and locations of diseased myocardium on simulated BSP may provide valuable clinical information about disease onset and/or progression.

However, the relation between abnormal ventricular activation and the corresponding ECGs still requires more fundamental understanding. Specifically on the relation between ECG waveform changes and the pathological wave propagation in the presence of structural myocardial disease. Invasive mapping procedures have already provided a lot of information about local electrical dysfunction of the myocardium. The presence of late potentials, low bipolar and unipolar voltages and fractionation of local electrograms is directly related to the disruption of the activation sequence due to the presence of fibrous or fibrofatty tissue.<sup>6,7</sup> Additionally, the voltage of unipolar signals is shown to be related to the presence of epicardial and/or transmural scar tissue.<sup>8-10</sup>

The relation between abnormal ventricular activation and ECG waveforms can also be investigated by ECG simulation. To simulate the ECG, two types of models are required. The first model is the cardiac source model, representing the electrical currents generated by the myocardial cells. And second, the volume conductor model, which describes the effect of these generated currents on potentials throughout the torso. A well-known interactive ECG simulation program is ECGsim<sup>11,12</sup>; a program based on the equivalent dipole layer (EDL) cardiac source model and boundary element method-based volume conductor. The EDL source model is based on work by Wilson and shown to be also valid in homogeneous anisotropic tissue by Geselowitz.<sup>13,14</sup> He observed that potentials generated outside the heart by the electric activity of all myocardial cells is proportional to the potentials generated by a simulated dipole layer at the surface of that mass, with the dipole layer strength proportional to the upstroke of the local transmembrane potential provided we can assume homogeneous anisotropy ratios. The EDL is positioned at the endocardial and epicardial surface bounding the myocardium. At each element of this surface model, local source strength is defined by the local transmembrane potential. Adjusting the local timing of depolarization or repolarization result in changes in the simulated BSP.

The presence of diseased myocardium, such as scar, within the myocardial mass,

breaks the equivalence of the dipole layer. In order to restore the equivalence, the boundary between normal and diseased myocardium must be included in the model. In earlier studies, old myocardial infarctions were simulated by removing parts of the ventricular anatomical model, thereby creating a hole in the anatomy.<sup>15</sup> This method can be used for cases of homogeneous transmural scar without any surviving myocardium, as is often the case in ischemic heart disease. However, in other cases of ischemic heart disease, surviving tissue is present within dense scarred regions. Furthermore, in case of progressive fibrofatty myocardial scarring, as in some inherited cardiomyopathies, strands of normal and fibrofatty myocardium are intermingled in diseased areas. Thus, diseased regions remain partially electrically active which consequently affects recorded potentials. The aim of this study was to evaluate a new method to incorporate local electrical abnormalities into the EDL simulation method. In this simulation study, we studied the effect on corresponding simulated BSP. Additionally, we compared simulations with our method to recordings in one patient who underwent an invasive EAM.

## Materials and Methods

### *EDL-based simulation of potentials*

EDL-based ECG simulation relates the electrical activity at the endocardial and epicardial surface to potentials within and at the body surface (Figure 1). In the EDL-source description, the potential ( $\Phi(t, \vec{y})$ ) generated at any location  $\vec{y}$  and time  $t$  on and within the body surface is given by:

$$\Phi(t, \vec{y}) = \int_{S_v} A(\vec{y}, \vec{x}) V_m(t, \vec{x}) d\omega(\vec{y}, \vec{x})$$

With  $V_m(t, \vec{x})$  the upstroke of the transmembrane potential at position  $\vec{x}$  on the surface of the ventricular myocardial mass ( $S_v$ ) at time  $t$ ,  $d\omega(\vec{y}, \vec{x})$  the solid angle of the infinitesimal surface element  $dS(\vec{x})$  observed from  $\vec{y}$ .  $A(\vec{y}, \vec{x})$  denotes the transfer matrix that expresses the effect of the volume conductor. A model of the volume conductor is typically obtained from MR or CT imaging. The surfaces of all anatomical structures are discretized as closed triangulated surface meshes.  $A(\vec{y}, \vec{x})$  is computed using the boundary element method from each triangle of the discretized ventricular surface towards each observation point at or within the torso<sup>16,17</sup>

The electric activity at the myocardial surface at position  $\vec{x}$  follows the local transmembrane potential waveform.<sup>18,19</sup> At each node, the source strength is proportional to the local transmembrane potentials. Based on the observation that the potential step across the activation wavefront within the myocardium is 40 mV, the dipole layer strength is calibrated such that a completely activated equivalent source element generates the same potential drop.<sup>20,21</sup> The local potential step across a uniform dipole layer is equal to the dipole layer strength (in A/m) divided by the conductivity value of the heart (in S/m).<sup>22</sup> With a potential step of 40 mV and

conductivity value of 0.2 S/m, the normal dipole layer strength is 8  $\mu\text{A}/\text{mm}$ . In the research described in this paper, we specifically studied the effect of activation wave changes on simulated BSP, thus focusing on the depolarization phase. The local potential  $V_m(t; \delta)$  is defined as a step function where the local potential ( $V_m$ ) in the depolarized state was set to one and in the resting state to zero. The local body surface potential is described as a function of the local depolarization ( $\delta$ ) time at the surface is given by:

$$\Phi(t, \vec{y}) = \int_{S_v} A(\vec{y}, \vec{x}) V_m(t; \delta) d\omega(\vec{y}, \vec{x})$$

To reflect the propagation of depolarization over each discretized triangle elements at the surface of the myocardium, the source strength at time  $t$  of a triangle partially activated is weighted with the fraction of the triangle that is activated at  $t$ , as previously described.<sup>17</sup>

Simulating diseased ventricular myocardium: the patch

Because the presence of fibrofatty tissue breaks the equivalence of the dipole layer at the myocardial surface, we divided our segmented ventricular model into separate parts wherein we either simulate normal or diseased myocardium. By specifically including these as separate components within the segmented ventricular model, the equivalence of the EDL is restored (Figure 2A). This provides the opportunity to represent both electrically active and passive myocardial cells within the specific region, similarly to a fibroblast model. The parts representing diseased, non-activatable myocardium are hereafter called patches. Different activation characteristics were

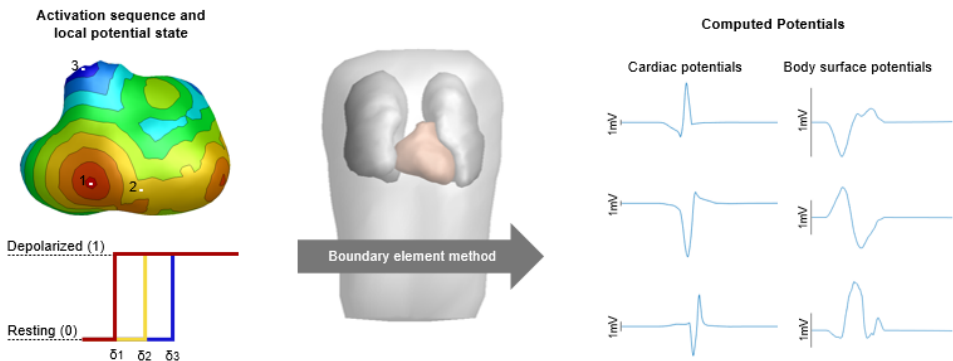


**Figure 1.** Schematic overview of the computation of potentials. The simulated activation sequences, constructed transmembrane potentials and the boundary element method compute the volume conductor effect to compute cardiac and body surface potentials. Activation timing is displayed from red (early) to blue (late), corresponding local potential states were displayed for 3 sites of interest with the color of the displayed potential corresponding to the local activation timing with  $t$  denoting local activation timing. Computed cardiac and body surface potentials were displayed with the height of the black bar indicating 1 mV. The displayed body surface potentials are taken from the 64-lead setup, specifically lead 12 positioned two intercostal spaces above V1, lead 22 positioned at the lower sternum and lead 57 positioned at the right side of the back are displayed.

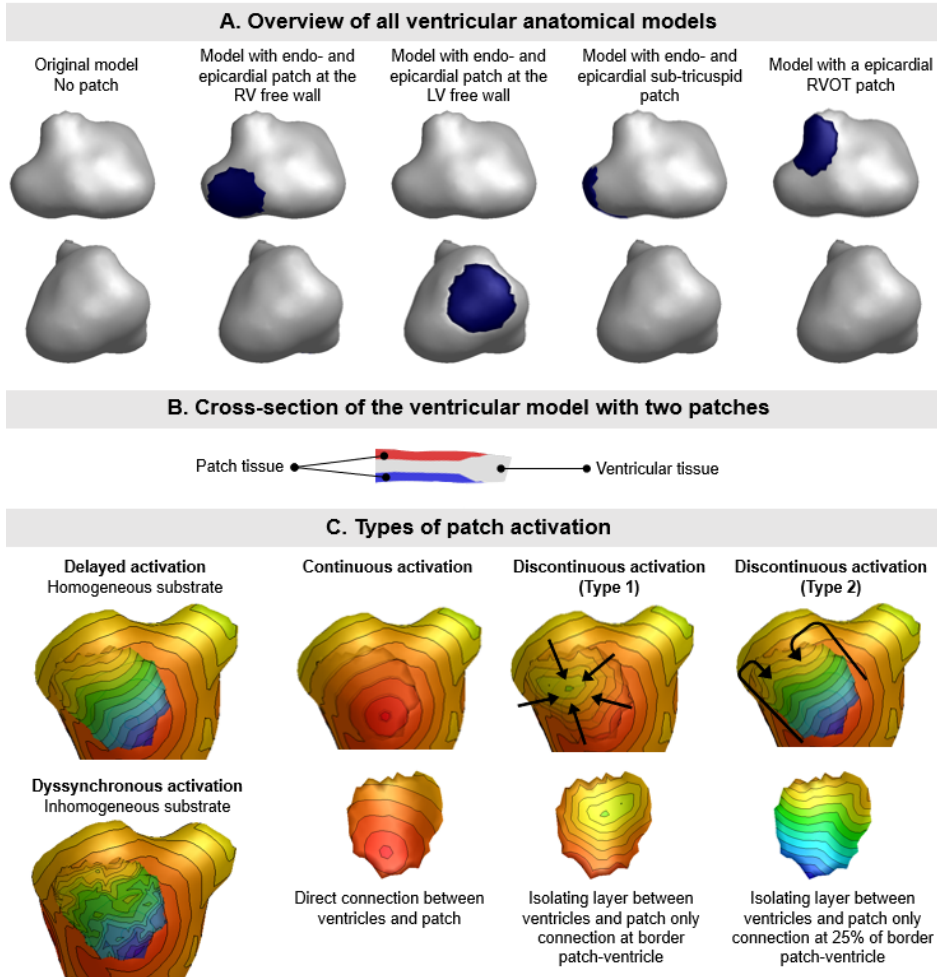


**Figure 2.** Ventricular patch model overview and simulation characteristics. A: The four different patch locations used for the simulation studies are displayed. The location of the patch is indicated by the blue region on the epicardium. Where indicated with endo- and epicardial patch, an opposing endocardial is present with the same size as the displayed epicardial patch. B: Patches (red, endocardial and blue, epicardial) were embedded within the ventricular tissue (gray), thereby not changing the outer shape of the ventricular model. C: Different types of activation sequences (delayed, dyssynchronous, continuous and discontinuous) of the patches are displayed as local activation timing maps from red (early) to blue (late) with isochrone steps of 10 ms. The isolating layer between the ventricles and patch is indicated in black on the inside of the patch. The ventricular activation sequence of the myocardium (excluding the patch) used in this study was equal for all models.

assigned to patches to represent different types of diseased myocardium. The patches were embedded within the segmented ventricular model so that the outer shape of the ventricular model remains intact to a model without patches, but creating a mid-myocardial border between normal and diseased parts. At the location of the patch, the nodes of the normal ventricular model are pushed inward, creating a local dent (Figure 2B). The inner surface of the patch is an exact copy of the nodes at the patch-ventricular border so the nodes were exactly opposing each other. Separate volume conductor models were computed per source (e.g. ventricles and/or patch(es)).

Cardiac CT was used to create patient specific anatomical models of the ventricular myocardium, blood pools, lungs and torso in the current study. The assigned conductivity values were 0.2 S/m for the thorax, patch and ventricular myocardium, 0.04 S/m for the lungs and 0.6 S/m for the blood cavities.<sup>21,23-25</sup> To generate the local potential, we set the local potential to 0 (resting) or 1 (depolarized) depending on the local depolarization timing (Figure 1). The contribution of currents generated by each part (healthy and diseased) on BSP was accounted for based on the superposition principle.

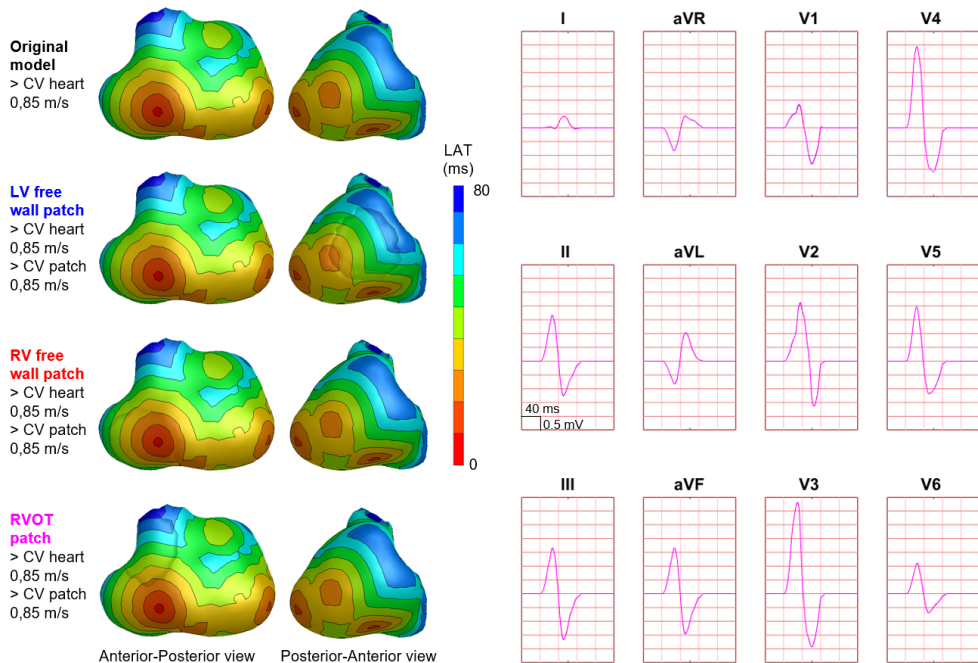


**Figure 3.** Effect of patch incorporation within the ventricular model. For both the original model and three of the models with patch, normal ventricular and patch activation were computed. Activation sequences were displayed from red (early) to blue (late). All simulated BSP signals overlap, as can be observed in the presented standard 12-lead ECG. One cube in the 12-lead ECG corresponds to 40 ms (width) and 0.5 mV (height) as also indicated in lead II.

**Table 1.** Summary of patch simulation characteristics

Patch simulation type	Affected patch	Type of patch activation	Patch simulation characteristics	Connection patch/healthy
Delayed patch activation	Endocardial Epicardial	Homogeneous	0.25-0.65 m/s 0 ms random	Inner patch surface 100%
Delayed type 1 patch activation	Endocardial Epicardial	Homogeneous	0.25-0.65 m/s 0 ms random	Outer ring 100%
Delayed type 2 patch activation	Endocardial Epicardial	Homogeneous	0.25-0.65 m/s 0 ms random	Outer ring 25%
Dyssynchronous patch activation	Endocardial Epicardial	Inhomogeneous	0.45 m/s 30-90 ms random	Inner patch surface 100%
Dyssynchronous type 1 patch activation	Endocardial Epicardial	Inhomogeneous	0.45 m/s 30-90 ms random	Outer ring 100%
Dyssynchronous type 2 patch activation	Endocardial Epicardial	Inhomogeneous	0.45 m/s 30-90 ms random	Outer ring 25%

### Simulation study

To assess the effect of different types of patch activation sequences on BSP, one patient specific (male, 57 y.o.) anatomical model was created using GeomPEACS.<sup>26</sup> The anatomical model contained the triangulated surface meshes of the ventricular myocardium, blood pools, torso and lungs. Using this set, three subsets of ventricular models with endocardial and opposing epicardial patches at different locations in both the right and left ventricle and one model with only an epicardial patch in the right ventricular outflow tract (RVOT) were created (Figure 2A).

### Simulating normal ventricular activation

A case of normal ventricular activation (e.g. sinus rhythm) with an intact His-Purkinje network was simulated by using a set of seven distinct foci (four on the left ventricular (LV) and three on the right ventricular (RV) endocardium) as starting points of activation and the fastest route algorithm.<sup>27</sup> A constant propagation velocity of 0.85 m/s along the myocardial surface was selected, and a 2.5 times slower propagation perpendicular to the wall (Figure 2C). For all anatomical models, the normal ventricular activation sequence was the same.

### Simulating patch activation

The fastest route algorithm was also used to compute the patch activation sequences, with a set propagation velocity and additional characteristics depending on the type of simulated substrate. When using the same propagation velocity for the patch and the ventricles, simulated BSP were the same as the original model (Figure 3), as expected.

Three distinct types of abnormal patch activation sequences were simulated to assess their effect on simulated BSP (Table 1): (1) delayed patch activation due to



homogeneous activation wave slowing, (2) dyssynchronous patch activation due to inhomogeneous myocardial substrate and (3) discontinuous patch activation by simulating an isolating layer between normal ventricular and patch myocardium. For the delayed patch simulations, propagation velocity ranged between 0.85 m/s (normal) and 0.25 m/s (severe disease). To simulate dyssynchronous patch activation, a gaussian noise generator (rand function MATLAB) was used with activation times that differed 0-90 ms from normal. Three types of discontinuous patch activations were simulated (Figure 2C): the part of the patch in direct contact with the myocardium was either fully connected with the normal ventricular model, or only the outer ring of the patch was connected to the ventricular model (type 1), or only the latest 25% of the outer ring were connected to the ventricular model (type 2). Depending on the electrical connection between ventricular and patch tissue (Figure 2C), nodes directly in contact with the ventricular model were assigned the same activation timing as the ventricular nodes.

To account for the presence of fibrofatty tissue, we assumed that with increasing amount of fibrofatty tissue, the percentage of electrically active cells within the region decreases linearly. At some distance, this corresponds to an activation wavefront with a dipole layer strength of less than the normal 8 mA/m. Consequently, the strength of equivalent dipole layer at the surface of the patch was heuristically scaled by the simulated percentage of healthy myocardium within the patch.

### Statistical analysis

To compare different simulations to the case without any patch (i.e. assumed as normal), the effect on signal amplitude, QRS duration and QRS morphology was assessed. Furthermore, the most affected leads were determined using a 64-lead BSP simulation setup where the most affected lead was determined as the lead with the lowest Pearson's correlation coefficient (CC) comparing abnormal to normal QRS. Normally distributed variables were reported as mean  $\pm$  standard deviation and non-normally distributed data were reported as median with interquartile range. Differences between normally distributed data was tested for significance using unpaired students t test and non-normal data were compared using Mann-Whitney U test.

### *Clinical case - Invasive electro-anatomical mapping*

One patient (male, 65 y.o.) referred for invasive EAM and ablation was enrolled. The EAM procedure was clinically indicated because of recurrent ventricular arrhythmia due to structural myocardial disease (arrhythmogenic cardiomyopathy). The patient is a carrier of a pathogenic plakophilin-2 mutation, which is associated with the development of arrhythmogenic cardiomyopathy. As a part of the clinical workup prior to the EAM procedure, the patient underwent cardiac computed tomography imaging. For study purposes, 64-lead BSP mapping was performed on the day prior to

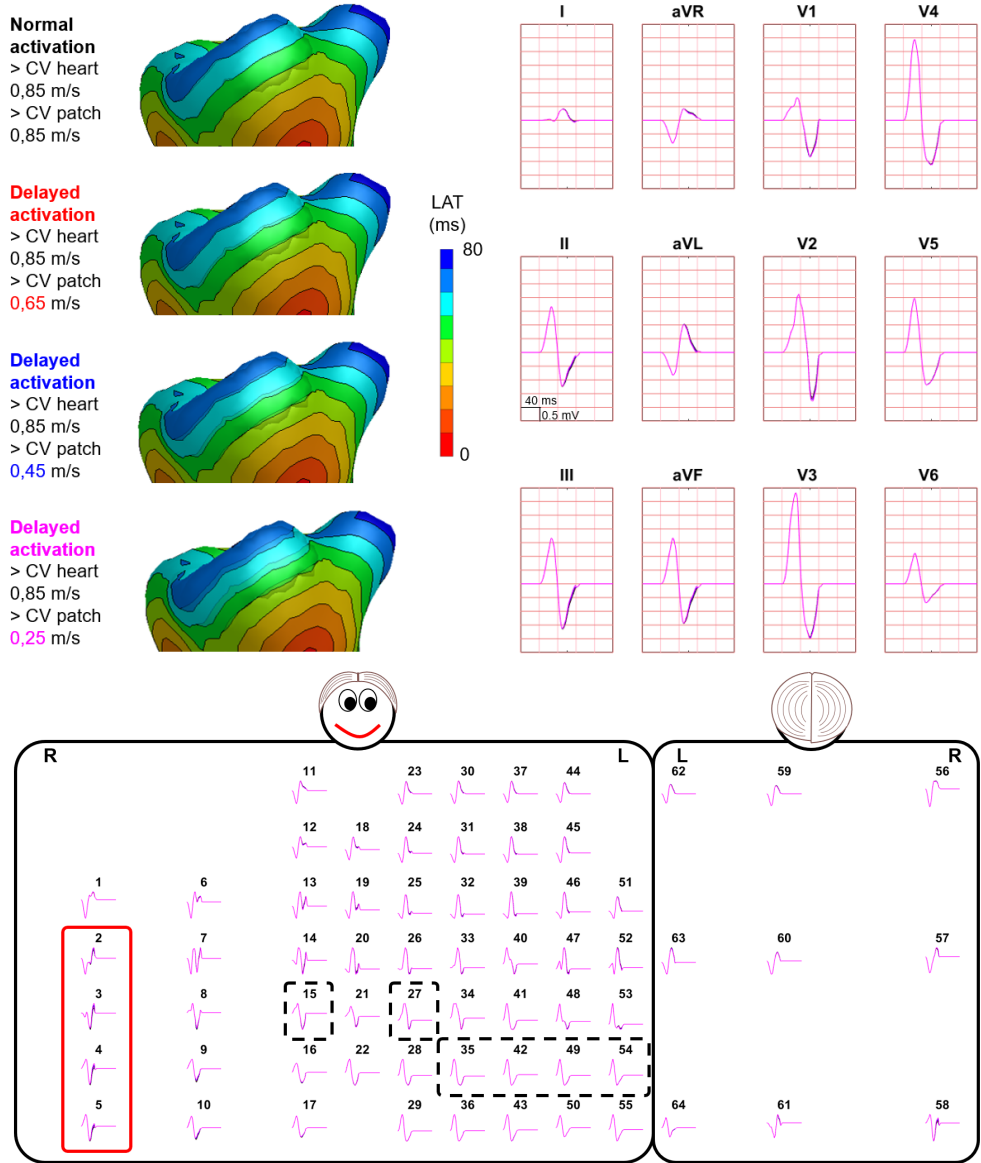


**Figure 4.** Effect of delayed patch activation on body surface potentials. Representative example of the effect of delayed patch activation reducing the propagation velocity through the patch. Activation sequences of the patches and ventricles are displayed from red (early) to blue (late) with isochrone steps of 10 ms. All simulated BSP are displayed in the simulated 12-lead ECG and the 64-lead BSP. The colors in the ECG correspond to the colors stated in the left column with the simulation characteristics. Within the 64-lead BSP, maximum changes in QRS complex were observed in the leads indicated with the red box. Electrode position of the 12-lead ECG was indicated by the black dashed boxes. One cube in the 12-lead ECG corresponds to 40 ms (width) and 0.5 mV (height) as also indicated in lead II.

EAM. The study protocol was approved by the local institutional review board (UMC Utrecht, The Netherlands, protocol nr. 17/628). The patient gave informed consent prior to BSP mapping and the study was conducted according to the declaration of Helsinki. During EAM, the epicardium and RV endocardium were mapped using a cardiac mapping system with the multipolar HD-grid catheter (Advisor<sup>TM</sup>, Ensite Precision, Abbott).

Patient specific anatomical models of the ventricular myocardium, blood pools, lungs and torso were created and electrode positions captured with a 3D camera were registered to the torso model. A patch at the basal region of the RV endocardium was created, in the same region as abnormal electrograms were observed during EAM. Normal ventricular activation with an intact His-Purkinje network was simulated using a set of 8 foci in combination with a tuned propagation velocity of 1 m/s. Location of the foci and propagation velocity were tuned to ensure that the simulated QRS-complex waveform in the extremity leads was similar to patient specific recorded QRS-complex waveforms and QRS duration (100 ms). Arrhythmogenic cardiomyopathy

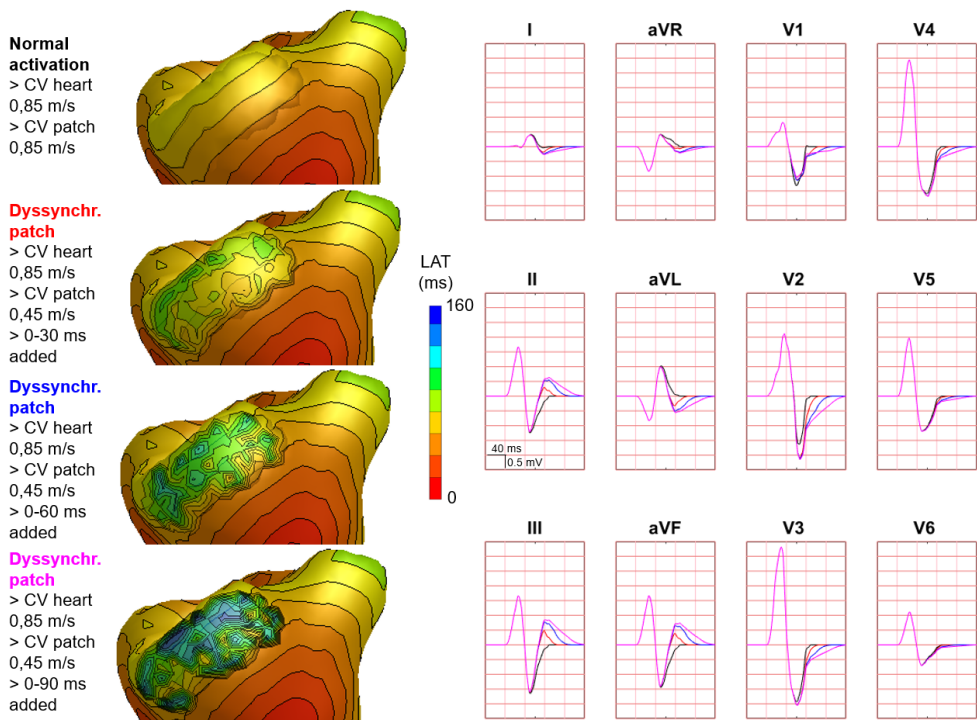


**Figure 5.** Effect of dyssynchronous patch activation on body surface potentials. Representative example of the effect of dyssynchronous patch activation. Activation sequences of the patches and ventricles are displayed from red (early) to blue (late) with isochrone steps of 10 ms. Simulated BSP are displayed as 12-lead ECG. The colors in the ECG correspond to the colors stated in the left column with the simulation characteristics. Isochronal crowding that is observed on the patch increases by increasing the amount of added jitter. One cube in the 12-lead ECG corresponds to 40 ms (width) and 0.5 mV (height) as also indicated in lead II.

is characterized by defects in intercellular connections, e.g. the intercalated discs, resulting in a combination of altered intercellular impulse propagation and progressive fibro-fatty replacement of healthy myocardium. Therefore, dyssynchronous patch activation was simulated using a propagation velocity of 0.85 m/s and adding random noise within the range of 0-50 ms. To represent the presence of fibrofatty tissue, a uniform source strength of 50% (4 mA/m) was used for the patch.

Epicardial and endocardial electrograms

After the procedure, all electrograms obtained prior to ablation were manually checked for validity. The local activation timing was determined at the maximal absolute amplitude of the bipolar signal, which corresponds to the maximum downslope (dV/dt) in unipolar signals. Data were exported as raw electrograms with location, annotated local activation timing and bipolar voltage. For the simulated case, local activation timing was set as the time instance of upstroke of transmembrane potential amplitude. Bipolar electrograms were computed by subtracting the unipolar electrogram of direct neighboring nodes. Per node, bipolar voltage was calculated as the maximum potential difference between the node and any of its neighbors. For

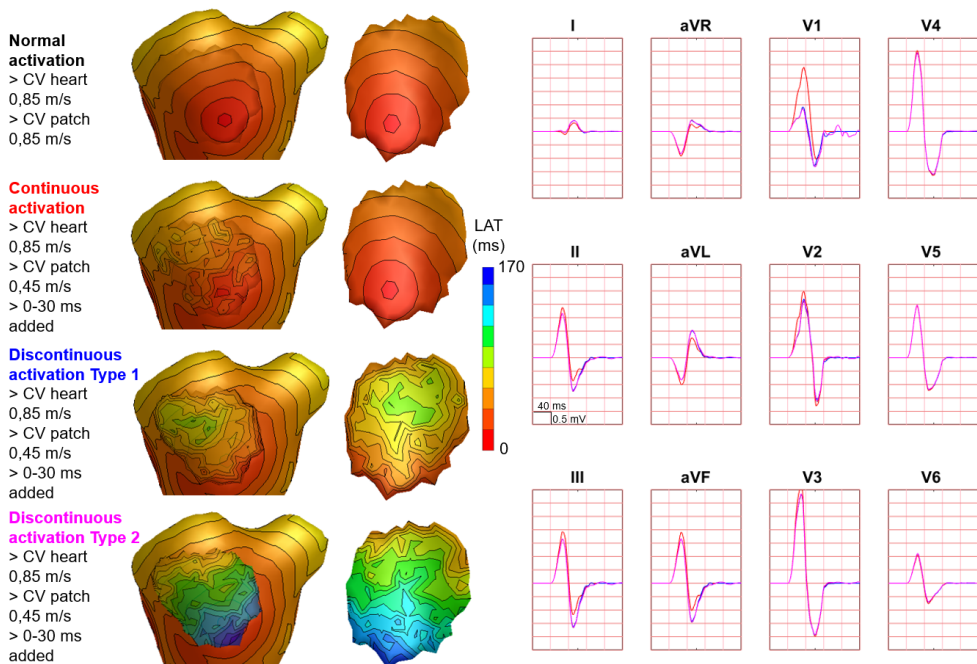


**Figure 6.** Effect of discontinuous patch activation on body surface potentials. Representative example of the effect of different types of discontinuous patch activations on body surface potentials. Activation sequences of the patches and ventricles are from red (early) to blue (late) with isochrone steps of 10 ms. All simulated BSP are displayed in the simulated 12-lead ECG. The colors in the ECG correspond to the colors stated in the left column with the simulation characteristics. With different patch simulations, most changes were observed in V1, where the magnitude of the effect differed between simulations. One cube in the 12-lead ECG corresponds to 40 ms (width) and 0.5 mV (height) as also indicated in lead II.

both the recorded and the simulated case of the same patient, local activation timing maps and bipolar voltage maps were constructed.

## Results

### Simulation study

Hundred-fifty-three patch activation sequences were simulated for each of the different types; delayed (Figure 4), dyssynchronous (Figure 5) and discontinuous (Figure 6) with the same underlying normal ventricular activation sequence. By only slowing down the propagation velocity over and through the patch (Figure 4), the overall activation wave remains similar to normal ventricular activation, while the activation timing range over the patch increases. In case of dyssynchronous patch activation (Figure 5), the total patch activation timing increased and the effect of an inhomogeneous substrate is observed by increasing local activation timing differences. Discontinuous patch activation due to an ‘isolating’ layer between patch and normal ventricular myocardium, resulted in a patch activation initiated at the edge of the patch (Figure 6). The direction of activation through the patch differed depending on the connection between the ventricular myocardium and the patch.

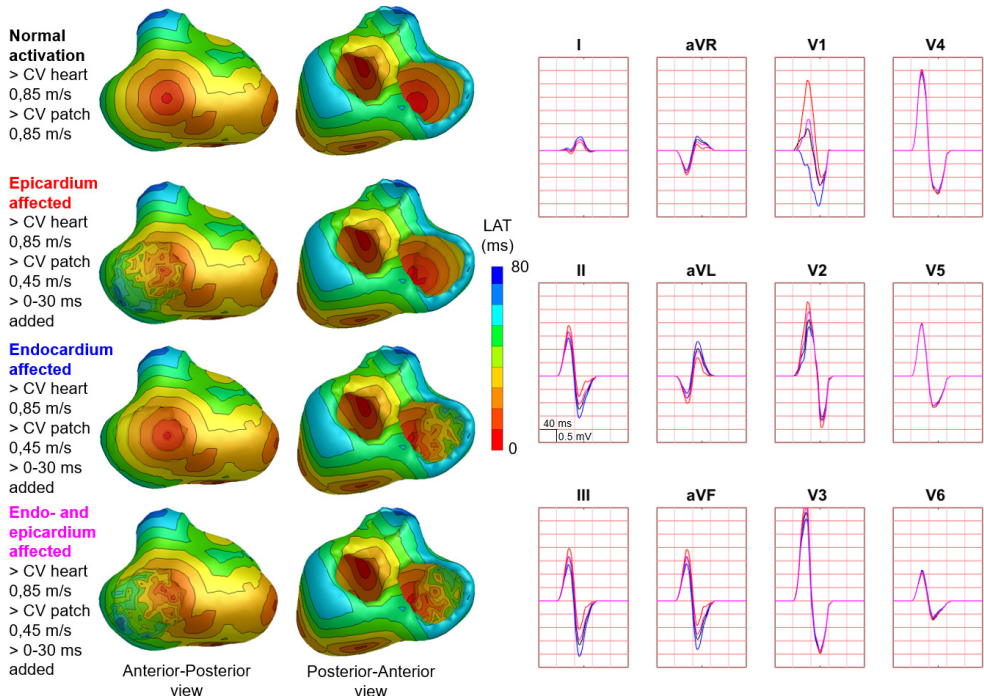


**Figure 7.** Effect of diseased endocardial vs epicardial patch activation on body surface potentials. Representative example of the effect of diseased endocardial and/or epicardial patch activation on body surface potentials. Activation sequences of the patches and ventricles are displayed from red (early) to blue (late) with isochrone steps of 10 ms. All simulated BSP are displayed in the simulated 12-lead ECG. The colors in the ECG correspond to the colors stated in the left column with the simulation characteristics. With endocardial vs epicardial patch location, the effect in leads with maximum effect was opposed. One cube in the 12-lead ECG corresponds to 40 ms (width) and 0.5 mV (height) as also indicated in lead II.

Abnormal patch activation affects both QRS morphology (fragmentation, amplitude changes) and/or QRS duration. Median [range] total activation duration for the simulation of the activation sequence was 114 [88;279] ms with the RV free wall patch, 117 [88;269] ms with the LV free wall patch, 114 [88;211] ms with the RV tricuspid valve patch and 130 [88;273] ms with the RVOT patch. For the severely prolonged activation sequences, observed amplitude at end-QRS was low. Overall QRS-CC was 0.99 [0.98;1.00], and a significant difference ( $p < 0.001$ ) between delayed versus dyssynchronous and continuous versus discontinuous patch activation was observed (Table 2). Compared to dyssynchronous patch activation (Figure 5), homogeneous delayed patch activation (Figure 4) showed limited effect on the simulated BSPs. The effect of the different types of discontinuous patch activation resulted in variable effect within the QRS complex when assessing the onset and duration of abnormal BSP (Figure 6). When comparing discontinuous type 1 to type 2, the effect on QRS morphology is less for type 1. In type 2, there are clear signs of late activation in the simulated BSP after complete ventricular activation. In epicardial vs endocardial

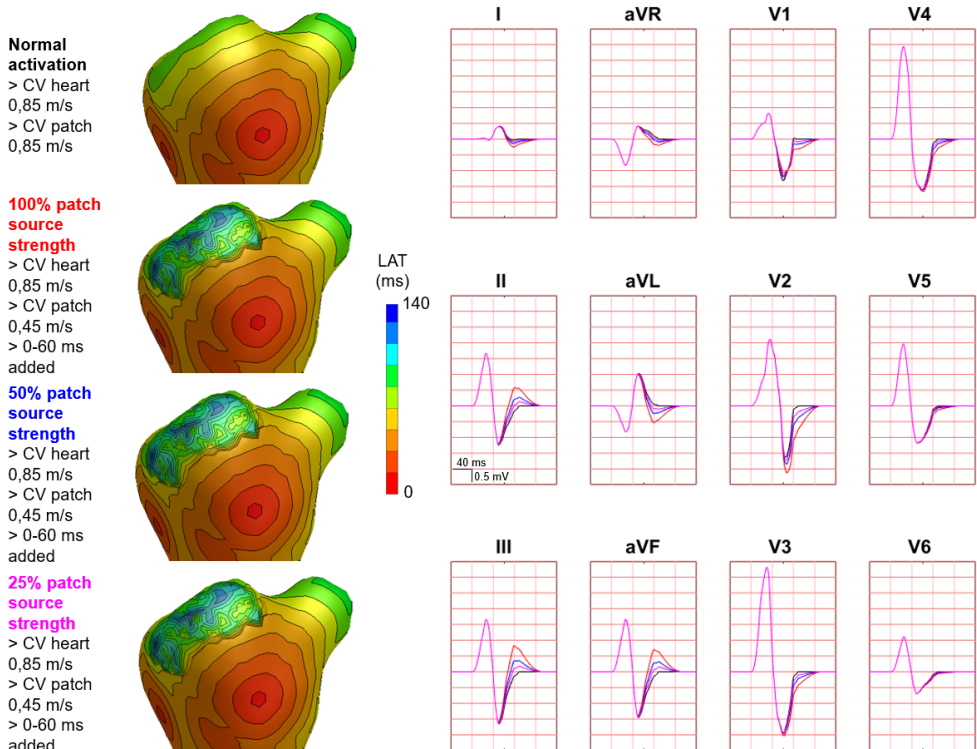


**Figure 8.** Effect of decreasing source strength on body surface potentials. Representative example of the effect of source strength reduction body surface potentials. Activation sequences of the patches and ventricles are displayed from red (early) to blue (late) with isochrone steps of 10 ms. All simulated BSP are displayed in the simulated 12-lead ECG. The colors in the ECG correspond to the colors stated in the left column with the simulation characteristics. With decreasing source strength, the magnitude of effect on the BSP reduced. One cube in the 12-lead ECG corresponds to 40 ms (width) and 0.5 mV (height).



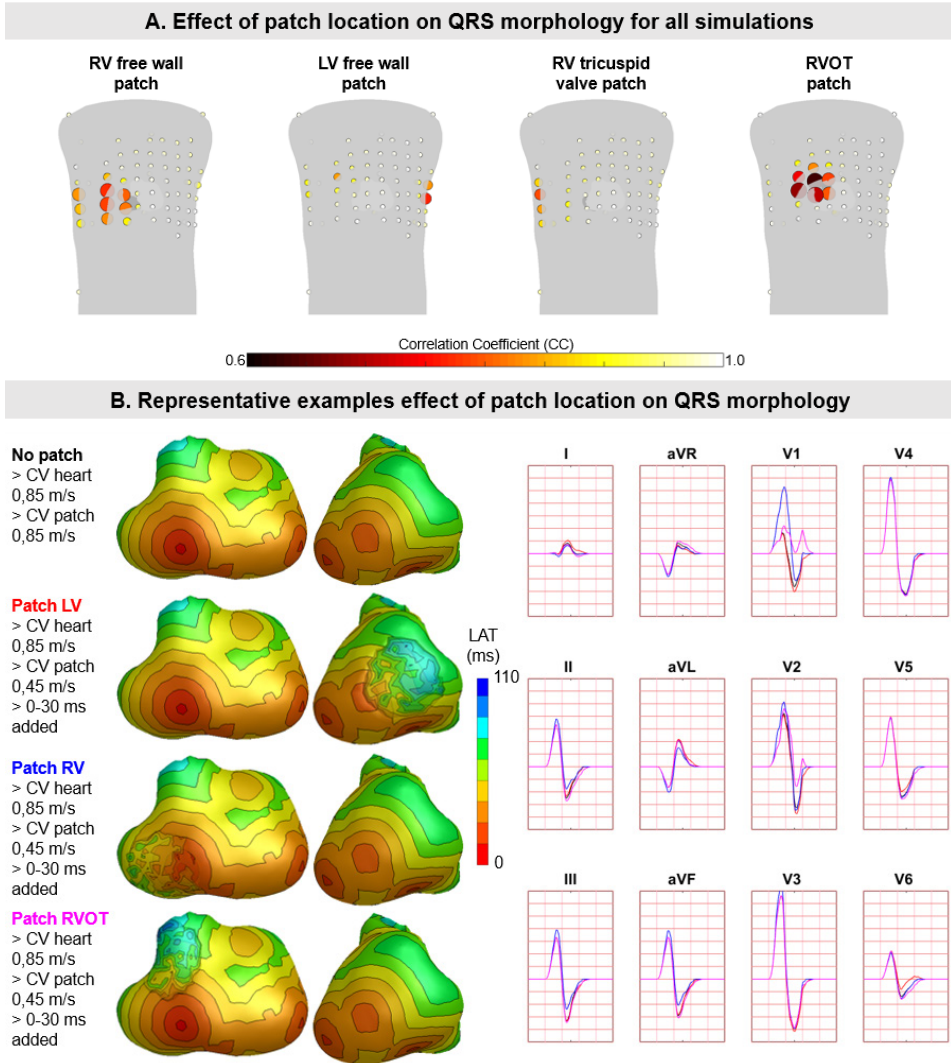


**Figure 9.** The effect of patch location on simulated body surface potentials. A: The mean  $\pm$  standard deviation of correlation coefficient (CC) per BPS lead between normal and diseased BSP. Each lead is represented by a dot with the color representing average CC (range 0.6-1) and size representing the magnitude in standard deviation of CC. The heart contour (light grey) with patch (dark grey) is displayed within the torso. B: Representative example of the effect of patch location on BSP. Activation sequences of the patches and ventricles are displayed from red (early) to blue (late) with isochrone steps of 10 ms. Simulated BSP are displayed for the standard 12-lead ECG. The colors in the ECG correspond to the colors stated in the left column with the simulation characteristics. One cube in the 12-lead ECG corresponds to 40 ms (width) and 0.5 mV (height).

**Table 2.** Overview of simulation characteristics and resulting QRS-CC.

Patch simulation type	Median	IQR1	IQR3	Min	Max
Delayed patch activation	1.00	0.99	1.00	0.20	1.00
Delayed type 1 patch activation	1.00	1.00	1.00	0.96	1.00
Delayed type 2 patch activation	1.00	1.00	1.00	0.96	1.00
Dyssynchronous patch activation	0.97	0.92	0.99	-0.28	1.00
Dyssynchronous type 1 patch activation	0.98	0.93	1.00	-0.09	1.00
Dyssynchronous type 2 patch activation	0.98	0.95	1.00	0.12	1.00

*IQR1 = interquartile range lower quartile, IQR3 = upper quartile, min = minimum value, max = maximum value.*

disease (Figure 7), the effect on the BSP of the abnormal activation sequence is opposite. Heuristically decreasing source strength of the patches resulted in a decrease in amplitude of the potentials generated by the patch on the BSP (Figure 8). The lead position in which the BSP waveform is affected most is directly related to the location of the diseased myocardium (Figure 9A). Furthermore, the vicinity of the patch to a site of early ventricular activation is related to the timing of initial QRS morphology changes (Figure 9B).

#### *Clinical case - Invasive electro-anatomical mapping*

Invasive recorded and simulated local activation timing maps and bipolar voltage maps were created (Figure 10). For the recorded and simulated EAM, spacing between unipolar electrograms was 3 mm and  $5 \pm 1$  mm, respectively. The recorded and simulated local activation times ranged between 0-130 and 0-132 ms, respectively. All electrograms considered were obtained prior to ablation. Median bipolar voltage of these EAM electrograms was 0.5 versus 4.5 mV in the regions within and outside the diseased area. For the simulated maps, median bipolar values were 7.1 mV and 11.8 mV within and outside the simulated diseased area, respectively. In both the recorded and simulated cardiac electrograms, fractionation and late potentials were observed in the diseased areas (Figure 10).

In the included patient (QRS duration 100 ms) who underwent EAM, fragmentation and low-QRS amplitude was observed in the recorded BSP in leads located at the right anterior side of the chest. The morphology of the QRS complexes comparing recorded to simulated (Figure 10), were similar and fragmentation at end-QRS was observed.

## **Discussion**

In this article we introduce a new method to simulate local myocardial disease and its effect on simulated EDL-based potentials. This new method enables the simulation of activation sequences in myocardium with strands/islands of surviving and fibrofatty tissue. Different types of myocardial disease with specific activation characteristics (delay, dyssynchrony, discontinuity) can be simulated which directly gives insight into the effect on simulated BSP which can in turn be related to different cardiac diseases.



The findings from the simulation study were substantiated by the invasive EAM case of a patient with arrhythmogenic cardiomyopathy. The incorporation of structural defects with partially surviving myocardium in EDL-based ECG simulation is relatively easy to implement. The technique not only can aid teaching in the context of ECG waveform changes due to specific pathology, but might also be used in the non-invasive inverse estimation of activation in the presence of inhomogeneous scar, as occurs in for example arrhythmogenic cardiomyopathy or Brugada syndrome.

### *Effect of structural abnormalities on potentials*

This new EDL method increases the understanding of ECG waveform changes due to diseased myocardium with distinct activation sequences. By changing the simulation characteristics like propagation velocity, activation wave dyssynchrony/discontinuity and source strength, the effect of abnormal patch activation can be investigated and related to waveform changes in both electrograms and BSP. With the described method, the general effect of a substrate consisting of both fibrofatty and healthy myocardium is modeled, thereby capturing the overall effect of a certain substrate on observed potentials. The patch may also be used to represent scar with small channels of viable tissue, which may provide isthmuses for reentry. By adjusting the connection between patch and ventricular tissue, such a scar can be modeled, providing also the possibility for a mid-myocardial point of reentry.

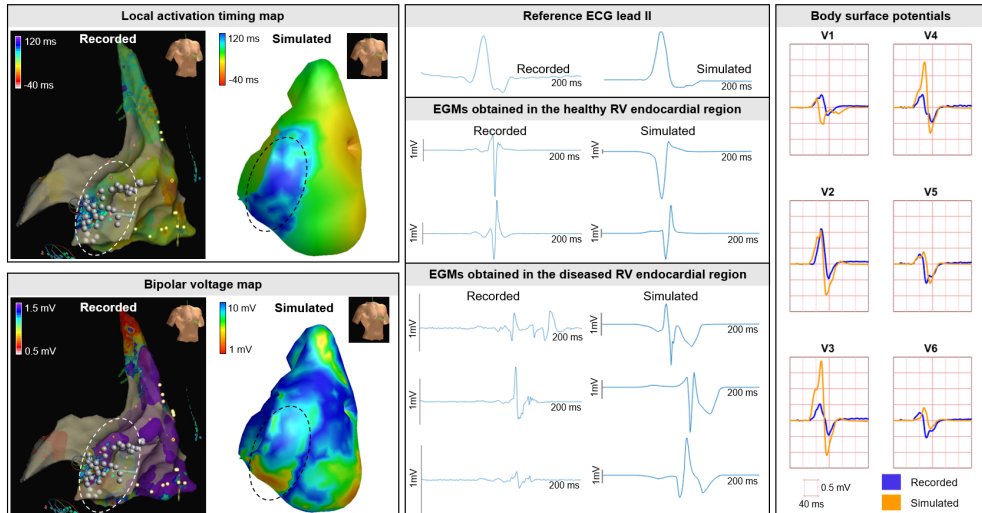


**Figure 10.** Clinical EAM case. Recorded and simulated electro-anatomical map (EAM). Local activation timing and bipolar voltage maps of the RV endocardium are displayed from red (early/low) to blue (late/high). Recorded and simulated bipolar cardiac electrograms are displayed for healthy and diseased regions. Within diseased regions (dashed circles), fragmentation and late potentials occur in recorded and simulated electrograms. Ablation was performed and indicated with the white dots. Recorded and simulated body surface potentials. The BSP is displayed per lead for the QRS complex for the precordial signals V1-V6 from the standard 12-lead ECG. One cube in the 12-lead ECG corresponds to 40 ms (width) and 0.5 mV (height).

In regions with severe scarring, low-voltage, late and fragmented potentials are observed during EAM procedures<sup>6-10</sup> as well as in our simulations (Figure 10). However, the presence of myocardial disease cannot always be identified in recorded BSP, possibly due to the anatomical location of the substrate, its vicinity to an early site of activation (Figure 5) or due to the low local changes in potentials<sup>28,29</sup>, resulting in relatively small, possibly mid-QRS changes<sup>30</sup>. Whereas such pathological changes may not be as apparent as fragmentation<sup>31</sup> or prolonged terminal activation duration<sup>32</sup>, they still may be highly relevant to monitor disease progression. The presence of scarred tissue can be assessed using late gadolinium enhancement (LGE)-CMR imaging.<sup>33</sup> Regions with LGE are associated with the presence of abnormal electrocardiograms during EAM and ventricular arrhythmias.<sup>34</sup> By also taking into account areas with LGE presence, patient specific EDL-based modeling and risk-stratification may be further improved.

#### *Clinical implications to monitor disease progression*

In this study, we observed that subtle changes in the cardiac activation were not always visible in the standard 12-lead ECG (Figure 5). In inherited cardiomyopathies, subtle changes in cardiac activation may however be a sign of disease progression and increased risk for ventricular arrhythmias. For instance; in arrhythmogenic cardiomyopathy, most structural and electrical signs of myocardial disease are observed in the basal area of the RV free wall.<sup>35-37</sup> When modeling this type of disease, the largest changes in BSP occurred in leads not included in the standard 12-lead ECG (Figure 5). A previous study using echocardiography<sup>38</sup> observed early structural signs of disease in the absence of ECG abnormalities in the 12-lead ECG. This may be explained by the fact that the standard 12-lead ECG inadequately images (subtle) ECG changes due to substrate location. Furthermore, the current task force criteria for arrhythmogenic cardiomyopathy mainly focuses on end-QRS ECG abnormalities.<sup>36</sup> However, depending on the location of the substrate and its vicinity to early sites of activation, changes throughout the QRS complex (e.g. changing RS-amplitude ratio) may be an important indicator of disease progression.

#### *Identification of new ECG features to identify disease*

The importance of the identification of subtle ECG changes to detect disease is also demonstrated within the field of ECG-based artificial intelligence. With deep neural networks, low ejection fraction<sup>39</sup>, LV hypertrophy<sup>40</sup>, early signs of inherited cardiomyopathy<sup>41</sup> and electrolyte imbalance<sup>42,43</sup> can be identified from the apparently normal 12-lead ECG. Furthermore, atrial fibrillation<sup>44,45</sup> and life-threatening ventricular arrhythmias<sup>40</sup> can be predicted using the 12-lead ECG during sinus rhythm. The findings of ECG-based deep neural networks may be further substantiated through ECG simulation. By focusing on the underlying pathology, observed pathological waveform changes in the 12-lead ECG may be explained by systematically evaluating the effect of substrates on QRS morphology. Thus, together with ECG-based

artificial intelligence, the new ECG simulation technique may aid the discovery of yet unidentified pathological waveform changes to detect and monitor disease onset and progression.

#### *Patch simulation characteristics*

To demonstrate the effect of different types of patch activations on BSP, patch source strength was set equal to ventricular source strength and propagation velocities to simulate delayed activation were set far below (0.25 m/s) real physiological values (0.85 m/s). With the simulation of an isolating mid-myocardial layer (discontinuous activation type 1&2), a mid-myocardial line of block was simulated and activation sequences and BSPs were both clearly affected (Figure 6). Without this isolating layer, changes in BSP were observed in the initial part of the QRS complex. With an isolating layer, the type of connection determined the effect on simulated BSP; for type 1 disconnection, the effect on BSP was difficult to distinguish from normal, whereas the effect of type 2 was clearly observed in the ST-segment as fragmentation.

Whereas simulated propagation velocity values, the homogeneous isolating mid-myocardial layer and used source strength were not completely realistic for in-human substrates, the effect of abnormal activation sequences on simulated BSP was clearly distinguishable. In reality, source strength of diseased myocardium is lower compared to healthy myocardium due to the presence of fibrofatty tissue<sup>10,29</sup>. By decreasing patch source strength, the presence of fibrofatty tissue was accounted for, directly resulting in less evident effect on the BSP (Figure 8). This finding is in line with observations during clinical EAM; where fragmented and late potentials can be observed without evident pathological signs in recorded BSP.

#### *Comparison to other EDL-models of disease*

The fundamental difference between our new method and the method to simulate transmural scar by creating a hole in the ventricular anatomical model, is the ability to model the presence of partially- versus completely electrically inactive myocardium.<sup>15</sup> While creating a hole in the segmented ventricular anatomical model is appropriate to simulate a region that is completely electrically inactive, it is not for partially active substrates.<sup>7,10,28,29</sup> With patches, the presence of diseased and healthy myocardium within the same region was modeled, similarly to incorporating a fibroblast model. This method thus serves as a more adequate representation of myocardium in e.g. border zones of old myocardial infarctions or substrates in inherited cardiomyopathies. In the current study we embedded epicardial and endocardial patches, which cannot represent transmural scar. In future studies, we aim to combine both methods by creating a hole and filling this hole with a patch representing locally transmurally diseased tissue.

### *Enhancing our understanding of pathological BSP*

Nowadays, thorough understanding of the relation between pathological cardiac electric activity and corresponding BSP requires extensive electrophysiological and anatomical training within the field of electrophysiology. However, for teaching purposes, a tool to demonstrate this relation provides important insight in the basic aspects of electrocardiography. By interactively testing the effect of different disease-types on the activation sequence in the well-known known ECGsim-tool<sup>11,12</sup>, their effect on corresponding BSP can be directly observed and teaching of the aspects of electrocardiography is further improved. Furthermore, from insights obtained from ECG simulations, non-invasive inverse estimation of activation sequences can be further optimized to further improve early detection and disease risk-stratification.

### *Limitations*

In this study, we used a ventricular activation sequence initiated at six different sites with an average myocardial conduction velocity of 0.85 m/s as our normal reference to study the effect of different patch activation on the QRS wave. We are aware that this ventricular activation sequence resulted in ECG patterns clinically categorized as abnormal (e.g. V1 RS pattern, prominent S in V6, aVR QS pattern and aVL QR pattern). These observations are likely to be the consequence of the relatively simple representation of normal ventricular activation, compared to complex true activation sequence. As the main goal of this study is to demonstrate the *change* by the presence of scar tissue, this does not compromise the conclusions of the study. The new method described in this article was not strictly validated in the current study. The comparison shown in Figure 3-8 and the comparison with clinical data (Figure 10) give strong evidence, that the new method produces reasonable results. Future studies will focus on testing the validity of this new EDL approach for modeling different cardiac diseases. Depending on the type of substrate and disease severity, the most appropriate method to model the local activation wavefront can be chosen.

When embedding a patch in the ventricular model a local dent was created consequently affecting the ventricular distance matrix. As activation sequences were computed using the fastest route algorithm, the local dent directly affected computed activation sequences and corresponding BSP. In tissue surrounding diseased areas, a decrease in activation times is not expected as anisotropy is likely to more pronounced in this tissue beneath the patches (e.g. diseased tissue). We therefore assumed that when embedding a patch, waveform propagation locally slows in ventricular tissue. To model this, the distance matrix computed for a model without patches was used to compute ventricular activation sequences also in the ventricular model with embedded patches. From a physiological point of view, we effectively increased local anisotropy.

## **Conclusion**

A new method to describe the effect of (partially) electrically active substrate in EDL-based ECG simulation was established. Changes in cardiac activation sequence were directly related to changes in BSP. Insights obtained from the simulation study were in agreement with the presented clinical cases. With this new method, further in-depth understanding of the effect of pathological activation sequences on BSP can be obtained. The method will be incorporated into the next generation of ECGsim and thus be available to everybody. With these insights, risk-stratification and understanding of disease progression in cardiomyopathies may be further improved.

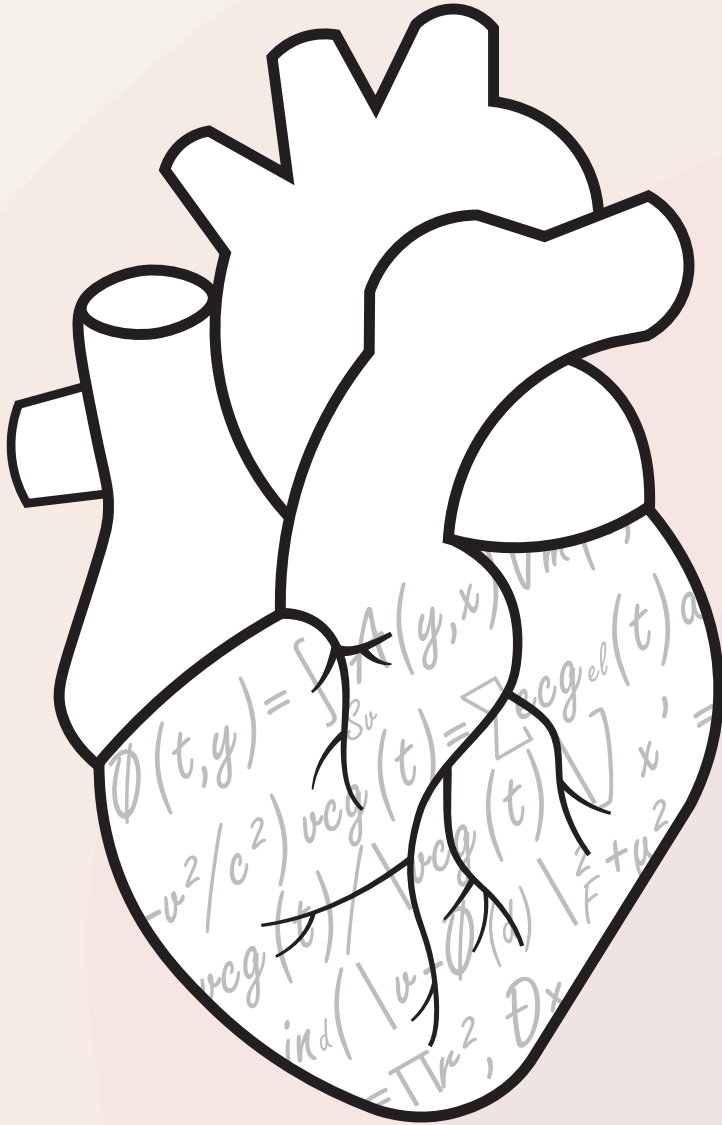
### *Acknowledgements*

This work was supported by the Dutch Heart Foundation (grant numbers CVON2015-12 eDETECT and QRS-Vision 2018B007).

## References

1. Kligfield P, Gettes LS, Bailey JJ, Childers R, Deal BJ, Hancock EW, et al. Recommendations for the Standardization and Interpretation of the Electrocardiogram: Part I: The Electrocardiogram and Its Technology. A Scientific Statement From the American Heart Association Electrocardiography and Arrhythmias Committee, Council on Clinical Cardiology; the American College of Cardiology Foundation; and the Heart Rhythm Society Endorsed by the International Society for Computerized Electrocardiology. *Circulation*. 2007;115(10).
2. Surawicz B, Childers R, Deal BJ, Gettes LS. AHA/ACCF/HRS Recommendations for the Standardization and Interpretation of the Electrocardiogram: Part III: Intraventricular Conduction Disturbances: A Scientific Statement From the American Heart Association Electrocardiography and Arrhythmias Committee, Council on Clinical Cardiology; the American College of Cardiology Foundation; and the Heart Rhythm Society: Endorsed by the International Society for Computerized Electrocardiology. *Circulation*. 2009;119(10):e235-e40.
3. Hancock EW, Deal BJ, Mirvis DM, Okin P, Kligfield P, Gettes LS. AHA/ACCF/HRS Recommendations for the Standardization and Interpretation of the Electrocardiogram: Part V: electrocardiogram changes associated with cardiac chamber hypertrophy a scientific statement from the American Heart Association Electrocardiography and Arrhythmias Committee, Council on Clinical Cardiology; the American College of Cardiology Foundation; and the Heart Rhythm Society Endorsed by the International Society for Computerized Electrocardiology. *Journal of the American College of Cardiology*. 2009;53(11):992-1002.
4. Rautaharju PM, Park LP, Chaitman BR, Rautaharju F, Zhang Z-M. The Novacode criteria for classification of ECG abnormalities and their clinically significant progression and regression. *J Electrocardiol*. 1998;31(3):157-87.
5. Dössel O, Luongo G, Nagel C, Loewe A. Computer modeling of the heart for ECG interpretation—a review. *Hearts*. 2021;2(3):350-68.
6. De Bakker J, Van Capelle F, Janse MJ, Tasseron S, Vermeulen JT, de Jonge N, et al. Slow conduction in the infarcted human heart. 'Zigzag' course of activation. *Circulation*. 1993;88(3):915-26.
7. Aliot EM, Stevenson WG, Almendral-Garrote JM, Bogun F, Calkins CH, Delacretaz E, et al. EHRA/HRS Expert Consensus on Catheter Ablation of Ventricular Arrhythmias 2009-06-01 00:00:00. 771-817 p.
8. Marchlinski FE, Callans DJ, Gottlieb CD, Zado E. Linear ablation lesions for control of unmappable ventricular tachycardia in patients with ischemic and nonischemic cardiomyopathy. *Circulation*. 2000;101(11):1288-96.
9. Soejima K, Stevenson WG, Maisel WH, Sapp JL, Epstein LM. Electrically unexcitable scar mapping based on pacing threshold for identification of the reentry circuit isthmus: feasibility for guiding ventricular tachycardia ablation. *Circulation*. 2002;106(13):1678-83.
10. Glashan CA, Androulakis AF, Tao Q, Glashan RN, Wisse LJ, Ebert M, et al. Whole human heart histology to validate electroanatomical voltage mapping in patients with non-ischaemic cardiomyopathy and ventricular tachycardia. *Eur Heart J*. 2018;39(31):2867-75.
11. van Oosterom A, Oostendorp TF, van Dam PM. Potential applications of the new ECGSIM. *J Electrocardiol*. 2011;44(5):577-83.
12. van Dam PM, Oostendorp TF, van Oosterom A. ECGSIM: Interactive Simulation of the ECG for Teaching and Research Purposes. *Computing in Cardiology 2010*;37:841-4.
13. Geselowitz DB. The Concept of an Equivalent Cardiac Generator. *Biomed Sci Instrum*. 1963;25:325-30.
14. Wilson FN, Macleod AG, Barker PS. The Distribution of Action Currents produced by the Heart Muscle and Other Excitable Tissues immersed in Conducting Media. *J Gen Physiol*. 1933;16:423-56.
15. Oostendorp TF, Ham Wv. Non-invasive estimation of the activation sequence of the heart: modeling of old myocardial infarctions. *Biomed Tech*. 2001;46 suppl. 2:54-6.
16. Oostendorp T, van Oosterom A. The potential distribution generated by surface electrodes in inhomogeneous volume conductors of arbitrary shape. *IEEE Trans Biomed Eng*. 1991;38(5):409-17.
17. Tate JD, Schuler S, Dössel O, MacLeod RS, Oostendorp TF, editors. Correcting undersampled cardiac sources in equivalent double layer forward simulations. International Conference on Functional Imaging and Modeling of the Heart; 2019: Springer.
18. van Oosterom A. The Singular Value Decomposition of the T wave: Its Link with a Biophysical Model of Repolarization. *Int J Bioelectromagnetism*. 2002;4:59-60.
19. van Oosterom A. The dominant T wave and its significance. *J Cardiovasc Electrophysiol*. 2003;14(10 Suppl):S180-7.
20. van Oosterom A. Cell Models - Macroscopic Source Descriptions. In: Macfarlane PW, Lawrie TTV, editors. *Comprehensive Electrocardiology*. 1. 1 ed. Oxford: Pergamon Press; 1989. p. 155-79.
21. van Oosterom A. Genesis of the T wave as based on an equivalent surface source model. *Journal of Electrocardiography*. 2001;34(Supplement 2001):217-27.
22. Plonsey R, Barr RC. *Bioelectricity: A Quantitative Approach*. New York: Springer; 2011.
23. van Oosterom A, Huiskamp GJM. The effect of torso inhomogeneities on body surface potentials quantified by using tailored geometry. *J Electrocardiol*. 1989;22:53-72.
24. Gulrajani RM, Mailloux GE. A simulation study of the effects of torso inhomogeneities on electrocardiographic potentials, using realistic heart and torso models. *Circulation Research*. 1983;52:45-56.
25. Huiskamp G, Van Oosterom A. The depolarization sequence of the human heart surface computed from measured body surface potentials. *IEEE Trans Biomed Eng*. 1988;35(12):1047-58.
26. van Dam PM, Gordon JP, Laks MM, Boyle NG. Development of new anatomy reconstruction software to localize cardiac isochrones to the cardiac surface from the 12 lead ECG. *J Electrocardiol*. 2015;48(6):959-65.
27. van Dam PM, Oostendorp TF, van Oosterom A. Application of the fastest route algorithm in the interactive simula-

- tion of the effect of local ischemia on the ECG. *Med Biol Eng Comput.* 2009;47(1):11-20.
28. De Bakker JM, Janse MJ, Van Capelle FJ, Durrer D. Endocardial mapping by simultaneous recording of endocardial electrograms during cardiac surgery for ventricular aneurysm. *Journal of the American College of Cardiology.* 1983;2(5):947-53.
  29. Klein H, Karp R, Kouchoukos N, Zorn Jr G, James T, Waldo A. Intraoperative electrophysiologic mapping of the ventricles during sinus rhythm in patients with a previous myocardial infarction. Identification of the electrophysiologic substrate of ventricular arrhythmias. *Circulation.* 1982;66(4):847-53.
  30. Prineas RJ, Crow RS, Zhang Z-M. *The Minnesota code manual of electrocardiographic findings*: Springer Science & Business Media; 2009.
  31. Das MK, Zipes DP. Fragmented QRS: a predictor of mortality and sudden cardiac death. *Heart Rhythm.* 2009;6(3):S8-S14.
  32. Cox MG, Nelen MR, Wilde AA, Wiesfeld AC, SMAGT J, Jvd, Loh P, et al. Activation delay and VT parameters in arrhythmogenic right ventricular dysplasia/cardiomyopathy: toward improvement of diagnostic ECG criteria. *J Cardiovasc Electrophysiol.* 2008;19(8):775-81.
  33. Iles LM, Ellims AH, Llewellyn H, Hare JL, Kaye DM, McLean CA, et al. Histological validation of cardiac magnetic resonance analysis of regional and diffuse interstitial myocardial fibrosis. *European Heart Journal-Cardiovascular Imaging.* 2015;16(1):14-22.
  34. Di Marco A, Anguera I, Schmitt M, Klem I, Neilan TG, White JA, et al. Late gadolinium enhancement and the risk for ventricular arrhythmias or sudden death in dilated cardiomyopathy: systematic review and meta-analysis. *JACC: Heart Failure.* 2017;5(1):28-38.
  35. Corrado D, Basso C, Thiene G, McKenna WJ, Davies MJ, Fontaliran F, et al. Spectrum of clinicopathologic manifestations of arrhythmogenic right ventricular cardiomyopathy/dysplasia: a multicenter study. *Journal of the American College of Cardiology.* 1997;30(6):1512-20.
  36. Marcus FI, McKenna WJ, Sherrill D, Basso C, Bauce B, Bluemke DA, et al. Diagnosis of arrhythmogenic right ventricular cardiomyopathy/dysplasia: proposed modification of the task force criteria. *Circulation.* 2010;121(13):1533-41.
  37. Te Riele AS, James CA, Phillips B, Rastegar N, Bhonsale A, Groeneweg JA, et al. Mutation-positive arrhythmogenic right ventricular dysplasia/cardiomyopathy: the triangle of dysplasia displaced. *J Cardiovasc Electrophysiol.* 2013;24(12):1311-20.
  38. Mast TP, Taha K, Cramer MJ, Lumens J, van der Heijden JF, Bouma BJ, et al. The prognostic value of right ventricular deformation imaging in early arrhythmogenic right ventricular cardiomyopathy. *JACC: Cardiovascular Imaging.* 2019;12(3):446-55.
  39. Yao X, Rushlow DR, Inselman JW, McCoy RG, Thacher TD, Behnken EM, et al. Artificial intelligence-enabled electrocardiograms for identification of patients with low ejection fraction: a pragmatic, randomized clinical trial. *Nat Med.* 2021;27(5):815-9.
  40. Ko W-Y, Siontis KC, Attia ZI, Carter RE, Kapa S, Ommen SR, et al. Detection of hypertrophic cardiomyopathy using a convolutional neural network-enabled electrocardiogram. *Journal of the American College of Cardiology.* 2020;75(7):722-33.
  41. van de Leur RR, Taha K, Bos MN, van der Heijden JF, Gupta D, Cramer MJ, et al. Discovering and visualizing disease-specific electrocardiogram features using deep learning: proof-of-concept in phospholamban gene mutation carriers. *Circ Arrhythm Electrophysiol.* 2021;14(2):e009056.
  42. Galloway CD, Valys AV, Shreibati JB, Treiman DL, Petterson FL, Gundotra VP, et al. Development and validation of a deep-learning model to screen for hyperkalemia from the electrocardiogram. *JAMA cardiology.* 2019;4(5):428-36.
  43. Pilia N, Severi S, Raimann J, Genovesi S, Dössel O, Kotanko P, et al. Quantification and classification of potassium and calcium disorders with the electrocardiogram: What do clinical studies, modeling, and reconstruction tell us? *APL bioengineering.* 2020;4(4):041501.
  44. Attia ZI, Noseworthy PA, Lopez-Jimenez F, Asirvatham SJ, Deshmukh AJ, Gersh BJ, et al. An artificial intelligence-enabled ECG algorithm for the identification of patients with atrial fibrillation during sinus rhythm: a retrospective analysis of outcome prediction. *The Lancet.* 2019;394(10201):861-7.
  45. Nagel C, Luongo G, Azzolin L, Schuler S, Dössel O, Loewe A. Non-Invasive and Quantitative Estimation of Left Atrial Fibrosis Based on P Waves of the 12-Lead ECG—A Large-Scale Computational Study Covering Anatomical Variability. *Journal of Clinical Medicine.* 2021;10(8):1797.





# Part II

## Linking the 12-lead ECG to cardiac anatomy

### **Chapter 6**

Novel CineECG enables anatomical 3D localization and classification of bundle branch blocks

### **Chapter 7**

CineECG: A novel method to image the average activation sequence in the heart from the 12-lead ECG



$\emptyset$

$(x, y) = \int_{S_u}$

$v_2 / c^2$

$v_{cg}$

$v_{cg}$

ind

## Chapter 6

Novel CineECG enables anatomical 3D localization  
and classification of bundle branch blocks

MJ Boonstra, BN Hilderink, ET Locati, FW Asselbergs, P Loh, and PM van Dam.

*EP Europace. 2021 Mar 4;23(23 Suppl 1):i80-i87*

## **Abstract**

Ventricular conduction disorders can induce arrhythmias and impair cardiac function. Bundle branch blocks (BBBs) are diagnosed by 12-lead electrocardiogram (ECG), but discrimination between BBBs and normal tracings can be challenging. CineECG computes the temporo-spatial trajectory of activation waveforms in a 3D heart model from 12-lead ECGs. Recently, in Brugada patients, CineECG has localized the terminal components of ventricular depolarization to right ventricle outflow tract (RVOT), coincident with arrhythmogenic substrate localization detected by epicardial electro-anatomical maps. This abnormality was not found in normal or right BBB (RBBB) patients. This study aimed at exploring whether CineECG can improve the discrimination between left BBB (LBBB)/RBBB, and incomplete RBBB (iRBBB).

We utilized 500 12-lead ECGs from the online Physionet-XL-PTB-Diagnostic ECG Database with a certified ECG diagnosis. The mean temporo-spatial isochrone trajectory was calculated and projected into the anatomical 3D heart model. We established five CineECG classes: 'Normal', 'iRBBB', 'RBBB', 'LBBB', and 'Undetermined', to which each tracing was allocated. We determined the accuracy of CineECG classification with the gold standard diagnosis. A total of 391 ECGs were analysed (9 ECGs were excluded for noise) and 240/266 were correctly classified as 'normal', 14/17 as 'iRBBB', 55/55 as 'RBBB', 51/51 as 'LBBB', and 31 as 'undetermined'. The terminal mean temporal spatial isochrone contained most information about the BBB localization.

CineECG provided the anatomical localization of different BBBs and accurately differentiated between normal, LBBB and RBBB, and iRBBB. CineECG may aid clinical diagnostic work-up, potentially contributing to the difficult discrimination between normal, iRBBB, and Brugada patients.

## Introduction

Normal ventricular activation is mediated through the His-Purkinje system, which rapidly distributes the electrical depolarization wave to the left ventricular (LV) and right ventricular (RV) endocardium.<sup>1-4</sup> The His-bundle system originates at the AV-node and directly divides into several major branches. These major branches divide numerously and terminate in a dense distribution of Purkinje fibres, distributed in a large part of the ventricular endocardium. Conduction defects in one (or more) of these mayor branches regionally delay activation. Ventricular conduction disorders may induce arrhythmias<sup>5</sup> and may impair cardiac function, due to the asynchronous ventricular activation.<sup>6,7</sup> Intra-ventricular conduction disorders are typically referred to as bundle branch blocks (BBBs) and are currently identified using the standard 12-lead electrocardiogram (ECG).

The diagnostic value of the standard 12-lead ECG is limited by the difficulty of linking the ECG data directly to cardiac anatomy. Furthermore, mechanical noise, and inconsistency and variability in electrode positioning may significantly influence recorded ECG waveforms, thereby directly affecting ECG interpretation.<sup>8-10</sup> These factors may contribute to the challenges of the discrimination between BBB and normal tracings. For many decades, the vectorcardiogram (VCG) was thought to overcome these issues as it represents the direction of cardiac activity, either depolarization or repolarization.<sup>11</sup> However, the relation between the VCG and cardiac anatomy remains complex. Therefore, the identification of BBB using the 12-lead ECG remains cumbersome, even for expert ECG-readers.

Complete and incomplete BBB are identified by specific 12-lead ECG waveform characteristics. However, incomplete BBBs may be difficult to detect as the late activated area is relatively small resulting in subtle ECG waveform changes.<sup>12</sup> Moreover, while in the past, incomplete right bundle branch block (iRBBB) and right bundle branch block (RBBB) were typically thought to be benign findings in young adults, more recent studies suggest that they may be associated with severe disease, in both symptomatic and asymptomatic patients.<sup>13</sup> Thus, patients found to have such abnormalities should undergo careful examination to exclude cardiac disease. Furthermore, iRBBB waveform characteristics may resemble non-diagnostic waveform abnormalities detected in patients with suspect Brugada syndrome (BrS), referred to as Type 2 or 3 BrS patterns. Often, even expert cardiologists do not agree on ECG interpretations of BrS patterns, providing inconsistent and discordant diagnostic conclusions.<sup>14</sup> Therefore, the correct identification of iRBBB, is of major clinical relevance.

The CineECG method, computes the mean temporo-spatial isochrone (mTSI) trajectory of ECG waveforms and projects this into a 3D heart model, thereby representing the mean trajectory of the ventricular electrical activation at any time

interval related to ventricular anatomy.<sup>15,16</sup> Recently, in Brugada patients, both with spontaneous or with Ajmaline-induced Type 1 pattern, CineECG has localized the terminal components of ventricular depolarization to the right ventricle outflow tract (RVOT). This localization coincided with the anatomical arrhythmogenic substrate location detected by epicardial potential–duration maps. This abnormality was not found in normal subjects or in RBBB patients. CineECG may be a useful tool to more accurately identify conduction disorders in specific areas of the heart, such as LV, septum, or RV, overcoming the challenges of the standard 12-lead ECG interpretation.

This study aimed at exploring whether abnormalities of the mTSI trajectory computed by CineECG can allow a simple and precise identification of bundle branch conduction defects, thereby providing a more objective and reproducible discrimination between normal, left BBB (LBBB), RBBB, and iRBBB compared with the standard interpretation of the 12-lead ECG.

## Methods

### *CineECG method*

CineECG relates electrical cardiac activity to cardiac anatomy by computing the mTSI trajectory. In summary, the mTSI trajectory is derived from the VCG, computed from 12-lead ECG while taking into account the electrode positions on the thorax. Subsequently, a constant conduction velocity is used to project the location of the mTSI trajectory per time interval inside the heart model (Supplementary material online, Methods).<sup>17</sup> The mTSI trajectory thus describes the mean direction of all simultaneous ventricular electrical activity during the activation and recovery of the heart, where cardiac activation is related to cardiac anatomy (Figure 1).<sup>15,17</sup> In this study, the MRI-based heart/torso anatomical model of a 58-year-old male with standard electrode positions was used in all cases.<sup>17</sup> The mTSI was computed according to the standard CineECG method.<sup>15,17</sup> The origin of the mTSI trajectory is located in the LV septum.<sup>18</sup>

The root mean square (RMS) curve from all recorded ECG leads was used to identify the onset and end of ventricular activation. Two fiducial points are identified: QRS onset (Figure 1, white line) and QRS end (Figure 1, red line). The mTSI trajectories were displayed by the standard four-chamber view, the right and left anterior oblique views (Figure 2).<sup>18</sup> This enables the quantification of the relation between cardiac anatomy and the mTSI. Establishing the relation between the cardiac anatomy and the (terminal) direction of the mTSI, allows depiction of the region of latest activation during depolarization.

Per recording, one template beat was selected and semi-automatically QRS onset and QRS end were determined (Figure 1, left panel). Then, up to eight eligible beats were automatically selected based on similarity of the QRS complex to the template

beat (QRS correlation  $>0.99$  and relative difference  $<0.15$ ). For all selected beats, the mTSI trajectory was computed.

#### *Electrocardiogram data and validation of the database*

A total of 500 ECGs were utilized from the certified classified Physionet XL PTB Diagnostic ECG Database (500 Hz, <https://physionet.org/content/ptb-xl/1.0.1/>, Table 1). To comply with the CineECG data structure, signals were resampled to 1000 Hz using linear interpolation. ECGs were classified as either no conduction disturbances (normal), iRBBB, complete right bundle branch block (RBBB), complete left bundle branch block (LBBB), or other conduction disturbances. ECGs with other conduction disturbances [e.g. left anterior fascicular block (LAFB), left posterior fascicular block (LPFB), unspecified intra-ventricular conduction disturbance (IVCD), or bifascicular blocks] were excluded from analysis.

Due to inconsistencies in the PTB database classification observed prior to the CineECG analysis, two trained experts (B.N.H. and M.J.B.) independently re-evaluated all ECG classifications according to the AHA Guidelines.<sup>19</sup> The classifications of B.N.H. and M.J.B. were combined, inconsistencies identified and consensus was reached from a definitive classification. Compared with the PTB database-classification, a total of 151 ECGs were reclassified. A total of 109 ECGs were excluded from analysis

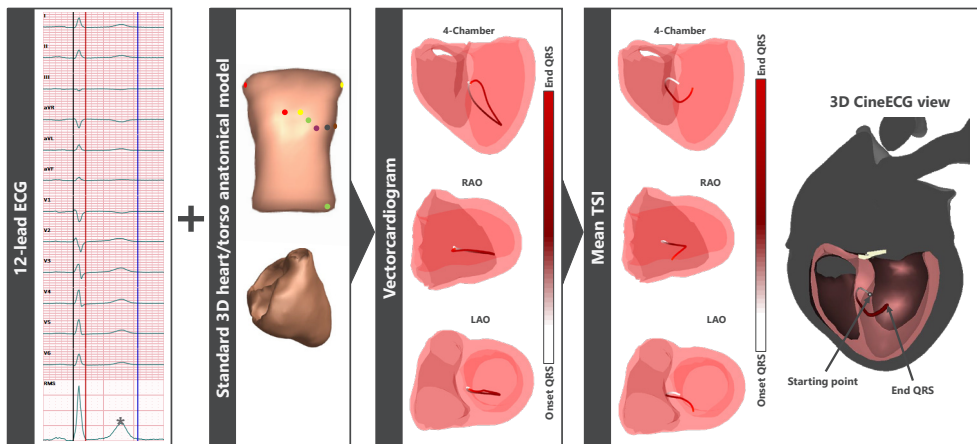


**Figure 1.** The computation of the mean temporal spatial isochrone (mTSI) trajectory. First, the standard 12-lead electrocardiogram (ECG, left box) is used to compute the vectorcardiogram. Subsequently the mTSI locations are computed with starting point at the center of the ventricular mass projected into the LV septum (right box, arrow starting point) by taking into account electrode positions and the anatomical location of the heart. The mTSI trajectory is constructed as the 3D location of activation per millisecond moving with a velocity of 0.7 m/s. The QRS complex is segmented using the white and red line. These colors correspond to the colors in the vectorcardiogram and mTSI trajectory, which is displayed in two-dimensional view and three-dimensional view (3D CineECG view). Trajectories are either displayed in the four-chamber view (4-chamber), the left anterior oblique view (LAO), the right anterior oblique view (RAO) or the anterior posterior view (AP).

as those were classified as either noise, LAFB, LPFB, IVCD, or bifascicular blocks. The definitive classification was used as gold standard.

#### *CineECG parameters*

For all 2993 beats from the included 391 ECGs, the following CineECG parameters were computed to describe the mTSI trajectory:

#### Three-dimensional area

The 3D mTSI area is defined as the area encapsulated by the mTSI trajectory. The QRS area is defined as the area under the X, Y, and Z leads which are used to compute the VCG.<sup>20</sup>

#### Mean temporal spatial isochrone location

For each mTSI 1 ms time interval, the mTSI location is determined; e.g. inside the septum, the LV, or the RV. The initial (first 25 ms), average, and terminal (last 25 ms) locations of the mTSI are determined. Each time interval location is labelled to one of the designated areas and displayed as the ratio per area class. During normal activation, a trans-septal activation wavefront is expected to be present as activation is first initiated at the LV septum and then moves towards the RV. If the initial trajectory is located >10ms inside the septum, a trans-septal initial vector is classified as present.

#### Mean temporal spatial isochrone direction

The main direction is identified as the ratio of activation directed from anterior to posterior, right to left, or apex to base with respect to the cardiac anatomy, different from the traditional azimuth, and elevation known from VCG analysis which are referenced to the thorax. This ratio is calculated by determining per time interval the direction of the mTSI trajectory. A positive direction indicates movement towards the posterior, left, or basal area, respectively. A value of zero indicates no movement towards the denoted area. The more positive or negative the value; the more the mTSI trajectory moves towards, respectively, away from the area. The initial (first 25 ms), average and terminal (last 25 ms) mTSI trajectory direction was determined.

#### Trans-cardiac ratio

The trans-cardiac ratio (TCR) is the ratio of the 3D distance between the location of QRS onset and QRS end and heart-model size.<sup>16</sup> The minimal TCR is the ratio of the 3D distance between the location of QRS onset and the closest point of the mTSI trajectory to the onset after 60% of the QRS duration and heart-model size.

#### Heart axis

A frontal and transversal heart axis were defined by calculating the angle between the left to right axis and a predefined location in the mTSI trajectory. An initial (25 ms),



average, and terminal (QRS end) location in the mTSI trajectory were computed.

### *CineECG classification*

Relevant CineECG parameter and cut-offs were identified using scatter plots, where the relevant parameter (y-axis) was scattered against QRS duration (x-axis). Based on this analysis and a previous study, all beats were classified using the CineECG parameters using the following criteria<sup>17</sup>:

1. Normal: QRS duration < 110 ms, TCR 2–40%, terminal-mTSI location RV < 50%, and the terminal transversal heart axis between  $-100^\circ$  and  $150^\circ$ .
2. RBBB: QRS duration  $\geq 120$  ms, TCR > 8%, terminal-mTSI location RV, or septum > 0. Terminal transversal heart axis  $< -50^\circ$  or  $> 50^\circ$ .
3. iRBBB QRS duration  $\geq 100$  and < 120 ms, minimal TCR < 15%, mTSI location in RV. Terminal transversal heart axis  $< -75^\circ$  or  $> 75^\circ$ .
4. LBBB: QRS duration  $\geq 120$  ms, TCR > 35%, average transversal HA terminal QRS between 0 and 100, complete mTSI location >70% inside the LV.
5. Undetermined: any other value for the above-mentioned CineECG parameters.

If in a given ECG, different beats were allocated to different CineECG classes, the final CineECG class of the complete ECG was determined by identifying the most frequently assigned CineECG class over all considered beats.

### *Statistical analysis*

All statistical analysis was performed using MATLAB (2017a). The percentage of correctly classified ECGs was determined as well as sensitivity, specificity, negative predictive value, positive predictive value, accuracy, and F1-score were determined per subgroup. Baseline characteristics were tested for statistically significant difference using one-way ANOVA or Chi-squared tests for continuous, respectively, categorical variables. A value of  $P < 0.05$  was considered statistically significant.

## **Results**

The clinical, ECG, and CineECG characteristics of the 391 cases grouped by their clinical diagnosis are provided in Table 1. As can be observed, the age between clinical groups differed significantly ( $P < 0.0001$ ). Furthermore, all CineECG-derived parameters differed significantly per group ( $P < 0.0001$ ).

### *Mean temporal spatial isochrone trajectory by each clinical group*

The average mTSI trajectories from all 2993 beats per clinical group are shown in Figure 2. Per time interval, the average mTSI location was computed (Figure 2, solid red line) and the standard deviation was calculated as the mean 3D distance between the average mTSI trajectory and individual mTSI trajectories (Figure 2, grey tubular envelope). A clear distinction between normal, RBBB, and LBBB activation

**Table 1.** The clinical, electrocardiographic and CineECG characteristics of the 391 cases grouped by their clinical diagnosis.

Clinical characteristics	Normal	iRBBB	RBBB	LBBB	p-value
Cases (n)	266	17	55	51	
Beats (n)	2065	126	409	393	
Age (years)	47±19	47±20	69±14	74±9	<0.0001
Gender (% male)	54%	35%	42%	59%	0.132
CineECG characteristics					
QRS duration (ms)	87±10	108±5	141±13	144±14	<0.0001
QT duration (ms)	395 ±34	411 ±42	439 ±58	431±54	<0.0001
TCR (%)	21 ±9	18 ± 8	41 ± 9	48 ± 4	<0.0001
Minimal TCR (%)	18 ± 10	11 ± 9	21 ± 15	48 ± 4	<0.0001
Transseptal vector present (%)	95	97	87	47	<0.0001
Angle transseptal initial vector (°)	129±28	134±23	123±30	82±37	<0.0001

Values are displayed as mean ± standard deviation, a p-value <0.05 was considered statistically significant. Abbreviations: iRBBB = incomplete right bundle branch block, RBBB = right bundle branch block, LBBB = left bundle branch block, QRS = QRS complex, QT = Q-wave to end T-wave, TCR = trans cardiac ratio.

can be observed. In RBBB activation, the initial part of the mTSI is similar to normal activation whereas in LBBB activation the initial trans-septal direction is not present. Differences between iRBBB and normal activation are less pronounced compared with the complete blocks.

#### Normal activation

In the 266 cases defined on the basis of the 12-lead ECG classification as normal, the mTSI trajectory was compact (Figure 2). The initial direction of the mTSI trajectory was mainly trans-septal, crossing the septal wall from left to right (Table 1). Thereafter, the main direction was towards the middle/basal area of the LV-free wall. Overall, the mTSI of the QRS stayed close to or inside the septum and terminated in the LV.

#### Incomplete bundle branch block activation

In the 17 cases defined as iRBBB, the mTSI trajectory was even more compact compared with the normal mTSI trajectory (Figure 2). The first part of the mTSI trajectory is similar to the normal mTSI trajectory. After the initial trans-septal movement, the

**Table 2.** The overall performance of the CineECG classification scheme for the classification of ECGs.

CineECG characteristics	Normal	iRBBB	RBBB	LBBB
Sensitivity	90.2	82.4	100	100
Specificity	99.2	96.5	100	100
Negative predictive value	82.4	99.2	100	100
Positive predictive value	99.6	51.9	100	100
Accuracy	94.7	63.6	100	100
F1-score	93.1	95.9	100	100

Values are displayed as percentages. Ranges of confidence intervals were equal to the mean presented in this table. Abbreviations: iRBBB = incomplete right bundle branch block, RBBB = right bundle branch block, LBBB = left bundle branch block.

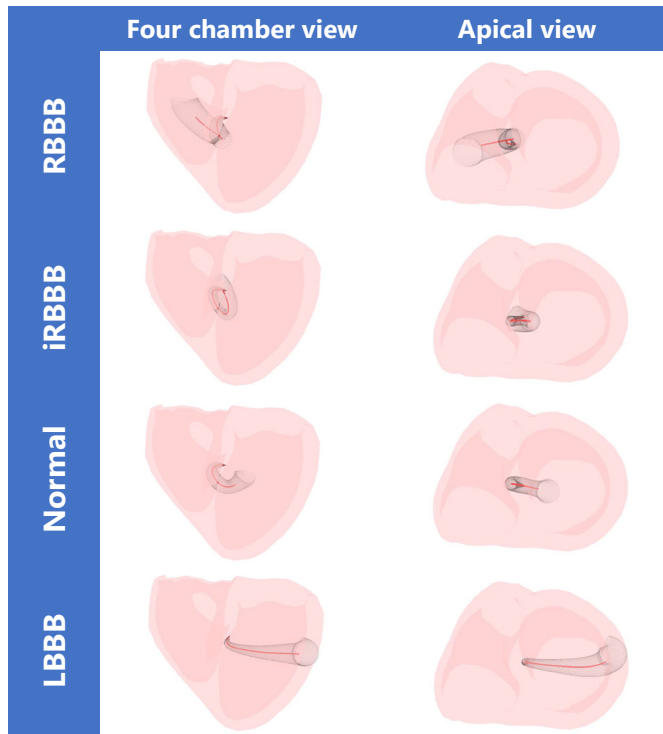


**Figure 2.** The average CineECG mTSI trajectories according to ECG diagnosis. For all four groups: normal, incomplete right bundle branch block (iRBBB), right bundle branch block (RBBB) and left bundle branch block (LBBB), mTSI trajectories are displayed in the four-chamber view (left column) and apical view (right column). The standard deviation around the average mTSI trajectory is indicated by the black tubular envelope and the mean mTSI direction is indicated in red.

mTSI starts moving towards the apex and back through the septal wall towards the LV. The terminal part points mostly towards the septal wall, indicating late activation in the RV. This compactness was reflected in a lower TCR and minimal TCR and the mTSI location was high for the septum.

#### *Right bundle branch block activation*

In the 55 cases defined as RBBB, the mTSI trajectory differed from the normal mTSI trajectory in its terminal QRS direction which was directed towards the right basal area (Figure 2), reflecting late ventricular activation in this region. Compared with normal TCR, the TCR was increased and increased mTSI location inside the RV was observed. The trans-septal vector was less present compared with normal and iRBBB mTSI trajectories (Table 1).

#### *Left bundle branch block activation*

In the majority of the 51 cases defined as LBBB, a trans-septal vector was absent in the mTSI trajectory. In these subjects, the mTSI moved from the LV septal wall

towards the LV-free wall, which was reflected in the mTSI location. The terminal mTSI of the QRS was directed to the LV-free wall (b), with a large TCR (Table 1), the mTSI was never located in the RV, and a trans-septal vector was less present (Table 1).

#### *CineECG classification output*

All 2993 beats (from 391 ECGs) were classified according to the CineECG criteria as either 'normal', 'iRBBB', 'RBBB', 'LBBB', or 'undetermined', and these classifications were used to determine the definitive CineECG class per ECG. Two-dimensional scatterplots were used to determine the relevancy and cut-off values per CineECG parameter (Figure 3A). In 41 ECGs, beats of one ECG were assigned to two or more CineECG classes, either to the 'normal', 'iRBBB', or 'undetermined' group and thereof 27 ECGs were classified correctly. Table 2 shows the detailed diagnostic performance of the CineECG classification for the different clinical groups. A high performance was obtained for normal, RBBB, and LBBB groups. For iRBBB activation, sensitivity was lower compared with the other groups. For RBBB and LBBB groups, the CineECG classification and the clinical diagnosis were always coincident (Figure 3B). Vice versa, less consistency between CineECG and clinical diagnosis was observed in discriminating between iRBBB from normal, especially in beats with a QRS duration between 100 and 110 ms.

## **Discussion**

This is the first study utilizing CineECG to characterize ventricular activation defects and classify BBB by using 3D anatomical characteristics of the mTSI trajectory. Using CineECG criteria, all RBBB and LBBB tracings, and most IRBB and normal tracings, were classified correctly in accordance with standard 12-lead clinical classification. CineECG provides an easy-to-use tool to obtain a comprehensive insight into the relation between ventricular activation and anatomy and is therefore helpful for clinicians to accurately discriminate between different conduction disorders. However, between iRBBB and normal activation, overlap exists between the clinical groups, particularly between 100 and 120ms QRS duration. A clear distinction between the types of blocks can be visually observed in the average mTSI trajectories (Figure 2). The terminal vector of the mTSI trajectory points towards the area of latest activation, thereby indicating the location of the block. However, the differentiation between an iRBBB and a normal pattern remains challenging and requires further optimization.

#### *The relation between mean temporal spatial isochrone and bundle branch block location*

The average mTSI trajectories observed in this study, clearly show distinct patterns for different types of BBB (Figure 2). For the complete BBB, a clearly deviating pattern from the normal can be observed. While in LBBB activation patterns, the mTSI trajectory mainly moves leftwards and inside the LV cavity, in RBBB activation patterns, the mTSI trajectory initially moves towards the LV cavity whereafter it

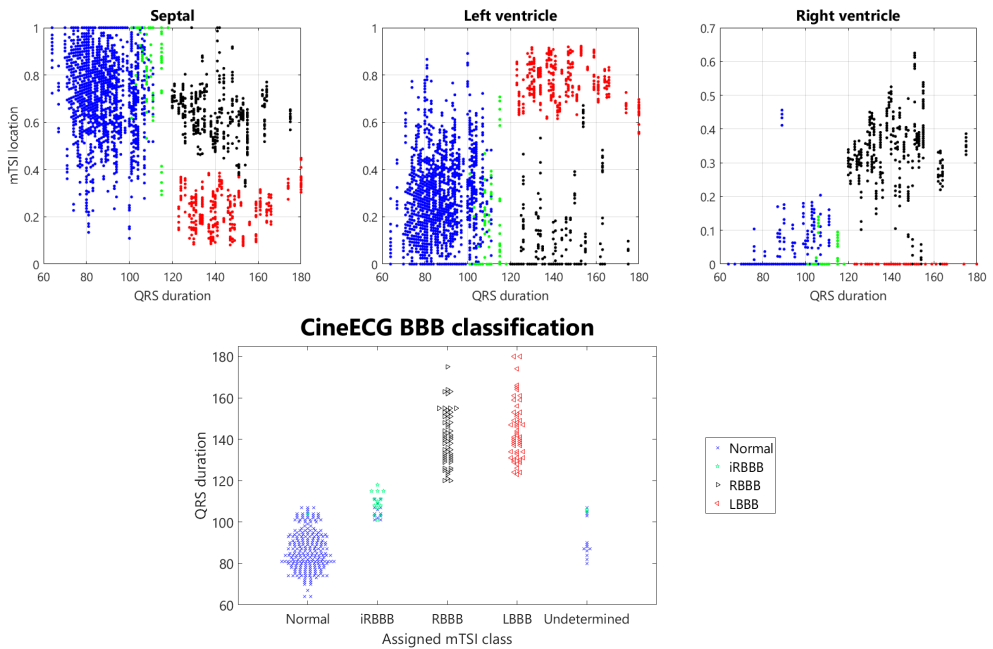


**Figure 3. A:** Setting the CineECG BBB classification criteria. A representative example of a two-dimensional scatterplot of all selected beats where the mTSI location parameter is scattered against QRS duration (x-axis). The dots in all plots designate measured mTSI location per beat plotted as a function of QRS duration, classified as either normal (blue), incomplete right bundle branch block (iRBBB, green), right bundle branch block (RBBB, black) or left bundle branch block (LBBB, red). As can be observed for LBBB, the mTSI location is most of the time located inside the left ventricular cavity and never in the right ventricular cavity, whereas for RBBB it is mainly located inside the right ventricular cavity. Such two-dimensional scatterplots were used to identify the relevancy and cut-off values of CineECG parameters. Mentioned CineECG criteria were set by a combination of data obtained in a previous study 17 and observations made in the current study. **B:** CineECG BBB Classification. The beat adjudication according to the CineECG criteria (x-axis) against QRS duration (y-axis) to show overlap between QRS duration but were assignment to a different group. Colors of the dots indicate the clinical group. The dots in all plots indicate measured values per beat plotted as a function of QRS duration, diagnosed as either normal (blue), right bundle branch block (iRBBB, black), incomplete RBBB (green) or left bundle branch block (LBBB, red).

moves towards the RV basal area (Figure 2). Thus, while the mTSI trajectory of LBBB solely moves leftwards, the mTSI trajectory for RBBB starts leftwards, and then goes rightwards. This may be explained by the larger amount of LV myocardial mass, with respect to the RV myocardial mass, and thus LV activation is likely to conceal activation occurring in the RV. Since CineECG takes cardiac anatomy into account, mTSI trajectories might be viewed as a more reliable alternative to identifying BBB than the current ECG strict criteria for LBBB and RBBB, also considering inter-individual age and gender variation.<sup>6,12</sup>

#### *Clinical classification of incomplete right bundle branch block*

QRS duration is one of the main clinical characteristics to differentiate between normal, incomplete, and complete RBBB. An iRBBB is identified when QRS-duration ranges

between 110 and 120 ms, but may be wrongly classified in cases of incorrect manual or machine interpretation of the 12-lead ECG, further magnified due to inter-lead QRS duration differences. Therefore, a coherent way to measure the QRS duration is of utmost importance in order to correctly differentiate between normal and iRBBB activation. CineECG is likely to overcome these difficulties. In case of iRBBB, the mTSI trajectory is compact and stays within the septum and clearly differs from both normal and RBBB activation (Figure 2). Thus, (i) the temporo-spatial location of the mTSI trajectory contains all information about the direction and timing of ventricular depolarization and (ii) the mTSI terminal direction indicates the anatomical location of the block, by pointing towards the latest site of activation. With increasing QRS duration in iRBBB cases, a clear shift of the terminal mTSI direction towards the RV base was observed, becoming more similar to the RBBB mTSI trajectory (Figure 2).

#### *Comparison with standard 12-lead electrocardiogram assessment*

In this study, we validated our CineECG method with the clinical 12-lead ECG assessment. However, ultimately, the comparison of CineECG classification with standard 12-lead ECG clinical assessment through invasive electro-anatomical activation mapping should be performed. Through invasive mapping, the true location of the BBB may be identified and the ability of CineECG and standard clinical 12-lead to identify these BBBs correctly can then be assessed.

#### *Starting point mean temporal spatial isochrone trajectory*

In CineECG, the starting point of the mTSI trajectory was set at the left side of the septal wall closest to the ventricular centre of mass. During normal activation, a trans-septal wavefront of activation moves from the LV side of the septum towards the right. However, in LBBB cases the trans-septal vector is reversed and thus classified as not present in 53% (Table 1). Therefore, this starting point may inadequately represent the true start of LBBB activation, as such activation starts at the RV septum or RV-free wall. Furthermore, due to intra-individual differences in bundle branch anatomy, this starting point may inadequately represent the true starting point of ventricular activation. The starting point therefore serves as a general starting point, but as shown in this study, CineECG provides an accurate concise way to assess average ventricular activation related into cardiac anatomy, where the starting point does not yet seem to be a constraint for the CineECG classification.

#### *Limitations*

The use of a standardized heart torso model, rather than a personalized model, may limit the accuracy of the presented results. The use of the standard torso/heart model enables the direct projection of the mTSI to the cardiac anatomy, but differences in heart anatomy and orientation, thorax anatomy and lead position are not accounted for. With age, the shape, position, and orientation of the heart in the torso may change. In this study, we used a standard anatomical heart/torso model based on

a 58-year-old male, which may adequately represent adult RBBB and LBBB male cases (Table 1) but may be inadequate for the younger iRBBB and normal cases and more generally, for female cases. Using a standardized heart/torso model may result in a larger CineECG parameter variation, caused by intra-individual variation in cardiac anatomy. Thus, the distribution of mTSI-derived parameters per BBB group encompass larger standard deviations as activation is referenced to a cardiac anatomy with an incorrect size, shape, and/or orientation, also relative to the thoracic model and electrode locations. Therefore, using a 3D camera to localize the ECG electrodes and the torso dimensions might increase the accuracy of our method.<sup>21-23</sup> These factors may be particularly relevant for the more accurate identification of iRBBB.

In PTB database, the number of IRBB cases was very small. Besides, we found some inconsistencies in the PTB database classification, particularly regarding iRBBB cases. Therefore, we revised all the included ECG and upon agreement of two independent experts, we came to a definitive classification of the PTB tracings which we used for the statistical analysis. Given the clinical relevance of analysis of the late depolarization signals, we plan to perform a prospective study studying CineECG characteristics of patients with different intra-ventricular conduction disorders.

#### *Future perspectives*

Ambiguity in the standard 12-lead ECG classification can be caused by the presence of intra-individual differences in cardiac anatomy (size, shape), cardiac orientation (due to age, effects of breathing, thoracic shape), bundle branch anatomy, the presence of cardiac disease (scar, myocarditis, fibrofatty tissue), and inconsistency in the placement of electrodes relative to the heart. All these factors may contribute to determine the ECG waveform morphology and 12-lead ECG diagnostic criteria of BBB may be present in the 12-lead ECG in the absence of a true BBB. Through CineECG, a more comprehensive view is given on the cardiac electrical activity using the 12-lead ECG, thereby providing a tool less prone to intra-individual characteristics. Further testing and optimization of this technique are still required. For example, the effect of the presence of scar or ischaemia, or more generally myocardial structural diseases, should be assessed in future studies. Furthermore, the ability of CineECG to correctly discriminate between iRBBB, RBBB, LBBB, unspecified intra-ventricular conduction disorders and left anterior and posterior hemiblocks, or even the coexistence of these conduction disturbances should be assessed.

## **Conclusions**

The advanced interpretation of the 12-lead ECG through the CineECG method proved to be a robust technique to differentiate between different intra-ventricular bundle branch conduction defects. The mTSI trajectory relates cardiac activation to cardiac anatomy, thereby directly identifying the anatomical location of the BBB, mostly indicated by the terminal part of the mTSI trajectory. The CineECG classification

was able to accurately discriminate between normal, RBBB, and LBBB cases. Further optimization of the classification algorithm may enhance the CineECG classification of iRBBB. The CineECG method, directly derived from 12-lead ECG, can be viewed as a non-invasive mapping tool and may improve the early recognition and the monitoring of the progression of intra-ventricular bundle branch conduction defects.

*Acknowledgements*

We would like to thank Judith van Oosterom for her proof reading of our manuscript. This work was supported by the Netherlands Cardiovascular Research Initiative, an initiative with support of the Dutch Heart Foundation (grant number QRS-Vision 2018B007). This paper is part of a supplement supported by an unrestricted grant from the Theo-Rossi di Montelera (TRM) foundation.

*Supplementary material*

Supplementary methods – CineECG methods available at: [https://academic.oup.com/europace/article/23/Supplement\\_1/i80/6158557#229816140](https://academic.oup.com/europace/article/23/Supplement_1/i80/6158557#229816140)



## References

1. Tawara S. Das Reizleitungssystem des Säugetierherzens. Eine Anatomisch-Histologische Studie über das Atrioventrikulärbündel und die Purkinjeschen Fäden. Jena: Gustav Fischer; 1906.
2. Tawara S. Die Topographie und Histologie der Brückenfasern. Ein Beitrag zur Lehre von der Bedeutung der Purkinjeschen fäden. Zentralb Physiol 1906;19:70–76.
3. Demoulin J and Kulbertus H. Histopathological examination of concept of left hemiblock. *British Heart Journal*. 1972;34:807.
4. Oosthoek PW, Viragh S, Lamers WH and Moorman AF. Immunohistochemical delineation of the conduction system. II: The atrioventricular node and Purkinje fibers. *Circulation Research*. 1993;73:482–491.
5. Kusumoto FM, Schoenfeld MH, Barrett C, Edgerton JR, Ellenbogen KA, Gold MR, Goldschlager NF, Hamilton RM, Joglar JA, Kim RJ, Lee R, Marine JE, McLeod CJ, Oken KR, Patton KK, Pellegrini CN, Selzman KA, Thompson A and Varosy PD. 2018 ACC/AHA/HRS Guideline on the Evaluation and Management of Patients With Bradycardia and Cardiac Conduction Delay: A Report of the American College of Cardiology/American Heart Association Task Force on Clinical Practice Guidelines and the Heart Rhythm Society. *Circulation*. 2019;140:e382–e482.
6. Strauss DG, Selvester RH and Wagner GS. Defining left bundle branch block in the era of cardiac resynchronization therapy. *Am J Cardiol*. 2011;107:927–34.
7. Vassallo JA, Cassidy DM, Marchlinski FE, Buxton AE, Waxman HL, Doherty JU and Josephson ME. Endocardial activation of left bundle branch block. *Circulation*. 1984;69:914–23.
8. Drew BJ and Adams MG. Clinical consequences of ST-segment changes caused by body position mimicking transient myocardial ischemia: hazards of ST-segment monitoring? *J Electrocardiol*. 2001;34:261–4.
9. Macfarlane PW, Colaco R, Stevens K, Reay P, Beckett C and Aitchison T. Precordial electrode placement in women. *Neth Heart J*. 2003;11:118–122.
10. Bond RR, Finlay DD, Nugent CD, Breen C, Guldenring D and Daly MJ. The effects of electrode misplacement on clinicians; interpretation of the standard 12-lead electrocardiogram. *European Journal of Internal Medicine*. 2012;23:610–615.
11. Frank E. General Theory of Heart-Vector Projection. *Circulation Research*. 1954;2:258–270.
12. Galeotti L, van Dam PM, Loring Z, Chan D and Strauss DG. Evaluating strict and conventional left bundle branch block criteria using electrocardiographic simulations. *Europace*. 2013;15:1816–21.
13. Nasir JM, Shah A and Jones S. THE SIGNIFICANCE OF INCOMPLETE AND COMPLETE RIGHT BUNDLE BRANCH BLOCKS IN YOUNG ADULTS. *Journal of the American College of Cardiology*. 2012;59:E1939.
14. Chevallier S, Forclaz A, Tenkorang J, Ahmad Y, Faouzi M, Graf D, Schlaepfer J and Pruvot E. New Electrocardiographic Criteria for Discriminating Between Brugada Types 2 and 3 Patterns and Incomplete Right Bundle Branch Block. *Journal of the American College of Cardiology*. 2011;58:2290–2298.
15. van Dam PM. A new anatomical view on the vector cardiogram: The mean temporal-spatial isochrones. *J Electrocardiol*. 2017;50:732–738.
16. Roudijk R, Loh KP and van Dam PM. Mean Temporal Spatial Isochrones Direction as Marker for Activation Delay in Patients with Arrhythmogenic Cardiomyopathy. *Computing in Cardiology*. 2018;45:1–4.
17. van Dam PM, Locati ET, Ciconte G, Borrelli V, Heilbron F, Santinelli V, Vicedomini G, Monasky MM, Micaglio E and Giannelli L. Novel CineECG Derived from Standard 12-Lead ECG Enables Right Ventricle Outflow Tract Localization of Electrical Substrate in Patients with Brugada Syndrome. *Circulation: Arrhythmia and Electrophysiology*. 2020;13:e008524.
18. Durrer D, van Dam RT, Freud GE, Janse MJ, Meijler FL and Arzbacher RC. Total excitation of the isolated human heart. *Circulation*. 1970;41:899–912.
19. Surawicz B, Childers R, Deal BJ and Gettes LS. AHA/ACC/HRS Recommendations for the Standardization and Interpretation of the Electrocardiogram: Part III: Intraventricular Conduction Disturbances: A Scientific Statement From the American Heart Association Electrocardiography and Arrhythmias Committee, Council on Clinical Cardiology; the American College of Cardiology Foundation; and the Heart Rhythm Society: Endorsed by the International Society for Computerized Electrocardiology. *Circulation*. 2009;119:e235–e240.
20. Kors JA, van Herpen G, Sittig AC and van Bommel JH. Reconstruction of the Frank vectorcardiogram from standard electrographic leads: diagnostic comparison of different methods. *Eur Heart J*. 1990;11:1083–1092.
21. van Stipdonk AM, Ter Horst I, Kloosterman M, Engels EB, Rienstra M, Crijns HJ, Vos MA, van Gelder IC, Prinzen FW and Meine M. QRS area is a strong determinant of outcome in cardiac resynchronization therapy. *Circulation: Arrhythmia and Electrophysiology*. 2018;11:e006497.
22. van Dam PM, Gordon JP and Laks M. Sensitivity of CIPS-computed PVC location to measurement errors in ECG electrode position: the need for the 3D camera. *J Electrocardiol*. 2014;47:788–93.
23. Alioui S, Kastelein M, EM vD and PM vD. Automatic Registration of 3D Camera Recording to Model for Leads Localization. *Computing in Cardiology*. 2017;44:4.
24. van Dam PM, Boyle NG, Laks MM and Tung R. Localization of premature ventricular contractions from the papillary muscles using the standard 12-lead electrocardiogram: a feasibility study using a novel cardiac isochrone positioning system. *Europace*. 2016;18:iv16–iv22.



$\emptyset$

$(x, y) = \int_{S_u}$

$v_2 / c^2$

$v_{cg}$

$v_{cg}$

ind

# Chapter 7

CineECG: A novel method to image the average activation sequence in the heart from the 12-lead ECG

MJ Boonstra, DH Brooks, P Loh, and PM van Dam.

*Computers in Biology and Medicine.* 2022 Feb; 141:105128

## Abstract

The standard 12-lead electrocardiogram (ECG) is a diagnostic tool to assess cardiac electrical activity. The vectorcardiogram is a related tool that represents that activity as the direction of a vector. In this work we investigate CineECG, a new 12-lead ECG based analysis method designed to directly estimate the average cardiac anatomical location of activation over time.

We describe CineECG calculation and a novel comparison parameter, the average isochrone position (AIP). In a model study, fourteen different activation sequences were simulated and corresponding 12-lead ECGs were computed. The CineECG was compared to AIP in terms of location and direction. In addition, 67-lead body surface potential maps from ten patients were used to study the sensitivity of CineECG to electrode mispositioning and anatomical model selection. Epicardial activation maps from four patients were used for further evaluation.

The average distance between CineECG and AIP across the fourteen sequences was  $23.7 \pm 2.4$  mm, with significantly better agreement in the terminal ( $27.3 \pm 5.7$  mm) versus the initial QRS segment ( $34.2 \pm 6.1$  mm). Up to four cm variation in electrode positioning produced an average distance of  $6.5 \pm 4.5$  mm between CineECG trajectories, while substituting a generic heart/torso model for a patient-specific one produced an average difference of  $6.1 \pm 4.8$  mm. Dominant epicardial activation map features were recovered.

Qualitatively, CineECG captured significant features of activation sequences and was robust to electrode misplacement. CineECG provides a realistic representation of the average cardiac activation in normal and diseased hearts. Especially the terminal segment of the CineECG might be useful to detect pathology.

## Introduction

The 12-lead ECG is one of the fundamental diagnostic tools in clinical practice to gain insight into cardiovascular abnormalities and arrhythmias. However, the interpretation of the ECG requires training and clinical expertise and is subject to considerable inter- and intra-clinician variability.<sup>1-3</sup> Additionally, the diagnostic value of the standard 12-lead ECG is limited by the difficulty of linking it directly to cardiac anatomy. The 12-lead ECG is also susceptible to human errors such as variability in electrode positioning<sup>4-6</sup>, which can significantly affect recorded ECG waveforms and consequently their interpretation by a clinician.<sup>2,7-9</sup> The clinical vectorcardiogram (VCG) was introduced as an approach to overcome this problem.<sup>10</sup> Furthermore, standard ECG-derived characteristics (e.g. QRS duration, axis or morphology) may indicate pathology give only a crude description of the global activation pattern, leaving out the temporo-spatial movement of cardiac activation.<sup>11,12</sup> In the VCG, the magnitude and direction of cardiac electrical activity are represented by a vector which changes in magnitude and angle rotating around a fixed location thereby giving a simple 3D representation of the cardiac electrical activity related to the thorax. However, in clinical use the VCG is difficult to relate to cardiac anatomy since it requires 3D rotation of the VCG from torso to heart axis. Moreover, the VCG still suffers from the large differences in amplitude, and remains sensitive to electrode positioning.<sup>13,14</sup> In particular, the fact that the origin of the VCG vector is assumed to be constant limits its ability to adequately describe the temporo-spatial anatomical patterns of cardiac activation, as well as the changes in those activation patterns due to localized tissue and conduction defects. Other approaches that explain cardiac activation through the reconstruction of a single moving dipole have showed promising results in the localization of the origin of ventricular tachycardias, but these methods required the use of a larger number of ECG electrodes<sup>15-17</sup> or have not yet been tested in normal ventricular activation<sup>18,19</sup>. In this study we investigate a novel approach by adding cardiac anatomy-based temporo-spatial variation to the computation of the VCG vector. We call this approach CineECG, in analogy to CineMRI.

CineECG attempts to image key temporo-spatial features of the activation sequence that are difficult to obtain reliably from direct ECG or VCG interpretation by employing a simplified anatomical model and a vector direction-oriented approach.<sup>20-22</sup> One approach towards obtaining temporo-spatial information from body surface potentials that has recently gained increasing attention is ECG Imaging (ECGI), including the dipole-based methods mentioned previously. ECGI generally solves some version of the inverse problem of electrocardiography to non-invasively reconstruct a complete characterization of cardiac electrical activity from body surface potential measurements. However, ECGI techniques require the acquisition of many more than 12 leads, are expensive and time-consuming, and again are sensitive to errors in electrode positions. With CineECG, a lightweight and less complex alternative to ECGI is provided as 1) the additional physical burden

on electrode number and placement is minimized and 2) the use of sophisticated and computationally expensive numerical techniques is not required. Specifically, CineECG is designed to estimate the ‘average position’ of cardiac activity<sup>1</sup> at each time instant at which the ECG is sampled, directly coupled to cardiac anatomy, from standard clinical 12-lead ECGs.<sup>22,23</sup> In previous studies, starting in 2017, we reported on a preliminary version of CineECG, which we called the mean Temporo-Spatial-Isochrone or mean-TSI trajectory. In these earlier studies, CineECG was shown to be a robust technique to detect substrates in Brugada Type-I patients<sup>20</sup> and to differentiate between different intraventricular bundle branch blocks<sup>21</sup> and the ‘normal’ CineECG was determined<sup>24</sup>.

However, a thorough methodological study and conceptual validation of the CineECG method has not yet been carried out. In this paper, we study both the accuracy of CineECG and its sensitivity to both electrode placement and to inaccuracy in the anatomical model when it is applied to a wide variety of cases of sinus rhythm. For this purpose, we used both simulated data and data from a cohort of patients obtained in a clinical setting. In our simulation study we take advantage of the known ground truth to study the relationship between cardiac isochrones and CineECG. To characterize an “average position of cardiac electrical activity” even when there are multiple wavefronts in sinus rhythm, we developed a measure of the average isochronal position (AIP) of the activation trajectory and compared it to trajectories constructed by CineECG. Using the patient data, we tested the effect on CineECG of electrode positioning variation and of the use of individualized versus standardized anatomical modeling. Additionally, we report on four of those clinical examples where epicardial mapping was available to further illustrate the relationship between CineECG and the recorded maps during sinus rhythm.

## Method

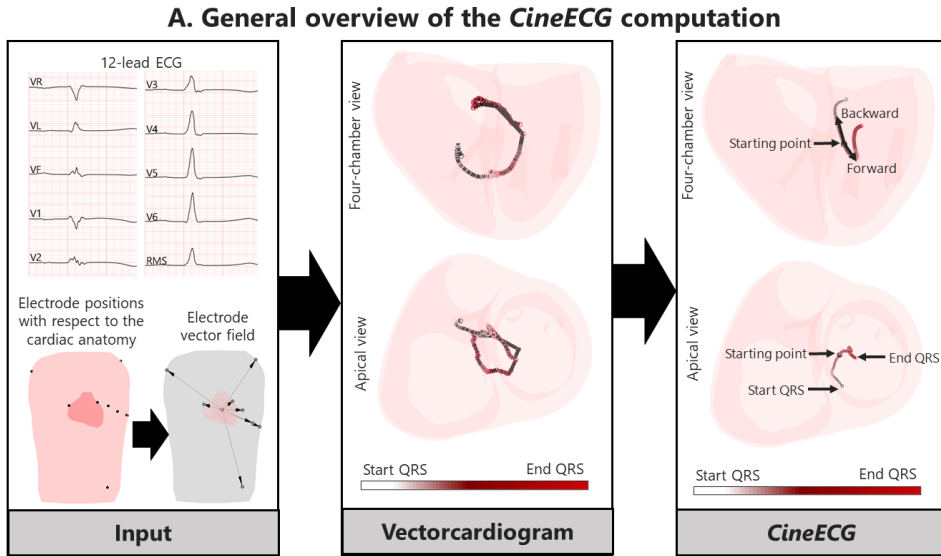
### *The CineECG method*

CineECG uses the 12-lead ECG to estimate the average position of cardiac activation waveforms within an anatomical 3D heart model (Figure 1). To compute the CineECG, three inputs are required: 1) a 3D anatomical heart model, 2) ECG electrode locations on the torso with respect to the heart model, and 3) the standard 12 lead ECG. The anatomical model is typically created using cardiothoracic imaging, either CT-based or MRI-based, onto which the electrode positions are registered<sup>2</sup>. Then the 12-lead ECG is used to compute the CineECG.<sup>20-22, 24</sup>

In short, the CineECG computation starts with an initialization step which specifies a starting point in space and time that is used to start the recursive CineECG calculations

<sup>1</sup> We use the phrase ‘average position of cardiac activation’ to represent the anatomical center of mass of all simultaneously active cardiac cells at a given time (that is, those cells undergoing a change in transmembrane potential at that time).

<sup>2</sup> In contrast to ECGI, we only need an anatomical model to cover the pre-cordial electrodes with respect to the cardiac anatomy



### B. CineECG computation per time interval

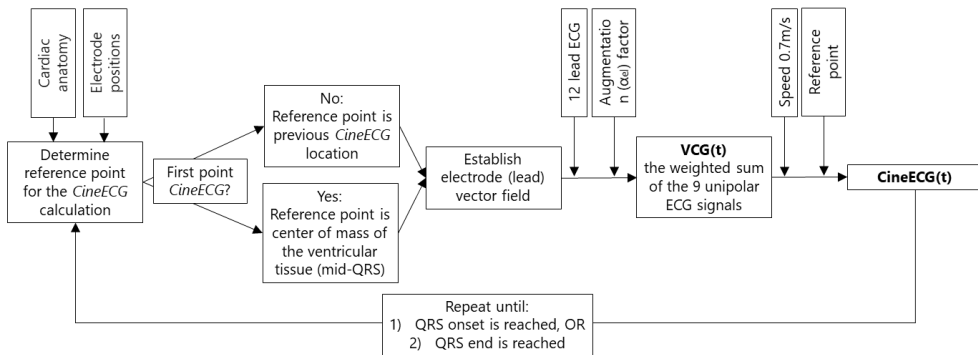


**Figure 1.** Schematic overview of the CineECG calculation in general (Panel A) and per time interval (Panel B). The heart/torso anatomical model, electrode positioning and the 12-lead ECG are the three inputs of the CineECG calculation. The cardiac anatomy and electrode positioning inputs can be either generic or subject specific, the ECG input is always case specific. The CineECG is computed each time sample of one millisecond. Using the electrode vector field (indicated with the arrows in the grey torso), ECG amplitude at the time interval and the augmentation factor ( $a_e$ ), the VCG is computed to determine the direction of the CineECG (Equation 1). Thereafter, the current CineECG location is calculated using a set constant speed of 0.7 m/s from the previous CineECG location in the direction indicated by VCG(t). The CineECG is calculated from mid QRS in a forward and backward fashion. The resulting VCG (A, second panel) and CineECG (A, third panel) are displayed from white (start QRS) to red (end QRS), and in addition the starting point is indicated in the CineECG panel.

(Figure 1). In the original CineECG method, this starting point was chosen in space as the closest point on the left septal wall to the center of mass of the heart and in time at the beginning of the QRS.<sup>20-22</sup> After further empirical consideration by taking cardiac electrophysiology into account, we now set the CineECG starting point spatially to the center of mass of the anatomical 3D heart model itself and temporally at mid-QRS. This change was made based on the assumption that at mid-QRS, half of the ventricular mass is activated and thus the location of the average wavefront at mid-QRS is approximated well by the center of mass, and that generally the largest mass of tissue is activated around this point in time. From that starting point the average cardiac activation position is propagated through the cardiac anatomy with a two-step procedure. In the first step a modified version of the VCG is computed from the 12-lead ECG at a given time sample using the current CineECG location. In the second step the direction of this VCG is used to determine the direction in which the average cardiac activation position will move from that location at a speed determined based on physiological propagation assumptions. The calculation proceeds recursively in this time-step-wise fashion until the entire activation sequence has been localized.

#### *Computation of the CineECG position over time*

To propagate the CineECG, we start the bi-directional recursive computation from the CineECG starting point in both space and time. For simplicity we will describe the computation going in the forward direction in time; the backward computation is essentially the same. At each time instant  $t$  we first compute the average direction of activation at time instance  $t$  (Equation 1, denoted as  $\overline{VCG}(t)$ ) using time-dependent lead vectors which point from the previous (time  $t-1$ ) CineECG location to each of the electrode locations, denoted  $\overline{r}_{el} - \overline{r}_{ref}(t)$ .  $\overline{r}_{el}$  points from the origin to the  $e^{th}$  electrode and  $\overline{r}_{ref}(t)$  points from the origin to the  $(t-1)$  CineECG location. We then normalize each lead vector by its length so that we have a set of nine unit vectors, one for each ECG electrode. The average direction of activation at time  $t$ ,  $\overline{VCG}(t)$  is then calculated as a weighted vector sum of these nine unit-vectors, where the weights are the amplitude of the unipolar ECG signals of the 12-lead ECG along with a scale correction factor  $\alpha_{el}$ :

$$\overline{VCG}(t) = \sum_{el=1}^9 ecg_{el}(t) \alpha_{el} \left( \frac{\overline{r}_{el} - \overline{r}_{ref}(t)}{\|\overline{r}_{el} - \overline{r}_{ref}(t)\|} \right) \quad \text{Equation 1}$$

where  $\alpha_{el}$  is used to account for differences in the distance from the heart to the  $e^{th}$  electrode. In practice, we set the  $e^{th}$  scale factor to 1 for the precordial leads and to 2 for the unaugmented extremity leads (Vr, Vl, and Vf). As a further refinement, we project the unaugmented extremity leads onto the frontal plane by setting the components of those lead vector in the anterior-posterior direction to 0 and only using the frontal (left-right and superior-inferior) components; this modification adds robustness as the anterior-posterior direction is most influenced by whether the extremity leads are placed according to the standard ankle-wrist location or the



adapted emergency Mason-Likar position. In summary,  $\overrightarrow{VCG}(t)$  is a vector sum over unit vectors pointing from the most recent CineECG location to the electrodes, where each unit vector is weighted by the value of the ECG on that electrode along with an additional geometric scale factor. Note that in effect, we assume that a reasonable origin for the ECG amplitudes is represented by an effective electrical center of the heart that changes with time as the activation wavefronts move through the myocardium. In effect we estimate that origin at each time step as  $\overrightarrow{CineECG}(t-1)$  which we then use to compute  $\overrightarrow{VCG}(t)$ .

In the second step of CineECG, starting from the CineECG location at time  $(t-1)$ ,  $\overrightarrow{CineECG}(t)$  is calculated by moving parallel to  $\overrightarrow{VCG}(t)$  at a constant propagation speed. We use  $speed = 0.7$  m/s as the assumed speed to balance the combination of 1) faster longitudinal propagation speed of about 0.85 m/s<sup>25-27</sup>, 2) 0.35 m/s for transmural propagation<sup>26,28</sup>, and 3) a higher speed in regions with a high density of Purkinje-myocardial junctions<sup>27</sup> that results in the sudden activation of regions near where these junctions are located. Writing this out moving in both directions in time we have, for the calculation that moves forward in time:

$$\overrightarrow{CineECG}(t) = \overrightarrow{CineECG}(t-1) + speed \frac{\overrightarrow{VCG}(t)}{\|\overrightarrow{VCG}(t)\|} \quad \text{Equation 2.1}$$

and for the calculation that moves backward in time:

$$\overrightarrow{CineECG}(t) = \overrightarrow{CineECG}(t+1) - speed \frac{\overrightarrow{VCG}(t)}{\|\overrightarrow{VCG}(t)\|} \quad \text{Equation 2.2}$$

Note that the last term in each equation normalizes the length of the directional change to 1, thus assuring that the propagation speed is determined by the chosen value of speed. This procedure is repeated forwards and backwards until all time instants in the QRS complex have been used. A detailed schematic overview of the calculation is displayed in Figure 1B.

#### *Ground truth characterization: Average isochrone position (AIP)*

To compare the CineECG to the simulated activation sequences, where we have full ground truth, we need to characterize the "average location" of all simultaneous activation wavefront isochrones in the heart to provide a direct comparison between cardiac isochrones and the CineECG, since that average location is what CineECG is designed to estimate from the ECG. To the best of our knowledge, this kind of metric over multiple simultaneous activation wavefronts has not been published before. Therefore, we developed a method to calculate an "average isochrone position" (AIP) sequence for cardiac activation. The AIP is based on the average location, per 5 ms interval, of the cardiac tissue activated during that interval. At each such interval, the AIP location is calculated by identifying the coordinates of all nodes with an activation time within the time interval and averaging those node locations, each multiplied by

a weight equal to the wall thickness at that node (Supplement A, slide 2). As a further refinement, the distance between two subsequent AIP locations was restricted to no more than 1.5 times the distance between the previous two AIP locations. This restriction was set to prevent unphysiologically large jumps between subsequent AIP locations which otherwise occurred in some cases when slight imbalances between the progression of activation in the left and right ventricles caused large jumps in the AIP. As a test, the AIP was calculated as described for a simulated case of a premature ventricular beat. In this case (Supplement A, slide 2), the AIP pathway approximated a straight line from the initial site of activation towards the latest site of activation. For more complex activation sequences like sinus rhythm, the AIP trajectory became more compact, as would be expected, reflecting the existence of multiple local wavefronts moving in different directions.

## Experimental methods

### Simulation Study

For the simulation study we calculated 14 His-Purkinje mediated activation sequences; six without, and eight with, a simulated conduction block in the bundle branch system. The fastest route algorithm<sup>29,30</sup> was used to simulate activation sequences with two to six foci located at multiple endocardial locations associated with His-Purkinje mediated ventricular activation<sup>25,31</sup>. Different sets of locations were chosen to simulate cases with (e.g. left or right) and without conduction block (Supplement A, slides 7-20). These calculations were carried out using the ECGsim software package

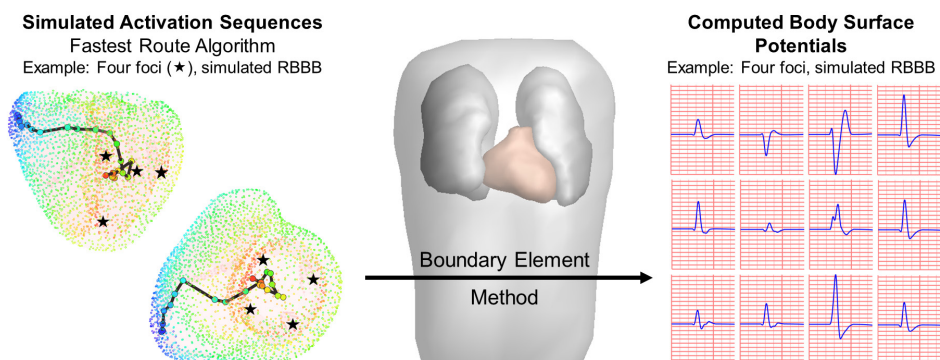


**Figure 2.** Schematic overview of the ECG simulation protocol. The patient specific heart/torso model and simulated activation sequences are used for the 12-lead ECG computation. Activation sequences were simulated by determining several foci (indicated with a ★) at the anatomical heart model where the activation sequence start. Using the fastest route algorithm, a set anisotropy ratio of 2,5 and set conduction velocity of 0.85 m/s, activation sequences were computed. The average isochrone position (AIP) was then calculated from these activation sequence using time intervals of 5 ms. Colors of the AIP trajectory and local activation timings correspond to the same time instance. These results are shown in the left panel, where the heart is shown in two orientations for greater clarity. Using the Boundary Element Method with the reference anatomy as described in the text, ECGs were simulated for all simulated activation sequences. In this figure, the RBBB activation sequence (normal left ventricular activation and delayed right ventricular free wall activity) is displayed as a representative example; all the simulated activation sequences are displayed in Supplement A.

(Figure 2).<sup>32-34</sup> Specifically, to simulate the activation sequences, a constant velocity of 0.85 m/s longitudinal to the myocardial muscle fibers was used with an anisotropy ratio of 2,5.<sup>25-28</sup> In close vicinity of foci (<1.5 cm), the velocity was set to 1.7 m/s at the endocardial surface to account for increased conduction velocities as seen in regions with a high density of Purkinje-myocardial junctions.<sup>27</sup> Among the set of activation sequences with conduction blocks, complete left and right bundle branch blocks (LBBB/RBBB) and incomplete BBB; left anterior/posterior fascicular block (LAFB/LPFB) and incomplete RBBB (iRBBB) were simulated. Once the activation sequences were calculated, synthetic 12-lead ECG data to use as input for the CineECG calculations was computed using the Boundary Element Method (Figure 2). A CT-based single patient specific model of the ventricles, lungs and torso (male, 21y) was used as the input geometry model. A volume conductor model for this geometry was computed with assigned conductivity values of 0.2 S/m for the thorax and ventricular tissue, 0.04 S/m for the lungs and 0.6 S/m for the blood cavities. The computed ECG data, the patient specific model used to simulate the ECG data and the standard 12-lead ECG precordial electrode positions were then used as input for the CineECG calculation.

The AIP and CineECG trajectories were compared per 5 ms interval for each simulated beat by computing 1) the distance between the average locations of the two trajectories in each interval, 2) the angle between their directions, 3) the closest distance of the trajectories to the septal wall and 4) the percentage of the trajectory located in the left and right ventricular cavities. Finally, average values of first three metrics for the complete QRS and the initial (first 25 ms) and terminal (last 25 ms) segments were determined.

#### *Patient study*

Ten patients referred for invasive electroanatomic catheter mapping (EAM) and ablation were enrolled in this study. The EAM procedure was clinically indicated because of either recurrent ventricular arrhythmia due to structural myocardial disease (prior myocarditis (three patients), arrhythmogenic cardiomyopathy (three patients) or dilated cardiomyopathy (two patients) or for symptomatic premature ventricular contractions (two patients). As a part of the clinical workup prior to the EAM procedure, all patients underwent clinical CT imaging. For study purposes, a 67-lead body surface potential mapping procedure was performed on the same day as the clinical CT imaging. The study protocol was approved by the local institutional review board (UMC Utrecht, Utrecht, The Netherlands, protocol nr. 17/628). All patients gave informed consent prior to body surface potential mapping procedure and the study was conducted according to the declaration of Helsinki. The measured in-vivo data in all patients were used to study the sensitivity of CineECG to shifts in electrode location and variation in the anatomical model with real ECG measurements.

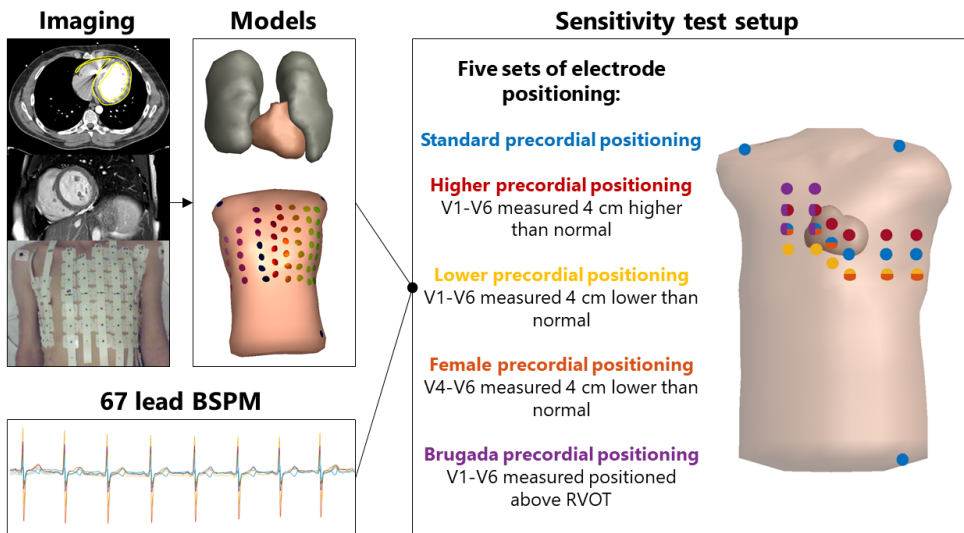
CT-based patient specific model of the ventricles, lungs and torso were created for all ten patients. Electrode positions were captured using a 3D camera setup and merged with the CT-based patient specific model of the torso.<sup>35</sup> To conduct these studies, several 12-lead ECGs were taken from the simultaneously measured 67-lead body surface potentials. Precise electrode positions of measured signals were determined based on the patient specific anatomical models (Figure 3, All setups). To assess the sensitivity of the CineECG computation to the anatomical model and case specific electrode placement, three different sensitivity studies were performed (Figure 3, Comparisons) which are further explained in the following sections. The electrode placement study was conducted to assess the sensitivity of the CineECG computation to possible electrode misplacement or disease specific electrode placement.<sup>2,4-9</sup> The following specific changes electrode positions were chosen as in clinical practice electrode misplacement mostly occurs by a higher or lower placement of the precordial electrodes. Furthermore, in women lead V3-V6 are often placed below the breasts, which is lower compared to the standard precordial lead placement. The Brugada electrode setup was chosen as this is a commonly used setup to determine whether the patient has Brugada syndrome. Specifically, the following three studies were conducted.

#### Patient specific anatomical model and case specific electrode positions

In the first study, patient specific modeling was used and five different but simultaneous ECGs were obtained from five different subsets of body surface electrodes as shown in the middle panel of Figure 3. Each of these five subsets of ECGs were used to compute the CineECG with the same individualized model (Figure 3, all sensitivity test setups). This study was used to specifically investigate the effect of different electrode positioning with corresponding 12-lead ECGs on the CineECG locations. For comparison purposes, the trajectories computed using the different electrode setups were compared to the trajectory computed using the patient specific standard electrode setup (Figure 3, blue setup).

#### Generic anatomical model and case specific electrode positions

In the second study, a generic anatomical model (male, 58 y, not one of the patient cases) was used, and the case specific electrode positions were registered to that model by registering the sternal line of the torso to the sternal line in the 3D camera images. This study was used to assess the effect of using a generic anatomical model instead of an individualized one. The trajectories computed in this study were compared to the trajectory computed using the patient specific anatomical model with the patient specific standard electrode setup (Figure 3, blue setup). To quantitatively compare the CineECG trajectories computed using subject specific vs generic anatomical models (and consequently starting point), all trajectories were aligned based on the starting point and then the comparisons were computed. The distance in starting point using the generic or subject specific model was determined.



**Comparisons**

**Comparison 1 (section 2.3.2.1)**

Assessing the effect of known electrode positioning with ECG signals obtained at these precise locations in combination with a subject specific anatomical model on the *CineECG* computation. Thus for the *CineECG* the following data was used:

- 1) Case specific electrode positioning,
- 2) Case specific ECG signals and
- 3) Subject specific anatomical model.

**Comparison 2 (section 2.3.2.2)**

Assessing the effect of known electrode positioning with ECG signals obtained at these precise locations in combination with a generic anatomical model on the *CineECG* computation. Thus for the *CineECG* the following data was used:

- 1) Case specific electrode positioning,
- 2) Case specific ECG signals and
- 3) Generic anatomical model.

**Comparison 3 (section 2.3.2.3)**

Assessing the effect of generic electrode positioning with ECG signals obtained at different (Comparison 1&2) locations in combination with a generic anatomical model on the *CineECG* computation. Thus for the *CineECG* the following data was used:

- 1) Generic electrode positioning,
- 2) Case specific ECG signals and
- 3) Generic anatomical model.

**Figure 3.** Schematic overview of the in-patient study setup. Cardiac CT or MRI were used to generate patient-specific heart/torso models while 3D camera photos were used to registered electrode positions on the chest. Using the electrodes, 67-lead body surface potential measurements were acquired (all shown in left panel) and five sets of 12-lead ECG configurations were extracted from those maps (middle panel). Specifically, the extremity leads were the same, but precordial positioning differed between the lead sets. This setup was used to conduct the three comparisons shown on the right, which are further elaborated in the text.

### Generic anatomical model and generic electrode positions

In the third study, the 12-lead ECGs obtained using the five different electrode location sets were used in combination with a generic anatomical model but with the standard, unmodified locations for the electrodes (Figure 3, blue setup). This study was used to specifically investigate the effect of using a generic anatomical model together with generic ECG electrode positions in the CineECG computation. The trajectories computed in this study were compared to the trajectory computed using the patient specific anatomical model with the patient specific standard electrode setup (Figure 3, blue setup). To quantitatively compare the CineECG trajectories computed using subject specific vs generic anatomical models (and consequently starting point), all trajectories were aligned based on the starting point and then the comparisons were computed.

### *CineECG compared to invasive catheter local activation time mapping procedure*

In four patients who were included in the in-patient study, a high density near complete (>70% of the CT-based epicardial surface and >50 nodes containing information about the last 25 ms of activation) epicardial local activation catheter map ( $5307 \pm 400$  local activation timing measurements) was made during sinus rhythm. Endocardial maps were not used as the local activation timing maps on the endocardium was only acquired for <70% (range 25%-65%) of endocardial surface and consisted on average of only  $540 \pm 487$  local activation timing measurements. The epicardial maps acquired in these four cases were qualitatively compared to the CineECG trajectories computed from the ECGs. Ventricular models from the invasive mapping system were registered to the CT based models and the last 25 ms of activation in these maps were displayed in the heart model along with the CineECG. To obtain a quantitative measure, the distance between the average location of the last 25 ms of the mapped invasive points (weighted to wall thickness) was compared to the average location of the corresponding CineECG time interval.

### *Statistical analysis and presentation of results*

Data are presented as mean  $\pm$  standard deviation or median [interquartile range (IQR)] as appropriate and the data are compared statistically using an (un)paired Student's t-test. A 2-sided P-value of <0.05 was considered significant. For the simulation study, differences between the location of the CineECG and AIP per 5 ms time intervals are presented as distances in mm and differences in direction as angles in degrees. For the in-patient study, differences between the location of the CineECG trajectory calculated using the patient specific anatomical model or with patient specific standard precordial electrode positioning and other CineECG trajectories per millisecond are also presented as distances in mm and differences between directions as angles in degrees.

For all studies, local activation timing maps were color mapped from red (earliest activation) to blue (latest activation) in both the four-chamber view and the apical view with the local activation times displayed. CineECG trajectories were colored from white (earliest activation) to red (latest activation) and AIP trajectories from white (earliest activation) to blue (latest activation), also in both the four-chamber and apical views.

**Table 1.** Results simulation study.

A. Location AIP/CineECG trajectory	Cases without conduction block (n=6)		Cases with (partial) right conduction block (n=3)		Cases with (partial) left conduction block (n=5)	
	AIP	CineECG	AIP	CineECG	AIP	CineECG
Distance between septum and complete trajectory (mm)	7±4	3±3	15±12	4±4	6±9	9±8
Distance between septum and initial segment (mm)	6±2	1±2	8±3	2±2	1±2	4±4
Distance between septum and terminal segment (mm)	7±7	1±1	29±16	7±5	18±12	17±10
Percentage trajectory >5mm away from septal wall (%)	67±10	24±10	14±5	5±1	7±2	11±3
Percentage trajectory located in the right cavity (%)	15±8	2±5	31±8	27±25	18±22	2±5
B. Comparison AIP to CineECG						
Number of active foci (n)	6		4-5		2-5	
Total activation duration (ms)	83±4.1		97±14		96±12	
Distance between AIP/CineECG complete segment (mm)	24±1		26±3		22±2	
Distance between AIP/CineECG initial segment (mm)	35±6		31±1		37±8	
Distance between AIP/CineECG middle segment (mm)	13±3		17±2		11±2	
Distance between AIP/CineECG terminal segment (mm)	27±1		31±5		20±2	
Angle between AIP/CineECG complete trajectory (degrees)	76±3		70±5		78±4	
Angle between AIP/CineECG initial segment (degrees)	113±15		101±10		108±18	
Angle between AIP/CineECG middle segment (degrees)	66±14		54±10		86±13	
Angle between AIP/CineECG terminal segment (degrees)	59±5		53±10		44±3	

Data are presented either range (number of active foci) or as mean ± standard deviation. The initial segment corresponds to the first 25 ms of the denoted trajectory, the middle segment to 25 ms around mid-QRS and the terminal segment to the last 25 ms of the trajectory. Distances are calculated between the locations of corresponding time intervals and angles are calculated between the normalized vectors indicating the direction of the trajectory. In cases with simulated conduction block, foci corresponding to specific sites at the left ventricular or right ventricular endocardial surface were not used. Simulated cases were incomplete and complete right bundle branch block, incomplete (e.g., left anterior or posterior fascicular block) or complete left bundle branch block with different left ventricular septal foci (See Supplement A for detailed information).



## Results

### Simulation Study

The AIP trajectories derived from different simulated activation sequences were quantitatively and qualitatively compared to the CineECG derived from the simulated ECGs computed from the same activation sequences. The CineECG of simulated activation sequences without conduction block (Supplements A, without conduction block 1-6) stayed closer to the septal wall compared to cases of simulated conduction blocks (Table 1A); specifically, the terminal segment was located further from the septum compared to the initial segment. In all cases, both the terminal CineECG and the terminal AIP were directed towards the latest activated area. For most of the cases both with and without conduction blocks, the CineECG trajectory stayed within the left ventricular cavity, except for the two cases where the focus at the right ventricular free wall was not present (Supplements A, iRBBB2 and RBBB) and consequently a higher percentage of the complete CineECG trajectory was located in the right ventricular cavity (Table 1B). Compared to the location of the CineECG, the AIP moved further from the septal wall and a higher percentage of the trajectory was located in the right ventricular cavity; for cases with left conduction blocks this was true for the initial AIP segment and for cases without conduction blocks or with right conduction block for the terminal AIP segment.

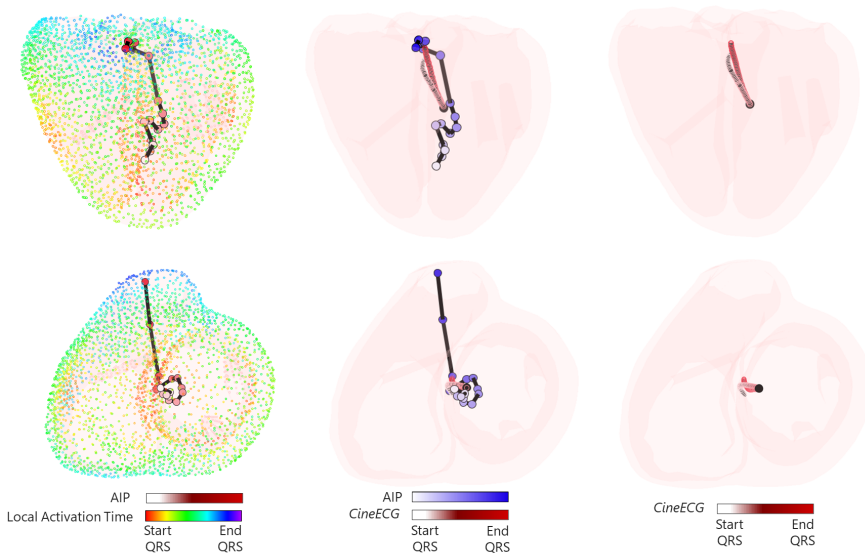


**Figure 4.** Representative example of a CineECG in a case without conduction block. To better visualize both reconstructions we show three columns of figures; each column shows one or two of the three quantities. The top and bottom rows show different views of the heart (four chamber and apical view) as described in the Methods. In the left panels we show local activation times throughout the heart along with the AIP calculated from them. In the middle panels we repeat the AIP and also show the CineECG trajectory for the same case. In the right panels we show just the CineECG for greater clarity. The QRS duration is 75 ms and the different time scales range from the start of the QRS to the end of the QRS for all three quantities as indicated in the legends.



A representative example of simulated activation without conduction block is displayed in Figure 4. All fourteen simulated activation sequences and CineECG and AIP trajectories are reported in Supplement A. Both the number and location of simulated foci affected the shape of the CineECG. For example, when comparing the AIP and CineECG displayed on slide 8 and 9 in Supplement A, both the CineECG and AIP are visually observed to be more compact when a high septal focus is present (Supplement A, slide 8) compared to when this focus is located at the mid-septum (Supplement A, slide 9). Decreasing the number of initial sites of activation (Supplement A, LBBB & RBBB) resulted in less compact CineECG in which the initial and terminal segments were located further away from the septum. The terminal segment of both the AIP and CineECG were directed towards the latest site of activation for all simulated activation sequences. Moreover, the first 15 ms of the CineECG was consistent with a transeptal vector directed towards the side of the septal wall which was activated second, that is, for simulated LBBB it pointed from right to left ventricle, while for all other activation sequences it pointed from left to right.

Quantitatively comparing CineECG to AIP, the average distance between the CineECG and AIP trajectories was  $23.7 \pm 2.4$  mm; in general, the terminal (last 25 ms of the trajectory) segment was statistically significantly closer to the AIP than the initial (first 25 ms of the trajectory) segment ( $34.2 \pm 6.1$  vs  $27.3 \pm 5.7$  mm,  $p=0.015$ ). The average angle between the CineECG and AIP direction per time step was  $76 \pm 5$  degrees; similarly, to the distances, the terminal segments of CineECG and AIP were significantly better aligned than the initial segments ( $107 \pm 15$  vs.  $51 \pm 9$  degrees,  $p < 0.001$ ). During the course of the activation, the directional differences between the AIP and CineECG decreased, whereas the distances between AIP and CineECG were lowest in the middle QRS segment (Table 1B). We note that the average initial difference, that is the average distance between the CineECG starting location (center of mass of the heart) and the AIP at the same time instant, precisely mid-QRS, was  $9.8 \pm 3.2$  mm.

#### *Patient study*

Representative examples of CineECG trajectories for two patients are shown in Figure 5; a patient with a normal narrow QRS complex (Figure 5A) and a patient with a pathologically wide QRS complex (Figure 5B). Whereas the trajectory in Figure 5A is more compact and has a clear initial transeptal movement, the CineECG for the pathological QRS complex moves from left to right, thereby clearly indicating the RV as the latest site of activation. For the rest of the ten patients, the results are displayed in Supplement B, Part A.

#### Patient specific anatomical model and case specific electrode positions

The use of body surface potential map derived ECG signals from different electrode

positions on the patient specific models (Figure 3, comparison 1) resulted in generally similar CineECG trajectories based on visual inspection; the trajectories all had comparable shapes (Figure 5A&B). For all patients, the median [IQR] distance between the trajectory computed using the standard electrode positions and those at the other electrode positions was 5.2[3.3;8.4] mm and the angle between the trajectories was 23[14;30] degrees. The Brugada electrode configuration (Figure 3, purple setup) resulted in the highest deviation in CineECG; a median difference in location of 9.9[7.2;12.8] mm and difference in direction of 39[32;43] degrees were found and the initial and terminal segments of the CineECG showed the highest deviation from the CineECG computed using the standard 12-lead ECG (Supplement B, Part A). Especially in Cases 5 and 7 (Supplement B, Part A) where the latest activation is localized in the RV, the terminal direction of the Brugada CineECG is more skewed towards the RVOT compared to the other trajectories as all electrodes are positioned on top of the RV and consequently, cardiac activity at the LV free wall or apex is not captured as well in the recorded ECG.

#### Generic anatomical model and case specific electrode positions

When replacing the patient specific model with a generic anatomical model, but retaining the case specific electrode positioning (Figure 3, Comparison 2), the median differences in distance reduced were 5.1[3.0;7.5] mm and angle differences were 18[14;20] degrees (Supplement B, Slide 3&4). The difference in starting point of the subject specific anatomical models and the generic anatomical model was on average  $52 \pm 20$  mm. The overlap in models is displayed in Supplement B, slide 5&6. There seemed to be a relation between the distance between the starting points and the error observed in the comparison of the CineECG trajectories (Supplement B, slide 7); specifically, when the distance increased, the differences between the trajectories also increased.

#### Generic anatomical model and generic electrode positions

When using a generic anatomical model with the standard electrode positions, but using the different 12-lead ECGs obtained from the body surface potential mapping procedure as the input for the CineECG computation, the median [IQR] distance between the trajectories was 5.0[2.2;7.7] mm and the average difference in direction was 20[11;30] degrees. The use of a generic anatomical model (Figure 3, Comparison 3) thus produced similar differences in distance and angle compared to the trajectories where patient specific information was used (Figure 3, Comparison 1).

#### *Comparison of CineECG to invasive mapping*

Results from the four patients with invasive epicardial maps are shown in Supplement B, Slide 19-23 Two patients (Patient 05 & 07) have three prominent areas of early activation (indicated with the white arrow) on the epicardial surface (Supplement B,

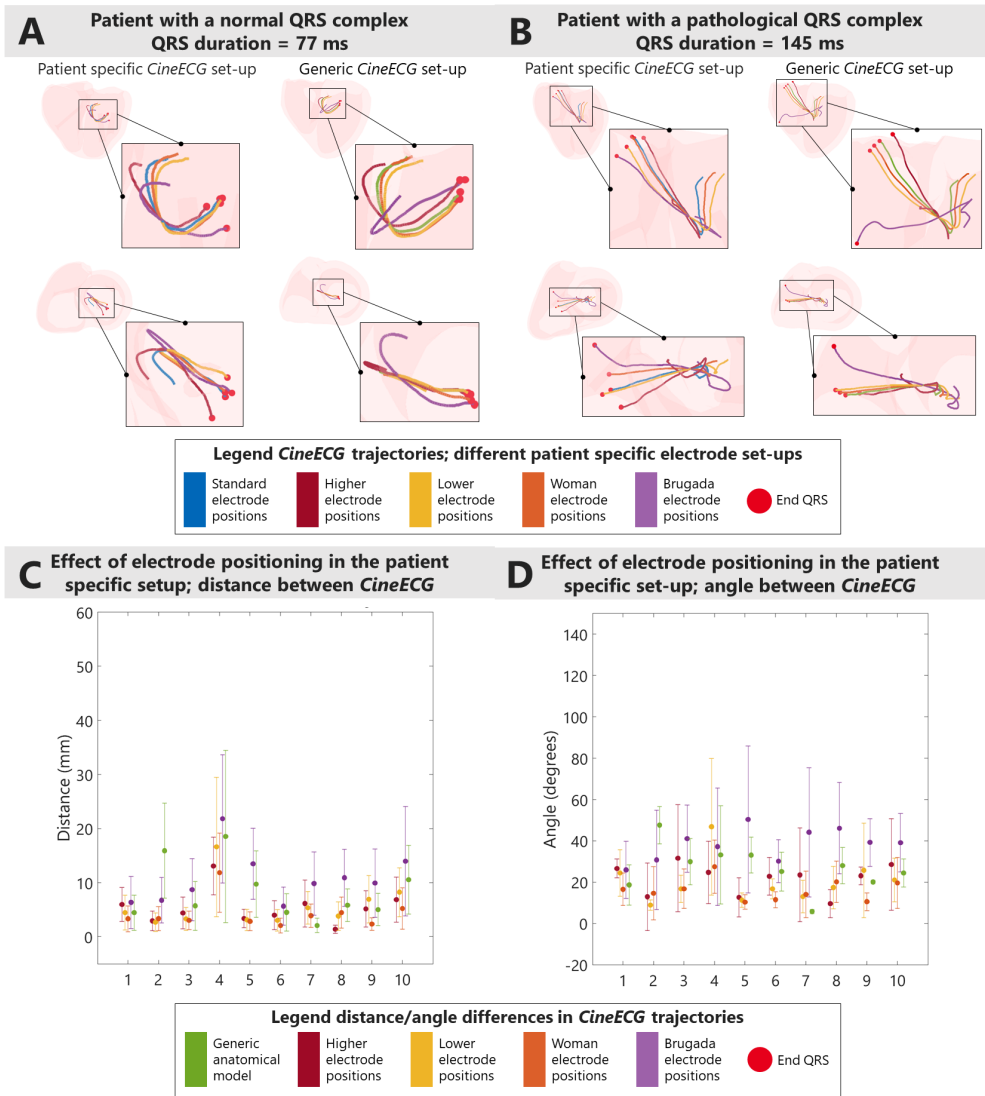


**Figure 5.** Effect of different electrode positions and the use of a standard model. A&B: Two representative examples of the CineECG calculated using different ECG electrode positions and a generic model are displayed. C: The mean (standard deviation) error in distance of the CineECG trajectories computed using different electrode positions per patient (x-axis) with respect to the CineECG calculated using the patient specific model with standard electrode positioning is displayed. D: the mean (standard deviation) error in direction per patient measured by the angle between vectors of the calculated VCG is displayed. The colors of the CineECG in Panel A and B correspond to the legends shown in Panel C and D.

Slide 22&23), whereas the other two (Patient 01 & 02) have only one (Supplement B, slide 20&21). When visually comparing the invasive maps and the CineECG, a larger total area of early activation at the epicardial surface corresponded to a more compact initial segment of the CineECG in the septal area, whereas in the cases with smaller early epicardial activation the CineECG was less compact and was directed from the site with early activation towards the site of late activation. In all cases the terminal segment of the CineECG trajectory was directed towards the latest site of activation. Quantitatively, the distances between the average location of the last 25 ms of the invasive mapped points and the terminal 25 ms of the CineECG was 35 mm for Patient 01, 24 mm for Patient 02, 17 mm for Patient 05 and 32 mm for Patient 07.

## Discussion

This is the first study evaluating the relationship between the 12-lead ECG based CineECG technique and cardiac activation sequences. Our results show that the CineECG is able to relate clinically meaningful components of cardiac activation to the cardiac anatomy. The relationship between cardiac activation isochrones and CineECG is especially clear during 1) the terminal segment of the QRS, where the CineECG moved towards the area of latest activation and 2) the initial segment, where the CineECG reliably corresponded to the direction of the transseptal vector of the QRS. Overall the AIP and CineECG trajectories corresponded well visually. Within limits, the CineECG is robust to electrode misplacement and even to model inaccuracies. The CineECG trajectories were similar when using a generic heart/torso model versus the patient specific anatomy and electrode positions were relatively close to the standard 12 lead ECG positions.

### *Evaluation of the AIP as an averaged representation of cardiac isochrones*

In the simulation study, the AIP was constructed from the simulated cardiac activation isochrones to determine an average position and direction of cardiac activation. Thus, the AIP could be used to quantitatively compare activation sequences with the CineECG. Our simulation results show that the AIP trajectory is a useful representation of that aspect of cardiac activation, although the initial transmural activation direction is captured with less accuracy. The cases without conduction blocks showed the most compact trajectories, close to the septum, whereas incomplete and complete bundle branch block trajectories showed a more elongated configuration, with increasing QRS duration. Typically, multiple activation wavefronts are present in the initial 2/3 of the cardiac activation, whereas in the terminal activation several of these waves have collided and tend to move in a single direction. This behavior is reflected in the computed AIP trajectories, as the initial segment remained within the center of the heart but the terminal segment moved in the average direction of remaining activation waves towards the latest activation sites. As the number of initial sites of activation decreased from 6 to 2, we observed that the initial segment of the AIP trajectory changed gradually from being more randomly oriented in the septal

center of the heart to moving more clearly in a single direction away from the average earliest site(s) of activation.

To the best of our knowledge, this approach to compute a trajectory to describe overall cardiac activation location and direction is novel. This information is normally assessed qualitatively by clinicians when interpreting the 12-lead ECG, but not computed explicitly in a quantitative manner. In this study it provided a useful comparison to both location and direction of the CineECG results.

#### *Comparison of CineECG to AIP*

When comparing the AIP to the CineECG, the initial segment of these trajectories were consistently further apart than the terminal segments of the trajectories. Indeed, the initial segment of the AIP stayed within the center of the heart generally moving in different directions compared to the CineECG, which had one consistent direction (Supplement A, SR1-SR6). The initial segment of the CineECG correctly indicated the direction of the septal activation, which is activated from left to right for activation sequences with the earliest site of activation at the left ventricular septum (Supplement A, all activations except LBBB3). Compared to the CineECG, the AIP trajectory did not show such a clear direction in the initial segment of the QRS, but rather stayed in the center of the heart. The variation in the number and location of initial sites of activation affect both the AIP and the CineECG. Decreasing the number of initial sites (e.g. comparing without vs with conduction block) resulted in a less compact CineECG and AIP trajectory. The location of high vs low septal foci in cases without conduction disorder (Supplement A, SR2&3) produced elongated shapes of both the CineECG and AIP.

A striking feature of the CineECG is a clear kink in the trajectory near mid QRS, suggesting a clear change in the average direction of activation. This kink close to mid-QRS is observed in both the CineECGs calculated in the simulation study (SR1-6, (i)RBBB) and the in-patient study (Patient 1,3 & 5-9). We believe that this kink is most likely accurately reflects a change in direction of activation; in cases without a conduction block from the initial dominant downward movement mainly over the septal wall to the upwards movement towards the basal area at end QRS (Supplement A, SR1-6). As for a simulated RBBB, the initial movement of the CineECG is dominated by the left ventricular activation whereas the terminal movement is dominated by a rightward movement, also resulting in a kink in the trajectory. This kink is less present for cases of LBBB, where the movement is clearly dominated from right to left during the complete activation cycle. This behavior is also present in the in-patient data, for example when comparing Patient 9 to Patient 10, where also a clear relation in QRS duration seems to exist. This observation also indicates the minor effect of the cardiac shape, size and orientation (within reasonable limits, e.g. not including dextrocardia) on the CineECG computation, as was also indicated

by the results found when substituting the patient-specific anatomy with a generic anatomical model.

The distance between the AIP and CineECG at mid-QRS was lower compared to the average distance over the complete trajectory (average distance  $9.8 \pm 3.2$  vs  $18.0 \pm 3.1$  mm, Figure 3B), indicating accurate estimation of the average location at mid-QRS as the center of mass for both narrow and prolonged QRS durations. Relating these distances to the size of the human heart (approximately  $120 \times 85 \times 60$  mm), we believe it is fair to say that this error is relatively small. To further investigate the sources of error in the CineECG, we repeated the CineECG calculation after correcting the starting point of the CineECG to the mid-QRS AIP location. However, the variation in distance between the CineECG and AIP trajectory remained similar to without this correction, suggesting that the error in starting point did not have a major effect on the discrepancies between CineECG and AIP. Based on these results, we believe that our choice to set the starting point of the CineECG calculation to the center of mass at mid-QRS (instead of on the LV septal wall at QRS onset, as in our previous reports) is appropriate.

The terminal segments of the AIP and CineECG aligned better in direction than the initial segments; a higher variability was found in both angle and distance of the initial segments of the AIP and CineECG compared to the terminal segments. (Table 1, Supplements A slide 3). Indeed, it is perhaps not surprising that the greater complexity of propagation during the initial segment of cardiac activation produced a decrease in agreement. In terms of CineECG, we note that in the initial segment, when multiple activation wavefronts are contributing to the recorded ECG signals and the number of wavefronts is generally larger, information about cardiac activation measured with ECG is more complex. Factors that influence the resulting ECGs are not only the number of wavefronts but also their directions and geometric relationships (i.e. whether they amplifying or canceling each other), volume conductor effects, and proximity effects (i.e., the distance between electrodes and activation wavefronts). To conclude, both the AIP and CineECG are intended to represent the average pathway of activation and when taking into account these factors, the agreement of CineECG and the AIP is reasonably good.

#### *Comparison of CineECG to the clinical VCG and ECG*

There are several ways in which we can consider comparisons of the CineECG with the VCG. With the VCG, the direction of average cardiac activation is explicitly imaged per time instance in the thoracic compartment<sup>10</sup>. The VCG can be directly computed from the ECG signals using dedicated weighing factors per ECG lead that are constant in time. The ECG amplitude that affects the VCG is determined by a combination of the area of the depolarizing surface and its geometric relationship to the electrodes. Thus, the activation of small areas in the heart is represented by a small amplitude

vector in the VCG and consequently may, in the case of subtle cardiac pathology, be overlooked. The CineECG direction is computed as a normalized vector, and thus small amplitude signals captured by the 12-lead ECG may become visible in this new representation. Additionally, the translation of the VCG to cardiac anatomy is left to the interpreter, in marked contrast to the CineECG which provides a direct localization in that anatomy.<sup>13,14,36</sup> Another way of conceptualizing CineECG is that it rotates the VCG from the body coordinate system to a heart coordinate system by redefining the tail location of the lead vectors at each time instant and then tracking the movement of the tail through cardiac activation. In effect, the fixed coefficients that related the ECG to the standard VCG vary in time in the CineECG as the estimated average activation location moves within the cardiac anatomy. Thus, with CineECG, additional temporal and spatial information about the direction and location of cardiac activation, compared to the VCG, is directly related to cardiac anatomy. In this sense, CineECG provides a more detailed view into cardiac activation and may therefore be able to identify subtle differences between activation sequences.

In current clinical practice, the clinical 12-lead ECG is most often to identify and describe cardiac abnormalities but interpretation of the 12-lead ECG is subject to inter- and intra-clinician variability and highly depends on the experience of the reader. For the average ECG reader, CineECG provides a fast way to gain insight into the direct relation between cardiac electrical activity and anatomy, thereby aiding interpretation of the 12-lead ECG. Furthermore, for example in the emergency department, subtle changes in cardiac electrical activity may be recognized earlier using CineECG to prevent serious acute cardiac deterioration. For the more experienced ECG reader, CineECG can provide a way to identify subtle signs of disease. The use of CineECG in clinical practice may be expanded to guide lead positioning in cardiac resynchronization therapy or to identify ischemic areas to guide percutaneous coronary interventions. Furthermore, as the technique is designed to image subtle changes in the cardiac activation sequence, the technique may be useful for clinical follow-up in genetic cardiomyopathies to identify the early onset of disease. In summary, the technique may be used to identify heterogenous conduction in diseased hearts to guide treatment strategies.

#### *Comparison of CineECG to ECG imaging*

CineECG can also be viewed as a lightweight and less intrusive alternative to ECGI in both a physical (e.g. number of electrodes) and a computational (e.g. algorithm complexity) sense, by capturing the activation of the heart with fewer technical requirements using a simplified model. The tradeoff is that CineECG only provides a summary representation of cardiac activation, in contrast to the locally imaged potential distributions and/or activation sequences obtained with ECGI. However, CineECG has a much lower cost in terms of algorithmic complexity and computation time, and, perhaps most important, does not need the large numbers of body surface



electrodes and the detailed patient specific cardiothoracic imaging and modelling generally required for ECGI. CineECG only uses the standard 12-lead ECG, a simple geometrical anatomical model and a computationally inexpensive mathematical model, which may thus be well suited for a variety of clinical settings. As CineECG is a fast technique designed to detect subtle changes in the average cardiac activation sequence, the technique could provide direct clinical additional insight in the critical care unit or the emergency department to detect acute cardiac deterioration.

Heuristically, CineECG can be related to ECGI methods that estimate the position and direction of single dipoles. Here the computed VCG signal is tuned by the  $\alpha_{el}$ -coefficient (Equation 1), instead of the detailed volume conductor models that are typical with ECGI. Specifically,  $\alpha_{el}$  represents a rough approximation of the relationship between the proximity of limb lead and precordial electrodes to the heart, effectively substituting for ECGI's regularized or other inversion of a forward model, itself computed by solving the underlying partial differential equations. Another major difference is that CineECG aims to localize the average activation of the heart, using the VCG direction rather than the ECG amplitude. It is well known that ECGI solves an inverse problem that is ill-posed, resulting in very high sensitivity to errors in the forward model.<sup>37-40</sup> Our results with CineECG may be an indication that using a model eliminating the effect of amplitude, but concentrating on accurate reconstruction of the average direction of propagation as measured on the body surface, may have certain advantages. It may, for example, provide clinically relevant parameters to distinguish different bundle branch blocks or structural cardiac pathology while also providing significant robustness to at least some level of electrode misplacement and model error. We believe that our CineECG results may motivate some interesting future analyses of this relationship between amplitude, direction, and robustness to ill-posedness.

#### *Robustness of CineECG to lead positioning*

In clinical practice, QRS morphology interpretation in specific leads is used to get an impression of the underlying cardiac activation sequence, but QRS morphology interpretation relies heavily on accurate electrode placement. The clinically accepted range of variation in electrode positioning is 20 mm; greater electrode misplacement may result in misdiagnosis.<sup>2,4,7,8,41</sup> In the present study, 67-lead body surface mapping was used to simulate differences of up to 40 mm in electrode positioning from the standard electrode position to assess the effect on the calculated CineECG (Figure 3). With the various electrode setups, we observed variation in location (distance:  $6.5 \pm 4.5$  mm) and direction (angle:  $24 \pm 12$ ) in the calculated CineECG, but the trajectory position and shape remained similar to the CineECG trajectory calculated using standard electrode positions (Figure 5C&D). The CineECG thus was robust in terms of varying electrode positioning in our tests, as the computed CineECG trajectory had the same shape for variations around standard precordial electrode positioning,



with the noted exception of the Brugada electrode positioning. Performance was however improved when simply adding the known electrode positions with respect to the heart, even if they were not in the standard location. These results indicate that the CineECG, poses added value in terms of ECG interpretation and that localizing electrodes on the torso, e.g. with the simple use of a 3D camera, considerably improves the robustness of the CineECG.<sup>35,42</sup>

#### *Robustness of CineECG to heart/torso anatomy model errors*

Anatomical differences between individuals may result in ECG variability, caused for example by differences in torso anatomy, age and weight.<sup>43-46</sup> Additional factors, like ECG acquisition just after a meal<sup>47,48</sup>, during respiration<sup>49,50</sup> and during pregnancy<sup>51</sup>, may also contribute to differences in the measured ECG because these factors all contribute to the position of the heart in the torso, and thus with respect to the electrodes, and also to the inhomogeneous conductivity of the intervening volume conductor and thus potentially affect both the acquired ECG and its derived parameters.<sup>52,53</sup>

In the present study, we tested for robustness to model inaccuracy by comparing a generic vs patient specific heart/torso model. When we substituted the generic model, the resulting variation in the CineECG was similar in distance to that from electrode mislocation using the patient specific model (Figure 5C&D). This may partly be explained by the difference in the starting point, relative to the electrode positions on the torso, between the generic and the subject specific anatomical model (Supplement B, slide 5-7). However, when we registered patient specific electrode positions to the generic anatomical model, this variation in the computed CineECG decreased substantially (Supplement B, slide 3&4). Thus capturing the patient specific electrode positions, again for example using a 3D camera setup, provides low-cost lightweight patient specific information about torso size and electrode position and could potentially be used with a generic anatomical model for the CineECG computation in the absence of patient specific anatomical imaging<sup>8,9,35,42</sup>, circumventing the need for expensive and time costly patient-specific cardiothoracic imaging and anatomical modeling. Additional accuracy might be obtained by creating a database of several generic anatomical hear/torso models, where the closest to a 'patient specific' generic anatomical model could be used for the CineECG computation to improve the accuracy of patient specific features derived from the CineECG. However, this suggestion needs to be further investigated in a bigger population prior before drawing any conclusions with regards to clinically sufficient accuracy.

#### *Invasive mapping study*

Reasonably accurate correspondence of local activation timings from the invasive EAM data to the CineECG trajectory were observed. In particular, the CineECG clearly

indicated the region of latest activation (Supplement B, slide 19-23). Furthermore, when an increased number of early sites of activation were present at the epicardium, the initial segment of the CineECG was more compact compared to the cases with fewer early sites of epicardial activation. Although sufficient measurements of the endocardium were not available to directly compare to the CineECG trajectories, inferences about endocardial activity from epicardial measurements were consistent with the findings in our simulation study; with an increasing number of foci, the initial CineECG was more compact. This observation increases somewhat our confidence that CineECG also correctly imaged the endocardial activity.

### *Limitations*

As our results and discussion show, the CineECG only recovers some parameters of cardiac activation that are useful for characterization of specific features of activation patterns, such as presence/absence or type of bundle branch blocks, location of terminal activation, and direction of initial activations. The key is that these have to be features specified by a trajectory of a spatial average of activation through QRS, CineECG is not intended as a replacement for either invasive mapping or full results from ECGI.

A limitation of the current CineECG method described here is that a constant speed of 0.7 m/s was used to compute the CineECG, determined based on balancing longitudinal and transverse propagation speed in myocardial muscle fibers (Section 2.1). However, in diseased hearts this assumption of a constant speed may be inadequate due to the (local) presence of scar or fibrofatty tissue. Additionally, as noted earlier, activation waves collide during the course of ventricular activation, which can lead to decreased velocity of the "average wavefront" if these waves annihilate each other. Further insight into the velocity of the 'average' activation waves from high density endocardial and epicardial local activation timing maps, perhaps using the proposed AIP, could be obtained for the different phases (presence of multiple vs collided waves) of cardiac activation to see if a more sophisticated method for determining speeds to use in CineECG would be useful.

Due to the spatial resolution of the anatomical heart model, the computation of the AIP trajectory using time intervals of one millisecond resulted in a jagged trajectory. The shape of the AIP trajectory was more affected by the spatial resolution of the model than the simulated activation sequence was. Increasing the time interval to 10 ms resulted in the loss of resolution in shape of the AIP trajectory and thus its ability to represent the cardiac activation pattern. To balance both the effect of the shape model resolution and to adequately represent the activation sequence, a time interval of five milliseconds was used for the computation of the AIP trajectory. Another limitation is that we used a simplified approach for the  $\alpha_{el}$ -coefficients, crudely correcting the volume conductor effects, i.e. using two constants weight values

(Equation 1) for limb versus precordial electrodes. During the course of the activation sequence, the relationship between the proximity of, especially, precordial leads and the average activation location may change significantly. One direction for future work is to focus on the incorporation of dynamic  $\alpha_{el}$ -coefficients using information from the changing electrode vector field, similar to what we do when computing the VCG. A second direction for future work related to the  $\alpha_{el}$ -coefficients is comparison between the use of Mason-Likar limb electrodes and foot-wrist electrodes on the CineECG computation. First the effect of this difference in limb electrode positioning on the CineECG computation should be investigated and secondly, more accurate  $\alpha_{el}$ -coefficients could perhaps be determined per limb-lead set-up.

Finally, a more comprehensive study with high density invasive maps (left and right endocardium and epicardium) is required to compare the AIP directly to the CineECG, providing perhaps a more complete evaluation of CineECG utility.

## Conclusion

We present and evaluate CineECG, a novel approach to determining the average activation location in the heart as a function of time from the 12-lead ECG and a simple anatomical model. With CineECG, a realistic representation of the average cardiac activation is provided and significant features of underlying cardiac activation isochrones were recovered that could be directly related to cardiac anatomy. Especially the terminal segment of the CineECG was observed to be useful for the reliable detection of areas of late activation in the ventricles. CineECG was relatively robust even when electrodes were shifted up to 40 mm from standard electrode positions and when a generic heart/torso model was used instead of a patient specific model. Our results corresponded well to cardiac invasive mapping in a small study limited to only the epicardium. In summary, CineECG directly relates a VCG-like sequence of propagation directions to the cardiac anatomy and provides a robust and stable mapping tool which may turn out to be broadly useful in the early recognition of cardiac structural abnormalities.

### *Acknowledgments*

This work was supported by the Dutch Heart Foundation [QRS-Vision 2018B007, 2018]. The sponsor had no role in the conducted research nor the submitted manuscript.

### *Supplementary material*

Available at:

<https://www.sciencedirect.com/science/article/pii/S0010482521009227#appsec1>

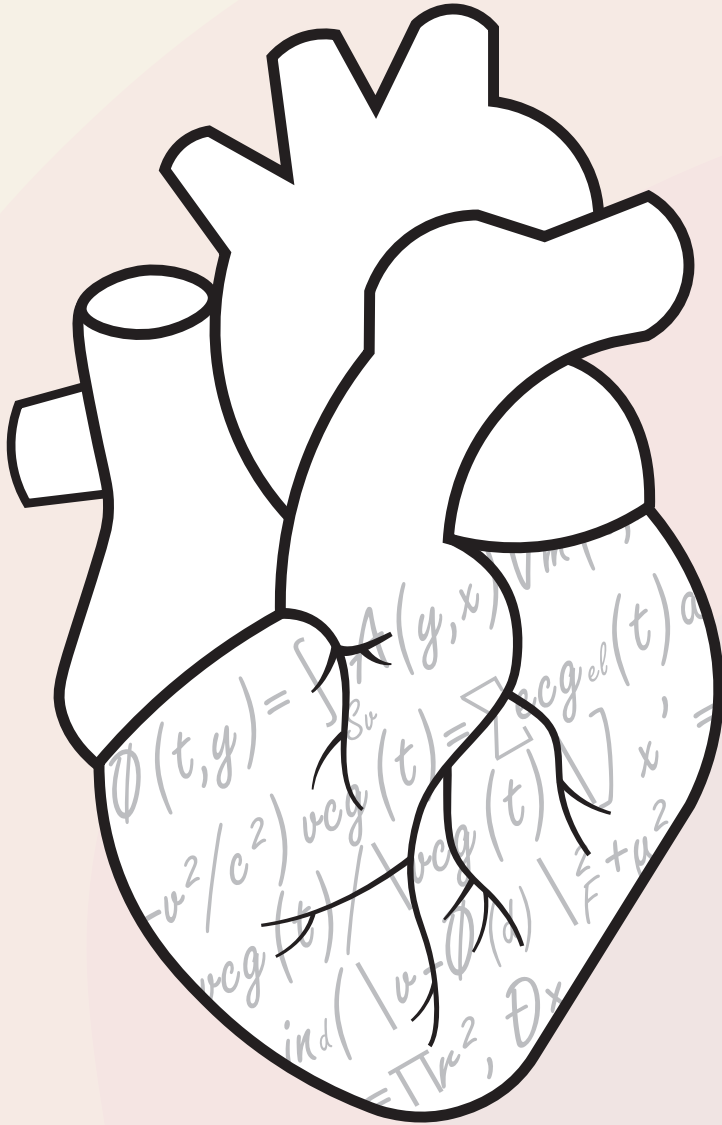
Supplement A – Comparison of CineECG to AIP

Supplement B – Effect of anatomical model on CineECG and comparison to invasive data

## References

1. Macfarlane P, Coloco R, Stevens K, et al. Precordial electrode placement in women. *Netherlands Heart Journal*. 2003;11(3):118.
2. Bond RR, Finlay D, Nugent C, et al. The effects of electrode misplacement on clinicians' interpretation of the standard 12-lead electrocardiogram. *European journal of internal medicine*. 2012;23(7):610-5. DOI: 10.1016/j.ejim.2012.03.011
3. Kadish AH, Buxton AE, Kennedy HL, et al. ACC/AHA clinical competence statement on electrocardiography and ambulatory electrocardiography: A report of the ACC/AHA/ACP-ASIM Task Force on Clinical Competence (ACC/AHA Committee to Develop a Clinical Competence Statement on Electrocardiography and Ambulatory Electrocardiography) Endorsed by the International Society for Holter and Noninvasive Electrocardiology. *Journal of the American College of Cardiology*. 2001;38(7):2091-100. DOI:10.1016/s0735-1097(01)01680-1
4. Kligfield P, Gettes LS, Bailey JJ, et al. Recommendations for the Standardization and Interpretation of the Electrocardiogram: Part I: The Electrocardiogram and Its Technology. A Scientific Statement From the American Heart Association Electrocardiography and Arrhythmias Committee, Council on Clinical Cardiology; the American College of Cardiology Foundation; and the Heart Rhythm Society Endorsed by the International Society for Computerized Electrocardiology. *Circulation*. 2007;115(10). DOI: 10.1016/j.jacc.2007.01.024
5. Michaels L, Cadoret RJ. Day-to-day variability in the normal electrocardiogram. *British heart journal*. 1967;29(6):913. DOI: 10.1136/hrt.29.6.913
6. Schijvenaars BJ, van Herpen G, Kors JA. Intraindividual variability in electrocardiograms. *J Electrocardiol*. 2008;41(3):190-6. DOI: 10.1016/j.jelectrocard.2008.01.012
7. Kania M, Rix H, Fereniec M, et al. The effect of precordial lead displacement on ECG morphology. *Med Biol Eng Comput*. 2014;52(2):109-19. DOI: 10.1007/s11517-013-1115-9
8. Hill N, Goodman J. Importance of accurate placement of precordial leads in the 12-lead electrocardiogram. *Heart & lung: the journal of critical care*. 1987;16(5):561-6.
9. Herman MV, Ingram DA, Levy JA, et al. Variability of electrocardiographic precordial lead placement: a method to improve accuracy and reliability. *Clin Cardiol*. 1991;14(6):469-76.
10. Frank E. General Theory of Heart-Vector Projection. *Circulation Research*. 1954;2(3):258-70.
11. Surawicz B, Childers R, Deal BJ, et al. AHA/ACCF/HRS Recommendations for the Standardization and Interpretation of the Electrocardiogram: Part III: Intraventricular Conduction Disturbances: A Scientific Statement From the American Heart Association Electrocardiography and Arrhythmias Committee, Council on Clinical Cardiology; the American College of Cardiology Foundation; and the Heart Rhythm Society: Endorsed by the International Society for Computerized Electrocardiology. *Circulation*. 2009;119(10):e235-e40. DOI: 10.1161/circulationaha.108.191095
12. Hancock E, Deal B, Mirvis D, et al. Recommendations for the standardization and interpretation of the electrocardiogram: part V: electrocardiogram changes associated with cardiac chamber hypertrophy: a scientific statement from the American Heart Association electrocardiography and arrhythmias committee. *Circulation*. 2009;119:e250-e61. DOI: 10.1016/j.jacc.2008.12.015
13. Willems JL, Poblete PF, Pipberger HV. Day-to-day variation of the normal orthogonal electrocardiogram and vectorcardiogram. *Circulation*. 1972;45(5):1057-64. DOI: 10.1161/01.cir.45.5.1057
14. Berson AS, Haisty WK, Pipberger HV. Electrode position effects on Frank lead electrocardiograms. *American heart journal*. 1978;95(4):463-73. DOI: 10.1016/0002-8703(78)90238-7
15. Fukuoka Y, Armoundas AA, Oostendorp TF, et al. Accuracy of a single equivalent moving dipole model in a realistic anatomic geometry torso model. *Comput Cardiol*. 2000;27:439-42.
16. Lv W, Lee K, Arai T, Barrett CD, et al. Accuracy of cardiac ablation catheter guidance by means of a single equivalent moving dipole inverse algorithm to identify sites of origin of cardiac electrical activation. *J Interv Card Electrophysiol*. 2020;58(3):323-31. DOI: 10.1007/s10840-019-00605-z
17. Svehlikova J, Teplan M, Tysler M. Geometrical constraint of sources in noninvasive localization of premature ventricular contractions. *J Electrocardiol*. 2018;51(3):370-7. DOI: 10.1016/j.jelectrocard.2018.02.013
18. van Dam PM, Boyle NG, Laks MM, et al. Localization of premature ventricular contractions from the papillary muscles using the standard 12-lead electrocardiogram: a feasibility study using a novel cardiac isochrone positioning system. *EP Europace*. 2016;18:iv16-iv22. DOI: 10.1093/europace/euw347
19. Misra S, van Dam P, Chrispin J, et al. Initial validation of a novel ECGI system for localization of premature ventricular contractions and ventricular tachycardia in structurally normal and abnormal hearts. *J Electrocardiol*. 2018;51(5):801-8. DOI: 10.1016/j.jelectrocard.2018.05.018
20. van Dam PM, Locati ET, Cicone G, et al. Novel CineECG Derived from Standard 12-Lead ECG Enables Right Ventricle Outflow Tract Localization of Electrical Substrate in Patients with Brugada Syndrome. *Circ Arrhythm Electrophysiol*. 2020;13(9):e008524. DOI: 10.1161/circep.120.008524
21. Boonstra MJ, Hilderink BN, Locati ET, et al. Novel CineECG enables anatomical 3D localization and classification of bundle branch blocks. *EP Europace*. 2021;23(Supplement\_1):i80-i7. DOI: 10.1093/europace/eaab396
22. van Dam PM. A new anatomical view on the vector cardiogram: The mean temporal-spatial isochrones. *J Electrocardiol*. 2017;50(6):732-8. DOI: 10.1016/j.jelectrocard.2017.08.010
23. Roudijk R, Loh P, Van Dam P. Mean temporal spatial isochrones direction as marker for activation delay in patients with arrhythmogenic cardiomyopathy. 2018 Computing in Cardiology Conference (CinC); 2018: IEEE.
24. van Dam PM, Boonstra M, Locati ET, Loh P. The relation of 12 lead ECG to the cardiac anatomy: The normal CineECG. *J Electrocardiol*. 2021. DOI: 10.1016/j.jelectrocard.2021.07.014
25. Durrer D, van Dam RT, Freud GE, et al. Total excitation of the isolated human heart. *Circulation*. 1970;41:899-912.

- DOI: 10.1161/01.cir.41.6.899
26. Greenbaum RA, Ho SY, Gibson DG, et al. Left ventricular fibre architecture in man. *Br Heart J*. 1981;45:248-63. DOI: 10.1136/hrt.45.3.248
  27. Myerburg RJ, Gelband H, Nilsson K, et al. The role of canine superficial ventricular muscle fibers in endocardial impulse distribution. *Circulation research*. 1978;42(1):27-35. DOI: 10.1161/01.res.42.1.27
  28. Clerc L. Directional differences of impulse spread in trabecular muscle from mammalian heart. *J Physiol*. 1976;255:335-46. DOI: 10.1113/jphysiol.1976.sp011283
  29. van Dam PM, Oostendorp TF, Linnenbank AC, et al. Non-invasive imaging of cardiac activation and recovery. *Ann Biomed Eng*. 2009;37(9):1739-56. DOI: 10.1007/s10439-009-9747-5
  30. van Dam PM, Oostendorp TF, van Oosterom A. Application of the fastest route algorithm in the interactive simulation of the effect of local ischemia on the ECG. *Med Biol Eng Comput*. 2009;47(1):11-20. DOI: 10.1007/s11517-008-0391-2
  31. Tawara S. Das Reizleitungssystem des Säugetierherzens. Eine Anatomisch-Histologische Studie über das Atrioventrikulärbündel und die Purkinjeschen Fäden. Jena: Gustav Fischer; 1906. DOI: 10.1007/s00399-006-0525-x
  32. van Oosterom A, Oostendorp T. ECGSIM; an interactive tool for studying the genesis of QRST waveforms. *Heart* 2004;90:165-8. DOI: 10.1136/hrt.2003.014662
  33. van Oosterom A, Oostendorp TF, van Dam PM. Potential applications of the new ECGSIM. *J Electrocardiol*. 2011;44(5):577-83. DOI: 10.1016/j.jelectrocard.2011.05.006
  34. Galeotti L, van Dam PM, Loring Z, et al. Evaluating strict and conventional left bundle branch block criteria using electrocardiographic simulations. *Europace*. 2013;15(12):1816-21. DOI: 10.1093/europace/eut132
  35. Alioui S, Kastelein M, van Dam EM, et al. Automatic registration of 3D camera recording to model for leads localization. 2017 Computing in Cardiology (CinC); 2017: IEEE.
  36. Kossmann CE, Brody DA, Burch GE, et al. Recommendations for standardization of leads and of specifications for instruments in electrocardiography and vectorcardiography. *Circulation*. 1967;35(3):583-602. DOI: 10.1161/01.cir.35.3.583
  37. Gulrajani RM, Savard P, Roberge FA. The inverse problem in electrocardiography: solution in terms of equivalent sources. *CRC Crit Rev in Biomed Eng*. 1988;16:171-214.
  38. Rudy Y, Oster HS. The electrocardiographic inverse problem. *Critical Review in Biomedical Engineering*. 1993;20(1).
  39. Huiskamp GJM, van Oosterom A. The depolarization sequence of the human heart surface computed from measured body surface potentials. *IEEE Transactions on Biomedical Engineering*. 1988;35(12):1047-58. DOI: 10.1109/10.8689
  40. Rudy Y. Noninvasive Electrocardiographic Imaging of Arrhythmogenic Substrates in Humans. *Circulation Research*. 2013;112(5):863-74. DOI: 10.1161/circresaha.112.279315
  41. Schijvenaars BJ, Kors JA, van Herpen G, et al. Effect of electrode positioning on ECG interpretation by computer. *J Electrocardiol*. 1997;30(3):247-56. DOI: 10.1016/s0022-0736(97)80010-6
  42. Roudijk RW, Boonstra MJ, Ruisch J, et al. Feasibility study of a 3D camera to reduce electrode repositioning errors during longitudinal ECG acquisition. *J Electrocardiol*. 2021;66:69-76. DOI: 10.1016/j.jelectrocard.2021.03.006
  43. Macfarlane PW. *Normal Limits*. Oxford: Pergamon Press; 1989. 1441-526 p.
  44. Rautaharju PM, Zhou SH, Calhoun HP. Ethnic differences in ECG amplitudes in North American white, black, and Hispanic men and women: effect of obesity and age. *J Electrocardiol*. 1994;27:20-31. DOI: 10.1016/s0022-0736(94)80040-5
  45. Hiss RG, Lamb LE, Allen MF. Electrocardiographic findings in 67,375 asymptomatic subjects: X. Normal values. *The American journal of cardiology*. 1960;6(1):200-31. DOI: 10.1016/0002-9149(60)90047-3
  46. Tuna N, Liedtke C-E. Correlations between the electrocardiogram and age, height, body weight and chest circumference. *Electrocardiology II*. 19: Karger Publishers; 1977. p. 17-20. DOI: 10.1159/000399612
  47. Simonson E, Alexander H, Henschel A, et al. The effect of meals on the electrocardiogram in normal subjects. *American heart journal*. 1946;32:202-14. DOI: 10.1016/0002-8703(46)90069-5
  48. Dota CD, Edvardsson N, Schutzer KM, et al. Inter- and intraday variability in major electrocardiogram intervals and amplitudes in healthy men and women. *Pacing and clinical electrophysiology*. 2003;26(1p2):361-6. DOI: 10.1046/j.1460-9592.2003.00050.x
  49. Einthoven W, Fahr G, de Waart A. Über die Richtung und die manifeste Grösse der Potential Schwankungen im menschlichen Herzen und über den Einfluss der Herzlage auf die Form des Elektrokardiogramms. *Pflugers Arch (Translated: Am Heart J)* 1950; 40: 163-211) 1913;150:275-315.
  50. Pallas-Areny R, Colominas-Balague J, Rosell FJ. The effect of respiration-induced heart movements on the ECG. *IEEE Transactions on Biomedical Engineering*. 1989;36(6):585-90. DOI: 10.1109/10.29452
  51. Carruth JE, Mirvis SB, Brogan DR, Wenger NK. The electrocardiogram in normal pregnancy. *American heart journal*. 1981;102(6):1075-8. DOI: 10.1016/0002-8703(81)90497-x
  52. Huiskamp GJ, van Oosterom A. Heart position and orientation in forward and inverse electrocardiography. *Med Biol Eng Comput*. 1992;30(6):613-20. DOI: 10.1007/bf02446793
  53. Hoekema R, Uijen GJH, van Erning L, van Oosterom A. Interindividual variability of multilead electrocardiographic recordings: influence of heart position. *J Electrocardiol*. 1999;32(2):137-48.



# **Part III**

## Enhancing the diagnostic value of the 12-lead ECG

### **Chapter 8**

Feasibility study of a 3D camera to reduce electrode repositioning errors during longitudinal ECG acquisition

### **Chapter 9**

Big Data and Artificial Intelligence: Opportunities and Threats in Electrophysiology



$\emptyset$

$(x, y) = \int_{x_0}^{x_1} \int_{y_0}^{y_1}$

$v_2 / c^2$

$v_{cg}$

$v_{cg}$

ind



## Chapter 8

Feasibility study of a 3D camera to reduce electrode repositioning errors during longitudinal ECG acquisition

RW Roudijk\*, MJ Boonstra\*, J Ruisch, M Kastelein, E van Dam, M Schellenkens, P Loh, and PM van Dam.

\*The first two authors contributed equally to this manuscript

*Journal of Electrocardiology* 2021 May;66(1):69-76

## **Abstract**

Longitudinal monitoring of sometimes subtle waveform changes of the 12-lead electrocardiogram (ECG) is complicated by patient-specific and technical factors, such as the inaccuracy of electrode repositioning. This feasibility study uses a 3D camera to reduce electrode repositioning errors, reduce ECG waveform variability and enable detailed longitudinal ECG monitoring.

Per subject, three clinical ECGs were obtained during routine clinical follow-up. Additionally, two ECGs were recorded guided by two 3D cameras, which were used to capture the precordial electrode locations and direct electrode repositioning. ECG waveforms and parameters were quantitatively compared between 3D camera guided ECGs and clinical ECGs. Euclidian distances between original and repositioned precordial electrodes from 3D guided ECGs were measured.

Twenty subjects (mean age  $65.1 \pm 8.2$  years, 35% females) were included. The ECG waveform variation between routine ECGs was significantly higher compared to 3D guided ECGs, for both the QRS complex (correlation coefficient = 0.90 vs 0.98,  $p < 0.001$ ) and the STT segment (correlation coefficient = 0.88 vs. 0.96,  $p < 0.001$ ). QTc interval variation was reduced for 3D camera guided ECGs compared to routine clinical ECGs (5.6 ms vs. 9.6 ms,  $p = 0.030$ ). The median distance between 3D guided repositioned electrodes was 10.0 [6.4–15.2] mm, and did differ between males and females ( $p = 0.076$ ).

3D guided repositioning of precordial electrodes resulted in, a low repositioning error, higher agreement between waveforms of consecutive ECGs and a reduction of QTc variation. These findings suggest that longitudinal monitoring of disease progression using 12-lead ECG waveforms is feasible in clinical practice.

## Introduction

The standard 12-lead electrocardiogram (ECG) is one of the fundamental diagnostic tools in clinical medicine.<sup>1</sup> The ECG visualizes the electrical activity of the heart by recording body surface potentials using electrodes positioned on the thorax of the patient. These electrode positions are standardized and based on anatomical landmarks.<sup>2</sup> In routine clinical practice, the ECG is used to diagnose both acute cardiac diseases such as acute coronary syndrome, and for longitudinal monitoring of cardiac diseases such as progression of cardiomyopathy.

During longitudinal follow-up, monitoring of sometimes subtle waveform changes by consecutive ECG recordings is complicated by patient specific factors and technical errors, thereby compromising day-to-day comparison of ECG waveforms (Figure 1).<sup>3,4</sup> ECG waveforms are influenced by heart rhythm, heart rate, cardiac anatomy, ventricular wall thickness, cardiac electrophysiology and cardiovascular disease.<sup>5</sup> Other factors vary only limited over time but may also influence ECG waveforms such as the orientation of the heart in the thorax and the shape of the thorax.<sup>6-8</sup> Furthermore, electrode (mis)placement is a major technical error source when recording ECGs in clinical practice.<sup>9</sup> Although minor shifts in precordial electrode

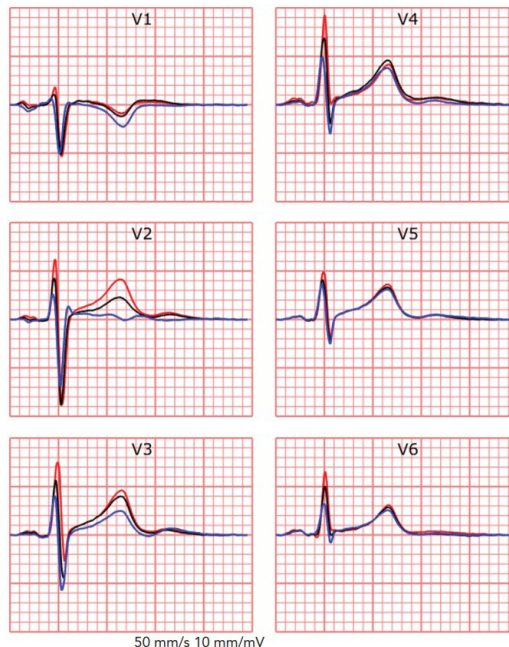


**Figure 1.** Effect of electrode position variation on ECG waveforms. Using simultaneous recordings of a 64-lead body surface potential map, the effect of electrode positioning of QRS and STT segment waveforms can be observed. Precordial leads were measured 4 cm upward (blue) or downward (red) referenced to the standard 12-lead electrode positioning (black). Limb leads were not displayed. The body surface potential map is a simultaneous measurement and thus the displayed beats were recorded simultaneously.

positions up to 10 mm have a mild influence, shifts of >20 mm significantly affect the ECG waveform morphology possibly resulting in misdiagnosis.<sup>10-12</sup> Variability in electrode positioning between consecutive ECG measurements is common and limits the applicability of the ECG during longitudinal monitoring of cardiovascular disease over time.<sup>10,13,14</sup> Therefore, achieving identical electrode positions during longitudinal follow-up measurements is likely to enhance the diagnostic value of long-term ECG monitoring.

For this purpose, a 3D camera application was developed to capture the position of precordial ECG electrodes and to allow for accurate electrode repositioning for consecutive 12-lead ECG recordings<sup>15,16,17</sup>. In this feasibility study the 3D camera algorithm was tested in a clinical setting. The accuracy of 3D camera guided electrode repositioning was assessed, and the variation in the ECG waveforms and parameters were compared between routine clinical practice and 3D camera guided electrode repositioning.

## Material and methods

### Patient population

Patients referred for routine clinical follow-up after a recent ablation procedure for paroxysmal or permanent atrial fibrillation (AF) or atrial flutter were enrolled

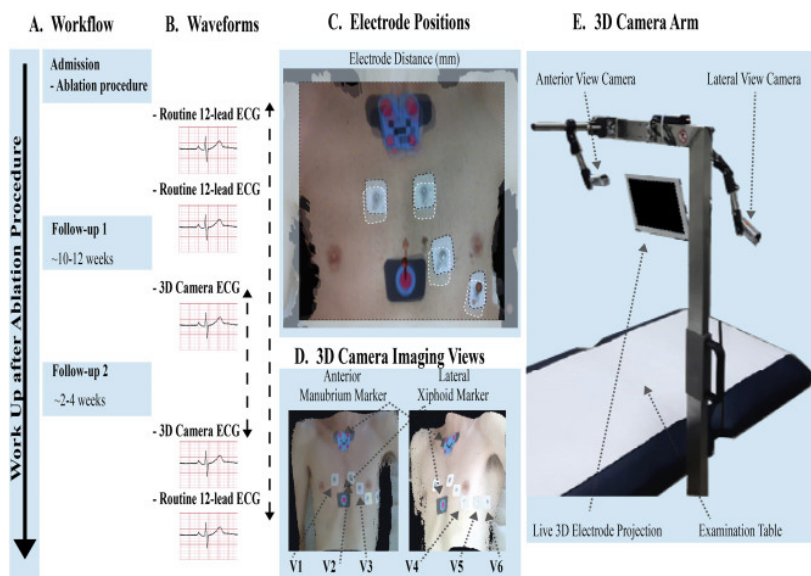


**Figure 2.** Study workflow. Workflow of the study. Panel A shows the routine follow-up and moments of ECG acquisition. Panel B depicts the ECG waveform comparisons between routine ECGs and 3D camera assisted ECGs using Pearson correlation coefficient and the root mean square. Panel C shows the comparison of two 3D photos with electrode positions from which the coordinates of the electrodes were compared. The 3D camera views, markers and electrode positions are shown in Panel D. The anterior view captures both anatomical markers and predominantly leads V1–4 and a lateral view captures leads V5–6. Panel E shows an overview of the two 3D cameras positioned on the camera arm.

in this study. Each subject underwent standard clinical follow-up after the ablation procedure and additionally two consecutive 3D camera guided ECG measurements were performed. The workflow of the study is described in Figure 2. The study protocol was approved by the local institutional review board (UMC Utrecht, Utrecht, the Netherlands, protocol nr.19/065). The study was conducted according to the declaration of Helsinki and all subjects gave informed consent.

### Data acquisition

For each subject, five ECGs were obtained (Figure 2): three routine clinical ECGs (GE Healthcare, MAC5500, Chicago, Illinois, USA, 0.67 Hz high-pass filter, 50 Hz notch filter, 150 Hz low pass filter, 500 Hz sampling frequency) with electrodes positioned according to routine clinical practice and two 3D camera guided ECGs (Mortara WAM, Welch Allyn, Skaneateles Falls, NY, USA, 0.05 Hz high-pass filter, 50 Hz notch filter, 150 Hz low pass filter 1000 Hz sampling frequency). The technicians recording the routine clinical ECGs were blinded to whether subjects participated in this study. Subjects with persistent AF at the moment of ECG recording were excluded from the analysis as this may affect QRS complex and STT segment waveform morphology (Figure 3). ECGs were recorded without cessation of or changes in antiarrhythmic drug therapy. The raw data were extracted from the data acquisition module and the median beat incorporated in this data was used for analysis.

### 3D camera ECGs

During the first study visit, a manubrium marker was placed on the thorax surface directly below the jugular notch and a xiphoid marker was placed directly below the xiphoid process (Figure 2). Ten ECG electrodes were positioned according routine clinical care using the ACC/HRS recommendations.<sup>2</sup> Precordial electrode positions

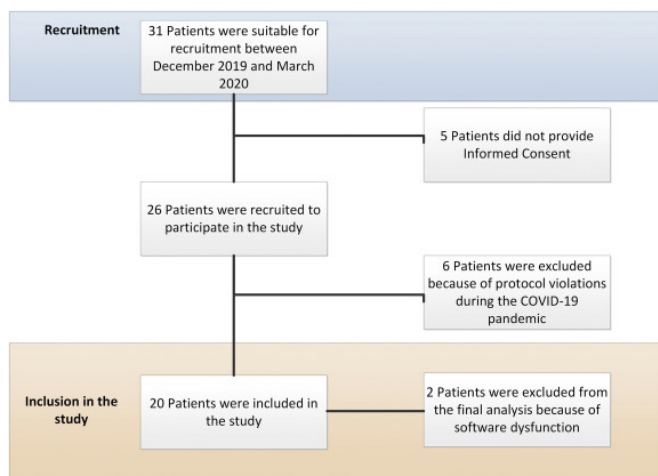


**Figure 3.** Flowchart with included and excluded patients. Flowchart showing the patients suitable for recruiting and the number of patients that were included in the final analysis.

were captured using two 3D cameras (Intel Real Sense D435) through a dedicated 3D camera software tool (QRS-VISION, PEACS BV, version 2).<sup>2,15,16</sup> The 3D cameras were mounted on a custom-made frame that was attached to the examination table to ensure a stable camera position. A standard 12-lead ECG recording was obtained (Figure 2). Limb electrodes were positioned at both wrists and the left leg, according to clinical standard practice. During offline analysis, captured 3D photos were fitted to a standard thoracic model and the precordial electrode positions were segmented based on both 3D photos (anterior and lateral, Figure 2). Precordial electrode locations were exported as six 3D vertices.

During the second study visit, the manubrium and xiphoid marker were repositioned as during the first visit. After capturing these anatomical markers and the thorax using 3D photos, the standard thoracic model was fitted to the 3D photos. Thereafter, precordial electrode positions from the first visit were projected onto the live 3D image stream on a tablet located above the patient (Figure 2, panel E). Next, the ECG electrodes were repositioned based on this live visualization and a second standard 12-lead ECG (Mortara) was obtained.

#### *Routine practice ECGs*

Prior to ablation, two 12-lead ECGs (GE) were obtained per subject according to routine clinical practice. The ECG electrodes were positioned by the ECG technician without the use of the 3D camera. After the second study visit, a third 12-lead ECG was obtained, also according to routine clinical practice.

#### *Offline ECG analysis*

For each subject, raw ECG data were exported from the ECG machines. From the raw data, the median beat computed by the ECG machines was used for analysis. Furthermore, ECG annotations of P wave onset, P wave end, QRS onset, QRS end, T-wave onset and T-wave end annotated by the automated ECG machine system were used. Thereof, RR interval, PR interval, P wave duration, QRS duration and QT interval were computed and used for analysis of ECG characteristics. The QT interval was then corrected (QTc) using the Bazett's formula.

#### *Comparison of ECG waveforms*

Two ECG waveform comparisons were performed: (1) between routine 12-lead ECGs performed at the outpatient clinic before and after ablation, and (2) the ECGs with electrode positions recorded by the 3D camera during the first and second visit (Figure 2, Panel B). To enable ECG waveform comparison, consecutive waveforms were aligned on the onset of the QRS complex. To allow for quantitative STT segment comparison and to enable waveform morphology comparison, the STT segments were normalized in time. The T<sub>peak</sub> was determined from a method proposed by van Oosterom<sup>18</sup>, based on the dominant T-wave signal represented by

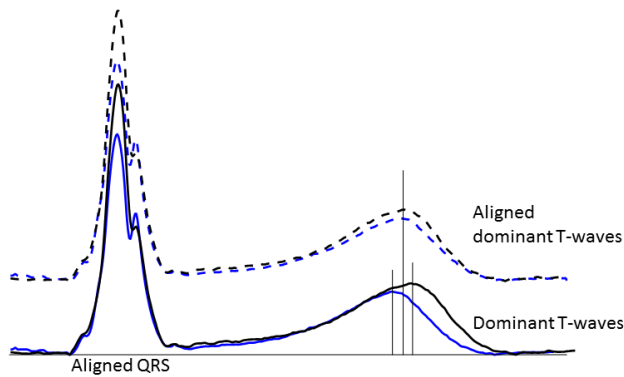


**Figure 4.** Alignment of ECGs. The alignment of median beats of two subsequently recorded ECGs using the RMSE signal of both QRS aligned (dotted line) waveforms. The STT segment of both signals are normalized, thereby enabling waveform comparison.

the root mean square of the STT segment of the ECG signals (Figure 4). Median beats were automatically aligned by minimizing the relative difference between the QRS complexes, where after STT segments were normalized.

#### *Comparison of electrode positions using the 3D Camera*

Median electrode positioning error between the first and second 3D camera guided ECGs was determined. Euclidian distances between precordial electrodes were measured using the electrode segmentations of the first and second 3D guided ECG (Figure 2, Panel C).

#### *Statistical analysis*

Data were presented as mean  $\pm$  standard deviation (SD) or median and interquartile range (IQR) as appropriate. Categorical variables were presented as numbers with percentages. Differences between electrode locations and ECG parameters were compared using a Student t-test, One-way ANOVA, Mann-Whitney U test, Kruskal Wallis test with Tukey or Dunn's correction for multiple comparisons as appropriate. For all subjects, the variation in QTc intervals of ECGs guided by the 3D camera (two QTc measurements per subject) and routine clinical ECGs (three QTc measurements per subject) was approximated by the variance of QTc values for each single subject over multiple measurements. The standard deviation for both sets of QTc measurements was calculated for all patients and compared between 3D guided ECGs and routine clinical ECGs using the Student t-test. A lower averaged standard deviation was expected when the 3D camera ECGs resulted in more consistent QTc measurements. ECG waveform morphologies were compared using Pearson's correlation coefficient (CC) and root mean square error (RMSE). Analysis was performed using GraphPad Prism (v8.3.0, La Jolla, California, USA) and R (v3.5.1, Foundation for Statistical Computing, Vienna, Austria). Two-tailed p-values of  $\leq 0.05$  were considered statistically significant.

## Results

### Population

Twenty subjects (mean  $65.1 \pm 8.2$  years old, 35% females) were included in the study (Table 1). The majority ( $n = 18$ , 90%) of subjects were in sinus rhythm at the moment of ECG recording, one (5%) had atrial pacing and one (5%) had ventricular pacing. Two patients were excluded from electrode positioning analysis because of software failure (Figure 3). Furthermore, due to the COVID-19 pandemic, 3D camera measurements were obtained within different time intervals, with a median of 16 [15–67] days.

### Comparison of ECG parameters

The comparison of ECG parameters is shown in Table 2. The RR intervals were significantly different when comparing 3D camera guided ECGs and routine clinical ECGs ( $p = 0.020$ ). Median values for QRS duration and QT interval did not differ significantly. Also, the median value for the QTc interval did not significantly differ

**Table 1.** Baseline characteristics.

	Avg $\pm$ SD or N (%)
Age (yrs)	$65.1 \pm 8.2$
Female	7/20 (35%)
Length (cm)	$178.6 \pm 8.8$
Weight (kg)	$85.6 \pm 10.3$
BSA (m <sup>2</sup> )	$2.05 \pm 0.2$
BMI (kg/m <sup>2</sup> )	$26.9 \pm 3.7$
<b>Rhythm baseline</b>	
Sinus rhythm	18 (90)
Atrial pacing	2 (10)
<b>Ablation procedure indication</b>	
Atrial Fibrillation	19 (95)
Atrial Flutter	4 (20)
<b>Comorbidity</b>	
CHA <sub>2</sub> DS <sub>2</sub> - VASc score	$1.6 \pm 1.3$
Sick Sinus Syndrome	3 (15)
Hypertension	7 (35)
Diabetes Mellitus	0 (0)
Hypercholesterolemia	3 (15)
Coronary Artery Disease	4 (20)
LVEF (%)	$54.9 \pm 7.5$
<b>Medication</b>	
Betablocker	6 (30)
Flecainide	10 (50)
Sotalol	5 (25)
Calcium antagonist	5 (20)
Amiodaron	0 (0)

Baseline characteristics of all subjects included in the study. Abbreviations: BMI = body mass index; BSA = body surface area; LVEF = left ventricular ejection fraction.



**Table 2.** Comparison of ECG parameters

	3D vs 3D ECGs	Routine vs Routine ECGs	P-value
RR interval (ms)	914 [779 - 1045]	839 [740 - 1000]	0.020
PR interval (ms)	169 [80 - 281]	156 [72 - 272]	0.458
P-wave duration	113 [97 - 123]	108 [64 - 172]	0.117
QRS duration (ms)	100 [92 - 108]	94 [88 - 100]	0.995
QT interval (ms)	403 [371 - 428]	404 [378 - 422]	0.999
QTc (ms, *)	401 [389 - 435]	429 [409 - 467]	0.450

Comparison of ECG parameters between ECGs performed with either assistance of the 3D camera or ECG performed during routine clinical practice. \* = ECG machine vendor derived QT interval correction for the RR interval using Bazett correction, ms = milliseconds.

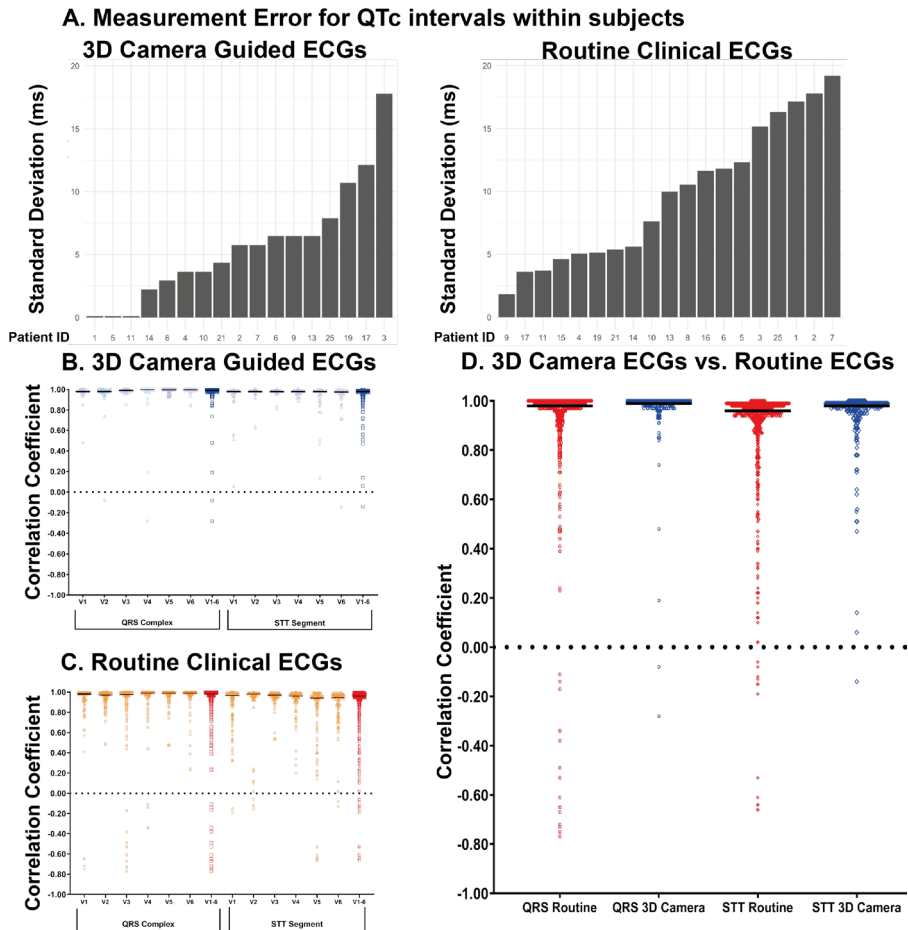


**Figure 5.** QTc interval and ECG waveform comparison. Panel A shows the measurement error within subjects for the QTc interval, stratified between 3D camera guided ECGs and routine clinical ECGs. Panel B shows the correlation coefficients between 3D camera guided ECGs (blue) and Panel C shows the correlation coefficients between routine clinical ECGs (red), stratified for the QRS complex and the STT segment. Panel D compares the correlation coefficients between 3D camera guided ECGs and routine clinical ECGs, stratified for the QRS complex ( $p < 0.001$ ) and the STT segment ( $p < 0.001$ ).

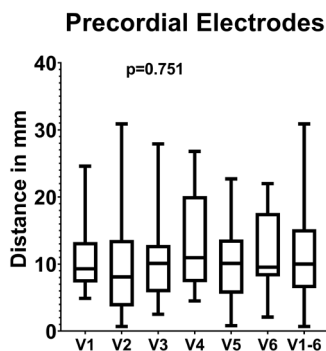


**Figure 6.** Distances between 3D Camera guided Repositioned Electrodes. Distances between the electrode position coordinates of 3D camera guided ECGs, stratified for the specific precordial leads and for all the overall distance between electrodes. Values are displayed as median (line in box) and interquartile range (error bars).

between 3D camera ECGs and routine ECGs. The consistency of ECG parameters during consecutive recordings in a single subject was evaluated by comparing the variation in standard deviation of the QTc intervals. A significantly smaller variation in QTc interval measurements was found within subjects comparing 3D guided to routine clinical ECGs (5.6 ms vs. 9.6 ms,  $p = 0.030$ , Figure 5A).

#### Comparison of electrode positions

The median distance between 3D camera guided repositioned electrodes was 10.0 [6.4–15.2] mm with the highest variation in V4 (Figure 6 and Table 4). There was no significant difference between specific precordial electrode positions ( $p = 0.751$ ). No significant difference between males and females (10.2 [7.5–16.9] vs. 8.7 [5.5–11.3],  $p = 0.076$ ) was observed. One subject was excluded from this analysis due to offline software malfunctioning and one was excluded due to subject mix-up.

**Table 4.** Differences for repositioned precordial leads electrode positions guided by the 3D camera.

Leads	Median distance (mm)
V1	9.3 [7.3 – 13.3]
V2	8.1 [3.7 – 13.6]
V3	10.1 [5.8 – 12.9]
V4	11.0 [7.3 – 20.2]
V5	10.1 [5.6 – 13.7]
V6	9.6 [8.2 – 17.6]
Overall (V1-6)	10.0 [6.4 – 15.2]
Overall males	10.2 [7.5 – 16.9]
Overall females	8.7 [5.5 – 11.3]
Overall sinus rhythm	10.1 [6.4 – 16.5]
Overall paced rhythms	8.6 [5.9 – 11.4]

Differences in millimeters (mm) between the electrode position coordinates from the 3D camera guided ECGs. Values are displayed as median and interquartile range.

**Table 3.** Waveform comparison

3D vs 3D ECGs			Routine vs Routine ECGs		CC 3D vs. Routine ECGs	RMS 3D vs. Routine ECGs
P-wave	CC	RMS [mV]	CC	RMS [mV]	P-value	P-value
V1	0.65 [0.11 – 0.90] (0.51, -0.80 – 0.99)	0.07 [0.03 – 0.17] (0.10, 0.01 – 0.35)	0.50 [0.01 – 0.88] (0.87, -0.75 – 1.0)	0.08 [0.03 – 0.13] (0.11, 0.01– 0.52)	0.361	<0.001
V2	0.60 [0.11 – 0.90] (0.47, -0.78 – 0.99)	0.10 [0.06 – 0.32] (0.18, 0.01 – 0.57)	0.52 [0.08 – 0.85] (0.95, 0.78 – 1.0)	0.15 [0.04 – 0.25] (0.18, 0.01– 0.83)	0.503	<0.001
V3	0.69 [0.16 – 0.91] (0.54, -0.61 – 0.99)	0.13 [0.06 – 0.41] (0.21, 0.01 – 0.69)	0.54 [-0.04– 0.83] (0.81, -0.77 – 1.0)	0.19 [0.06 – 0.27] (0.21, 0.01– 0.74)	0.106	<0.001
V4	0.63 [0.15 – 0.91] (0.52, -0.66 – 0.99)	0.16 [0.06 – 0.31] (0.21, 0.01 – 0.59)	0.61 [-0.08– 0.88] (0.91, -0.34 – 1.0)	0.16 [0.06 – 0.26] (0.20, 0.01– 0.84)	0.318	<0.001
V5	0.59 [-0.02 – 0.86] (0.45, -0.46 – 0.99)	0.11 [0.04 – 0.29] (0.20, 0.02 – 0.65)	0.58 [-0.09– 0.86] (0.94, 0.47 – 1.0)	0.16 [0.06 – 0.22] (0.17, 0.01 – 0.95)	0.762	<0.001
V6	0.59 [0.09 – 0.93] (0.47, -0.61 – 0.98)	0.09 [0.03 – 0.24] (0.14, 0.01 – 0.42)	0.60 [-0.13– 0.85] (0.94, 0.23 – 1.0)	0.09 [0.04 – 0.15] (0.11, 0.01– 0.61)	0.430	<0.001
V1-V6	0.62 [0.26 – 0.90] (0.50, -0.80 – 0.99)	0.11 [0.03 – 0.27] (0.17, 0.01 – 0.65)	0.56 [-0.05– 0.86] (0.41, -0.92 – 1.0)	0.13 [0.04 – 0.22] (0.16, 0.01– 0.95)	0.208	<0.001
QRS complex	CC	RMS [mV]	CC	RMS [mV]	P-value	P-value
V1	0.99 [0.97 – 0.99] (0.98, 0.93 – 1.00)	5 [3 – 29] (20, 2 – 81)	0.98 [0.91 – 0.99] (0.87, -0.75 – 1.0)	14 [7 – 64] (51, 1 – 438)	0.685	0.120
V2	0.99 [0.97 – 1.00] (0.99, 0.91 – 1.00)	9 [5 – 51] (37, 3 – 241)	0.97 [0.93 – 0.99] (0.95, 0.78 – 1.0)	23 [10 – 88] (63, 1 – 308)	0.583	0.643
V3	0.99 [0.98 – 1.00] (0.99, 0.96 – 1.00)	12 [5 – 44] (28, 3 – 122)	0.98 [0.88 – 0.99] (0.81, -0.77 – 1.0)	27 [13 – 79] (80, 3 – 461)	0.025	0.173
V4	1.00 [0.98 – 1.00] (0.93, -0.28 – 1.00)	15 [6 – 31] (34, 2 – 211)	0.99 [0.96 – 1.00] (0.91, -0.34 – 1.0)	22 [12 – 45] (54, 2 – 384)	0.424	>0.999
V5	1.00 [1.00 – 1.00] (0.99, 0.94 – 1.00)	15 [3.9 – 44.6] (29, 2 – 164)	0.99 [0.95 – 1.00] (0.94, 0.47 – 1.0)	19 [10 – 60] (61, 2 – 454)	<0.001	0.710
V6	1.00 [0.99 – 1.00] (0.96, 0.97 – 1.00)	9.7 [3.5 – 38.3] (20, 2 – 72)	0.99 [0.97 – 1.00] (0.94, 0.23 – 1.0)	17 [9 – 60] (45, 2 – 248)	0.004	0.085
V1-V6	0.99 [0.98 – 1.00] (0.98, -0.28 – 1.00)	11 [4 – 39] (38, 2– 241)	0.98 [0.94 – 1.00] (0.90, -0.75 – 1.0)	21 [10 – 64] (60, 1 – 461)	<0.001	<0.001
STT segment	CC	RMS [mV]	CC	RMS [mV]	P-value	P-value
V1	0.98 [0.93 – 0.99] (0.95, 0.55 – 1.00)	2 [1 – 36] (15, 1 – 60)	0.97 [0.87 – 0.99] (0.89, -0.19 – 1.0)	5 [3 – 39] (31, 1 – 222)	0.700	0.659
V2	0.98 [0.98 – 0.99] (0.99, 0.95 – 1.00)	3 [4 – 56] (27, 2 – 112)	0.98 [0.95 – 0.99] (0.93, -0.15 – 1.0)	10 [4 – 75] (40, 2 – 226)	0.234	0.680
V3	0.98 [0.98 – 0.99] (0.98, 0.96 – 1.00)	5 [3 – 56] (27, 1 – 94)	0.97 [0.95 – 0.99] (0.95, 0.53 – 1.0)	9 [4 – 81] (41, 1 – 151)	0.107	>0.999
V4	0.99 [0.96 – 0.99] (0.98, 0.92 – 1.00)	5 [2 – 57] (25, 1 – 106)	0.96 [0.92 – 0.98] (0.91, 0.20 – 1.0)	11 [4 – 54] (36, 1 – 182)	0.009	>0.999
V5	0.98 [0.88 – 0.99] (0.93, 0.47 – 1.00)	4 [1 – 37] (23, 1 – 99)	0.94 [0.82 – 0.97] (0.76, -0.66 – 1.0)	11 [4 – 57] (32, 1 – 160)	0.009	>0.999
V6	0.98 [0.93 – 0.99] (0.96, 0.72 – 1.00)	2 [1.2 – 31] (16, 1 – 68)	0.95 [0.86 – 0.97] (0.86, -0.13 – 0.99)	7 [3 – 35] (20, 1 – 90)	0.002	>0.999
V1-V6	0.98 [0.96 – 0.99] (0.96, 0.43 – 1.00)	4 [2 – 45] (22, 1 – 112)	0.96 [0.91 – 0.98] (0.88, -0.66 – 1.00)	9 [3 – 55] (33, 1 – 226)	<0.001	0.001

The correlation and root mean square of ECG waveforms. For the P-wave, QRS complex and STT segment, stratified for the precordial leads and an overall comparison which included leads V1-6. Values are displayed as median and [interquartile range], and (mean, full range). Abbreviations: CC = correlation coefficient, RMS = root mean square, ECG = electrocardiogram, 3D = three-dimensional.

### *Comparison of ECG waveforms*

The overall CC and RMSE for QRS complexes and the STT segments were significantly lower for the 3D camera guided ECGs compared to routine ECGs (average, median, interquartile range and full ranges are reported in Table 3 and Figure 5 Panel B-D). QRS waveforms of repeated 3D camera guided ECGs had an average CC of 0.98, with a range between  $-0.28$  to  $1.00$ . The QRS complexes of repeated ECGs derived from routine clinical practice had an average CC of 0.90 with a broader range between  $-0.75$  to  $1.00$ . The sensitivity of ECG signals to electrode misplacement, was shown in several cases. For example, in patient 11 the V4 electrode was misplaced by 11.4 mm, as determined by the 3D camera images, which resulted in a CC between repeated ECG waveforms of  $-0.28$ . The STT segments of 3D camera guided ECGs had an average CC of 0.96, ranging between 0.43 and  $1.00$ , while the STT segments of routine clinical practice ECGs had an average CC of 0.88, with a broader range between  $-0.66$  to  $1.00$ . The variation in QRS waveforms and STT segments was significantly higher between repeated routine clinical ECGs compared to repeated 3D camera guided ECGs ( $p < 0.001$  for QRS complexes and  $p < 0.001$  for STT segments).

## **Discussion**

The main findings of this study are: (1) 3D camera guided electrode (re)positioning is feasible, (2) the correlation between consecutive 3D camera guided ECGs was significantly higher (on average 8%) compared to consecutive ECGs performed during routine clinical practice, (3) the variation in QTc interval values was significantly smaller for 3D guided ECGs compared to routine clinical ECGs, and (4) median distances between 3D camera guided repositioned electrodes were well below the clinically accepted deviation (20 mm) for electrode repositioning.<sup>10,19,20</sup> These findings suggest that implementation of the described 3D camera algorithm may increase the diagnostic value of longitudinal monitoring of (subtle) ECG changes during clinical follow-up.

### *Agreement between ECG waveforms*

The variation in ECG waveforms of both the QRS complex and the STT segment was significantly higher in ECGs performed during routine clinical practice compared to 3D camera guided ECGs (Table 3, Figure 5D). Errors in positioning of the electrodes most likely have contributed to this difference as the interval between ECG measurements was rather short (median 16 days) and were not influenced by changes in drug therapy. This was also supported by the finding that rather small electrode repositioning errors, as determined by the 3D camera, already resulted in a significant low correlation value ( $-0.27$  in patient 11) when comparing ECG waveforms. Furthermore, comparison of P wave morphology showed no significant difference in variation between 3D camera guided ECGs and routine clinical practice, which may be explained by rather small P wave signals in the precordial leads. Reducing errors in electrode repositioning is relevant because the treating physician

needs to assess whether observed variations in ECG waveforms are due to newly developed cardiovascular disease, progression of cardiomyopathy, variations in cardiovascular physiological status or simply an effect of electrode (mis)placement. The implementation of the 3D camera to reduce errors in electrode positioning may enable this longitudinal monitoring of changes in ECG waveforms.

#### *Accuracy of repositioned electrodes*

To the best of our knowledge, this is the first study evaluating 3D camera guided 12-lead electrode (re)positioning.<sup>19</sup> Based on prior studies evaluating electrode positions using a panel of clinical experts, electrode shifts up to 20 mm were shown to produce clinically acceptable changes in ECG waveforms. Also, positioning of the lateral leads (V5–6) and positioning of precordial leads in female subjects was less accurate.<sup>19</sup> Earlier studies showed misplacement of electrode positions V2 and V3 had the largest effect on ECG waveforms.<sup>10,20</sup> In the present study, when using 3D camera guided electrode repositioning, a median distance of 10.0 mm was observed for all precordial leads which is favorable when performing longitudinal ECG monitoring of patients. The largest median distance in electrode repositioning was found in lead V4, this might be due to the location as the electrode was not positioned in full frontal view of both camera's and the image may be slightly distorted. Importantly, no significant differences in electrode distances were observed between sexes or specific leads thereby resulting in a more appropriate screening method.

#### *Clinical applications of the 3D camera method*

Prior studies that evaluated the repositioning of electrodes during consecutive measurements lacked an objective reference for comparison of electrode replacement.<sup>19</sup> Our study provided a clinical reference standard for comparison of electrode positions using acquired 3D images. Furthermore, the variation in ECG waveforms and ECG parameters of the 3D guided ECGs was remarkably small during serial measurements, even for serial QTc measurements within a single patient. 3D camera guided repositioning of electrodes may prove valuable when monitoring QTc interval variability in patients participating in a (pre-)clinical drug trials, during longitudinal monitoring of patients with cardiovascular disease or individuals with a presumed increased risk of developing cardiovascular disease. Furthermore, this technique may enable patients to reproduce electrode positions during ECG home monitoring using portable monitoring devices with a camera application.

#### *Challenges for clinical implementation*

Nowadays, the 12-lead ECG is a quickly and easily available diagnostic tool during acute situations like acute myocardial infarction or cardiac arrhythmias. This important character of the technique needs to be preserved, however aiding longitudinal monitoring using ECG waveforms requires further reduction in technical errors. To improve the accuracy of electrode positioning, the use of patches with

multiple integrated electrodes has been proposed. For example, a new electrode design with pre-positioned electrodes and pre-connected wires, was recently validated and showed reproducible ECGs. However, also in this study the differences in thorax shape remained a challenge.<sup>21</sup> The technique to (re)position electrodes presented in our study still requires anatomical landmarks during ECG acquisition, but the results of the present study show that repositioning of electrodes during follow-up is feasible and is less susceptible to differences in thorax shape.

The current study was performed in supine resting-position. Therefore, differences in body position on the performance of the 3D algorithm when utilized at the intensive care unit or coronary care unit were not accounted for in this study and must be assessed in subsequent studies.<sup>22</sup>

### *Limitations*

The small sample size, due to the COVID-pandemic, may influence the generalizability of the results. The electrode positions of the limb leads were not captured by the 3D camera, however, shifts of limb lead electrodes have shown to have less influence on the precordial ECG waveforms.<sup>10,20</sup> Of note, the limb lead electrodes were positioned on the shoulders for the first series of 10 patients whereas the last series of 10 patients had their limb lead electrodes positioned on the ankle and wrist. We included ECGs performed with ECG machines from two different ECG machine vendors with different sampling frequencies, which may have influenced the results of the study due to hardware and automated analysis differences in for example QRS onset detection. However, clinical difference in absolute values for QRS duration and QTc interval calculation remain small between vendor's algorithms.<sup>23</sup> Furthermore, the effects of variability in heart rate on QRS complex waveforms is yet unknown. Although variability in heart rate may affect QRS duration, a correction for heart rate on QRS duration was not performed, in line with standard clinical practice.<sup>24</sup>

### **Conclusion**

The 3D camera guided precordial electrode repositioning proved to be clinical feasible. Repositioning of electrodes guided by the 3D camera significantly reduced the variation of ECG waveforms and derived parameters such as the QTc interval, compared to routine clinical ECGs. The use of the 3D camera thus enables the longitudinal monitoring of the ECG waveforms, which may increase the diagnostic value of the ECG for patients with progressive cardiovascular disease or those individuals who are at risk of developing cardiovascular disease.

### *Acknowledgements*

This work was supported by the Dutch Heart Foundation (grant numbers CVON2015-12 eDETECT and QRS-Vision 2018B007).

## References

1. Holst H, Ohlsson M, Peterson C, Edenbrandt L. A confident decision support system for interpreting electrocardiograms. *Clin Physiol*. 1999;19(5):410-8.
2. Kligfield P, Gettes LS, Bailey JJ, Childers R, Deal BJ, Hancock EW, et al. Recommendations for the standardization and interpretation of the electrocardiogram: part I: the electrocardiogram and its technology a scientific statement from the American Heart Association Electrocardiography and Arrhythmias Committee, Council on Clinical Cardiology; the American College of Cardiology Foundation; and the Heart Rhythm Society endorsed by the International Society for Computerized Electrocardiology. *Journal of the American College of Cardiology*. 2007;49(10):1109-27.
3. Michaels L, Cadoret RJ. Day-to-day variability in the normal electrocardiogram. *British Heart Journal*. 1967;29(6):913-9.
4. Schijvenaars BJ, van Herpen G, Kors JA. Intraindividual variability in electrocardiograms. *J Electrocardiol*. 2008;41(3):190-6.
5. Durrer D, van Dam RT, Freud GE, Janse MJ, Meijler FL, Arzbaecher RC. Total excitation of the isolated human heart. *Circulation*. 1970;41(6):899-912.
6. Corlan AD, Macleod RS, De Ambroggi L. The effect of intrathoracic heart position on electrocardiogram autocorrelation maps. *J Electrocardiol*. 2005;38(2):87-94.
7. Hoekema R, Uijen GJ, van Oosterom A. On selecting a body surface mapping procedure. *J Electrocardiol*. 1999;32(2):93-101.
8. van Oosterom A, Hoekema R, Uijen GJ. Geometrical factors affecting the interindividual variability of the ECG and the VCG. *J Electrocardiol*. 2000;33 S:219-27.
9. García-Niebla J, Lllontop-García P, Valle-Racero JI, Serra-Autonell G, Batchvarov VN, De Luna AB. Technical Mistakes during the Acquisition of the Electrocardiogram. *Annals of Noninvasive Electrocardiology*. 2009;14(4):389-403.
10. Kania M, Rix H, Fereniec M, Zavala-Fernandez H, Janusek D, Mroczka T, et al. The effect of precordial lead displacement on ECG morphology. *Med Biol Eng Comput*. 2014;52(2):109-19.
11. Hill NE, Goodman JS. Importance of accurate placement of precordial leads in the 12-lead electrocardiogram. *Heart Lung*. 1987;16(5):561-6.
12. Herman MV, Ingram DA, Levy JA, Cook JR, Athans RJ. Variability of electrocardiographic precordial lead placement: a method to improve accuracy and reliability. *Clin Cardiol*. 1991;14(6):469-76.
13. Hedén B, Ohlsson M, Edenbrandt L, Rittner R, Pahlm O, Peterson C. Artificial neural networks for recognition of electrocardiographic lead reversal. *Am J Cardiol*. 1995;75(14):929-33.
14. Bond RR, Finlay DD, Nugent CD, Breen C, Guldenring D, Daly MJ. The effects of electrode misplacement on clinicians' interpretation of the standard 12-lead electrocardiogram. *Eur J Intern Med*. 2012;23(7):610-5.
15. Alioui S, Kastelein M, EM vD, PM vD, editors. *Automatic Registration of 3D Camera Recording to Model for Leads Localization*. Computing in Cardiology; 2017; Rennes, France: IEEE Computer Society Pres.
16. van Dam PM, Gordon JP, Laks M. Sensitivity of CIPS-computed PVC location to measurement errors in ECG electrode position: the need for the 3D camera. *J Electrocardiol*. 2014;47(6):788-93.
17. Perez-Alday EA, Thomas JA, Kabir M, Sedaghat G, Rogovoy N, van Dam E, et al. Torso geometry reconstruction and body surface electrode localization using three-dimensional photography. *J Electrocardiol*. 2018;51(1):60-7.
18. van Oosterom A. The dominant T wave. *J Electrocardiol*. 2004;37 Suppl:193-7.
19. McCann K, Holdgate A, Mahammad R, Waddington A. Accuracy of ECG electrode placement by emergency department clinicians. *Emerg Med Australas*. 2007;19(5):442-8.
20. Turzová M, Tysler M, Kneppo P. A model study of the sensitivity of body surface potential distribution to variations of electrode placement. *J Electrocardiol*. 1994;27(3):255-62.
21. Roy SK, Shah SU, Villa-Lopez E, Murillo M, Arenas N, Oshima K, et al. Comparison of electrocardiogram quality and clinical interpretations using prepositioned ECG electrodes and conventional individual electrodes. *J Electrocardiol*. 2020;59:126-33.
22. Adams MG, Drew BJ. Body Position Effects on the ECG. *Journal of Electrocardiology*. 1997;30(4):285-91.
23. Kligfield P, Badilini F, Denjoy I, Babaeizadeh S, Clark E, De Bie J, et al. Comparison of automated interval measurements by widely used algorithms in digital electrocardiographs. *Am Heart J*. 2018;200:1-10.
24. Mason JW, Strauss DG, Vaglio M, Badilini F. Correction of the QRS duration for heart rate. *J Electrocardiol*. 2019;54:1-4.



$\emptyset$

$(x, y) = \int_{x_0}^{x_1} \int_{y_0}^{y_1} \dots$

$v_2 / c^2$

$v_{cg}$

$S_u$

ind



# Chapter 9

## Big Data and Artificial Intelligence: Opportunities and Threats in Electrophysiology

RR van de Leur\*, MJ Boonstra\*, A Bagheri, RW Roudijk, A Sammani, K Taha, PAFM Doevendans, P van der Harst, PM van Dam, RJ Hassink, R van Es, and FW Asselbergs

\*The first two authors contributed equally to this manuscript

*Arrhythmia & electrophysiology review. 2020 Nov;9(3):146-154*

## **Abstract**

The combination of big data and artificial intelligence (AI) is having an increasing impact on the field of electrophysiology. Algorithms are created to improve the automated diagnosis of clinical ECGs or ambulatory rhythm devices. Furthermore, the use of AI during invasive electrophysiological studies or combining several diagnostic modalities into AI algorithms to aid diagnostics are being investigated. However, the clinical performance and applicability of created algorithms are yet unknown. In this narrative review, opportunities and threats of AI in the field of electrophysiology are described, mainly focusing on ECGs. Current opportunities are discussed with their potential clinical benefits as well as the challenges. Challenges in data acquisition, model performance, (external) validity, clinical implementation, algorithm interpretation as well as the ethical aspects of AI research are discussed. This article aims to guide clinicians in the evaluation of new AI applications for electrophysiology before their clinical implementation.

## Introduction

Clinical research that uses artificial intelligence (AI) and big data may aid the prediction and/or detection of subclinical cardiovascular diseases by providing additional knowledge about disease onset, progression or outcome. Clinical decision-making, disease diagnostics, risk prediction or individualised therapy may be informed by insights obtained from AI algorithms. As health records have become electronic, data from large populations are becoming increasingly accessible.<sup>1</sup> The use of AI algorithms in electrophysiology may be of particular interest as large data sets of ECGs are often readily available. Moreover, data are continuously generated by implantable devices, such as pacemakers, ICDs or loop recorders, or smartphone and smartwatch apps.<sup>2-6</sup>

Interpretation of ECGs relies on expert opinion and requires training and clinical expertise which is subjected to considerable inter- and intra-clinician variability.<sup>7-12</sup> Algorithms for the computerised interpretation of ECGs have been developed to facilitate clinical decision-making. However, these algorithms lack accuracy and may provide inaccurate diagnoses which may result in misdiagnosis when not reviewed carefully.<sup>13-18</sup>

Substantial progress in the development of AI in electrophysiology has been made, mainly concerning ECG-based deep neural networks (DNNs). DNNs have been tested to identify arrhythmias, to classify supraventricular tachycardias, to predict left ventricular ejection fraction, to identify disease development in serial ECG measurements, to predict left ventricular hypertrophy and to perform comprehensive triage of ECGs.<sup>6,19-23</sup> DNNs are likely to aid non-specialists with improved ECG diagnostics and may provide the opportunity to expose yet undiscovered ECG characteristics that indicate disease.

With this progress, the challenges and threats of using AI techniques in clinical practice become apparent. In this narrative review, recent progress of AI in the field of electrophysiology is discussed together with its opportunities and threats.

### *A Brief Introduction to Artificial Intelligence*

AI refers to mimicking human intelligence in computers to perform tasks that are not explicitly programmed. Machine learning (ML) is a branch of AI concerned with algorithms to train a model to perform a task. Two types of ML algorithms are supervised learning and unsupervised learning. Supervised learning refers to ML algorithms where input data are labelled with the outcome and the algorithm is trained to approximate the relation between input data and outcome. In unsupervised learning, input data are not labelled and the algorithm may discover data clusters in the input data.

In ML, an algorithm is trained to classify a data set based on several statistical and probability analyses. In the training phase, model parameters are iteratively tuned by penalising or rewarding the algorithm based on a true or false prediction. Deep learning is a sub-category of ML that uses DNNs as architecture to represent and learn from data. The main difference between deep learning and other ML algorithms is that DNNs can learn from raw data, such as ECG waveforms, in an end-to-end manner with extraction and classification united in the algorithm (Figure 1a). For example, in ECG-based DNNs, a matrix containing the time-stamped raw voltage values of each lead are used as input data. In other ML algorithms, features like heart rate or QRS duration are manually extracted from the ECG and used as input data for the classification algorithm.

To influence the speed and quality of the training phase, the setting of hyperparameters, such as the settings of the model architecture and training, is important. Furthermore, overfitting or underfitting the model to the available data set must be prevented. Overfitting can occur when a complex model is trained using a small data set. The model will precisely describe the training data set but fail to predict outcomes using other data (Figure 1b). On the other hand, when constraining the model too much, underfitting occurs (Figure 1b), also resulting in poor algorithm performance. To assess overfitting, a data set is usually divided into a training data

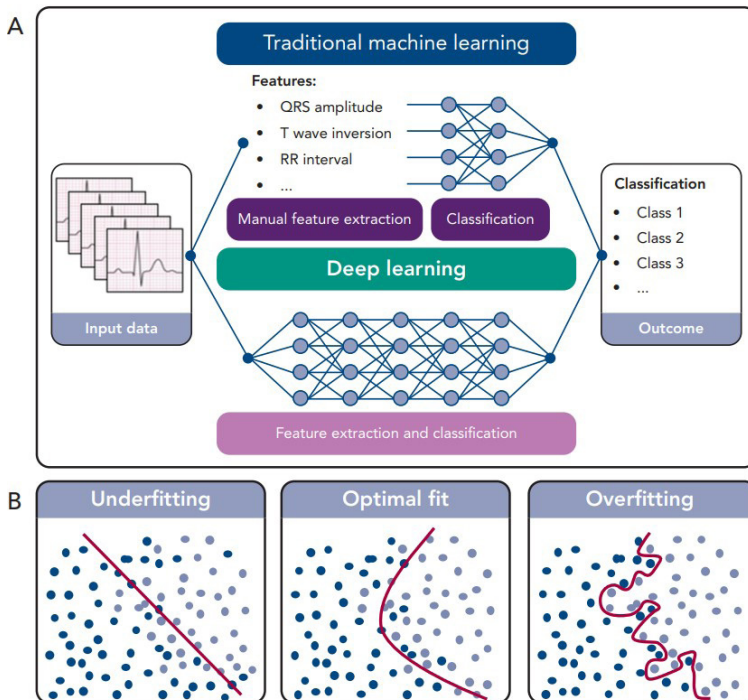


**Figure 1.** Traditional Machine Learning and Deep Learning with a Schematic Representation of Fitting a Model to a Data Set.

set, a validation data set and a test data set, or resampling methods are used, such as cross-validation or bootstrapping.<sup>24</sup>

To train and test ML algorithms, particularly DNNs, it is preferable to use a large data set, known as big data. Performance of highly dimensional algorithms – e.g., algorithms with many model parameters such as DNNs – depends on the size of the data set. For deep learning, more data is often required as DNNs have many non-linear parameters and non-linearity increases the flexibility of an algorithm. The size of a training data set has to reasonably approximate the relation between input data and outcome and the amount of testing data has to reasonably approximate the performance measures of the DNN.

Determining the exact size of a training and testing data set is difficult.<sup>25,26</sup> It depends on the complexity of algorithm (e.g. the number of variables), the type of the algorithm, the number of outcome classes and the difficulty of distinguishing between outcome classes as inter-class differences might be subtle. Therefore, size of the data set should be carefully reviewed for each algorithm. A rule of thumb for the adequate size of a validation data set is 50–100 patients per outcome class to determine overfitting. Recent studies published in the field of ECG-based DNNs used between 50,000 and 1.2 million patients.<sup>6,19,21,27</sup>

## Prerequisites for AI in Electrophysiology

Preferably, data used to create AI algorithms is objective, as subjectivity may introduce bias in the algorithm. To ensure clinical applicability of created algorithms, ease of access to input data, difference in data quality in different clinical settings as well as the intended use of the algorithm should be considered. In this section, we mainly focus on the data quality of ECGs, as these data are easily acquired and large data sets are readily available.

### *Technical Specifications of ECGs*

ECGs are obtained via electrodes on the body surface using an ECG device. The device samples the continuous body surface potentials and the recorded signals are filtered to obtain a clinically interpretable ECG.<sup>28</sup> As the diagnostic information of the ECG is contained below 100 Hz, a sampling rate of at least 200 Hz is required according to the Nyquist theorem.<sup>29–33</sup> Furthermore, an adequate resolution of at least 10  $\mu\text{V}$  is recommended to also obtain small amplitude fluctuations of the ECG signal. In the recorded signal, muscle activity, baseline wander, motion artefacts and powerline artefacts are also present, distorting the measured ECG. To remove noise and obtain an easily interpretable ECG, a combination of a high-pass filter of 0.67 Hz and a low-pass filter of 150–250 Hz is recommended, often combined with a notch filter of 50 Hz or 60 Hz. The inadequate setting of these filters might result in a loss of information such as QRS fragmentation or notching, slurring or distortion of the

ST segment. Furthermore, a loss of QRS amplitude of the recorded signal might be the result of the inappropriate combination of a high frequency cut-off and sampling frequency.<sup>28,34</sup> ECGs used as input for DNNs are often already filtered, thus potentially relevant information might already be lost. As DNNs process and interpret the input data differently, filtering might be unnecessary and potentially relevant information may be preserved. Furthermore, as filtering strategies differ between manufacturers and even different versions of ECG devices, the performance of DNNs might be affected when ECGs from different ECG devices are used as input data.

Apart from applied software settings, such as sampling frequency or filter settings, the hardware of ECG devices also differs between manufacturers. Differences in analogue to digital converters, type of electrodes used, or amplifiers also affect recorded ECGs. The effect of input data recorded using different ECG devices on the performance of AI algorithms is yet unknown. However, as acquisition methods may differ significantly between manufacturers, the performance of algorithms are likely to depend on the type or even version of the device.<sup>35</sup> Testing the performance of algorithms using ECGs recorded by different devices would illustrate the effect of these technical specifications on performance and generalisability.

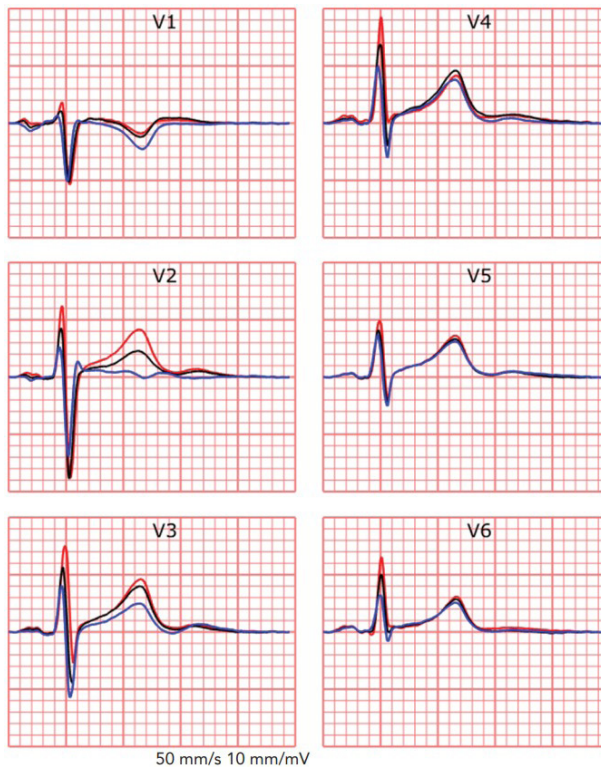


**Figure 2.** The Effect of Shifting Precordial Electrodes Upward or Downward. The effect of shifting precordial electrodes 4 m upward (blue) or downward (red) from standard 12-lead electrode positioning (black). Displayed signals were simultaneously recorded using a 64-electrode measurement set-up.

### ECG Electrodes

The recorded ECG is affected by electrode position with respect to the anatomical position of the heart and displacement of electrodes may result in misdiagnosis in a clinical setting.<sup>36,37</sup> For example, placement of limb electrodes on the trunk significantly affects the signal waveforms and lead reversal may mimic pathological conditions.<sup>38–41</sup> Furthermore, deviations in precordial electrode positions affect QRS and T wave morphology (Figure 2). Besides the effect of cardiac electrophysiological characteristics like anisotropy, His-Purkinje anatomy, myocardial disease and cardiac anatomy on measured ECGs, cardiac position and cardiac movement also affect the ECG.<sup>42–45</sup>

Conventional clinical ECGs mostly consist of the measurement of eight independent signals; two limb leads and six precordial leads (Figure 3b). The remaining four limb

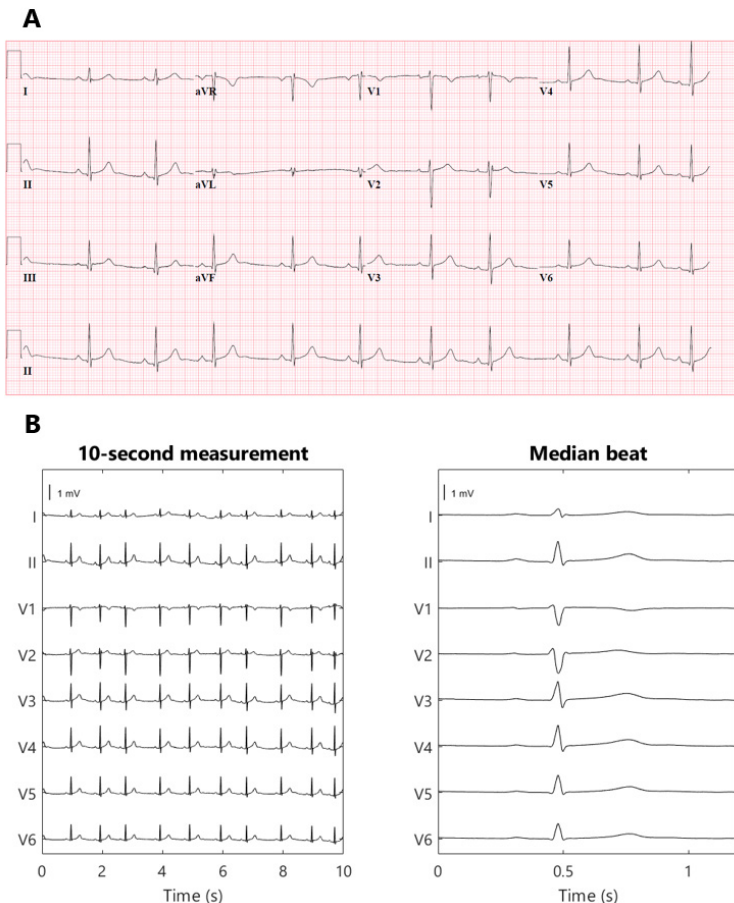


**Figure 3.** Standardised Clinical Visualised Signals. A: Three simultaneously recorded 2.5 second measurements and raw signals. B: A 10-second measurement and median beats of all recorded leads. Displayed signals are acquired using a General Electric Healthcare MAC 5500 ECG device.



leads are derived from the measured limb leads. However, body surface mapping studies identified the number of signals containing unique information up to 12 for ventricular depolarisation and up to 10 for ventricular repolarisation.<sup>46</sup> Theoretically, to measure all information about cardiac activity from the body surface, the number of electrodes should be at least the number of all unique measurements. However, conventional 12-lead ECG is widely accepted for most clinical applications. An adjustment of a lead position is only considered when a posterior or right ventricle MI or Brugada syndrome is suspected.<sup>27,47-50</sup>

The interpretation of ECGs by computers and humans is fundamentally different and factors like electrode positioning or lead misplacement might influence algorithms. However, the effect of electrode misplacement or reversal, disease-specific electrode positions or knowledge of lead positioning on the performance on DNNs remains to be identified. A recent study was able to identify misplaced chest electrodes, implying that the effect of electrode misplacement might be able to be identified and acknowledged by algorithms.<sup>51</sup> Studies have suggested that DNNs can achieve similar performance when fewer leads are used.<sup>50</sup>

#### *ECG Input Data Format*

ECGs can be obtained from the electronic database in three formats – visualised signals (as used in standard clinical practice), raw ECG signals or median beats. Raw signals are preferable for input for DNNs as visualised signals require digitisation, which results in a loss of signal resolution. Furthermore, raw ECG signals often consist of a continuous 10-second measurement of all recorded leads, whereas visualised signals may consist of 2.5 seconds per lead with only three simultaneously recorded signals per 2.5 seconds (Figure 3). A median beat per lead can also be used, computed from measured raw ECG signals or digitised visualised signals. Using the median beat might reduce noise, as noise is expected to cancel out by averaging all beats. Therefore, subtle changes in cardiac activation, invisible due to noise might become distinguishable for the algorithm. The use of the median beat may allow for precise analysis of waveform shapes or serial changes between individuals but rhythm information will be lost.

## **Opportunities for Artificial Intelligence in Electrophysiology**

### *Enhanced Automated ECG Diagnosis*

An important opportunity of AI in electrophysiology is the enhanced automated diagnosis of clinical 12-lead ECGs.<sup>8,11,12,20,52-54</sup> Adequate computerised algorithms are especially important when expert knowledge is not readily available, such as in pre-hospital care, non-specialist departments, or facilities that have minimal resources. If high-risk patients can be identified correctly, time-to-treatment can be reduced. However, currently available computerised ECG diagnosis algorithms lack accuracy.<sup>11</sup> Progress has been made in using DNNs to automate diagnosis or triage ECGs to



improve time-to-treatment and reduce workload.<sup>19,55</sup> Using very large data sets, DNNs can achieve high diagnostic performance and outperform cardiology residents and non-cardiologists.<sup>6,19</sup> Moreover, progress has been made in using ECG data for predictive modelling for AF in sinus rhythm ECGs or for the screening of hypertrophic cardiomyopathy.<sup>56-58</sup>

#### *Combining Other Diagnostic Modalities with ECG-based DNN*

Some studies have suggested the possibility of using ECG-based DNNs with other diagnostic modalities to screen for disorders that are currently not associated with the ECG. In these applications, DNNs are thought to be able to detect subtle ECG changes. For example, when combined with large laboratory data sets, patients with hyperkalaemia could be identified, or when combined with echocardiographic results, reduced ejection fraction or aortic stenosis could be identified. The created DNNs identified these three disorders from the ECG with high accuracy.<sup>21,50,59</sup> As a next step, supplementing ECG-based DNNs with body surface mapping data with a high spatial resolution (e.g. more than 12 measurement electrodes), inverse electrocardiography data or invasive electrophysiological mapping data, may result in the identification of subtle changes in the 12-lead ECG as a result of pathology.

#### *Artificial Intelligence for Invasive Electrophysiological Studies*

The application of AI before and during complex invasive electrophysiological procedures, such as electroanatomical mapping, is another major opportunity. By combining information from several diagnostic tools such as MRI, fluoroscopy or previous electroanatomical mapping procedures, invasive catheter ablation procedure time might be reduced through the accelerated identification of arrhythmogenic substrates. Also, new techniques such as ripple mapping may be of benefit during electroanatomical mapping studies.<sup>60</sup> Recent studies suggest that integration of fluoroscopy and electroanatomical mapping with MRI is feasible using conventional statistical techniques or ML, whereas others suggest the use of novel anatomical mapping systems to circumvent fluoroscopy.<sup>61-64</sup> Furthermore, several ML algorithms have been able to identify myocardial tissue properties using electrograms in vitro.<sup>65</sup>

#### *Ambulatory Device-based Screening for Cardiovascular Diseases*

One of the major current challenges in electrophysiology is the applicability of ambulatory rhythm devices in clinical practice. Several tools, such as implantable devices or smartwatch and smartphone-based devices, are becoming more widely used and continuously generate large amounts of data which would be impossible to evaluate manually.<sup>66</sup> Arrhythmia detection algorithms based on DNNs trained on large cohorts of ambulatory patients with a single-lead plethysmography or ECG device have shown similar diagnostic performance as cardiologists or implantable loop recorders.<sup>2,3,6</sup> Another interesting application of DNN algorithms are data from intracardiac electrograms before and during the activation of the defibrillator. Analysis

of the signals before the adverse event might provide insight into the mechanism of the ventricular arrhythmia, providing the clinician with valuable insights. Continuous monitoring also provides the possibility of identifying asymptomatic cardiac arrhythmias or detecting post-surgery complications. Early detection might overcome serious adverse events and significantly improve timely personalised healthcare.<sup>6,19</sup>

A promising benefit of smartphone applications for the early detection of cardiovascular disease is in early detection of AF. As AF is a risk factor for stroke, early detection may be important to prompt adequate anticoagulant treatment.<sup>67-69</sup> An irregular rhythm can be accurately detected using smartphone or smartwatch-acquired ECGs. Even predicting whether a patient will develop AF in the future using smartphone-acquired ECGs recorded during sinus rhythm has been recently reported.<sup>69,70</sup> Also, camera-based photoplethysmography recordings can be used to differentiate between irregular and regular cardiac rhythm.<sup>71,72</sup> However, under-detection of asymptomatic AF is expected as the use of applications requires active use and people are likely to only use applications when they have a health complaint. Therefore, a non-contact method with facial photoplethysmography recordings during regular smartphone use may be an interesting option to explore.<sup>70,73,74</sup>

Apart from the detection of asymptomatic AF, the prediction or early detection of ventricular arrhythmias using smartphone-based techniques are potentially clinically relevant. For example, smartphone-based monitoring of people with a known pathogenetic mutation might aid the early detection of disease onset. In some pathogenetic mutations, this may be especially relevant as sudden cardiac death can be the first manifestation of the disease. In these patients, close monitoring to prevent these adverse events by starting early treatment when subclinical signs are detected may provide clinical benefit.

## **Threats of Artificial Intelligence in Electrophysiology**

### *Data-driven Versus Hypothesis-driven Research*

Data from electronic health records are almost always retrospectively collected, leading to data-driven research, instead of hypothesis-driven research. Research questions are often formulated based on readily available data, which increases the possibility of incidental findings and spurious correlations. While correlation might be sufficient for some predictive algorithms, causal relationships remain of the utmost importance to define pathophysiological relationships and ultimately for the clinical implementation of AI algorithms. Therefore, big data research is argued to be in most cases solely used to generate hypotheses and controlled clinical trials remain necessary to validate these hypotheses. When AI is used to identify novel pathophysiological phenotypes, e.g. with specific ECG features, sequential prospective studies and clinical trials are crucial.<sup>75</sup>

### *Input Data*

Adequate labelling of input data is important for supervised learning.<sup>18,76,77</sup> Inadequate labelling of ECGs or the presence of pacemaker artefacts, comorbidities affecting the ECG or medication affecting the rhythm or conduction, might influence the performance of DNNs.<sup>13–18</sup> Instead of true disease characteristics, ECG changes due to clinical interventions are used by the DNN to classify ECGs. For example, a DNN using chest X-rays provided insight into long-term mortality, but the presence of a thoracic drain and inadequately labelled input data resulted in an algorithm that was unsuitable for clinical decision-making.<sup>77–80</sup> Therefore, the critical review of computerised labels and the identification of important features used by the DNN are essential.

Data extracted from ambulatory devices consist of real-time continuous monitoring data outside the hospital. As the signal acquisition is performed outside a standardised environment, signals are prone to errors. ECGs are more often exposed to noise due to motion artefacts, muscle activity artefacts, loosened or moved electrodes and alternating powerline artefacts. To accurately assess ambulatory data without the interference of artefacts, signals should be denoised or a quality control mechanism should be implemented. For both methods, noise should be accurately identified and adaptive filtering or noise qualification implemented.<sup>81–83</sup> However, as filtering might remove information, rapid real-time quality reporting of the presence of noise in the acquired signal is thought to be beneficial. With concise instructions, users can make adjustments to reduce artefacts and the quality of the recording will improve. Different analysis requires different levels of data quality and through classification recorded data quality, the threshold for user notification can be adjusted per analysis.<sup>84,85</sup>

### *Generalisability and Clinical Implementation*

With the increasing number of studies on ML algorithms, generalisability and implementation is one of the most important challenges to overcome. Diagnostic or prognostic prediction model research, from simple logistic regression to highly sophisticated DNNs, is characterised by three phases:

- > Development and internal validation.
- > External validation and updating for other patients.
- > Assessment of the implementation of the model in clinical practice and its impact on patient outcomes.<sup>86,87</sup>

During internal validation, the predictive performance of the model is assessed using the development data set through train-test splitting, cross-validation or bootstrapping. Internal validation is however insufficient to test generalisability of the model in 'similar but different' individuals. Therefore, external validation of established models is important before clinical implementation. A model can be

externally validated through temporal (same institution, later period), geographical (a different institution with a similar patient group) or domain (different patient group) validation. Finally, implementation studies, such as cluster randomised trials, before and after studies or decision-analytic modelling studies, are required to assess the effect of implementing the model in clinical care.<sup>86,87</sup>

Most studies in automated ECG prediction and diagnosis performed some type of external validation. However, no study using external validation in a different patient group or implementation study has been published so far. A study has shown similar accuracy to predict low ejection fraction from the ECG using a DNN through temporal validation as in the development study.<sup>88</sup> A promising finding was a similar performance of the algorithm for different ethnic subgroups, even if the algorithm was trained on one subgroup.<sup>89</sup> As a final step to validate this algorithm, a cluster randomised trial is currently being performed. This might provide valuable insight into the clinical usefulness of ECG-based DNNs.<sup>90</sup>

Implementation studies for algorithms using ambulatory plethysmography and ECG data are ongoing. For example, the Apple Heart Study assessed the implementation of smartphone-based AF detection.<sup>5</sup> More than 400,000 patients who used a mobile application were included, but only 450 patients were analysed. Implementation was proven feasible as the number of false alarms was low, but the study lacks insight into the effect of smartphone-based AF detection on patient outcome. Currently, the Heart Health Study Using Digital Technology to Investigate if Early AF Diagnosis Reduces the Risk of Thromboembolic Events Like Stroke IN the Real-world Environment (HEARTLINE; NCT04276441) is randomising patients to use the smartwatch monitoring device. The need for treatment with anticoagulation of patients with device-detected subclinical AF is also being investigated.<sup>4</sup>

A final step for the successful clinical implementation of AI is to inform its users about adequate use of the algorithm. Standardised leaflets have been proposed to instruct clinicians when, and more importantly when not, to use an algorithm.<sup>91</sup> This is particularly important if an algorithm is trained on a cohort using a specific subgroup of patients. Then, applying the model to a different population may potentially result in misdiagnosis. Therefore, describing the predictive performance in different subgroups, such as different age, sex, ethnicity and disease stage, is of utmost importance as AI algorithms are able to identify these by themselves.<sup>89,92-94</sup> However, as most ML algorithms are still considered to be 'black boxes', algorithm bias might remain difficult to detect.

### *Interpretability*

Many sophisticated ML methods are considered black boxes as they have many model parameters and abstractions. This is in contrast with the more conventional statistical

methods used in medical research, such as logistic regression and decision trees, where the influence of a predictor on the outcome is clear. The trade of complexity of models and interpretability for improved accuracy is important to acknowledge; with increased complexity of the network, interpretation becomes more complicated. But interpretability remains important to investigate false positives and negatives, to detect biased or overfitted models, to improve trust in new models or to use

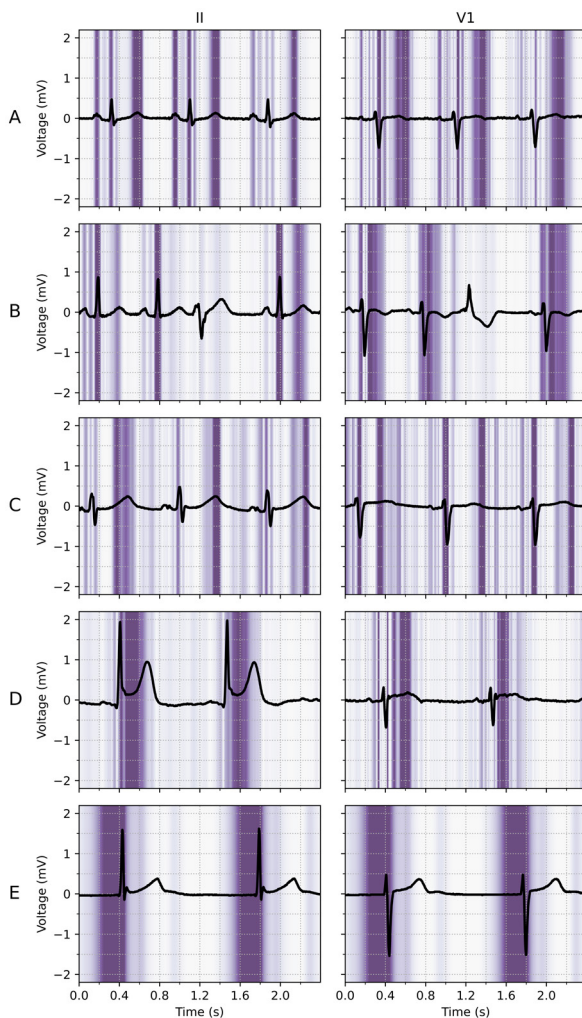


**Figure 4.** Important Regions for the Deep Neural Network to Predict Whether an ECG is Normal, Abnormal or Acute. ECG leads II and V1 with a superimposed guided Grad-CAM visualisation showing regions important for the deep neural network to predict whether an ECG is normal, abnormal or acute. A and B: Normal ECGs with focus on the P wave, QRS-complex, and T wave, while correctly ignoring a premature ventricular complex. C: Abnormal ECG with a long QT interval and a focus on the beginning and end of the QT-segment. D and E: Acute ECGs with an inferior ST-segment elevation MI (D) and a focus on the ST-segment and with a junctional escape rhythm (E) and a focus on the pre-QRS-segment, where the P wave is missing. Source: van de Leur et al. 2020.<sup>19</sup> Reproduced from the American Heart Association, Inc., by Wiley Blackwell under a Creative Commons (CC BY-NC-ND 4.0) licence.

the algorithms as a feature detector.<sup>95</sup> Within electrophysiology, few studies have investigated how the AI algorithms came to a certain result. For DNNs, three recent studies visualised individual examples using Guided Grad-CAM, a technique to show what the networks focus on. They showed that the DNN used the same segment of the ECG that a physician would use (Figure 4).<sup>19,27,96-98</sup>

Visualisation techniques may provide the ECG locations which the algorithms find important, but do not identify the specific feature. Therefore, the opportunity to identify additional ECG features remains dependent on expert opinion and analysis of the data by a clinician is still required. Visualisation techniques and their results are promising and help to increase trust in DNNs for ECG analysis, but additional work is needed to further improve the interpretability of AI algorithms in clinical practice.<sup>99,100</sup>

### *Uncertainty Estimation*

In contrast to physicians or conventional statistical methods, DNNs struggle to inform their users when they do not know and to give uncertainty measures about their predictions. Current models always output a diagnosis or prediction, even if they have not seen the input before. In a real-world setting, clinicians acknowledge uncertainty and consult colleagues or literature but a DNN always makes a prediction. Therefore, methods that incorporate uncertainty are essential before implementation of such algorithms is possible.<sup>101</sup>

Ideally, the algorithm provides results only when it reaches a high threshold of certainty, while the uncertain cases will still be reviewed by a clinician.<sup>101</sup> For DNNs, several new techniques are available to obtain uncertainty measures, such as Bayesian deep learning, Monte Carlo dropout and ensemble learning, but these have never been applied in electrophysiological research.<sup>102</sup> They have been applied to detect diabetic retinopathy in fundus images using DNNs, where one study showed that overall accuracy could be improved when uncertain cases were referred to a physician.<sup>103</sup> Another study suggested that uncertainty measures were able to detect when a different type of scanner was used that the algorithm had not seen before.<sup>35</sup> Combining uncertainty with active or online learning allows the network to learn from previously uncertain cases, which are now reviewed by an expert.<sup>104</sup>

### *Ethical Aspects*

Several other ethical and legal challenges within the field of AI in healthcare are yet to be identified, such as patient privacy, poor quality algorithms, algorithm transparency and liability concerns. Data are subjected to privacy protections, confidentiality and data ownership, therefore requiring specific individual consent for use and reuse of data. However, by increasing the size of the data set, anonymisation techniques used nowadays might be inadequate and eventually result in the identification of patients.<sup>105,106</sup> As large data sets are required for DNNs, collaboration between institutions becomes inevitable. To facilitate data exchange, platforms have been

**Table 1.** Systematic Overview of Relevant Threats of AI Algorithms in Electrophysiology

Domain	Key points	Questions
Algorithm inputs	Subjects	Is an appropriate data source used with clean in- and exclusion criteria?
	Data	Is the (ECG) data of sufficient quality? Concerning ambulatory data; is continuous assessment of quality of data performed?
Algorithm performance	Robustness	How does the model perform? Was there a reasonable number of subjects? Were ECGs equally sampled per subject?
	Overfitting and optimism	Was overfitting assessed using internal validation with train-test splitting, cross-validation or bootstrapping? Was the validation dataset of sufficient size (> 100 participants with the outcome)?
	External validation	Are there external validation studies in different temporal, geographical or domain patient groups?
	Subgroups	Is subgroup analysis provided to minimize the risk of poor performance in subgroups? Is bias based on ethnicity, gender or other demographic factors present?
Algorithm implementation	Subjects	Is the population to use the algorithm similar to the (external) validation population? Is the disease prevalence similar?
	Data	Is the algorithm evaluated on the used diagnostic device of a specific manufacturer? Was data standardized according to general agreements?
	Implementation studies	Are there implementation studies (such as RCTs or before-after studies) performed? Does implementation of the model positively influence patient outcomes?
	Interpretation and uncertainty	Are there possibilities to check the predictions of the model in clinical practice (using visualizations)? Does the model provide uncertainty measures? How does the model deal with ECG noise or electrode misplacements? Is there a clear flowchart to refer specific uncertain cases to a physician?
	Ethical and legal	Are the ethical and legal aspects sufficiently addressed?

*RCT = randomised controlled trial.*

established to allow for safe and consistent data-sharing between institutions.<sup>107</sup> However, these databases may still contain sensitive personal data.<sup>54,108</sup> Therefore, federated learning architectures are proposed that provide data-sharing while simultaneously obviating the need to share sensitive personal data. An example of this is the anDREea Consortium ([andrea-consortium.org](http://andrea-consortium.org)).

Another concerning privacy aspect is the continuous data acquisition through smartphone-based applications. In these commercial applications, data ownership



and security are vulnerable. Security between smartphones and applications is heterogeneous and data may be stored on commercial and poorly secured servers. Clear regulations and policies should be in place before these applications can enter the clinical arena.

Data sets contain information about medical history and treatment but may also encompass demographics, religious status or socioeconomic status. Apart from medical information, sensitive personal data might be taken into account by developed algorithms, possibly resulting in discrimination in areas such as ethnicity, gender or religion.<sup>54,108-110</sup>

As described, DNNs are black boxes wherein input data is classified. An estimate of the competency of an algorithm can be made through the interpretation of DNNs and the incorporation of uncertainty measures. Traditionally, clinical practice mainly depends on the competency of a clinician. Decisions about diagnoses and treatments are based on widely accepted clinical standards and the level of competency is protected by continuous intensive medical training. In the case of adverse events, clinicians are held responsible if they deviated from standard clinical care. However, the medical liability of the DNN remains questionable. Incorrect computerised medical diagnoses or treatments result in adverse outcomes, thereby raising the question: who is accountable for a misdiagnosis based on an AI algorithm.

To guide the evaluation of ML algorithms, in particular DNNs, and accompanying literature in electrophysiology, a systematic overview of all relevant threats discussed in this review is presented in Table 1.

## **Conclusion**

Many exciting opportunities arise when AI is applied to medical data, especially in cardiology and electrophysiology. New ECG features, accurate automatic ECG diagnostics and new clinical insights can be rapidly obtained using AI technology. In the near future, AI is likely to become one of the most valuable assets in clinical practice. However, as with every technique, AI has its limitations. To ensure the correct use of AI in a clinical setting, every clinician working with AI should be able to recognise the threats, limitations and challenges of the technique. Furthermore, clinicians and data scientists should closely collaborate to ensure the creation of clinically applicable and useful AI algorithms.



## References

1. Hemingway H, Asselbergs FW, Danesh J, et al. Big data from electronic health records for early and late translational cardiovascular research: challenges and potential. *European heart journal* 2018;39(16):1481–95. <https://doi.org/10.1093/eurheartj/ehx487>; PMID: 29370377.
2. Wasserlauf J, You C, Patel R, et al. Smartwatch Performance for the Detection and Quantification of Atrial Fibrillation. *Circulation: Arrhythmia and Electrophysiology* 2019;12(6):1–9. <https://doi.org/10.1161/CIRCEP.118.006834>; PMID: 31113234.
3. Bumgarner JM, Lambert CT, Hussein AA, et al. Smartwatch Algorithm for Automated Detection of Atrial Fibrillation. *Journal of the American College of Cardiology* 2018;71(21):2381–8. <https://doi.org/10.1016/j.jacc.2018.03.003>; PMID: 29535065.
4. Lopes RD, Alings M, Connolly SJ, et al. Rationale and design of the apixaban for the reduction of thrombo-embolism in patients with device-detected sub-clinical atrial fibrillation (ARTESiA) trial. *American heart journal* 2017;189:137–45. <https://doi.org/10.1016/j.ahj.2017.04.008>; PMID: 28625370.
5. Perez M v, Mahaffey KW, Hedlin H, et al. Large-scale assessment of a smartwatch to identify atrial fibrillation. *New England Journal of Medicine* 2019;381(20):1909–17. <https://doi.org/10.1056/NEJMoa1901183>; PMID: 31722151.
6. Hannun AY, Rajpurkar P, Haghpanahi M, et al. Cardiologist-level arrhythmia detection and classification in ambulatory electrocardiograms using a deep neural network. *Nature Medicine* 2019;25(January). <https://doi.org/10.1038/s41591-018-0268-3>; PMID: 30617320.
7. Kadish AH, Buxton AE, Kennedy HL, et al. ACC/AHA Clinical Competence Statement on Electrocardiography and Ambulatory Electrocardiography A Report of the ACC/AHA/ACP-ASIM Task Force on Clinical Competence (ACC/AHA Committee to Develop a Clinical Competence Statement on Electrocardiography and Amb. 2001; <https://doi.org/10.1161/circ.104.25.3169>; PMID: 11738321.
8. Salerno SM, Alguire PC, Waxman HS. Competency in interpretation of 12-lead electrocardiograms: a summary and appraisal of published evidence. *Annals of Internal Medicine* 2003;138(9):751–60. [https://doi.org/10.1389/138\(9\):751-60](https://doi.org/10.1389/138(9):751-60); PMID: 12729431.
9. Hill AC, Miyake CY, Grady S, et al. Accuracy of interpretation of preparticipation screening electrocardiograms. *The Journal of pediatrics* 2011;159(5):783–8. <https://doi.org/10.1016/j.jpeds.2011.05.014>; PMID: 21752393.
10. Dores H, Santos JF, Dinis P, et al. Variability in interpretation of the electrocardiogram in athletes: another limitation in pre-competitive screening. *Revista Portuguesa de Cardiologia (English Edition)* 2017;36(6):443–9. <https://doi.org/10.1016/j.repc.2016.07.013>; PMID: 28599797.
11. Schläpfer J, Wellens HJ. Computer-Interpreted Electrocardiograms Benefits and Limitations. *J Am Coll Cardiol* 2017;70(9):1183–92. <https://doi.org/10.1016/j.jacc.2017.07.723>; PMID: 28838369.
12. Viskin S, Rosovski U, Sands AJ, et al. Inaccurate electrocardiographic interpretation of long QT: the majority of physicians cannot recognize a long QT when they see one. *Heart Rhythm* 2005;2(6):569–74. <https://doi.org/10.1016/j.hrthm.2005.02.011>; PMID: 15922261.
13. Willems JL, Abreu-Lima C, Arnaud P, et al. The diagnostic performance of computer programs for the interpretation of electrocardiograms. *New England Journal of Medicine* 1991;325(25):1767–73. <https://doi.org/10.1056/NEJM199112193252503>; PMID: 1834940.
14. Guglin ME, Thatai D. Common errors in computer electrocardiogram interpretation. *International journal of cardiology* 2006;106(2):232–7. <https://doi.org/10.1016/j.ijcard.2005.02.007>; PMID: 16321696.
15. Shah AP, Rubin SA. Errors in the computerized electrocardiogram interpretation of cardiac rhythm. *Journal of electrocardiology* 2007;40(5):385–90. <https://doi.org/10.1016/j.jelectrocard.2007.03.008>; PMID: 17531257.
16. Bae MH, Lee JH, Yang DH, et al. Erroneous computer electrocardiogram interpretation of atrial fibrillation and its clinical consequences. *Clinical cardiology* 2012;35(6):348–53. <https://doi.org/10.1002/clc.22000>; PMID: 22644921.
17. Anh D, Krishnan S, Bogun F. Accuracy of electrocardiogram interpretation by cardiologists in the setting of incorrect computer analysis. *Journal of electrocardiology* 2006;39(3):343–5. <https://doi.org/10.1016/j.jelectrocard.2006.02.002>; PMID: 16777525.
18. Zhang K, Aleexenko V, Jeevaratnam K. Computational approaches for detection of cardiac rhythm abnormalities: Are we there yet? *Journal of Electrocardiology* 2020;59:28–34. <https://doi.org/10.1016/j.jelectrocard.2019.12.009>; PMID: 31954954.
19. van de Leur RR, Blom LJ, Gavves E, et al. Automatic Triage of 12-Lead Electrocardiograms Using Deep Convolutional Neural Networks. *Journal of the American Heart Association* 2020;9(e015138). <https://doi.org/10.1161/JAHA.119.015138>; PMID: 32406296.
20. Perlman O, Katz A, Amit G, et al. Supraventricular tachycardia classification in the 12-lead ECG using atrial waves detection and a clinically based tree scheme. *IEEE journal of biomedical and health informatics* 2015;20(6):1513–20. <https://doi.org/10.1109/JBHI.2015.2478076>; PMID: 26415192.
21. Attia ZI, Kapa S, Lopez-Jimenez F, et al. Screening for cardiac contractile dysfunction using an artificial intelligence-enabled electrocardiogram. *Nature Medicine* 2019;25(1):70–4. <https://doi.org/10.1038/s41591-018-0240-2>; PMID: 30617318.
22. Sbrollini A, de Jongh MC, ter Haar CC, et al. Serial electrocardiography to detect newly emerging or aggravating cardiac pathology: a deep-learning approach. *Biomedical engineering online* 2019;18(1):15. <https://doi.org/10.1186/s12938-019-0630-9>; PMID: 30755195.
23. Wu JM-T, Tsai M-H, Xiao S-H, et al. A deep neural network electrocardiogram analysis framework for left ventricular hypertrophy prediction. *Journal of Ambient Intelligence and Humanized Computing* 2020;1–17. <https://doi.org/10.1007/s12646-020-01513-8>; PMID: 32406296.

- org/10.1007/s12652-020-01826-1.
24. Hastie T, Tibshirani R, Friedman J. *The elements of statistical learning: data mining, inference, and prediction*. 2009, Springer Science & Business Media, New York City.
  25. van der Ploeg T, Austin PC, Steyerberg EW. Modern modelling techniques are data hungry: a simulation study for predicting dichotomous endpoints. *BMC medical research methodology* 2014;14(1):137. <https://doi.org/10.1186/1471-2288-14-137>; PMID: 25532820.
  26. Collins GS, Ogundimu EO, Altman DG. Sample size considerations for the external validation of a multivariable prognostic model: a resampling study. *Statistics in medicine* 2016;35(2):214–26. <https://doi.org/10.1002/sim.6787>; PMID: 26553135.
  27. Raghunath S, Cerna AEU, Jing L, et al. Prediction of mortality from 12-lead electrocardiogram voltage data using a deep neural network. *Nature Medicine* 2020;1–6. <https://doi.org/10.1038/s41591-020-0870-z>; PMID: 32393799.
  28. Kligfield P, Gettes LS, Bailey JJ, et al. Recommendations for the standardization and interpretation of the electrocardiogram: part I: the electrocardiogram and its technology a scientific statement from the American Heart Association Electrocardiography and Arrhythmias Committee, Council on Clin. *Journal of the American College of Cardiology* 2007;49(10):1109–27. <https://doi.org/10.1016/j.jacc.2007.01.024>; PMID: 17349896.
  29. Jain R, Singh R, Yamini S, et al. Fragmented ECG as a Risk Marker in Cardiovascular Diseases. *Current Cardiology Reviews* 2014;10(3):277–86. <https://doi.org/10.2174/1573403x10666140514103451>; PMID: 24827794.
  30. Korkmaz A, Yildiz A, Demir M, et al. The relationship between fragmented QRS and functional significance of coronary lesions. *Journal of Electrocardiology* 2017;50(3):282–6. <https://doi.org/10.1016/j.jelectrocard.2017.01.005>; PMID: 28117101.
  31. Das MK, Zipes DP. Fragmented QRS: A predictor of mortality and sudden cardiac death. *Heart Rhythm* 2009;6(3 SUPPL). <https://doi.org/10.1016/j.hrthm.2008.10.019>; PMID: 19251229.
  32. Thakor N v, Webster JG, Tompkins WJ. Estimation of QRS Complex Power Spectra for Design of a QRS Filter. *IEEE Transactions on Biomedical Engineering* 1984;BME-31(11):702–6. <https://doi.org/10.1109/tbme.1984.325393>; PMID: 6500590.
  33. Thakor N v, Webster JG, Tompkins WJ. Optimal QRS detector. *Medical & Biological Engineering & Computing* 1983;21(3):343–50. <https://doi.org/10.1007/bf02478504>; PMID: 6876910.
  34. Garcia-Niebla J, Serra-Autonell G, de Luna AB. Brugada syndrome electrocardiographic pattern as a result of improper application of a high pass filter. *American Journal of Cardiology* 2012;110(2):318–20. <https://doi.org/10.1016/j.amjcard.2012.04.038>; PMID: 22732021.
  35. de Fauw J, Ledsam JR, Romera-Paredes B, et al. Clinically applicable deep learning for diagnosis and referral in retinal disease. *Nature medicine* 2018;24(9):1342–50. <https://doi.org/10.1038/s41591-018-0107-6>; PMID: 30104768.
  36. Herman M v, Ingram DA, Levy JA, et al. Variability of electrocardiographic precordial lead placement: a method to improve accuracy and reliability. *Clinical cardiology* 1991;14(6):469–76. PMID: 1810683.
  37. Hill NE, Goodman JS. Importance of accurate placement of precordial leads in the 12-lead electrocardiogram. *Heart & lung: the journal of critical care* 1987;16(5):561. <https://doi.org/10.1007/s11517-013-1115-9>; PMID: 3308780.
  38. Chanarin N, Caplin J, Peacock A. "Pseudo reinfarction": a consequence of electrocardiogram lead transposition following myocardial infarction. *Clinical cardiology* 1990;13(9):668–9. <https://doi.org/10.1002/clc.4960130916>; PMID: 2208827.
  39. Peberdy MA, Ornato JP. Recognition of electrocardiographic lead misplacements. *The American Journal of Emergency Medicine* 1993;11(4):403–5. [https://doi.org/10.1016/0735-6757\(93\)90177-d](https://doi.org/10.1016/0735-6757(93)90177-d); PMID: 8216526.
  40. Rautaharju PM, Prineas RJ, Crow RS, et al. The effect of modified limb electrode positions on electrocardiographic wave amplitudes. *Journal of Electrocardiology* 1980;13(2):109–13. [https://doi.org/10.1016/s0022-0736\(80\)80040-9](https://doi.org/10.1016/s0022-0736(80)80040-9); PMID: 7365351.
  41. Rajaganesan R, Ludlam CL, Francis DP, et al. Accuracy in ECG lead placement among technicians, nurses, general physicians and cardiologists. *International Journal of Clinical Practice* 2007;62(1):65–70. <https://doi.org/10.1111/j.1742-1241.2007.01390.x>; PMID: 17764456.
  42. van Oosterom A, Hoekema R, Uijen GJH. Geometrical factors affecting the interindividual variability of the ECG and the VCG. *Journal of electrocardiology* 2000;33:219–28. <https://doi.org/10.1054/jelc.2000.20356>; PMID: 11265725.
  43. Hoekema R, Uijen GJH, van Erning L, et al. Interindividual variability of multilead electrocardiographic recordings: influence of heart position. *Journal of electrocardiology* 1999;32(2):137–48. [https://doi.org/10.1016/S1053-0770\(99\)90050-2](https://doi.org/10.1016/S1053-0770(99)90050-2); PMID: 10338032.
  44. Mincholé A, Zacur E, Ariga R, et al. MRI-based computational torso/biventricular multiscale models to investigate the impact of anatomical variability on the ECG QRS complex. *Frontiers in physiology* 2019;10:1103. <https://doi.org/10.3389/fphys.2019.01103>; PMID: 31507458.
  45. Nguy en UC, Potse M, Regoli F, et al. An in-silico analysis of the effect of heart position and orientation on the ECG morphology and vectorcardiogram parameters in patients with heart failure and intraventricular conduction defects. *Journal of Electrocardiology* 2015;48(4):617–25. <https://doi.org/10.1016/j.jelectrocard.2015.05.004>; PMID: 26025201.
  46. Hoekema R, Uijen G, van Oosterom A. The number of independent signals in body surface maps. *Methods of information in medicine* 1999;38(02):119–24. <https://doi.org/10.1055/s-0038-1634176>; PMID: 10431516.
  47. Shimizu W, Matsuo K, Takagi M, et al. Body Surface Distribution and Response to Drugs of ST Segment Elevation in Brugada Syndrome: Clinical Implication of Eighty-Seven-Lead Body Surface Potential Mapping and Its Application to Twelve-Lead Electrocardiograms. *Journal of Cardiovascular Electrophysiology* 2000;11(4):396–404. <https://doi.org/10.1111/j.1540-8167.2000.tb00334.x>; PMID: 10809492.
  48. Priori SG, Blomstr om-Lundqvist C, Mazzanti A, et al. 2015 ESC Guidelines for the management of patients with ventricular arrhythmias and the prevention of sudden cardiac death. *European Heart Journal* 2015;36(41):2793–867.

- <https://doi.org/10.1093/eurheartj/ehv316>; PMID: 26837728.
49. Ibáñez B, James S, Agevall S, et al. 2017 ESC Guidelines for the management of acute myocardial infarction in patients presenting with ST-segment elevation. *Revista española de cardiología (English ed)* 2017;70(12):1082. <https://doi.org/10.1016/j.rec.2017.11.010>; PMID: 29198432.
  50. Galloway CD, Valys A v., Shreibati JB, et al. Development and Validation of a Deep-Learning Model to Screen for Hyperkalemia From the Electrocardiogram. *JAMA Cardiology* 2019;55905:1–9. <https://doi.org/10.1001/jamacardio.2019.0640>; PMID: 30942845.
  51. Rjooob K, Bond R, Finlay D, et al. Data driven feature selection and machine learning to detect misplaced V1 and V2 chest electrodes when recording the 12 lead electrocardiogram. *Journal of electrocardiology* 2019;57:39–43. <https://doi.org/10.1016/j.jelectrocard.2019.08.017>; PMID: 31476727.
  52. Hong S, Zhou Y, Shang J, et al. Opportunities and Challenges in Deep Learning Methods on Electrocardiogram Data: A Systematic Review. *ArXiv*. Available at: <https://arxiv.org/abs/2001.01550>. Published: December 2019. Accessed: May 12, 2020.
  53. Helbing D. Societal, Economic, Ethical and Legal Challenges of the Digital Revolution: From Big Data to Deep Learning, Artificial Intelligence, and Manipulative Technologies. *SSRN Electronic Journal* 2015; <https://doi.org/10.2139/ssrn.2594352>.
  54. Balthazar P, Harri P, Prater A, et al. Protecting Your Patients' Interests in the Era of Big Data, Artificial Intelligence, and Predictive Analytics. *Journal of the American College of Radiology* 2018;15(3):580–6. <https://doi.org/10.1016/j.jacr.2017.11.035>; PMID: 29402532.
  55. Ribeiro AH, Ribeiro MH, Paixão GMM, et al. Automatic diagnosis of the 12-lead ECG using a deep neural network. *Nature communications* 2020;11(1):1–9. <https://doi.org/10.1038/s41467-020-15432-4>; PMID: 32273514.
  56. Attia ZI, Noseworthy PA, Lopez-Jimenez F, et al. An artificial intelligence-enabled ECG algorithm for the identification of patients with atrial fibrillation during sinus rhythm: a retrospective analysis of outcome prediction. *The Lancet* 2019;6736(19):1–7. [https://doi.org/10.1016/S0140-6736\(19\)31721-0](https://doi.org/10.1016/S0140-6736(19)31721-0); PMID: 31378392.
  57. Ko W-Y, Siontis KC, Attia ZI, et al. Detection of Hypertrophic Cardiomyopathy Using a Convolutional Neural Network-Enabled Electrocardiogram. *Journal of the American College of Cardiology* 2020;75(7):722–33. <https://doi.org/10.1016/j.jacc.2019.12.030>; PMID: 32081280.
  58. Attia ZI, Sugrue A, Asirvatham SJ, et al. Noninvasive assessment of dofetilide plasma concentration using a deep learning (neural network) analysis of the surface electrocardiogram: A proof of concept study. *PLoS ONE* 2018;13(8):1–12. <https://doi.org/10.1371/journal.pone.0201059>; PMID: 30133452.
  59. Kwon JM, Lee SY, Jeon KH, et al. Deep Learning-Based Algorithm for Detecting Aortic Stenosis Using Electrocardiography. *Journal of the American Heart Association* 2020;9(7):e014717. <https://doi.org/10.1161/JAHA.119.014717>; PMID: 32200712.
  60. Katritsis G, Luther V, Kanagaratnam P, et al. Arrhythmia mechanisms revealed by ripple mapping. *Arrhythmia & Electrophysiology Review* 2018;7(4):261. <https://doi.org/10.15420/aer.2018.44.3>; PMID: 30588314.
  61. van den Broek HT, Wenker S, van de Leur R, et al. 3D Myocardial Scar Prediction Model Derived from Multimodality Analysis of Electromechanical Mapping and Magnetic Resonance Imaging. *Journal of cardiovascular translational research* 2019;12(6):517–27. <https://doi.org/10.1007/s12265-019-09899-w>; PMID: 31338795.
  62. van Es R, van den Broek HT, van der Naald M, et al. Validation of a novel stand-alone software tool for image guided cardiac catheter therapy. *The international journal of cardiovascular imaging* 2019;35(2):225–35. <https://doi.org/10.1007/s10554-019-01541-9>; PMID: 30689193.
  63. Zollei L, Grimson E, Norbash A, et al. 2D-3D rigid registration of X-ray fluoroscopy and CT images using mutual information and sparsely sampled histogram estimators. In: *IEEE Computer Society. Proceedings of the 2001 IEEE Computer Society Conference on Computer Vision and Pattern Recognition. CVPR 2001 IEEE*. Kauai, HI, USA: IEEE, 2001(2);II–II. <https://doi.org/10.1109/CVPR.2001.991032>.
  64. Walsh KA, Galvin J, Keaney J, et al. First experience with zero-fluoroscopic ablation for supraventricular tachycardias using a novel impedance and magnetic-field-based mapping system. *Clinical Research in Cardiology* 2018;107(7):578–85. <https://doi.org/10.1007/s00392-018-1220-8>; PMID: 29476203.
  65. Cantwell CD, Mohamied Y, Tzortzis KN, et al. Rethinking multiscale cardiac electrophysiology with machine learning and predictive modelling. *Computers in biology and medicine* 2019;104:339–51. <https://doi.org/10.1016/j.compbiomed.2018.10.015>; PMID: 30442428.
  66. Bansal A, Joshi R. Portable out-of-hospital electrocardiography: A review of current technologies. *Journal of Arrhythmia* 2018;(December 2017):129–38. <https://doi.org/10.1002/joa3.12035>; PMID: 29657588
  67. Mairesse GH, Moran P, van Gelder IC, et al. Screening for atrial fibrillation: a European heart rhythm Association (EHRA) consensus document endorsed by the heart rhythm Society (HRS), Asia Pacific heart rhythm Society (APHRS), and Sociedad Latinoamericana de Estimulación Cardíaca Y Electrofisiología (SOLAECE). *Ep Europace* 2017;19(10):1589–623. <https://doi.org/10.1093/europace/eux177>; PMID: 29048522.
  68. Freedman B, Camm J, Calkins H, et al. Screening for atrial fibrillation: a report of the AF-SCREEN international collaboration. *Circulation* 2017;135(19):1851–67. <https://doi.org/10.1161/CIRCULATIONAHA.116.026693>; PMID: 28483832.
  69. Wegner FK, Kochhäuser S, Ellermann C, et al. Prospective blinded Evaluation of the smartphone-based AliveCor Kardia ECG monitor for Atrial Fibrillation detection: The PEAK-AF study. *European Journal of Internal Medicine* 2020;73:72–5. <https://doi.org/10.1016/j.ejim.2019.11.018>; PMID: 31806411.
  70. Galloway C, Treiman D, Shreibati J, et al. 5105 A deep neural network predicts atrial fibrillation from normal ECGs recorded on a smartphone-enabled device. *European Heart Journal* 2019;40(Supplement\_1):ehz746-0041. <https://doi.org/10.1093/eurheartj/ehz746.0041>.
  71. Brasier N, Raichle CJ, Dörr M, et al. Detection of atrial fibrillation with a smartphone camera: first prospective, interna-

- tional, two-centre, clinical validation study (DETECT AF PRO). *Ep Europace* 2019;21(1):41–7. <https://doi.org/10.1093/europace/euy176>; PMID: 30085018.
72. McManus DD, Chong JW, Soni A, et al. PULSE-SMART: pulse-based arrhythmia discrimination using a novel smartphone application. *Journal of cardiovascular electrophysiology* 2016;27(1):51–7. <https://doi.org/10.1111/jce.12842>; PMID: 26391728.
  73. Couderc J-P, Kyal S, Mestha LK, et al. Detection of atrial fibrillation using contactless facial video monitoring. *Heart Rhythm* 2015;12(1):195–201. <https://doi.org/10.1016/j.hrthm.2014.08.035>; PMID: 25179488.
  74. Yan BP, Lai WHS, Chan CKY, et al. Contact-free screening of atrial fibrillation by a smartphone using facial pulse photoplethysmographic signals. *Journal of the American Heart Association* 2018;7(8):e008585. <https://doi.org/10.1161/JAHA.118.008585>; PMID: 29622592.
  75. Caliebe A, Leverkus F, Antes G, et al. Does big data require a methodological change in medical research? *BMC medical research methodology* 2019;19(1):125. <https://doi.org/10.1186/s12874-019-0774-0>; PMID: 31208367.
  76. Hashimoto DA, Rosman G, Rus D, et al. Artificial Intelligence in Surgery. *Annals of Surgery* 2018;268(1):70–6. <https://doi.org/10.1097/sla.0000000000002693>; PMID: 29389679.
  77. Wang X, Peng Y, Lu L, et al. Chestx-ray8: Hospital-scale chest x-ray database and benchmarks on weakly-supervised classification and localization of common thorax diseases. In: *IEEE. Proceedings of the IEEE conference on computer vision and pattern recognition*. Honolulu, HI, USA, 2017;2097–106. <https://doi.org/10.1109/CVPR.2017.369>.
  78. Lu MT, Ivanov A, Mayrhofer T, et al. Deep Learning to Assess Long-term Mortality From Chest Radiographs. *JAMA Network Open* 2019;2(7):e197416. <https://doi.org/10.1001/jamanetworkopen.2019.7416>; PMID: 31322692.
  79. Baltruschat IM, Nickisch H, Grass M, et al. Comparison of Deep Learning Approaches for Multi-Label Chest X-Ray Classification. *Scientific Reports* 2019;9(1). <https://doi.org/10.1038/s41598-019-42294-8>; PMID: 31011155.
  80. Oakden-Rayner L. Exploring the ChestXray14 dataset: problems. Wordpress: Luke Oakden Rayner 2017. <https://doi.org/10.1016/j.acra.2019.10.006>; PMID: 31706792.
  81. Moeyersons J, Smets E, Morales J, et al. Artefact detection and quality assessment of ambulatory ECG signals. *Computer methods and programs in biomedicine* 2019;182:105050. <https://doi.org/10.1016/j.cmpb.2019.105050>; PMID: 31473442.
  82. Clifford GD, Behar J, Li Q, et al. Signal quality indices and data fusion for determining clinical acceptability of electrocardiograms. *Physiological measurement* 2012;33(9):1419. <https://doi.org/10.1088/0967-3334/33/9/1419>; PMID: 22902749.
  83. Xia H, Garcia GA, McBride JC, et al. Computer algorithms for evaluating the quality of ECGs in real time. In: *IEEE. 2011 Computing in Cardiology*. Hangzhou, China, 2011;369–72.
  84. Li Q, Rajagopalan C, Clifford GD. A machine learning approach to multi-level ECG signal quality classification. *Computer methods and programs in biomedicine* 2014;117(3):435–47. <https://doi.org/10.1016/j.cmpb.2014.09.002>; PMID: 25306242.
  85. Redmond SJ, Xie Y, Chang D, et al. Electrocardiogram signal quality measures for unsupervised telehealth environments. *Physiological Measurement* 2012;33(9):1517. <https://doi.org/10.1088/0967-3334/33/9/1517>; PMID: 22903004.
  86. Moons KGM, Kengne AP, Grobbee DE, et al. Risk prediction models: II. External validation, model updating, and impact assessment. *Heart* 2012;98(9):691–8. <https://doi.org/10.1136/heartjnl-2011-301247>; PMID: 22397946.
  87. Park SH, Han K. Methodologic guide for evaluating clinical performance and effect of artificial intelligence technology for medical diagnosis and prediction. *Radiology* 2018;286(3):800–9. <https://doi.org/10.1148/radiol.2017171920>; PMID: 29309734.
  88. Attia ZI, Kapa S, Yao X, et al. Prospective validation of a deep learning electrocardiogram algorithm for the detection of left ventricular systolic dysfunction. *Journal of Cardiovascular Electrophysiology* 2019;30(5):668–74. <https://doi.org/10.1111/jce.13889>; PMID: 30821035.
  89. Noseworthy PA, Attia ZI, Brewer LC, et al. Assessing and Mitigating Bias in Medical Artificial Intelligence: The Effects of Race and Ethnicity on a Deep Learning Model for ECG Analysis. *Circulation Arrhythmia and electrophysiology* 2020;(March):208–14. <https://doi.org/10.1161/CIRCEP.119.007988>; PMID: 32064914.
  90. Yao X, McCoy RG, Friedman PA, et al. ECG AI-Guided Screening for Low Ejection Fraction (EAGLE): Rationale and design of a pragmatic cluster randomized trial. *American Heart Journal* 2020;219:31–6. <https://doi.org/10.1016/j.ahj.2019.10.007>; PMID: 31710842.
  91. Sendak MP, Gao M, Brajer N, et al. Presenting machine learning model information to clinical end users with model facts labels. *NPJ Digital Medicine* 2020;3(1):1–4. <https://doi.org/10.1038/s41746-020-0253-3>; PMID: 32219182.
  92. Macfarlane PW, Katibi IA, Hamde ST, et al. Racial differences in the ECG—selected aspects. *Journal of electrocardiology* 2014;47(6):809–14. <https://doi.org/10.1016/j.jelectrocard.2014.08.003>; PMID: 25193321.
  93. Rijnbeek PR, van Herpen G, Bots ML, et al. Normal values of the electrocardiogram for ages 16–90 years. *Journal of electrocardiology* 2014;47(6):914–21. <https://doi.org/10.1016/j.jelectrocard.2014.07.022>; PMID: 25194872.
  94. Attia ZI, Friedman PA, Noseworthy PA, et al. Age and Sex Estimation Using Artificial Intelligence From Standard 12-Lead ECGs. *Circulation: Arrhythmia and Electrophysiology* 2019;12(9):1–11. <https://doi.org/10.1161/CIRCEP.119.007284>; PMID: 31450977.
  95. Carvalho D v, Pereira EM, Cardoso JS. Machine Learning Interpretability: A Survey on Methods and Metrics. *Electronics* 2019;8(8):832. <https://doi.org/10.3390/electronics8080832>.
  96. Selvaraju RR, Cogswell M, Das A, et al. Grad-cam: Visual explanations from deep networks via gradient-based localization. In: *Proceedings of the IEEE international conference on computer vision* 2017. Venice, Italy; 2017;618–26.
  97. Springenberg JT, Dosovitskiy A, Brox T, et al. Striving for simplicity: The all convolutional net. San Diego, United States: *International Conference on Learning Representations*. 2015;1–14.

98. Strodthoff N, Strodthoff C. Detecting and interpreting myocardial infarction using fully convolutional neural networks. *Physiological measurement* 2019;40(1):015001. <https://doi.org/10.1088/1361-6579/aaf34d>; PMID: 30523982.
99. The LRM. Opening the black box of machine learning. *The Lancet Respiratory medicine* 2018;6(11):801. [https://doi.org/10.1016/S2213-2600\(18\)30425-9](https://doi.org/10.1016/S2213-2600(18)30425-9); PMID: 30343029.
100. Sturmfels P, Lundberg S, Lee S-I. Visualizing the Impact of Feature Attribution Baselines. *Distill* 2020;5(1):e22. <https://doi.org/10.23915/distill.00022>.
101. Filos A, Farquhar S, Gomez AN, et al. A Systematic Comparison of Bayesian Deep Learning Robustness in Diabetic Retinopathy Tasks. *ArXiv*. Available at: <https://arxiv.org/abs/1912.10481>. Published: December 2019. Accessed: June 2, 2020.
102. Tagasovska N, Lopez-Paz D. Single-Model Uncertainties for Deep Learning. In: *Advances in Neural Information Processing Systems*. Vancouver, Canada, 2019;6414–25.
103. Leibig C, Allken V, Ayhan MS, et al. Leveraging uncertainty information from deep neural networks for disease detection. *Scientific reports* 2017;7(1):1–14. <https://doi.org/10.1038/s41598-017-17876-z>; PMID: 29259224.
104. Gal Y, Islam R, Ghahramani Z. Deep bayesian active learning with image data. *ArXiv*. Available at: <https://arxiv.org/abs/1703.02910>. Published: March 2017. Accessed: June 2, 2020.
105. Carter RE, Attia ZI, Lopez-Jimenez F, et al. Pragmatic considerations for fostering reproducible research in artificial intelligence. *NPJ digital medicine* 2019;2(1):1–3. <https://doi.org/10.1038/s41746-019-0120-2>; PMID: 31304388.
106. Rocher L, Hendrickx JM, de Montjoye Y-A. Estimating the success of re-identifications in incomplete datasets using generative models. *Nature communications* 2019;10(1):1–9. <https://doi.org/10.1038/s41467-019-10933-3>; PMID: 31337762.
107. Mandel JC, Kreda DA, Mandl KD, et al. SMART on FHIR: a standards-based, interoperable apps platform for electronic health records. *Journal of the American Medical Informatics Association* 2016;23(5):899–908. <https://doi.org/10.1093/jamia/ocv189>; PMID: 26911829.
108. Vayena E, Blasimme A. Health Research with Big Data: Time for Systemic Oversight. *The Journal of Law, Medicine & Ethics* 2018;46(1):119–29. <https://doi.org/10.1177/1073110518766026>; PMID: 30034208.
109. Vayena E, Blasimme A. Biomedical Big Data: New Models of Control Over Access, Use and Governance. *Journal of Bioethical Inquiry* 2017;14(4):501–13. <https://doi.org/10.1007/s11673-017-9809-6>; PMID: 28983835.
110. McCall B. What does the GDPR mean for the medical community? *The Lancet* 2018;391(10127):1249–50. [https://doi.org/10.1016/s0140-6736\(18\)30739-6](https://doi.org/10.1016/s0140-6736(18)30739-6); PMID: 29619949.
111. Wolff RF, Moons KGM, Riley RD, et al. PROBAST: a tool to assess the risk of bias and applicability of prediction model studies. *Annals of internal medicine* 2019;170(1):51–8. PMID: 30596875.



$\emptyset$

$(x, y)$

$v_2 / c^2$

$v_{cg}$

$= \int_{S_u}$

$S_u$

ind



## Chapter 10

General discussion and future perspectives



The electrocardiogram (ECG) plays an important role in the systematic assessment of cardiac electrical (dys)function within current clinical practice. Through waveform morphology assessment, important insight in underlying cardiac pathology can be obtained. But with the ECG only a rather distant view on cardiac electrical activity is provided, as it displays the potential resulting from the spatial summation of all electrical activity. Within this thesis we focused on non-invasive ECG-based techniques to obtain additional information on cardiac electrical activity. Subtle changes in cardiac electrical activity, due to for example slow disease progression as observed in inherited cardiomyopathies, may be uncovered by linking cardiac electrical activity measured with the ECG to cardiac anatomy. However, currently available techniques require optimization to improve the estimation during normal ventricular activation.

Inherited cardiomyopathies are associated with a broad spectrum of potentially lethal phenotypes characterized by structural and electrical myocardial remodeling. Nowadays, extensive clinical work-up is carried out to identify any phenotypic ACM expression. With the TFC, several clinical characteristics with a high specificity for ACM were identified to guide clinical diagnosis and monitoring.<sup>1</sup> However, due to heterogeneous disease penetrance and slow disease progression, risk-stratification in phenotype-negative individuals remains challenging. With the development of new diagnostic tools, the detection of subtle signs of disease may be enabled.

Recently, a lot of progress has been made to identify structural and mechanical defects in ACM. With MRI-based feature mapping, T1-mapping and echocardiography-based deformation imaging early mechanical signs of ACM can be identified, even prior to identifiable pathological changes in the 12-lead ECG.<sup>2-4</sup> This is unexpected as from a pathophysiological point-of-view, both electrical and structural signs are expected to develop in parallel due to the cell-to-cell adhesion defects.<sup>5</sup> These observations imply that the 12-lead ECG may not be sensitive enough to uncover the first electrical signs of disease.

In this thesis, we described the optimization of equivalent dipole layer (EDL)-based iECG for normal ventricular activation (chapter 2), compared this to invasive measurements (chapter 3) and evaluated the iECG method in ACM variant carriers with a broad clinical manifestation of disease (chapter 4) for its ability to identify subtle signs of disease progression. Additionally, the firsts step towards accurate disease modeling in EDL-based ECG simulations was described (chapter 5). We also methodologically reviewed CineECG (chapter 6), a mathematically lightweight and less intrusive iECG procedure and conceptually validated it in individuals with a bundle branch block (chapter 7). A new method to improve the diagnostic yield of the ECG (chapter 8) was described and opportunities and challenges of ECG-based artificial intelligence (AI, chapter 9) were set out. To conclude the thesis, I will



describe and discuss potential future research directions and clinical applications of the techniques described in this thesis in the current chapter.

### **Electrophysiological regularization of EDL-based iECG**

The incorporation of an anatomy based His-Purkinje model in the iECG technique provided a first step towards a more accurate, physiologically based, estimation of a realistic cardiac activation sequence.<sup>6-10</sup> In the local activation timing (LAT) maps, estimated myocardial propagation velocity stayed within a physiological range and activation sequences were the result of several activation sequences arising from distinct, His-Purkinje related, regions. In narrow complexes, the number of initial sites of activation was higher, thereby providing a physiologically realistic estimation. When comparing the iECG LAT maps to invasive measurements, the non-invasive estimation in narrow QRS complexes matched the complex underlying activation pattern better compared to other methods.<sup>11,12</sup>

However, we are not there yet. Whereas the incorporation of the His-Purkinje model improved the non-invasive estimation of LAT maps, the presence of diseased myocardium breaks the equivalence of the used dipole layer. As a proof-of-concept, the new iECG method was applied in ACM variant carriers with a broad clinical manifestation of disease (chapter 5). Early-stage ACM, shows none to very limited structural defects and thus the underlying myocardium can be assumed homogeneous in electrical properties, i.e. the tissue is not likely to break the equivalence of the dipole layer. With the iECG method, iECG parameters that may be suitable to identify early disease which adhere to clinically observed disease progression. When evaluating RV iECG LAT maps in severe ACM cases, physiologically relevant (and expected) parameters like isochronal crowding, transmural LAT heterogeneity and regions of late activation were colocalized in regions with LGE-presence. This indicated the ability of the current iECG method to cope, at least to some extent, with this myocardial disease. Prognostic studies to evaluate the clinically added value and role of iECG in risk-stratification and early detection of ACM are however warranted. Whereas the findings obtained in the proof-of-concept study are promising, the incorporation of additional prior knowledge regarding structural defects is likely to provide a more reliable estimation of the cardiac electrical activity. Taking into account findings from LGE-cMR imaging, regions with myocardial disease requiring altered source parameters can be identified. Within these regions, the interplay between diseased and healthy regions may be more accurately modeled by implementing a patch-based EDL-based method (chapter 5).

A more technical optimization of the iECG method is proposed to reduce the error introduced by cardiac source sampling (i.e., the number of samples used to discretize the ventricular anatomical model). Due to spatial source undersampling, applied to reduce computational cost, a numerical error is introduced in the computation of

BSP.<sup>13</sup> Therefore, a filter is used to remove this error possibly also removing parts of the signal not caused by cardiac undersampling. In our modeling study (chapter 5), we used a triangle-based weighing method to remove this error in the BSP computation. Especially to correctly image large differences in local propagation velocity, this method is likely to further improve the numerical accuracy of EDL-based iECG. To implement this into the iECG procedure, the regularization operator used in the optimization procedure must be adapted, which is now based on the surface Laplacian<sup>14</sup>, taking into account the distance and angle between nodes. As the new BSP computation method is triangle based, the surface Laplacian can no longer be used as there are no distance/angles between triangles. Therefore, a new regularization operator, possibly taking into account the distance between adjacent nodes of the ventricular model, is required.

In the current iECG method, the shape of the transmembrane potential is approximated using two analytical sigmoidal functions based on the dominant T-wave.<sup>15</sup> For normal ventricular repolarization, this method may be accurate, but in the presence of cellular pathology a more sophisticated method is required. Ultimately, a cellular-based model underlying the generation of the local transmembrane potential would provide the opportunity to incorporate disease specific cellular pathology in the iECG method. Furthermore, cell-to-cell interactions and the presence of different cell types (e.g. healthy and disease) within a region can be modeled. The resulting average transmembrane potential in a region may then be used in EDL-based iECG. Whereas such cellular models are computationally expensive, additional important insight in the development of the cardiac substrate can be obtained. Furthermore, the interaction between activation and repolarization, and consequently possible increased susceptibility to arrhythmias<sup>16</sup>, can be investigated more thoroughly.

### **Current clinical work-up and iECG techniques**

To date, risk-stratification in both phenotype-positive and -negative individuals remains challenging. A potential (synergistic) role of known and constantly improved ECG-, cMR-, echocardiographic- and biomarker-based techniques will likely provide improved diagnosis, monitoring and risk-stratification to titrate individualized treatment in both phenotype-positive and -negative individuals. Ultimately, by assessing inter-modality correspondence, further in-depth characterization of disease progression and the underlying pathophysiological process is obtained. With iECG techniques, additional information regarding the electrophysiological substrate may be obtained. Insight in substrate changes may provide additional information on treatment effect and may be used as a surrogate outcome for clinical trials. Furthermore, the identification and characterization of the substrate may be used to guide and evaluate treatment regimen choices (e.g., medication, ablation or ICD implantation) and guide invasive electrophysiological mapping studies.

Both CineECG and EDL-based iECG may provide additional insight in cardiac electrical activity next to the 12-lead ECG. Whereas CineECG is a lightweight iECG technique providing merely a summary of cardiac electrical activity, EDL-based iECG is complex providing detailed insight of the electrophysiological substrate. In current clinical practice, CineECG can be more easily applied when using its generic anatomical model and its clinically added value may be already evaluated by using retrospective 12-lead ECG data. Small changes in the standard 12-lead ECG may become identifiable using the technique.<sup>17</sup> But still, as is the case with the 12-lead ECG, clinicians, possibly helped by AI-techniques, should learn how to interpret the CineECG and consequently the interpretation is dependent on the reader experience. The technique is very promising and future studies will determine the diagnostic yield and role of the CineECG in the acute setting and in regular clinical follow-up.<sup>18</sup>

For EDL-based iECG, incorporation in the clinical workflow may be more complicated as the technique requires the use of extensive (>67-leads) BSP measurements and subject specific anatomical model segmentation. Furthermore, overall robustness of iECG techniques to variation in cardiac segmentation and ECG preprocessing techniques are currently investigated.<sup>19,20</sup> With the development of mathematical methods to determine both positional and geometrical information from the ECG, iECG methods are further improved.<sup>21,22</sup> With these techniques, the eventual error introduced by these effectors can be reduced, to improve clinical applicability of iECG techniques.

The application of a patch-work iECG method, combining different techniques to one, creates the opportunity to combine the strengths of different iECG methods, consequently likely to improve the accuracy of iECG methods.<sup>23,24</sup> A more detailed and robust characterization of electrophysiological properties in complex substrates may be enabled. Another exciting opportunity is the application of data-driven models. The well-known iECG techniques are mostly physics/electrophysiology-based models. Data-driven models to regularize iECG estimations may potentially improve the iECG estimation, as current studies have shown that such models outperform Tikhonov regularization methods.<sup>25,26</sup> Furthermore, with variational auto encoders we may partially, but hopefully completely, uncover the complexity of the true volume conductor resulting in recorded BSP to further optimize the models used to compute BSP. Additionally, data-driven models may also be used to predict the occurrence of arrhythmic events.<sup>27,28</sup> However, as solely data-driven models may ignore underlying physics and electrophysiology, frameworks capable to understand underlying physics (e.g. patient specific geometry) may further improve such methods.<sup>29,30</sup>

### **Enhancing 12-lead based ECG-based diagnostics**

The ECG contains a lot of information, more than currently used/accessible in clinical practice. This is also indicated by the recent developments in the field of 12-lead

ECG-based artificial intelligence (AI). With just the 12-lead ECG, it is possible to estimate reduced LV ejection fraction<sup>31</sup>, LV hypertrophy<sup>32</sup>, early signs of inherited cardiomyopathy<sup>33</sup> and hyperkalemia<sup>34</sup>. Furthermore, atrial fibrillation<sup>35</sup> and patient outcomes<sup>36,37</sup> can be predicted using the 12-lead ECG during sinus rhythm.

It is however important to realize that these models work with the probability of developing an event, based on the given population and employing only the variables selected by the model from this particular group. With a slight change in population, the model will inherently change and on an individual level the prediction may change radically whereas overall model performance remains equal. The population of the model is therefore very important; in an individual with an indefinite number of variables (not all contained in the model), there is a probability of having reduced EF based on the variables selected by the model, thereby not taking into account other variables the individual has. Consequently, when putting the same individual several times in the same situation again and again, the number of times this individual will have a reduced EF is not the same as the probability thereof predicted by the model; the individual simply has a reduced EF or not. Therefore, the ECG may indicate that there is a high probability of having reduced EF. But if the interpreter believes that is wrong based on an observation in that particular individual which is not included in the model, the interpreter is probably right. Thereby of course keeping in mind that this again is based on a probability calculation clinicians perform subconsciously through years of experience, much like AI.

Keeping this in mind, in order to further optimize AI-based algorithms, all possible available data should be collected and models should continue learning with this new data. To facilitate this, it is important to develop pipelines for data structuring and preprocessing, to provide generalized infrastructures to share data and to provide the opportunity for federated learning and external validation. Furthermore, developments in natural language processing will provide access to even more data and data collected during day-to-day activities will further provide additional information. Besides using real-world patient data, datasets consisting of synthetic patient data and ECG signals based on a combination of real-world data and mathematical modeling, may further support AI-based research. With the AI-based techniques, novel parameters to monitor disease onset and progression may be identified in a more objective way.<sup>33</sup> Developed AI-algorithms however remain to be a black box and currently advancements are made to explain the model-based decision to identify ECG-based features which can be used in clinical practice.<sup>33,38-41</sup>

Another way to improve the diagnostic yield of the ECG is to reduce the most common error during ECG acquisition; electrode repositioning.<sup>42-46</sup> Using 3D camera guided electrode positioning, consecutive ECG acquisition is stabilized and more subtle changes in the cardiac activation sequence may be detected. Furthermore, as

recent studies suggest that not all information regarding cardiac electrical activity is captured with the 12-lead ECG, disease specific electrode positioning may be warranted.<sup>47-50</sup> With the use of 3D camera guided electrode (re)positioning, adherence to such a disease specific electrode position is most likely improved, therewith further improving the diagnostic yield of the 12-lead ECG.

### **Concluding remarks and future perspectives**

Both CineECG and EDL-based iECG may provide complementary information to the other tools currently used in ACM diagnosis. The EDL-based in-depth characterization of the electrophysiological substrate in ACM may enhance treatment titration and risk-stratification. As CineECG only requires a 12-lead ECG, the technique may also be employed at home, therewith possibly enabling earlier detection of disease. In future studies, the added value and role of the promising techniques in the current diagnostic work-up and risk-stratification techniques in ACM should be determined. Furthermore, by combining physics, electrophysiology and data-driven models, iECG methods can be further optimized. In combination with new echocardiographic and cMR techniques, risk-stratification in ACM patients can be further improved.

With the new advancements in the field of ECG-based AI, a lot of new exciting opportunities for future research are opening up. By combining findings from ECG-based techniques and tools to assess cardiac structure and mechanical function, risk-stratification in ACM of both phenotype negative and positive individuals will likely be further enhanced. Also, when combining findings from the 12-lead ECG, CineECG and AI based predictions, these findings may together prove valuable in the identification of individuals at risk for events.

Scientists are curious and, in their curiosity, they try to understand and describe physical processes in the world using for example mathematical models. With regards to iECG techniques, a lot of advancements were already made within the past and are still ongoing. With each step made, the accurate non-invasive estimation of cardiac activity comes more and more within reach. With the research described in this thesis we hope to have also contributed a bit to this purpose. But the most basic law in science will always remain; with each question answered, (luckily) at least three new ones are generated.

## References

1. Te Riele AS, James CA, Groeneweg JA, Sawant AC, Kammers K, Murray B, et al. Approach to family screening in arrhythmogenic right ventricular dysplasia/cardiomyopathy. *Eur Heart J*. 2016;37(9):755-63.
2. Bourfiss M, Prakken N, James C, Planken R, Boekholdt S, Ahmetagic D, et al. Prognostic value of strain by feature-tracking cardiac magnetic resonance in arrhythmogenic right ventricular cardiomyopathy. *European Heart Journal-Cardiovascular Imaging*. 2022.
3. Mast TP, Teske AJ, Walmsley J, van der Heijden JF, van Es R, Prinzen FW, et al. Right ventricular imaging and computer simulation for electromechanical substrate characterization in arrhythmogenic right ventricular cardiomyopathy. *Journal of the American College of Cardiology*. 2016;68(20):2185-97.
4. Taha K, Mast TP, Cramer MJ, van der Heijden JF, Asselbergs FW, Doevendans PA, et al. Evaluation of disease progression in arrhythmogenic cardiomyopathy: the change of echocardiographic deformation characteristics over time. *Cardiovascular Imaging*. 2020;13(2\_Part\_2):631-4.
5. Costa S, Cerrone M, Saguner AM, Brunnkhorst C, Delmar M, Duru F. Arrhythmogenic cardiomyopathy: An in-depth look at molecular mechanisms and clinical correlates. *Trends in Cardiovascular Medicine*. 2021;31(7):395-402.
6. Vigmond EJ, Stuyvers BD. Modeling our understanding of the His-Purkinje system. *Progress in biophysics and molecular biology*. 2016;120(1-3):179-88.
7. Cardone-Noott L, Bueno-Orovio A, Minchola A, Zenzemi N, Rodriguez B. Human ventricular activation sequence and the simulation of the electrocardiographic QRS complex and its variability in healthy and intraventricular block conditions. *EP Europace*. 2016;18(suppl\_4):iv4-iv15.
8. Pezzuto S, Prinzen FW, Potse M, Maffessanti F, Regoli F, Caputo ML, et al. Reconstruction of three-dimensional biventricular activation based on the 12-lead electrocardiogram via patient-specific modelling. *EP Europace*. 2021;23(4):640-7.
9. Gillette K, Gsell MA, Prassl AJ, Karabelas E, Reiter U, Reiter G, et al. A Framework for the generation of digital twins of cardiac electrophysiology from clinical 12-leads ECGs. *Med Image Anal*. 2021;71:102080.
10. Cocherova E, Svehlikova J, Tysler M, editors. *Activation Propagation in Cardiac Ventricles Using the Model with the Conducting System*. World Congress on Medical Physics and Biomedical Engineering 2018; 2019: Springer.
11. Duchateau J, Sacher F, Pambrun T, Derval N, Chamorro-Servent J, Denis A, et al. Performance and limitations of noninvasive cardiac activation mapping. *Heart Rhythm*. 2019;16(3):435-42.
12. Boonstra MJ, Roudijk RW, Brummel R, Kassenberg W, Blom LJ, Oostendorp TF, et al. Modeling the His-Purkinje Effect in Non-invasive Estimation of Endocardial and Epicardial Ventricular Activation. *Ann Biomed Eng*. 2022:1-17.
13. Tate JD, Schuler S, Dössel O, MacLeod RS, Oostendorp TF, editors. *Correcting undersampled cardiac sources in equivalent double layer forward simulations*. International Conference on Functional Imaging and Modeling of the Heart; 2019: Springer.
14. Huiskamp GJM. Difference formulas for the surface Laplacian on a triangulated surface. *J of Comp Phys*. 1991;95:477-96.
15. van Oosterom A. The dominant T wave and its significance. *J Cardiovasc Electrophysiol*. 2003;14(10 Suppl):S180-7.
16. Cluitmans MJ, Bear LR, Nguyễn UC, van Rees B, Stoks J, Ter Bekke RM, et al. Noninvasive detection of spatiotemporal activation-repolarization interactions that prime idiopathic ventricular fibrillation. *Science Translational Medicine*. 2021;13(620):eabi9317.
17. van Dam PM, Locati ET, Ciconte G, Borrelli V, Heilbron F, Santinelli V, et al. Novel CineECG Derived from Standard 12-Lead ECG Enables Right Ventricle Outflow Tract Localization of Electrical Substrate in Patients with Brugada Syndrome. *Circ Arrhythm Electrophysiol*. 2020;13(9):e008524.
18. Boonstra M, Kloosterman M, Asselbergs F, Van Dam P, Loh P. Novel CineECG to identify disease onset and progression in pathogenic plakophilin-2 mutation carriers. *Europace*. 2022;24(Supplement\_1):euac053. 40.
19. Tate JD, Good WW, Zenzemi N, Boonstra M, Dam Pv, Brooks DH, et al., editors. *Uncertainty quantification of the effects of segmentation variability in ecgi*. International Conference on Functional Imaging and Modeling of the Heart; 2021: Springer.
20. Bear LR, Dogrusoz YS, Good W, Svehlikova J, Coll-Font J, van Dam E, et al. The impact of torso signal processing on noninvasive electrocardiographic imaging reconstructions. *IEEE Transactions on Biomedical Engineering*. 2020;68(2):436-47.
21. Gyawali PK, Murkute JV, Toloubidokhti M, Jiang X, Horacek BM, Sapp JL, et al. Learning to disentangle inter-subject anatomical variations in electrocardiographic data. *IEEE Transactions on Biomedical Engineering*. 2021;69(2):860-70.
22. Bergquist JA, Coll-Font J, Zenger B, Rupp LC, Good WW, Brooks DH, et al. Reconstruction of cardiac position using body surface potentials. *Computers in biology and medicine*. 2022;142:105174.
23. Bouhamama O, Potse M, Bear L, Weynans L, editors. *A patchwork method to improve the performance of the current ECG methods for sinus rhythm*. VPH 2020-International Conference on the Virtual Physiological Human; 2020.
24. Schuler S, Schaufelberger M, Bear LR, Bergquist JA, Cluitmans MJ, Coll-Font J, et al. Reducing line-of-block artifacts in cardiac activation maps estimated using ecg imaging: A comparison of source models and estimation methods. *IEEE Transactions on Biomedical Engineering*. 2021;69(6):2041-52.
25. Onak ÖN, Erenler T, Dogrusoz YS. A Novel Data-Adaptive Regression Framework Based on Multivariate Adaptive Regression Splines for Electrocardiographic Imaging. *IEEE Transactions on Biomedical Engineering*. 2021;69(2):963-74.
26. Dogrusoz YS, Dubois R, Abell E, Cluitmans M, Bear LR, editors. *Electrocardiographic Imaging of Sinus Rhythm in Pig Hearts Using Bayesian Maximum A Posteriori Estimation*. 2021 Computing in Cardiology (CinC); 2021: IEEE.
27. Deng D, Prakosa A, Shade J, Nikolov P, Trayanova NA. Sensitivity of ablation targets prediction to electrophysiological

- cal parameter variability in image-based computational models of ventricular tachycardia in post-infarction patients. *Frontiers in physiology*. 2019;10:628.
28. Popescu DM, Shade JK, Lai C, Aronis KN, Ouyang D, Moorthy MV, et al. Arrhythmic sudden death survival prediction using deep learning analysis of scarring in the heart. *Nature Cardiovascular Research*. 2022;1(4):334-43.
  29. Jiang X, Missel R, Toloubidokhti M, Li Z, Gharbia O, Sapp JL, et al., editors. Label-Free Physics-Informed Image Sequence Reconstruction with Disentangled Spatial-Temporal Modeling. *International Conference on Medical Image Computing and Computer-Assisted Intervention*; 2021: Springer.
  30. Toloubidokhti M, Gyawali PK, Gharbia OA, Jiang X, Font JC, Bergquist JA, et al., editors. Deep adaptive electrocardiographic imaging with generative forward model for error reduction. *International Conference on Functional Imaging and Modeling of the Heart*; 2021: Springer.
  31. Yao X, Rushlow DR, Inselman JW, McCoy RG, Thacher TD, Behnken EM, et al. Artificial intelligence-enabled electrocardiograms for identification of patients with low ejection fraction: a pragmatic, randomized clinical trial. *Nat Med*. 2021;27(5):815-9.
  32. Ko W-Y, Siontis KC, Attia ZI, Carter RE, Kapa S, Ommen SR, et al. Detection of hypertrophic cardiomyopathy using a convolutional neural network-enabled electrocardiogram. *Journal of the American College of Cardiology*. 2020;75(7):722-33.
  33. van de Leur RR, Taha K, Bos MN, van der Heijden JF, Gupta D, Cramer MJ, et al. Discovering and visualizing disease-specific electrocardiogram features using deep learning: proof-of-concept in phospholamban gene mutation carriers. *Circ Arrhythm Electrophysiol*. 2021;14(2):e009056.
  34. Galloway CD, Valys AV, Shreibati JB, Treiman DL, Petterson FL, Gundotra VP, et al. Development and validation of a deep-learning model to screen for hyperkalemia from the electrocardiogram. *JAMA cardiology*. 2019;4(5):428-36.
  35. Attia ZI, Noseworthy PA, Lopez-Jimenez F, Asirvatham SJ, Deshmukh AJ, Gersh BJ, et al. An artificial intelligence-enabled ECG algorithm for the identification of patients with atrial fibrillation during sinus rhythm: a retrospective analysis of outcome prediction. *The Lancet*. 2019;394(10201):861-7.
  36. Wouters PC, van de Leur RR, Vessies MB, van Stipdonk AM, Ghossein MA, Hassink RJ, et al. Electrocardiogram-based deep learning improves outcome prediction following cardiac resynchronization therapy. *Eur Heart J*. 2023.
  37. Sammani A, Van de Leur RR, Henkens MT, Meine M, Loh P, Hassink RJ, et al. Life-threatening ventricular arrhythmia prediction in patients with dilated cardiomyopathy using explainable electrocardiogram-based deep neural networks. *Europace*. 2022;24(10):1645-54.
  38. Bos MN, van de Leur RR, Vranken JF, Gupta DK, van der Harst P, Doevendans PA, et al., editors. Automated comprehensive interpretation of 12-lead electrocardiograms using pre-trained exponentially dilated causal convolutional neural networks. *2020 Computing in Cardiology*; 2020: IEEE.
  39. van de Leur RR, Blom LJ, Gavves E, Hof IE, van der Heijden JF, Clappers NC, et al. Automatic triage of 12-lead ECGs using deep convolutional neural networks. *Journal of the American Heart Association*. 2020;9(10):e015138.
  40. Vranken JF, van de Leur RR, Gupta DK, Juarez Orozco LE, Hassink RJ, van der Harst P, et al. Uncertainty estimation for deep learning-based automated analysis of 12-lead electrocardiograms. *European Heart Journal-Digital Health*. 2021;2(3):401-15.
  41. van de Leur RR, Bos MN, Taha K, Sammani A, Yeung MW, van Duijvenboden S, et al. Improving explainability of deep neural network-based electrocardiogram interpretation using variational auto-encoders. *European Heart Journal-Digital Health*. 2022;3(3):390-404.
  42. Kligfield P, Gettes LS, Bailey JJ, Childers R, Deal BJ, Hancock EW, et al. Recommendations for the Standardization and Interpretation of the Electrocardiogram: Part I: The Electrocardiogram and Its Technology. A Scientific Statement From the American Heart Association Electrocardiography and Arrhythmias Committee, Council on Clinical Cardiology, the American College of Cardiology Foundation, and the Heart Rhythm Society Endorsed by the International Society for Computerized Electrocardiology. *Circulation*. 2007;115(10).
  43. Kania M, Rix H, Fereniec M, Zavala-Fernandez H, Janusek D, Mroczka T, et al. The effect of precordial lead displacement on ECG morphology. *Med Biol Eng Comput*. 2014;52(2):109-19.
  44. Hill N, Goodman J. Importance of accurate placement of precordial leads in the 12-lead electrocardiogram. *Heart & lung: the journal of critical care*. 1987;16(5):561-6.
  45. Bond RR, Finlay D, Nugent C, Breen C, Guldenring D, Daly M. The effects of electrode misplacement on clinicians' interpretation of the standard 12-lead electrocardiogram. *European journal of internal medicine*. 2012;23(7):610-5.
  46. Schijvenaars BJ, Kors JA, van Herpen G, Kornreich F, van Bommel JH. Effect of electrode positioning on ECG interpretation by computer. *J Electrocardiol*. 1997;30(3):247-56.
  47. Meo M, Bonizzi P, Bear LR, Cluitmans M, Abell E, Haissaguerre M, et al. Body surface mapping of ventricular repolarization heterogeneity: an ex-vivo multiparameter study. *Frontiers in physiology*. 2020;11:933.
  48. Kommata V, Elshafie M, Sciaraffia E, Perez M, Augustine R, Blomström-Lundqvist C. QRS dispersion detected in ARVC patients and healthy gene carriers using 252-leads body surface mapping: an explorative study of a potential diagnostic tool for arrhythmogenic right ventricular cardiomyopathy. *Pacing and Clinical Electrophysiology*. 2021;44(8):1355-64.
  49. Kommata V, Sciaraffia E, Blomström-Lundqvist C. Repolarisation abnormalities unmasked with a 252-lead BSM system in patients with ARVC and healthy Gene Carriers. *Pacing and Clinical Electrophysiology*. 2022.
  50. Kloosterman M, Boonstra MJ, Kirkels FP, van Dam PM, Loh P. PO-713-08 Body Surface Mapping to Detect Early Signs of Disease in PKP2-Pathogenic Mutation Carriers. *Heart Rhythm*. 2022;19(5):S487.





$\emptyset$

$(x, y) = \int_{S_u}$

$v_2 / c^2$

$v_{cg}$

$v_{cg}$

ind





# Appendix

English summary  
Nederlandse samenvatting  
List of publications  
Dankwoord / Acknowledgements  
Curriculum vitae

## English summary

The electrocardiogram (ECG) plays an important role in systematically assessing cardiac electrical function, but the standard 12-lead ECG only provides only a distant view on cardiac electrical activity. Using non-invasive inverse ECG techniques, additional information on cardiac electrical activity can be obtained by linking cardiac electrical activity to cardiac anatomy. This may enable the identification of subtle disease progression in cases of arrhythmogenic cardiomyopathy during normal ventricular activation.

Arrhythmogenic cardiomyopathy is characterized by structural and electrical myocardial remodeling and can manifest as a broad range of lethal phenotypes. Historically, arrhythmogenic cardiomyopathy was described as a predominant (but not exclusive) right-sided disease and called arrhythmogenic right ventricular cardiomyopathy; the best characterized type of arrhythmogenic cardiomyopathy. Increased awareness, identification of genes associated with arrhythmogenic cardiomyopathy and improved genetic cascade screening leads to more genotype-positive, yet phenotype-negative individuals to be evaluated and followed up. The predictive value of genetic testing is limited by incomplete penetrance and high variability in disease onset, progression and severity. In arrhythmogenic cardiomyopathy, electrical remodeling can precede structural and functional changes and sudden cardiac death can be the first disease manifestation. This highlights the need for accurate screening and risk-stratification strategies. Task Force Criteria (TFC) were established to standardize clinical diagnosis of arrhythmogenic right ventricular cardiomyopathy but risk-stratification remains challenging. In this thesis, several ECG-based techniques are described which may have the potential to improve the diagnostic process in the identification and risk-stratification of arrhythmogenic cardiomyopathy, as described in **Chapter 1**.

The first part of this thesis focusses on describing the optimization of a traditional inverse ECG technique. With this inverse ECG technique, non-invasive insight in endocardial and epicardial cardiac electrical activity can be obtained by combining 67-lead ECG data with patient specific CT/MRI-based anatomical models. The application of such an inverse ECG technique in individuals at risk to develop arrhythmogenic cardiomyopathy may improve current clinical practice. Reconstructing ventricular activation in paced beats and premature ventricular complexes using the inverse ECG techniques described in literature already yielded reasonable accuracy. However, during normal ventricular activation (e.g., sinus rhythm), utility of these inverse ECG techniques are limited. To be able to identify early signs of arrhythmogenic cardiomyopathy development, accurate imaging of sinus rhythm is of importance. Therefore, in **Chapter 2**, we report on our work regarding the optimization of the inverse ECG technique for the estimation of sinus rhythm and report on its performance. With the incorporation of a subject-specific anatomy-based model

of the His-Purkinje system a physiologically realistic and robust estimation of the ventricular activation sequence is obtained. Subsequently, in **Chapter 3**, we describe the performance of the optimized inverse ECG technique by comparing the estimated ventricular activation maps to invasively measured maps. Overall, estimated activation sequences had good agreement with the invasively measured activation maps, including those of narrow QRS complexes. The optimized inverse ECG technique detected local abnormalities in the activation sequence in pathogenic variant carriers with and without any clinical signs of disease, as described in **Chapter 4**. The proof-of-concept study indicated that with the optimized inverse ECG technique, local electrophysiological characteristics of the arrhythmogenic substrate may be non-invasively identified and quantified. Besides insight in activation patterns over the surface, also insight in transmural activation patterns is obtained. By combining this information, the presence of mid-myocardial scar may be revealed. Future studies should focus on the prognostic value of inverse ECG derived characteristics on clinical outcomes. Although the results are very promising, the accuracy and resolution of inverse ECG techniques still remains debatable. To further optimize the performance of the inverse ECG technique, we present a new method to model myocardial disease in ECG simulation in **Chapter 5**. With this approach, (partially) electrically active substrate was modelled and the effect of the substrate on the ECG was assessed. The new patch-based approach created a realistic relation between ECG waveforms and underlying activation sequences. Such a method can contribute to improved understanding of the effect of cardiomyopathy on obtained ECG, both for educational and clinical purposes.

Traditional inverse ECG techniques are mathematically complex and computationally demanding. They require many more leads to obtain an accurate estimation of the activation sequence than the standard 12-lead ECG, which in application is expensive and time-consuming. With CineECG, a new method was introduced in an attempt to image key features of the activation sequence that are difficult to reliably obtain from the ECG. Additional information is obtained as CineECG relates cardiac electrical activity to cardiac anatomy. The technique uses just the standard 12-lead ECG thereby minimizing the additional burden of electrode numbers. In **Chapter 6** CineECG was conceptually validated in cases of bundle branch blocks and the CineECG indicated the anatomical location of the bundle branch block, whereby the terminal part of the CineECG contained the most information. After further evaluation, the method was optimized and validated through a simulation study, as described in **Chapter 7**. Overall, CineECG captured significant features of activation sequences and is robust for electrode misplacement and use of generic anatomical model. The obtained CineECG was recovered dominant features of invasively measured activation sequences. The study indicated that CineECG provides succinct but realistic information regarding the average activation sequence.

The most widespread use of the standard 12-lead ECG in current clinical practice is to assess cardiac rhythm, investigate waveform morphology and conduction times by performing standardized measurements. Specifically in the detection of arrhythmogenic cardiomyopathy, changes in the complete waveform morphology are of interest, but currently only changes at the end of the QRS complex and global changes of the T-wave are used to monitor disease progression. Other signs of disease progression may be contained within the captured ECG, but accurate assessment of such subtle changes is limited as inconsistencies in electrode positioning also result in ECG waveform changes. In such cases, it remains uncertain whether differences between subsequent ECGs are due to pathology or electrode (mis)placement. To this end, we introduce a method to reduce electrode placement misplacement (**Chapter 8**). The application of a 3D-camera reduced the variation in obtained ECG waveforms and its derived measurements compared to current clinical practice. With this new technique, the identification of subtle changes in the QRS complex during arrhythmogenic cardiomyopathy follow-up may be improved. Subtle signs of disease are present in the ECG but currently undetectable by the human eye, as indicated by the recently developed ECG-based artificial intelligence algorithms. In **Chapter 9**, we describe how such algorithms may aid current clinical practice together with its potential benefits and challenges. New ECG features, automatic ECG diagnostics and improved clinical insight can be obtained using artificial intelligence techniques. With such algorithms, the complex nature of disease progression in arrhythmogenic cardiomyopathy may be further unraveled. But to ensure the correct use of artificial intelligence in a clinical setting, explainability of methods should be improved and end-users should be able to recognize the limitations of the technique.

To conclude the thesis, the application of techniques presented in this thesis to enhance diagnosis and risk-stratification in arrhythmogenic cardiomyopathy is described in **Chapter 10**. The techniques are viewed within the context of possible fields of application in current clinical practice. The described inverse ECG techniques (Part I and II) may provide complementary information by providing in-depth characterization of the arrhythmogenic substrate (Part I) or a global view on cardiac activation (Part II) linked to anatomy. The added value of these techniques in the current diagnostic work-up and risk-stratification for arrhythmogenic cardiomyopathy should be investigated in future studies. By further enhancing the diagnostic yield of the 12-lead ECG (Part III), early detection and risk-stratification in arrhythmogenic cardiomyopathy will likely be further enhanced.

## Nederlandse samenvatting

Het electrocardiogram (ECG), ook wel hartfilmpje genoemd, speelt een belangrijke rol in het systematisch beoordelen van de elektrische activiteit van het hart. Het standaard 12-kanaals ECG geeft hierin echter alleen een globaal inzicht. Met niet-invasieve inverse ECG-technieken kan extra informatie worden verkregen over de elektrische hartactiviteit door deze te koppelen aan de hart anatomie. Hiermee kunnen mogelijk subtiele tekenen van ziekteprogressie worden gedetecteerd bij patiënten met aritmogene cardiomyopathie, ook wanneer er verder nog geen uitingen van ziekte zijn gevonden.

Aritmogene cardiomyopathie wordt gekenmerkt door zowel een structurele- als elektrische veranderingen in hartspierweefsel en kan zich uiten in verschillende, mogelijk ook fatale, vormen. Aritmogene cardiomyopathie werd eerder beschreven als een ziekte die voornamelijk, maar niet alleen, het rechterventrikel aantast en werd daarom aritmogene rechterventrikel cardiomyopathie genoemd; de best omschreven vorm van aritmogene cardiomyopathie. Een verhoogd besef van het bestaan van aritmogene cardiomyopathie in combinatie met de ontwikkelingen binnen genetisch onderzoek heeft ervoor gezorgd dat er bij steeds meer mensen een erfelijke aanleg voor aritmogene cardiomyopathie wordt vastgesteld zonder dat ze tekenen van ziekte hebben. Bij hen bestaat de kans dat aritmogene cardiomyopathie zich ontwikkelt, maar het is onbekend wanneer, in wat voor vorm en hoe ernstig de ziekte zich zal uiten. Daarom worden deze mensen klinisch regelmatig gecontroleerd op uitingen van aritmogene cardiomyopathie. Elektrische veranderingen in de hartspier kunnen voorafgaan aan structurele en mechanische veranderingen en plotse hartdood kan het eerste teken zijn van ziekte. Daarom is adequate vroeg-detectie en risico-stratificatie erg belangrijk. De Task Force Criteria voor aritmogene rechterventrikel cardiomyopathie zijn opgesteld om klinische diagnose te standaardiseren, maar adequate risico-stratificatie blijft een uitdaging. In dit proefschrift worden verschillende op het ECG gebaseerde technieken omschreven die mogelijk adequate vroeg-detectie en risico-stratificatie bij aritmogene cardiomyopathie kunnen verbeteren, zoals omschreven in **Hoofdstuk 1**.

In het eerste deel van dit proefschrift wordt de optimalisatie van een traditionele inverse ECG techniek omschreven. Met deze techniek wordt op een niet-invasieve manier gedetailleerd inzicht verkregen in de elektrische hartactiviteit door een 67-kanaals ECG te combineren met patiënt specifieke anatomische modellen. Het gebruik van deze inverse ECG techniek bij mensen met een erfelijke aanleg voor aritmogene cardiomyopathie zou de huidige klinische diagnostiek en risico-stratificatie kunnen verbeteren. Met de inverse ECG technieken omschreven in de wetenschappelijke literatuur kan een goede schatting worden gemaakt van de elektrische hartactiviteit bij ventriculaire pacing of een prematuur ventriculaire complex. Maar voor het schatten van normale elektrische hartactiviteit (sinusritme), zijn deze inverse ECG

technieken echter niet accuraat genoeg. Om vroege tekenen van aritmogene cardiomyopathie te kunnen detecteren, is nauwkeurige beeldvorming van sinusritme juist erg belangrijk. In **Hoofdstuk 2** beschrijven we ons werk over de optimalisatie van de inverse ECG techniek voor het schatten van sinusritme en laten we zien hoe goed de nieuwe techniek normale elektrische hartactiviteit kan schatten. Door een patiënt-specifiek, op anatomie gebaseerd model van het His-Purkinje systeem toe te voegen aan de inverse ECG techniek, wordt een fysiologisch realistische en robuuste schatting van normale elektrische hartactiviteit verkregen. In **Hoofdstuk 3** wordt de overeenstemming tussen de niet-invasieve met inverse ECG geschatte en invasief gemeten elektrische hartactiviteit beschreven. Over het algemeen kwamen de met inverse ECG geschatte activatiepatronen goed overeen met de invasief gemeten patronen, ook bij smalle QRS-complexen. Met de geoptimaliseerde inverse ECG techniek werden lokale afwijkingen in elektrische hartactiviteit ontdekt bij mensen met een erfelijke aanleg voor aritmogene cardiomyopathie zonder tekenen van ziekte uiting, dit is omschreven in **Hoofdstuk 4**. Deze proof-of-concept studie geeft de indicatie dat we met de geoptimaliseerde inverse ECG techniek op een niet-invasieve manier inzicht kunnen krijgen in lokale elektrofysiologische karakteristieken van het aritmogene substraat. Naast inzicht in de elektrische hartactiviteit over de hartwand heen, kan ook inzicht worden verkregen in elektrische hartactiviteit door de wand heen. Door deze informatie te combineren kan de aanwezigheid van ziek hartspierweefsel middenin de hartwand mogelijk ook worden ontdekt. Verdere studies zijn nodig om de prognostische waarde van het gebruik van de geoptimaliseerde inverse ECG techniek op klinische uitkomsten uit te wijzen. De resultaten van deze studie zijn veelbelovend, maar de nauwkeurigheid en resolutie van de inverse ECG techniek blijft discutabel. Om de nauwkeurigheid van de inverse ECG techniek verder te optimaliseren beschrijven we in **Hoofdstuk 5** een methode om hartspierziekte te modelleren in ECG-simulaties. Met deze methode werd (gedeeltelijk) elektrisch actief hartspierweefsel gemodelleerd en het effect op het ECG werd onderzocht. Met de nieuwe methode werd een realistische relatie tussen ECG-golfvormen en elektrische hartactiviteit gerealiseerd. Met de methode kan een beter begrip van het effect van hartspierweefselziekte op het opgenomen ECG worden verkregen, zowel voor educatieve als klinische doeleinden.

Traditionele inverse ECG technieken zijn wiskundig complex en vergen veel rekenkracht. De technieken hebben veel meer ECG-afleidingen nodig om een accurate inschatting te maken van de elektrische hartactiviteit dan de standaard 12-kanaals ECG, waardoor de toepassing van deze technieken in de klinische praktijk duur en tijdrovend is. CineECG is een nieuwe methode die belangrijke kenmerken van de elektrische hartactiviteit in kaart probeert te brengen die lastig uit het ECG af te leiden zijn. Deze extra informatie is verkregen doordat CineECG de elektrische hartactiviteit relateert aan de hart anatomie. De techniek maakt gebruik van het standaard 12-kanaals ECG, waarmee het elektroden aantal wordt geminimaliseerd. In **Hoofdstuk**

**6** wordt CineECG conceptueel gevalideerd in patiënten met een bundeltakblok en de CineECG gaf inzicht in de anatomische locatie van dat bundeltakblok. Het laatste deel van de CineECG bevatte daarvoor de meeste informatie. De methode werd verder geoptimaliseerd en gevalideerd in een simulatiestudie, zoals beschreven in **Hoofdstuk 7**. Met CineECG werden belangrijke kenmerken van de elektrische hartactiviteit vastgelegd en de uitkomst was bestand tegen electrode plaatsing en het gebruik van een algemeen anatomisch model. Dominante kenmerken van invasief gemeten elektrische hartactiviteit waren aanwezig in de CineECG. Uit de studie bleek dat CineECG beknopte maar realistische informatie geeft over de globale elektrische hartactiviteit.

In de huidige klinische praktijk wordt het standaard 12-kanaals ECG gebruikt voor het beoordelen van het hartritme, golfvorm morfologie en geleidingstijden door gestandaardiseerde metingen te doen. Om aritmogene cardiomyopathie te detecteren is het observeren van (subtiële) veranderingen van de ECG golfvorm van belang, momenteel worden echter alleen veranderingen aan het eind van het QRS-complex of globale veranderingen in de T-golf gebruikt voor monitoring. Tekenen van ziekteprogressie kunnen aanwezig zijn in het opgenomen ECG, maar momenteel wordt nauwkeurige beoordeling van zulke subtiële veranderingen gelimiteerd door variatie in ECG electrode positie, wat direct effect heeft op de opgenomen ECG-golfvormen. Hierdoor is het onzeker of golfvorm verschillen tussen ECG's worden veroorzaakt door ziekteprogressie of afwijking in ECG electrode positie. Daarvoor wordt in **Hoofdstuk 8** een methode geïntroduceerd om de variatie in electrode herplaatsing te verkleinen. Het gebruik van de 3D-camera gebaseerde techniek verminderde de variatie in opgenomen ECG-golfvormen en de daarvan afgeleide metingen in vergelijking tot de methode die momenteel wordt gebruikt in de kliniek. Met de nieuwe techniek kan inzicht worden verkregen in subtiële veranderingen van ECG-golfvormen, waarmee de detectie van ziekteprogressie kan worden verbeterd. Dat er subtiële tekenen van hartspierziekte aanwezig zijn in het ECG die niet altijd duidelijk waarneembaar zijn wordt geïmpliceerd door recent ontwikkelde op ECG-gebaseerde kunstmatige (artificial) intelligentie algoritmen. In **Hoofdstuk 9** beschrijven we hoe dergelijke algoritmen de huidige klinische praktijk kunnen ondersteunen en wat potentiële voordelen en uitdagingen zijn bij het gebruik van zulke algoritmen. Met behulp van kunstmatige intelligentie technieken zouden nieuwe ECG kenmerken, automatische ECG diagnose en extra klinische kennis kunnen worden verkregen. De complexe aard van ziekteprogressie bij aritmogene cardiomyopathie kan hiermee verder worden ontrafeld. Om een juist gebruik van zulke technieken te verzekeren in de klinische setting is het echter van belang om te onderzoeken waarop een algoritme een beslissing maakt en moeten eindgebruikers de beperkingen van de techniek kunnen herkennen.

Ter afsluiting van de thesis wordt in **Hoofdstuk 10** de toepassing van de technieken beschreven voor de verbetering van de diagnose en risico-stratificatie bij aritmogene cardiomyopathie. De technieken worden bediscussieerd in de context van de mogelijke toepassing in de klinische praktijk. Verder worden suggesties gedaan voor toekomstig onderzoek om de technieken verder te verbeteren. De beschreven inverse ECG-technieken (Deel I en II) kunnen aanvullende informatie geven over het aritmogene substraat (Deel I) en het globale beeld van de elektrische hartactiviteit (Deel II) gekoppeld aan de hartanatomie verduidelijken. Er worden suggesties gedaan voor toekomstige studies ter verbetering van deze technieken. De toegevoegde waarde van de technieken binnen het huidige diagnostisch onderzoek zal in toekomstige studies verder moeten worden onderzocht. Verbetering van de diagnostische waarde van het 12-leads ECG (deel III) kan de vroeg-detectie en risico-stratificatie bij aritmogene cardiomyopathie waarschijnlijk verbeteren.



## List of publications

1. Big Data and Artificial Intelligence: Opportunities and Threats in Electrophysiology. **MJ Boonstra\***, RR van de Leur\*, A Bagheri, RW Roudijk, A Sammani, K Taha, PAFM Doevendans, P van der Harst, PM van Dam, RJ Hassink, R van Es, and FW Asselbergs. \*Denotes shared first authorship. *Arrhythmia & Electrophysiology Review*, 2020.
2. Novel CineECG enables anatomical 3D localization and classification of bundle branch blocks. **MJ Boonstra**, BN Hilderink, ET Locati, FW Asselbergs, P Loh, and PM van Dam. *EP Europace*, 2020.
3. Feasibility study of a 3D camera to reduce electrode repositioning errors during longitudinal ECG acquisition. **MJ Boonstra\***, RW Roudijk\*, J Ruisch, M Kastelein, E van Dam, M Schellenkens, P Loh, and P.M.van Dam. \* Denotes shared first author ship. *Journal of Electrocardiology*, 2021.
4. Risk stratification and subclinical phenotyping of dilated and/or arrhythmogenic cardiomyopathy mutation-positive relatives: CVON eDETECT consortium. RW Roudijk, K Taha, M Bourfiss, P Loh, L van den Heuvel, **MJ Boonstra**, F van Lint et al. *Netherlands Heart Journal*, 2021.
5. Comparing Non-invasive Inverse Electrocardiography With Invasive Endocardial and Epicardial Electroanatomical Mapping During Sinus Rhythm. **MJ Boonstra\***, RW Roudijk\*, R Brummel, W Kassenberg, LJ Blom, TF Oostendorp, ASJM te Riele, JF van der Heijden, FW Asselbergs, PM van Dam, and P Loh. \* Denotes shared first author ship. *Frontiers in Physiology*, 2021.
6. Modeling the His-Purkinje Effect in Non-invasive Estimation of Endocardial and Epicardial Ventricular Activation. **MJ Boonstra\***, RW Roudijk\*, R Brummel, W Kassenberg, LJ Blom, TF Oostendorp, ASJM te Riele, JF van der Heijden, FW Asselbergs, PM van Dam, and P Loh. \* Denotes shared first author ship. *Annals in Biomedical Engineering*, 2021.
7. CineECG: A novel method to image the average activation sequence in the heart from the 12-lead ECG. **MJ Boonstra**, DH Brooks, P Loh, and PM van Dam. *Computers in Biology and Medicine*, 2021.
8. Uncertainty quantification of the effects of segmentation variability in ecgi. JD Tate, WW Good, N Zenzemi, **MJ Boonstra**, PM van Dam, DH Brooks, A Narayan, and RS MacLeod. *International Conference on Functional Imaging and Modeling of the Heart*, 2021.
9. The relation of 12 lead ECG to the cardiac anatomy: the normal CineECG. PM van Dam, **MJ Boonstra**, ET Locati, and P Loh. *Journal of Electrocardiology*, 2021.
10. ECG-based techniques to enhance clinical practice in cardiac genetic disease management. **MJ Boonstra**, M Kloosterman, I van der Schaaf, RW Roudijk, PM van Dam, and P Loh. *Journal of Electrocardiology*, 2022.
11. The Effect of Segmentation Variability in Forward ECG Simulation. Ondrusova B, **Boonstra MJ**, Svehlikova J, Brooks D, van Dam P, Rababah AS, Narayan A, MacLeod R, Zenzemi N, Tate J. *Computing in Cardiology, IEEE*, 2022.
12. Effect of Segmentation Uncertainty on the ECGI Inverse Problem Solution and Source Localization. N Gassa, **MJ Boonstra**, B Ondrusova, J Svehlikova, D Brooks, A Narayan, AS Rababah, PM van Dam, RS MacLeod, JD Tate, N Zenzemi. *Computing in Cardiology, IEEE*, 2022.
13. CineECG illustrating the ventricular activation sequence in progressive AV-junctional conduction block. I van der Schaaf, M Kloosterman, **MJ Boonstra**, PM van Dam, APM Gorgels. *Journal of Electrocardiology* 2023.
14. Non-invasive inverse ECG for the early detection and risk-stratification in arrhythmogenic cardiomyopathy, a proof-of-concept study. **MJ Boonstra**, RW Roudijk, M Bourfiss, M Kloosterman, LJ Blom, J Ruisch, I van der Schaaf, BK Velthuis, FW Asselbergs, ASJM te Riele, PM van Dam, P Loh. In preparation.
15. Natural course of electrocardiographic features in Arrhythmogenic Right Ventricular Cardiomyopathy in relation to ventricular arrhythmic events. A Svensson, J Carlson, H Kjaerulf Jensen, **MJ Boonstra**, M Tétreault-Langlois, P Dahlberg, H Bundgaard, A Hørby Christensen, JH Svendsen, J Cadrin-Tourigny, ASJM te Riele, PG Platonov. In preparation.

## Dankwoord / Acknowledgements

De afgelopen jaren heb ik met veel plezier promotieonderzoek mogen doen bij de afdeling cardiologie van het UMC Utrecht. Het onderzoek dat beschreven staat in dit proefschrift was zonder alle mensen die daarbij betrokken waren niet mogelijk geweest. Ik wil graag iedereen bedanken die een directe of indirecte bijdrage heeft geleverd aan dit proefschrift. In het bijzonder wil ik bedanken:

Mijn promotor, beste **Folkert**, bedankt voor al je hulp en begeleiding tijdens het promotietraject. Er is geen moment geweest dat jij niet klaar staat, altijd kwam er een snelle reactie terug. Ideeën over nieuwe projecten, snelle gedachtengangen en je visie op het grote plaatje in combinatie met je diverse onderzoeksgroep hebben me altijd gestimuleerd groter te denken en verder te gaan. Heel erg bedankt voor al je hulp, de gezellige uitjes en ook de mogelijkheid verder te gaan met onderzoek!

Mijn co-promotoren, **Peter** en **Peter**, haha ja welke bedoel ik nou? Uit de mailtjes en tijdens de wekelijkse besprekingen werd dat vaak gelukkig wel snel duidelijk; binnen de elektrofysiologie duidelijk een eigen domein.

Beste **Peter-techniek**, ik weet nog goed dat ik in mijn eerste week in Nieuwerbrug langs kwam en je me alle scripts, programma's, data, boeken, artikelen en wat nog allemaal nog meer gaf. Na een snelle uitleg en installatie van GeomPEACS zei je "Ja ga er maar gewoon mee bezig, daar leer je het meest van!" en zat ik die dag direct met mijn handen in de onderzoeks-modder. Al dacht ik dat moment *hoe ga ik alles begrijpen en weten?!*, was het een grote stimulans dat juist deze manier centraal stond en heb ik daar heel veel van geleerd. Bedankt voor al je vertrouwen, mogelijkheden, spar- en nadenk momenten, snelle oplossingen, vernieuwende blikken, en vooral ook enthousiasme tijdens het traject.

Beste **Peter-kliniek**, bedankt voor alle vertrouwen op zowel op technisch als klinisch aspect. Ik heb altijd veel geleerd van de wekelijkse besprekingen, EAM en onderzoeks besprekingen. Met soms toch echt wel wat extra context van mij over de technische punten die werden besproken gaf je input van de klinische kant veel waardevolle inzichten. Heel erg bedankt hulp, input en oog voor klinisch detail en toepassingen, ik heb daar veel van geleerd.

I would like to thank the members of my assessment committee **Prof. dr. O. Doessel**, **Prof. dr. P.A.F.M. Doevendans**, **Prof. dr. R.S. MacLeod**, **Prof. dr. J.P. van Tintelen**, **Prof. dr. M.A. Vos** for taking the time to review this thesis.

I would like to thank all co-authors and colleagues for their contributions to the research described in this thesis. **Thom**, bedankt voor je enthousiasme, tijd, de mogelijkheid tot samenwerking en de input die je gaf vanuit de technische basis. Ik

heb heel erg veel van je geleerd en de manier waarop je de meest lastige technische onderwerpen wist te verwoorden dat het bijna simpel leek, daarvan sta ik nog steeds versteld. **Dana**, it was a pleasure working together and discussing the mathematical basis of the CineECG technique. Your eye for detail on methodological aspects, thoroughness and honest opinion were truly amazing and your happy smile when talking about your travels to your family made my days.

Aan alle leden van het ACM-onderzoeksteam van het UMC Utrecht willen bedanken en de ACM-dokters, in het bijzonder **Judith** en **Jeroen**, voor het gedetailleerd vastleggen van de klinische bevindingen bij ACM-patiënten en jullie bereidheid bij te dragen aan het ECGi onderzoek. **Anneline**, heel erg bedankt voor de samenwerking en input over de vroegdetectie van ACM substraat met ECGi technieken, je oog voor detail, doorzettingsvermogen en enthousiasme zijn bewonderingswaardig. **Maarten-Jan**, heel erg bedankt voor je enthousiasme en ideeën, er is nog zo super veel leuks te doen! **Toon**, bedankt voor je interesse, kritische en leuke vragen en je input op het ECGi werk vanuit de medische fysiologie, daar heb ik veel van geleerd. **Peter** (van Tintelen), bedankt voor je enthousiasme, kennis en out-of-the-box vragen binnen de genetische context, dit gaf veel enthousiasme verder te denken.

De belletjes met **Martin**, **Eelco** en **Hans** hebben vaak metingen, voortgangsverslagen en grant-aanvragen gered. Welke storing of vraag dan ook, jullie stonden altijd klaar met een snel antwoord en oplossing. De keren dat ik bij jullie mocht werken in Nieuwerbrug waren altijd een feestje. Heel erg bedankt voor jullie hulp en vooral ook gezelligheid!

Aan alle leden van de staf cardiologie van het UMC Utrecht, bedankt voor alle onderwijsmomenten en de mogelijkheid van jullie te leren. Alle HCK-helden, bedankt voor de gezelligheid tijdens de procedures. **Wil** en **Rolf**, bedankt voor jullie hulp, grapjes, tijd, inzicht en uitleg bij het maken van de EAM maps. **Marcel**, heel erg bedankt voor je enthousiasme en hulp met het Ensite systeem. Je uitleg, enthousiasme en technische kennis wakkerden mijn enthousiasme alleen maar verder aan.

Bedankt alle medewerkers van de hart- en longfunctie voor jullie enthousiaste gesprekken, altijd bereidheid tot het zoeken van een oplossing en vooral ook de sleutel voor de meetapparatuur! **Laura**, **Dorine** en **Mitzy** heel erg bedankt voor jullie hulp bij het regelen van kamertjes voor metingen, enthousiasme en altijd tijd voor een vrolijk gesprek! **Sergio**, heel erg bedankt voor je hulp bij de metingen, we konden altijd op je rekenen en je vraag of ik weer zo veel elektroden ging plakken maakte altijd mijn dag. De dames van het stafsecretariaat, **Katinka**, **Sylvia**, **Tamara** en **Christa**, heel erg bedankt voor jullie hulp altijd en dat ik af en toe bij jullie mocht komen werken, dat was altijd erg gezellig! **Jantine**, heel erg bedankt voor alles, ja echt alles, waar je ons in ondersteunde, er was niets wat je niet wist.

Bedankt aan alle mede-onderzoekers binnen het UMC Utrecht bij de cardiologie, medische fysiologie, experimentele cardiologie en klinische genetica, **Stephanie, Esmee, Diantha, Marijn, Rutger, Philippe, Floriaan, Mehran, Marion, Jorna, Frank, Magdalena, Alicia, Rosanne, Nicole, Anne-Mar, Timion, Hugo**, bedankt voor jullie interesse in het onderzoek en gezelligheid tussen het werk door, tijdens overleggen, koffie momentjes, congressen, etentjes en uitjes. In het speciaal ook de Asselbergsgroepsgeenootjes; **Mimount, Marijke, Rob, Janine, Feddo, Karim, Arjan, Laurens, Lieke, Fahima, Mark, Steven** en **Thomas**, bedankt voor alle gezelligheid op de kamer, tijdens de bi-weekly's, verwondering Folkert's snelle denkproces, etentjes en uitjes. Het was altijd gezellig, zeiltochtjes soms spannend en er was altijd ruimte voor een goed gesprek. **Manon** en **Iris**, ik vind het echt heel leuk dat jullie het ECGi werk doorzetten en vond het heel leuk dat ik jullie start in jullie PhD traject heb mee mogen maken. Heel veel succes en ook vooral plezier en ik blijf heel benieuwd wat jullie allemaal zullen vinden! **Yvonne**, although you often took away the sunlight in the room, you always brightened my day. Together we reduced the overall room-stress level with good conversations, laughter and the best input on manuscript figures, thanks a lot. **Sanne**, bedankt voor alle meet, electrodeplak, -geklodder en -gepoets, koffie-, cup-a-soup-, en vooral ook gezellige momenten samen tot in de late uurtjes. We konden samen alles relativeren, bedankt voor alle goede gesprekken, je hulp en interesse op persoonlijk en op onderzoeks gebied.

Alle studenten, **Laura, Janna** en **Manon** bedankt voor jullie enthousiasme, interesse en inzet voor de projecten, ik vond het erg leuk samen te werken en van jullie te leren! **Manon**, eerst een M2, toen M3, nu Ph'er, super leuk dat je bij ons bleef. Heel veel succes en plezier, ik hoop dat er nog veel 'leuke' BSMs je kant op komen en weet zeker dat je repolarisatie verder zal ontrafelen!

Mijn TG-studievrienden, **Judith, Iris, Wouter, Mathijs** en **Eline**, al was het niet vaak, wanneer we elkaar zagen was het altijd gezellig, bedankt daarvoor en ik vond het erg leuk dat je me kwam vergezellen in Utrecht **Eline!**

To all national and international colleagues in the ECG imaging community, many thanks for the opportunity to be a part of your enthusiastic, supportive and research minded group. Thanks for all the interesting meetings and discussions, it showed me the strength of collaboration and trust in research. **Jess, Rob, Beata, Jana, Nejib, Narimane** and **Ali**, thanks for our collaboration in the CEI-MB working group, the discussions always inspired me and I learned a lot. I always looked forward to our meetings. **Beata**, I really loved working together on the forward simulation project and in the process, we became very good friends. Thanks a lot for all your time and support both in personal and work live, they always make me smile from ear to ear. **Jake** and **Job**, thanks for being co-chairs during the executive board meetings and **Nika**, you are a true inspiration, thanks for starting the CEI-ML group.

To all my new colleagues of the datatools4heart consortium, medical informatics department and department of cardiology at the Amsterdam UMC, many thanks for welcoming me, making me a part of your groups and your positive energy during the last phase of my PhD. **Xènia**, I love to keep on laughing our eyes out together when working on much more ethical and study annexes!

Mijn middelbare school viendinnetjes, **Maja**, **Annelies** en **Carlijn**, ook al zagen we elkaar weinig, het was altijd gezellig en we zaten zo weer in ons oude vertrouwde gedrag; lekker kinderachtig maar heel fijn. **Maja**, bedankt voor alle wandeling met de altijd enthousiaste Nout en Linneke door de zon, regen en wind in het wonderschone maar drekkige Almere. De momenten en avonden samen dat waren voor mij echte oplaad momenten en door de goede gesprekken die we hadden kwam ik vaak toch weer met beide benen op de grond en gaven me energie door te zetten.

Mijn paranimfen, **Fahima** en **Rob**, ik vind het een eer dat jullie aan mijn zijde willen staan, heel erg bedankt! **Rob**, ik vond het erg leuk intensief met je samen te werken op de projecten en heb veel van je geleerd. **Fahima**, bedankt voor alle fijne gesprekken samen, ook al zijn onze onderzoeksonderwerpen totaal anders, we kwamen goed door onze struggles heen.

Lieve **pap** en **mam**, bedankt voor jullie onvoorwaardelijke steun in alles wat ik doe. Jullie staan altijd voor me klaar en ik kan altijd bij jullie terecht. Pap, de telefoongesprekken over de wetenschapsbijlage, mijn onderzoek, onze taal, en wat dan niet ook waren altijd genieten. Bedankt voor jullie rust en ook de rem die jullie er soms op zetten. Lieve **Eltjo** en **Jente**, mijn grote kleine broertjes. Heel erg bedankt voor jullie steun, maar ook vooral voor de mogelijkheid gewoon soms thuis even lekker gewoon debiel te zijn, nu ook samen met **Miranda**. Lieve **oma**, **Boonstra-** en **Zwaagstra-familie** heel erg bedankt voor jullie interesse en steun. Elke keer als we elkaar zagen kon ik rekenen op bemoedigende woorden, vernieuwende inzichten en vooral ook leuke, gezellige en fijne momenten. **Rima**, **Nico** en **Sarah**, bedankt voor alle fijne en ontspannende avonden en jullie interesse in het werk dat ik doe.

Lieve **Bashar**, jij kent me als geen ander en bent de afgelopen jaren mijn grootste steun geweest. Je weet wat ik denk en samen vinden we altijd een antwoord op welke vraag dan ook, of het nou onderzoek of persoonlijk is. Bedankt voor al je hulp, vertrouwen en steun, dat je altijd klaarstaat, je eerlijkheid dat iets soms niet zo verstandig is en dat ik nu toch wel echt even een gewichtje omhoog moet. Zonder jouw liefde, steun en vertrouwen had ik hier nu niet gestaan. Bedankt voor alle mooie momenten samen en alle keren dat we buikpijn hadden van het lachen. Ik vind het echt heel erg fijn hoe we tot in de diepte kunnen praten, hoe je altijd alles begrijpt, soms misschien nog ook wel eens beter dan ik. Ik kijk heel erg uit naar het maken van heel veel nieuwe mooie herinneringen samen.



## Curriculum vitae

Machteld Johanna Boonstra was born on 25 August 1993 in Groningen, to Albert Louis Boonstra and Alida Zwaagstra and grew up in Yde together with her younger brothers. She graduated secondary education at the Maartenscollege, Haren, in 2011. She started the academic program Technical Medicine at the University of Twente, Enschede, September 2011. The program provided a solid background in science, technology medicine and patient care. Next to her studies, Machteld volunteered at Scouting Vries and was an active committee member at her study association, SV Paradoks. During her masters program she specialized in medical signal analysis and physiology. Machteld has conducted internships at various different clinical sites, including the department of intensive care medicine (Radboud UMC, Nijmegen), pediatrics (Medisch Spectrum Twente, Enschede), otorhinolaryngology (Radboud UMC, Nijmegen), and the transplant center (UMC Groningen, Groningen). In July 2018, she graduated under the supervision of Paul Elbers at the intensive care unit of the VU Medical Center, Amsterdam. Her master thesis focused on assessing right ventricular contractile function using echocardiography in ICU patients. During her internship, she also discovered her interest in electrocardiography. From August 2018 to December 2018, she supervised exercise tests at the department of cardiology in the Amsterdam UMC, and improved her ability in ECG interpretation. Following, she started her PhD on ECG imaging supervised by dr. Peter van Dam, dr. Peter Loh, and prof. dr. Folkert Asselbergs at the department of cardiology in the UMC Utrecht. During her PhD, she focussed on different ECG-based techniques for the detection and characterization of the arrhythmogenic substrate in pathogenic mutation carriers. During her time as a PhD student, she actively participated in the international consortium of ECG imaging as the chair of the model building working group, where she collaborated on describing the effect of variation in anatomical segmentation on the forward simulation of ECG signals. In 2022, she finished her PhD, the results of which are presented in this thesis.

After completing her PhD, Machteld aims to continue her career as a technical physician in the department of cardiology, focusing on the development and implementation of tools to improve cross-institutional collaboration in data-driven research.

